University of Modena and Reggio Emilia
Doctorate School in Industrial Innovation Engineering

Highly-regular Laser-induced Periodic Surface Structures: Mechanisms, Methods and Applications

Doctoral dissertation of:
Iaroslav Gnilitskyi

Advisor:
Prof. Leonardo Orazi

Doctorate School Dean:
Mauro Dell'Amico

This dissertation is submitted for the degree of
Doctor of Philosophy
2017 – XXVIII Cycle

Abstract

The nanostructures with excellent uniformity also known as Laser-Induced Periodic Surface Structures (LIPSS) were observed for the first time in 1965. Since that time and until our days LIPSS based applications have been characterized by low-speed, lack of uniformity and poor repeatability over large areas. A relatively low speed in LIPSS generation strongly limits the transfer of LIPSS direct-writing methods from laboratories to industry. Presented in this thesis, highly-regular LIPSS (HR-LIPSS) overcomes all these problems and permit the fabrication of extremely uniform nanostructures, with excellent long-range repeatability and at high-speed. HR-LIPSS show bifurcation-free structure evenly treated at the rate acceptable for industrial use. HR-LIPSS have been generated on surfaces of Mo, various types of steel, Ti, Ti alloy, Zr and Si setting new standards with regard to regularity and speed of treatment. A novel theoretical model is proposed to explain the regularity of the structures on a number of materials and predicts whether HR-LIPSS can be formed. The physical origin of the LIPSS regularity is identified and linked with the length of surface plasmon-polaritons (L_{SPP}), of the excited surface electromagnetic waves (SEWs). Moreover, the methods for ultrafast generation of HR-LIPSS on metallic and non-metallic surfaces is described in details. To generate HR-LIPSS three conditions must be simultaneously fulfilled, particularly, the relationship between the size of the area illuminated and the length of decay of the SEW; the relationship between the pulse duration and the time to obtain the thermodynamic equilibrium in the crystal lattice; the relationship between the applied intensity and the absorptivity of the material so as to obtain a strong ablation scheme. In this regime, the several competing and complementary processes that drive the evolution of the laser-excited surface under single or very few overlapping pulses are investigated. Further, HR-LIPSS on metals and semiconductors were systematically investigated in various fields including mechanics, medicines, optoelectronics, photovoltaics, electronics, nano-and-microfluidics, anti-icing and others. So, for tribological applications it was observed that LIPSS treatment modify the coefficient of friction in both dry and lubricated conditions. Results demonstrates a higher ratio of cells growth on laser-nanostructured surfaces compared to untreated ones for dental implants. It outlines the preliminary results of LIPSS treatment on surfaces of molds for micro injection molding to improve the flow of polymer.

Results on surface wettability outlined that HR-LIPSS treatments permit to change the surface behaviour from hydrophilic to hydrophobic behaviour on aluminium, copper and stainless steel surfaces. The presented results about the adhesive properties of nanotextured Ti6Al4V show the relationship between adhesion strength and LIPSS. This technology also showed eye-catching appearance and can serve as a decoration, counterfeit prevention or identification marking of any company products. Highly-regular laser induced 1D periodic surface structures on Si substrate with following Au nanoparticles self-assembling on the top of grating grooves support excitation of the surface plasmon resonance that opens a perspective for fabrication of unique and cheap plasmonic sensors. Finally, it should to noticed, that HR-LIPSS developed during this PhD course permits to produce a multifunctional surface that can be applied in numerous applications. The excellent control of generation laser-induced periodic structures at reduced number of pulses may now enable the new era of laser nanoprocessing on large area for the development of new applications.

Publications

Journal articles

“Mechanisms of high-regularity periodic structuring of silicon surface by sub-MHz repetition rate ultrashort laser pulses”, I. Gnilitskyi, V. Gruzdev, N. M. Bulgakova, T. Mocek and L. Orazi, Applied Physics Letters, doi: 10.1063/1.4963784 (2016).

"Innovative high-speed femtosecond laser nano-patterning for improved adhesive bonding of Ti6Al4V titanium alloy", G. Rotella, L. Orazi, M. Alfano, S. Candamano, Ia. Gnilitskyi, CIRP Journal of Manufacturing Science and Technology, doi: 10.1016/j.cirpj.2016.10.003 (2016).

“Nano Patterning of Stainless Steel with Nonlinear Laser Lithography for Enhanced Tribological Properties”, Ia. Gnilitskyi, F. Rotundo, I. Pavlov, S. Ilday, C. Martini, F. Omer Ilday and L. Orazi, Tribology International, doi: 10.1016/j.triboint.2016.03.011 (2015).

“Nonlinear Laser Litography to control surface properties in stainless steel”, L. Orazi, Ia. Gnilitskyi, I. Pavlov, P. Serro, S. Ilday, F. O. Ilday, CIRP Annals – Manufacturing Technology, v. 64, No. 1, pp. 193-196 (2015).

“The structure, phase composition and microhardness of vacuum-arc multilayered Ti/Al, Ti/Cu, Ti/Fe, Ti/Zr deposits with different thicknesses of alternating sublayers”, A. Demchyshyn, I. Gnilitskyi, L. Orazi, and A. Ascari, Applied Surface Science, v. 342, pp. 127-135 (2015).

"Laser nanopatterning for wettability applications", L. Orazi, I. Gnilitskyi and A. P. Serro, Journal of Micro-and Nano-Manufacturing, v. 5, 021008-1(2017).

Conference proceedings

“Diffraction Gratings Prepared by HR-LIPSS for New Surface Plasmon-Polariton Photodetectors & Sensors”, Iaroslav Gnilitskyi, Sergiy Mamykin, Mykhaylo Dusheyko, Tatiana Borodinova, Nataliya Maksimchuk and Leonardo Orazi, Frontiers in Optics 2016, New York, USA 17-21 October, 2016 (Poster presentation).

“Formation and Application of highly-regular LIPSS on Surface of Silicon Crystals”, Ia. Gnilitskyi, V. Gruzdev, N. M. Bulgakova, L. Orazi, Frontiers in Optics 2016, New York, USA 17-21 October, 2016 (Poster presentation).

"Highly Regular Nanostructuring of Si Surface by Ultrashort Laser Pulses", I. Gnilitskyi, L. Orazi, N. M. Bulgakova, V. Gruzdev, CLEO USA, San Jose, California, USA, 5-10 June, 2016 (Oral presentation).

"Self-assembling of Gold Nanoparticles on Si-based Laser Nanotextured 1D Surface for Plasmonic Application", I. Gnilitskyi, M. Dusheyko, T. Borodinova, S. Mamykin, N. Maksimchuk, A. Ivaschuk, Yu. Yakymenko and L. Orazi, CLEO USA, San Jose, California, USA, 5-10 June, 2016 (Oral presentation).

"Cell and Tissue Response to Modified by Laser-induced Periodic Surface Structures Biocompatible Materials for Dental Implants", Ia. Gnilitskyi, M. Pogorielov, D. Dobrota, R. Viter, L. Orazi and O. Mischenko, CLEO USA, San Jose, California, USA, 5-10 June, 2016 (Oral presentation).

"Silicon 1D nanostructuring: experiment, model and application", I. Gnilitskyi, L. Orazi, N. M. Bulgakova, V. Gruzdev, SLIMS, Venice, Italy, 2016.

"Highly Regular LIPSS on Silicon Decorated with Gold Nanoparticles for Plasmonic Applications", Ia. Gnilitskyi, L. Orazi, M. Dusheyko, T. Borodinova, S. Mamykin, N. Maksimchuk, A. Ivaschuk and Y. Yakymenko, IEEE 36th International Conference on Electronics and Nanotechnology ELNANO-2016, April 19-21, Kyiv, Ukraine

"Laser-Patterning of Stainless Steel with Nonlinear Laser Lithography for Enhanced Tribological Properties" Ia. Gnilitskyi, F. Rotundo, I. Pavlov, S. Ilday, C. Martini, F. Omer Ilday and L. Orazi, CLEO Europe, Munich, Germany, 21-25 June, 2015 (Oral presentation).

"Nonlinear Laser Lithography for Enhanced Tribological Properties", Ia. Gnilitskyi, I. Pavlov, F. Rotundo, L. Orazi, C. Martini and F. Omer Ilday, CLEO USA, 10-15 May, 2015, (Oral presentation).

"Strongly anisotropic wetting on highly-uniform self-similar molybdenum nanogrooves", Ia. Gnilitskyi, I. Pavlov, A. Rota, M. Messori, S. Ilday, S. Yavas, L. Orazi and F. Omer Ilday, NanoPT2015, Porto, Portugal ,11-13 February 2015 (Oral presentation).

"Effects of induced periodic surface structure technology on polymer filling flow and molded parts wettability in micro injection molding", Lucchetta G., Crema L., Sorgato M., Orazi L., Gnilitskyi I., (Proceedings of AITEM - National Italian Congress, Palermo, Italy, September 2015)

Patents

Gnilitskyi, I., Orazi, L., Derrien, T. J.-Y., Bulgakova, N. M. & Mocek, T. Method of ultrafast laser writing of highly-regular periodic structures on metallic materials (2016) with registration number **PV 2016 - 424,** data of registration: **11.07.2016**

Iaroslav Gnilitskyi, Sergiy Mamykin, Mykhaylo Dusheyko, Tatiana Borodinova, Nataliia Maksimchuk and Leonardo Orazi, Plasmon-polariton resonance platform for sensors/ biosensors based on highly-regular laser-induced surface periodic structures as a diffraction grating on the surface of a semiconductor (2016) with registration number **a 2016 10991,** data of registration: **01.11.2016**

Individual grants and prizes

Individual Grant from **Nanoscience Foundries & Fine Analysis (NFFA.eu)** on "Highly-regular laser-induced periodic surface structures for plasmonic applications" on period from 1.04.2017 to 1.08.2017

One of the best presentation on International conference NanoPT2015, Porto, Portugal ,11-13 February 2015. Topic of the presentation: “Strongly anisotropic wetting on highly-uniform self-similar molybdenum nanogrooves”.

Acknowledgments

This PhD thesis is the result of a collaborative work that involved more than 12 scientific groups and companies from different countries. Each of these groups has been made essential indirect contribution into this paper, and that's why I am under an obligation to them. The results of this collaboration were expressed in numerous articles, conferences, projects and even patents.

First of all, I would like to thank my supervisor Prof. Leonardo Orazi for assigning me such interesting topic and for assisting me within the whole process of the research. I am grateful to Leonardo for his support in numerous trips, also for his motivation, patience, advices and suggestions during my PhD.

Also, I would like to express my gratitude to prof. Fatih Omer Ilday and Dr. Ihor Pavlov for warm hosting me in their Ufolab in Bilkent University and allowing me to use their custom-built fiber femtosecond laser. Also, Prof. Omer Ilday taught me how to write papers in top-journals. I am so thankful to Dr. Pavlov who introduced to to the basics of fiber lasers construction me the basics of construction of fiber lasers.

I am also grateful to prof. Nadezhda M. Bulgakova and her research group, especially Thibault Derrien and Yoann Levy, who kindly helped me in theoretical and modelling support of my experiments.

The part of work, which is devoted to the issues of wettability, was done in lab of prof. Ana Paula Serro in Lisbon. There I have learned measurement of wetting in time, construction of unique experimental equipment and surface chemistry of materials. I would like to thank Prof. Ana Paula for her support and valuable advices.

The experiment and analysis on investigation tribological properties of nanostructures were carried out in Bologna University in collaboration with research group of prof. Carla Martini. I would like to thank her and Dr. Fabio Rotundo.

My sincere gratitude also goes to Prof. Maxim Pogorelov for hard work on medical experiments. The excellent results provided the basis for two European project proposals. I am grateful to Dr. Mykhaylo Dusheyko, Dr. Sergiy Mamykin and Dr. Tania Borodinova for their contribution in join research on plasmon resonance based on Si nanostructures. Also, I would like

to thank Giuseppe D'Amelio (Optoprim, Monza), who provided me with an opportunity to work in his lab on commercial femtosecond laser "Pharos".

Finally, I am grateful to Prof. Vitaly Gruzdev for hosting me and providing with theoretical support in his lab in Missouri University.

“Nothing is as it seems, but something is everything it is made out to be.” ― Carrol Bryant

Table of Contents

List of Figures

List of Tables

List of Acronyms

AB - Alamar Blue
AFM - atomic force microscope
AR - as received
BE - binding energies
CA - contact angle
CDEW - composite diffracted evanescent wave
COF - coefficient of friction
CT - chemical treatment
DLC - diamond-like carbon
DLOA - dispersion of LIPSS orientation angles
EDX - energy dispersive X-ray
ELID - electrolytic in-process dressing
EQE - external quantum efficiency
FDTD - finite-difference time domain
FIB - focus ion beam
FWHM - full with at half maximum
HDFa - Human Dermal Fibroblasts-Adult
HLIPSS - hexagonal laser-induced periodic surface structures
HR-LIPSS - highly-regular laser-induced periodic surface structures
HR-PS - highly-regular periodic structures
HSFL - high spatial frequency LIPSS
HWP - half-wave plate
LIPSS - laser-induced periodic surface structures
LSFL - low spatial frequency LIPSS
LSP - local surface plasmon
LT - laser treatment
µIM - micro injection molding
MSCs - mesenchymal stem cells
NLL - nonlinear laser lithography
NP - nanoparticles
PECVD - plasma chemical vapour deposition
RR - radiation remnants
SC - solar cells
SEM - scanning electron microscope
SEWs - surface electromagnetic waves
SP - surface plasmon
SPP - surface plasmon-polariton
SPPW - surface plasmon polariton wave
TAL - treated aluminium
TCU - treated cooper
TSS - treated stainless steel
TTM - two-temperature model

UV - ultra-violet
XPS - X-ray photoelectron spectroscopy

Chapter 1 Introduction

Functional nanostructured surfaces are of high interest for various scientific, biomedical and industrial applications. Numerous methods exist to produce nanostructured surfaces based on sputtering, chemical and plasma etching, chemical vapour deposition, self-assembly, nanoimprint, optical and physical lithography. Lithography techniques such as electron- and focused-ion- beam, and photolithography are most commonly used and provide high-precision nanostructuring. However, the lithography methods are multi-step, employing masks that make them costly and time-consuming.

Ultrashort laser irradiation is proven as a robust, cheaper alternative to lithography to nanostructure surfaces of various materials via formation of so-called laser-induced periodic surface structures (LIPSS). Several application fields have emerged, based on this process, such as modification of surface wetting and tribology properties, surface coloration and marking.

Achieving the control over nanostructure formation in these applications remains difficult because of high sensitivity of this process to the type of material and laser irradiation parameters that hinders reproducibility and uniformity of periodic patterns. Although the first observation of LIPSS made by Milton Birnbaum in 1965 revealed their good regularity considerable progress in controlling precision of LIPSS fabrication was made not long ago, though limited to specific materials.

LIPSS are a universal phenomenon that can be fabricated on metals, semiconductors and dielectrics upon irradiation with linearly polarized laser light. LIPSS usually occur as a surface relief composed by periodic structures. These periodic structures have strong correlation to laser wavelength and polarization. LIPSS can be generated for a wide range of pulse durations, even from continuous wave irradiation down to only a few femtoseconds.

From a fundamental point of view, the modelling of formation of proper regular LIPSS is a challenge in spite of more than two decades of research in that field. Mechanisms of LIPSS formation by femtosecond laser pulses are still not completely understood, but the common approach is based on the concept of interference between incident laser beam and laser-excited surface plasmon-polaritons supported by the presence of free electrons in metals.

From a technological point of view, LIPSS have a strong potential for industrial applications. As mentioned above, traditional optical fabrication techniques as optical lithography techniques require complex masks, while conventional lithography techniques such as e-beam lithography and ion-beam lithography require expensive equipment. Over those techniques LIPSS have several advantages, such as:

(i) Ability to process nearly all types of materials, including metals, semiconductors, glasses, and polymers;

(ii) Potential capability of processing non-planar surfaces;

(iii) Ability to produce nanostructures on surface areas from microscale to macroscale;

(iv) Mask-less single-step processing;

(v) It is feasible in an air environment, so avoids cost-expensive vacuum technologies;

(vi) The manufacturing process can be realized either serially or in-line.

In this thesis, highly-regular laser-induced periodic surface structures (HR-LIPSS) have been fabricated on metallic semiconductor surfaces at an unprecedented processing speed on a large area, and a record regularity in the obtained sub-wavelength structure at the first time.

Theoretically, the physical origin of the LIPSS regularity is identified and associated with the decay length (i.e. the mean free path of L_{SPP} (length of surface plasmon-polariton wave)), of the excited surface electromagnetic waves (SEWs). The dispersion of the LIPSS orientation angle with respect to the direction perpendicular to the polarization is successfully correlated with the SEWs decay length. The shorter is this length, the more regular can be the LIPSS. A material dependent criterion to obtain HR-LIPSS is proposed for numerous metallic materials: in addition of keeping scanning direction disaligned with the electric field, decreasing the spot size close to the SEW decay length is a key for obtaining highly regular structures. Theoretical predictions suggest that reducing the laser wavelength can permit to obtain HR-LIPSS on almost any metal. This new achievement in the control of the laser-induced periodic structure formation paves the way to transfer this technology to industrial applications based on nanostructuring of metals.

Besides the theoretical part, numerous applications based on LIPSS were also examined. Among them there are tribology, medical implants, micro injection molding, wettability, decoration, anti-counterfeiting and identification marking, plasmonic sensors based on plasmon resonance and solar cells.

Chapter 2 presents a state of the art of LIPSS. The aim of this chapter is to depict in details the theoretical models proposed to explain LIPSS phenomenon. Furthermore, full characterization of LIPSS is outlined, and dependence of LIPSS parameters on laser parameters is demonstrated. Also, it was described a broad range of LIPSS applications: mechanics, photonics, micro- / nanofluidics, solar cells and etc.

Chapter 3 presents the original methods to create highly-regular LIPSS on metals and semiconductors at extremely high speed.

Chapter 4 outlines a theoretical explanation was proposed which supports the scaling offered by a collection of experiments performed in similar conditions for several metallic materials.

Chapter 5 is dedicated to applications of high-speed HR-LIPSS, in particular for tribology, dental implants, wettability, enhance adhesive properties, colorizing and injection molding.

Chapter 6 presents results of generation HR-LIPSS on Silicon and outlines mechanism which occur during the formation of surface structures on these materials.

Chapter 7 discusses applications toward HR-LIPSS on semiconductor (silicon). Among them there are plasmon-resonance for sensors and biosensors and solar cells.

Chapter 8 summarizes the conclusions of this thesis and proposes recommendations for future research.

Chapter 2 LIPSS: state of the art

2.1 Observations and theories about LIPSS origins

Nanostructures are the structures of intermediate size between microscopic and molecular objects, usually measuring from 1 to hundreds of nanometers at least in one spatial dimension. In general, a nanotechnology is a technical field dealing with manipulation of matter on an atomic, molecular and supermolecular scale. By the term manipulation, it is particularly meant the technological goal of precisely manipulating atoms and molecules for fabrication of macroscale products [1].

With increasing demand for nanostructured materials, the technology of fast preparation and processing has been developing. However, there are many other pending problems to find an appropriate method for fast and cheap preparation of highly regular periodic structures on material surfaces. Several methods are typically used to produce nanostructures. Lithography techniques, such as additive and subtractive lithography [2][3][4] electron- and focused-ion beam lithographies and photolithography [5][6][7][8][9] are most commonly used and provide high precision nanostructuring. However, these techniques are time consuming, require high-cost and complex equipment and often results in low-speed processing.

One new, incoming method consist to irradiate solid targets by ultrashort laser pulses which leads to the formation of Laser-Induced Periodic Surface Structures [10][11][12] usually referred to as LIPSS. These structures represent a periodic surface relief whose orientation is directly connected with polarization of the laser light. LIPSS can be characterized by the following parameters: period - Λ, with of ripples - a, distance between ripples - b, height of structures - h (Fig. 1). A new parameter which determines a quality of the structures is (Dispersion of LIPSS Orientation Angles) DLOA, presented in this thesis. The main laser parameters that cause growing LIPSS and can affect their parameters are: laser wavelength (λ), laser polarization ($\vec{E}$), pulse duration (τ), angle of incidence of the laser beam onto the surface (θ), parallel ($\vec{p}$) or orthogonal ($\vec{s}$) polarization of the laser beam to plane of incidence, energy per pulse (E_p), fluence (F_0) (Fig. 2a). These parameters can describe LIPSS formation in a single laser spot, in the so-called intrapulse mode. A mode to generate LIPSS on a single area

is called intrapulse mode (Fig. 2b). In order to nanopattern a large area, also scanning parameters must be considered: scanning speed ($\overrightarrow{v_S}$), step between scanning lines (d) and overlapping between laser pulses (k) (Fig. 2c). These parameters describe the interpulse operating mode.

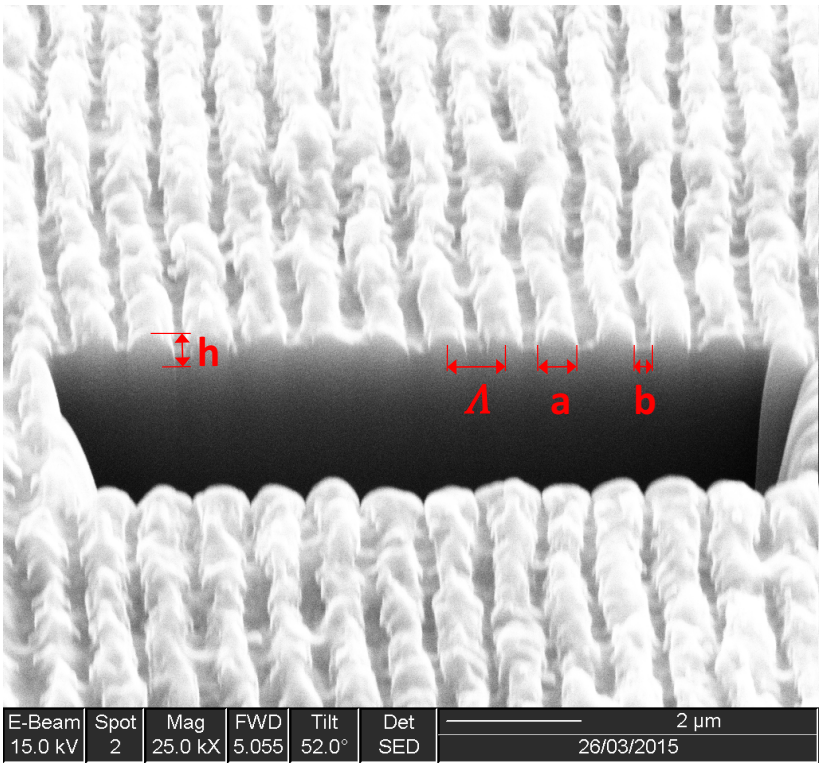

Figure 1. The parameters that characterize LIPSS.

LIPSS were firstly observed by Birnbaum in 1965 on a silicon surface irradiated with a ruby laser [13]. He described this phenomenon as a regular system of parallel straight lines and explained their production as the diffraction effects produced at the focus of a lens. According to his model, grooves are created by the removal of material at the positions of maximum electric field intensity. Furthermore, in 1973 Emmony [14] observed ripples on the germanium surface with a period close to laser wavelength (10.3 µm). He called these ripples "interference fringes" and attributed their formation to interference between incident and scattered laser irradiation.

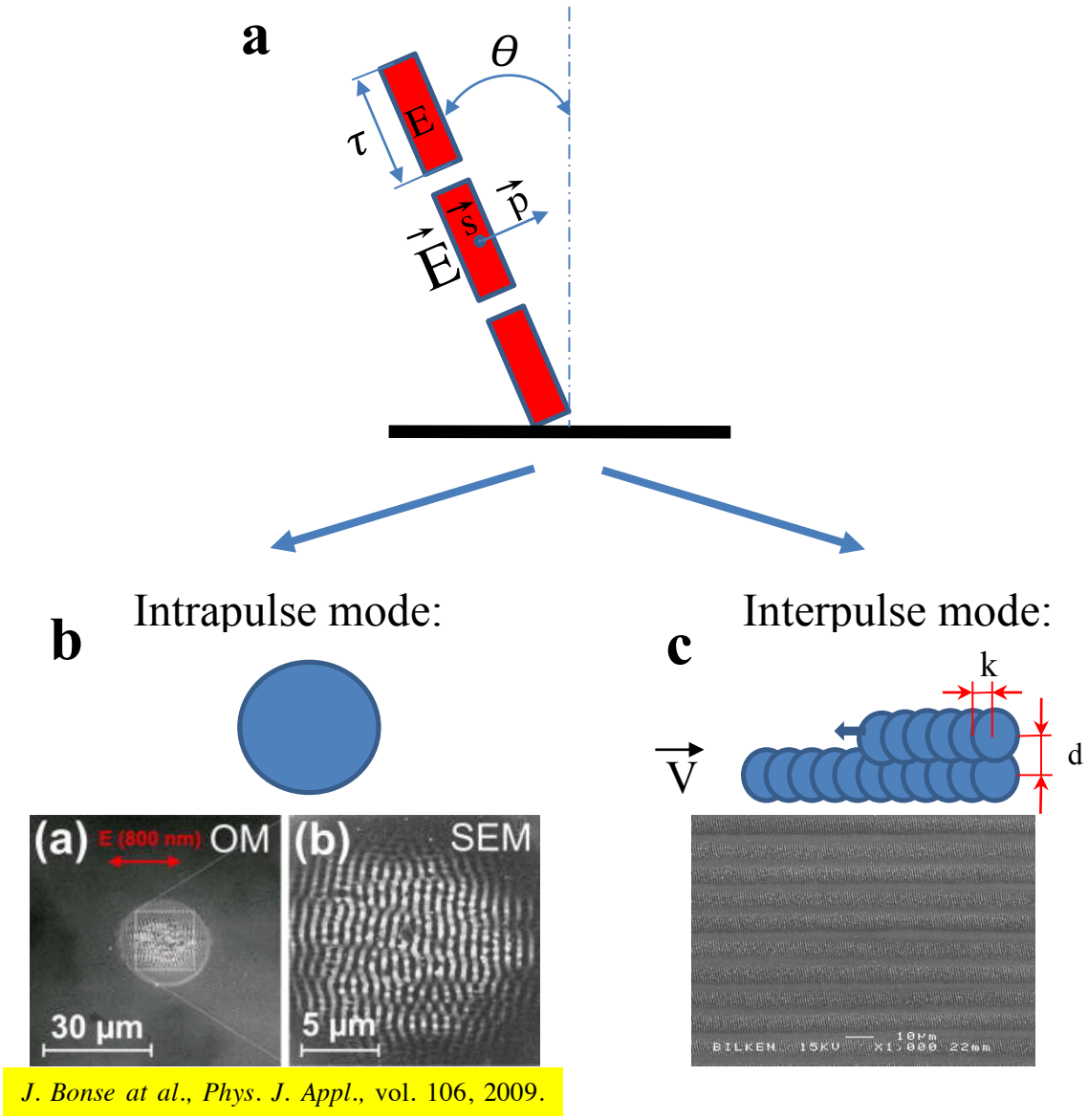

Figure 2. The main laser and scanning parameters that define LIPSS growing.

A pioneering theory that proposed an extended explanation of LIPSS formation was proposed by Sipe [15][16]. He was the first author who introduced the terminology "laser-induced periodic surface structures". Moreover, he also supported the theory by experiments and firstly demonstrated LIPSS on metals [17]. Sipe observed interaction between electromagnetic waves and rough surface. The rough part of the surface was called "selvedge" with the thickness that was significantly less than the laser wavelength (Fig. 3). The theory was based on the fact that periodic wave structures formed as a consequence of an inhomogeneous energy absorption. Hence, the rough surface has critical effect on growing LIPSS described by an efficacy factor η. According to Sipe [14, 15] the efficacy factor η determines the efficiency with which the

surface roughness leads to inhomogeneous absorption of radiation light. This is favourable for predicting the wave vector ($\vec{k}$) of LIPSS. The wave vector $\vec{k}$ is a function of laser parameters (polarization direction $\vec{E}$, wavelength λ, angle of incidence θ and others) and surface parameters (dielectric permittivity ε and surface roughness).

After almost 20 years with the appearance of femtosecond lasers scientific curiosity to LIPSS significantly increased. In 2000-2003 a new type of LIPSS was observed [18] [19][20] for the first time, named "non-classical" LIPSS with a period close to 1/10 of the laser wavelength. This type of LIPSS was called *High Spatial Frequency LIPSS* (HSFL) while classical LIPSS, with a period closed to the laser wavelength ($\Lambda \approx \lambda$) was called *Low Spatial Frequency LIPSS (LSFL)*.

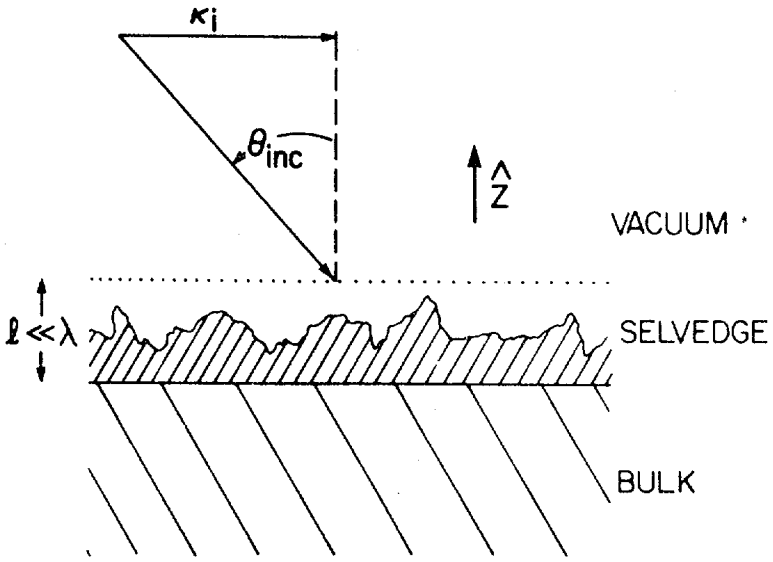

Figure 3. The geometry of light incident on a rough surface [14].

The model of Sipe offered no proper explanation for the existence of HSFL because it was essentially based on the concept of interference of incident and surface electromagnetic waves. However, one of the first studies about them was presented by Reif at al.[19] and it showed that HSFL can be oriented parallel or orthogonal respect to the laser polarization plane depending on the material. Their period can vary from 50 to 200 nm. Finally, Reif at al. proposed that HSFL grow through a self-organized reorganization of the irradiated material, accomplished with a surface instability as a result of surface erosion and atomic diffusion effects.

Various others approaches have been hypothesized to explain the existence of HSFL. Furthermore, Li at al. [21] suggested that the thin oxide layer formed during laser ablation of titanium can drive the creation of HSFL through delamination and spallation of this thin film. However, Liang at al. [22] observed that formation of HSFL at the glass surface occurs upon exposure to ultrashort pulses. In that case, no oxide layer can be formed. Finally, Bonse [23][23] proposed to combine the theory of Sipe with Drude`s model in order to take into account the optical response of the quasi-free conduction band electrons of the laser excited solids. This model allows self-consistently describe the laser-induced changes of the dielectric permittivity during the early stage of LIPSS formation on semiconductors upon irradiation with femtosecond laser pulses.

In 2010-2012, an approach based on finite-difference time calculations (FDTD) was used to solve numerically the electro-magnetic part of Sipe-Drude model [24]. The FDTD approach was extended also to larger sample depths, which are not directly accessible in the original Sipe theory. As an alternative approach, FDTD was used to calculate the optical absorption in idealized nanostructures and surface gratings, allowing to visualize ratings, allowing to visualize plasmonic dispersion relations, optical nearfields in the surface nanostructures, and to identify feedback mechanisms contributing to the HSFL [25].

Other theories of LIPSS generation were recently proposed. Among them the theory of Gurevich [26][27] considers hydrodynamic instabilities of melted or softened surfaces. This theory is based on the assumption that LIPSS cannot grow due to convection induced by either gravity or surface tension. Therefore, in this model it was supposed that the surface temperature profile is periodically modulated across the irradiated surface by an interference pattern (Fig. 4) and that the ablative hydrodynamic instabilities transform the modulated temperature into the height profile.

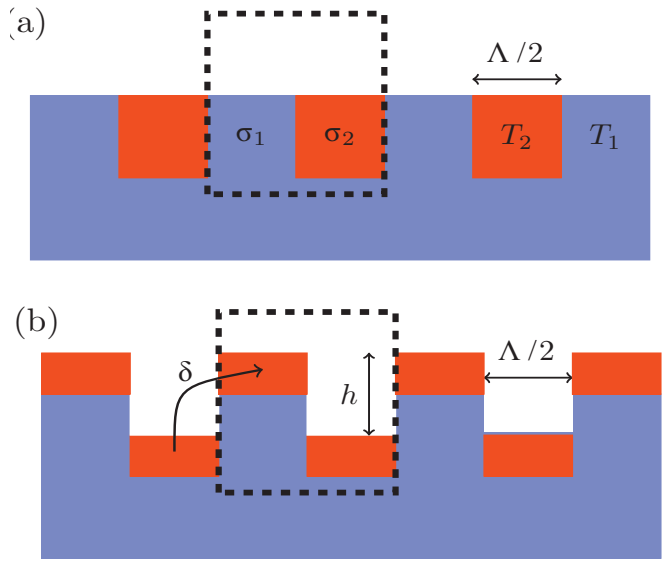

Figure 4. Schematic representation of the LIPSS formation mechanism based on the temperature-driven Marangoni instability. (a) Initial condition: constant surface profile; (b) energetically advantageous configuration: the surface is completely covered by the hot melt [26].

The most common LSFL model supposes that the generation of the nanostructures is due to the interference of Surface Electromagnetic Wave (SEW) with the incident laser wave exciting a coherent surface plasmon-polariton (SPP) waves [28][29][30][31]. What are these "surface plasmon-polariton waves"? Figure 5 can help in describe them:

- plasmon is a collective electronic oscillation mode in a gas of charged particles;
- plasmon-polariton is a coupled electron-photon oscillation mode;
- surface plasmon-polariton is a coupled electron-phonon oscillation mode bound to an interface.

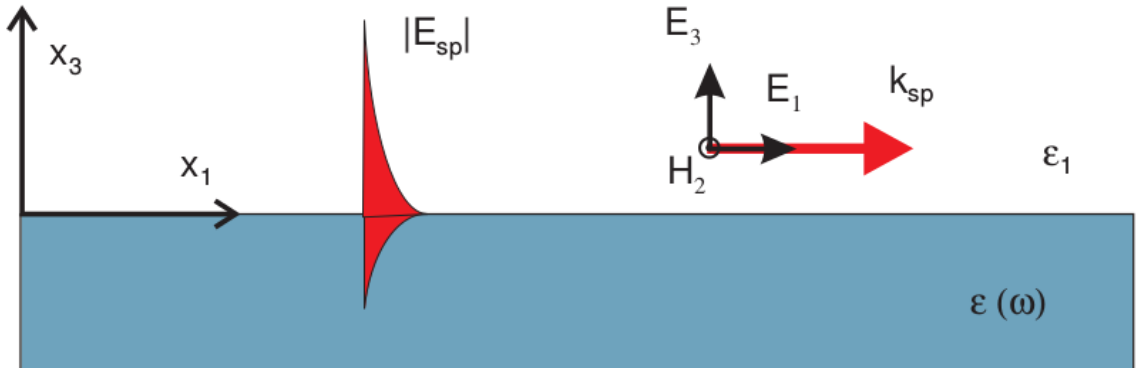

Figure 5. Sketch of a Surface Plasmon Polariton bounded at a metal/dielectric interface [32]. ε_1- positive dielectric constant in the half-space x3 > 0, $\varepsilon(w) = \varepsilon_1(w) + i\varepsilon_2(w)$ - complex dielectric function in the half-space x3 > 0, k_{SP} - wavenumber of the surface plasmon polariton, E_{SP} - electric field of the surface plasmon polariton.

These models has been extended by Makin [33] and predicts the formation of nanoripples with the spatial period equal to even fractions of the laser wavelength (λ , λ/2, λ/4, λ/8, and so on), including those due to the interference between the spatial harmonics of SPPs. This plasmon model is also well accomplished to explain the LSFL formation on semiconductors and dielectrics because these materials exhibit metallic behaviour due to the generation of free carriers caused in an under-surface by an intense ultrashort laser pulse. Both HSFL and LSFL are shown in Fig. 6.

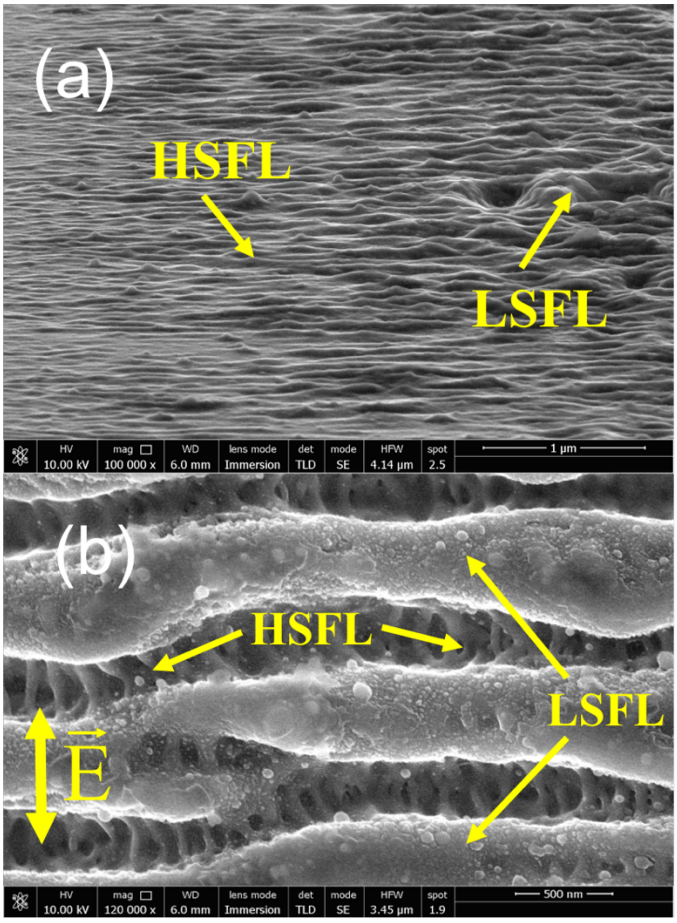

Figure 6. High spatial frequency LIPSS and low spatial frequency LIPSS generated on AISI 316L with the laser setup described in section 5.1.2.

The creation of all the mentioned above types of LIPSS is driven by one of two physical mechanisms: either non-ablative or ablative. In the latter one, the sub nanostructures are etched at a surface so that they are embedded into a thin layer (Fig. 7b), while the former one (Fig. 7a), recently presented in [34][35] and referred to as thermochemical, the LIPSS grow on the top of surface.

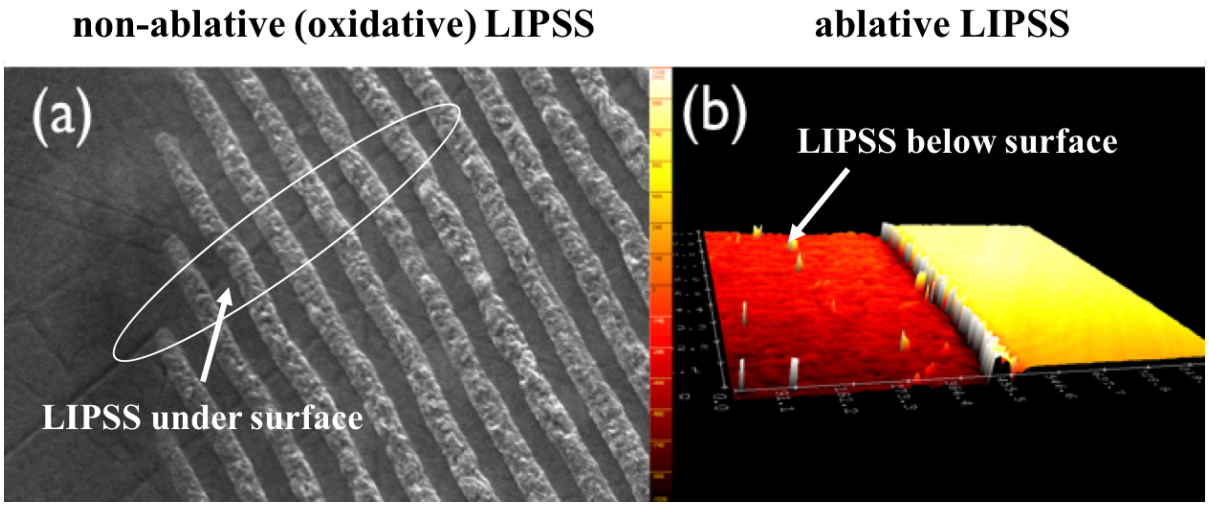

Figure 7. Anomalous (a) [34] and normal (b) types of LIPSS.

Thermochemical femtosecond LIPSS were firstly introduced by Oktem [34] and the process named Nonlinear Laser Lithography (NLL). The model which was proposed assumes the presence of both in positive and negative feedback (Fig. 8). The positive feedback is described below:

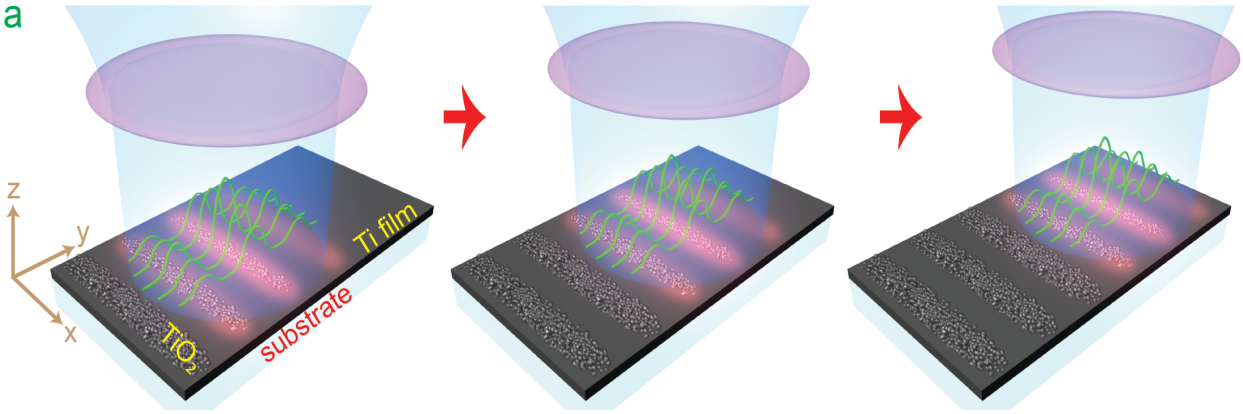

Figure 8. NLL model on Ti films [34].

1) A femtosecond laser beam focused on a titanium surface (Fig. 8). Laser light is scattered by existing structures. Scattered light interferes with incoming light, leading to field enhancement.

2) At the field-enhanced points, laser ablates titanium. This is all in air. So, ablated titanium reacts with oxygen, forming titanium oxide, which is optically transparent. With more titanium gone, these points scatter even better, creating even stronger field enhancement. This is positive feedback, leading to rapid growth.

Since negative feedback occurs while TiO_2 grows on top of the titanium, penetration of O_2 through the oxide layer decreases exponentially.

An overall classification of LIPSS is presented in Fig. 9. The LIPSS can be classified by physical mechanism of formation ("Ablation" or "Oxidation"). Then LIPSS that are created through "Ablation" mode can be distinguished via the period (Λ) on HSFL and LSFL. The latter type of LIPSS are divided through direction of ripples depending on the vector of the incident electric field and the type of material of the laser treatment on *LSFL* $\perp$ *to* $\vec{E}$ and *LSFL II to* $\vec{E}$. In the case of HSFL, they can be distinguished by a depth-to-period ratio ($A=h/\Lambda_{HSFL}$) on the HSFL (A>1) and HSFL (A<1). However, LIPSS, which are created through "Oxidation" physical mechanism have only one sort of LIPSS - thermochemical LIPSS (TLIPSS). All these types of LIPSS in details described below.

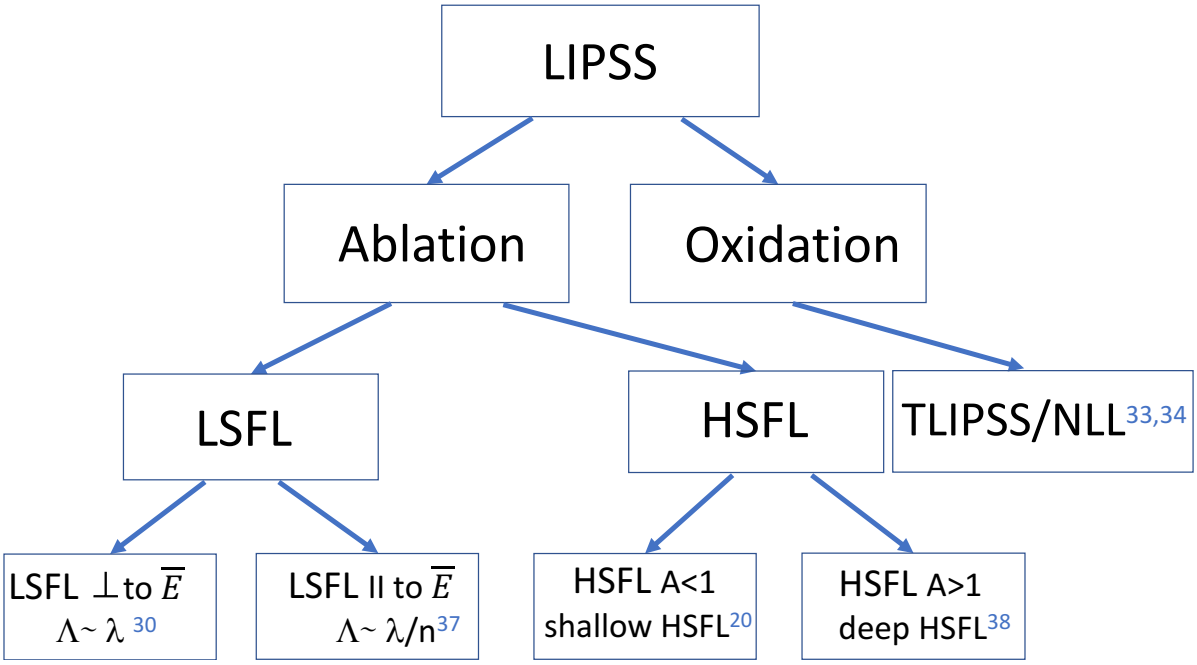

Figure 9. Classification of LIPSS.

As shown in Fig. 9, LSFL can be oriented either perpendicular or parallel to the direction of the laser polarization depending on the type of material. So, in materials, which are characterized by high density of free carriers such as metals or semiconductors the period is equal to the laser wavelength and the structures are perpendicularly oriented respect to the electric-field vector of laser polarization (*LSFL* $\perp$ *to* $\vec{E}$) [30][36]. For the ablation LSFL, the fluence per pulse has to be higher than the ablation threshold of the material in order to turn the LSFL to grow. In this case, ablation mechanism of LSFL growing takes place. This mechanism starts

from the mentioned above model of exciting on the surface of plasmon-polariton waves on the surface [37].

However, on dielectrics, i. e., materials with a wide band gap, another type of LSFL is created. Such LSFL are characterized by a period that is close to the laser wavelength divided by refractive index of the insulator material. The direction of ripples of this type of LIPSS is oriented parallel to the laser beam polarization (*LSFL II to* $\vec{E}$) in contrary to the LSFL on conducting surfaces. The existence of such type of LIPSS requires application of fluence per pulse that is above the ablation threshold of the dielectrics. As a rule, the pulse fluence is about an order of magnitude higher than that for metals of semiconductors. The high level of fluence required to produce LSFL on dielectric surfaces results from absence of free electrons in the conduction band prior to laser action. Therefore, the initial material cannot absorb laser radiation effectively and cannot support any kind of surface waves. This type of structure was described by Sipe [38] with his model of Radiation Remnants of electromagnetic field structures. He characterized the surface electromagnetic wave of a dielectric surface as a specific non-propagating electromagnetic mode close to the rough surface. This specific mechanism supports energy extraction from the incident radiation and its transfer to the material at the associated spatial frequencies.

HSFL have a period smaller than half of the wavelength and are classified in terms of materials and depth-to-period aspect ratio. On dielectrics and semiconductors, the HSFL directions are mostly observed orthogonal to electric field of laser pulses (Fig. 10), ripples are formed from individual nanocracks and their depth h can reach several hundreds of nanometers ($A = h / \Lambda_{HSFL} > 1$) [39] [36]. The mechanism of generation of those HSFL on the non-metal surfaces can be attributed to interplay between scattering/diffraction effects at the edges of the initially existing cracks and propagation via laser-ionized sub-surface layer of the material. The scattered waves can interfere with incident laser beam to produce and interference patter. However, its period is controlled by the optical response of the sub-surface layer that is partly ionized by laser radiation via the photoionization and/or avalanche ionization mechanisms. Those effects can result in various feedback effects that finally determine period and depth of the HSFL. Detailed mechanisms of the HSFL formation on non-metal surfaces are still not clear and are under intensive research.

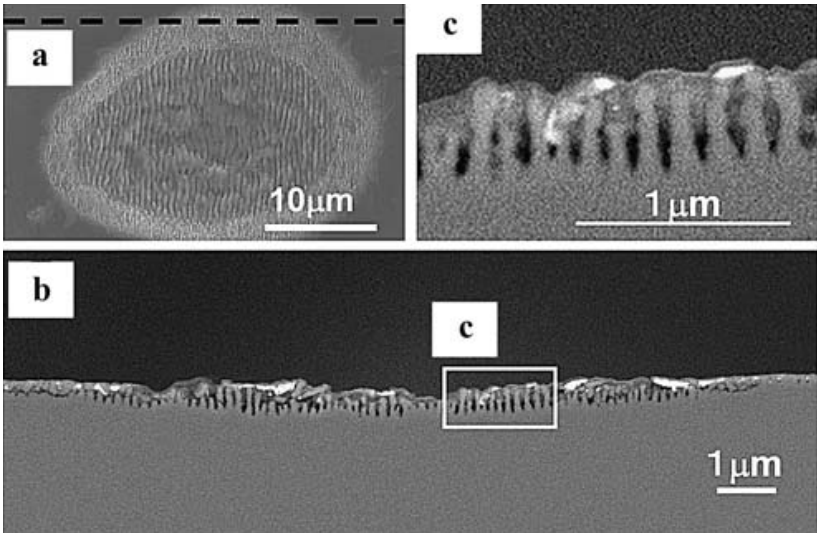

Figure 10. HSFL on dielectrics. The black dashed line displays the position where the cross-sectional profile was observed. (b) Cross-sectional SEM image of the whole irradiated area. Debris was found on the top of the ripple. (c) Magnified SEM image of area (c) in (b) [39].

In contrary, HSFL on metals on the other hand are parallel to electric field of laser radiation (HSFL II $\vec{E}$) (Fig. 6) [20][40][41], resulting in a depth-to-period aspect ratio $A = h / \Lambda_{HSFL} < 1$, the depth is a few tens of nanometers and the period is equal to 100 nm [36]. This type of HSFL consists of very narrow periodic grooves having shallow depth h of a few tens of nanometers only ($h << \Lambda_{HSFL}$) [36]. A generally accepted mechanism of the HSFL formation on metals considers through superficial oxidation or twinning effects during the solidification of a shallow laser-induced melt layer [21][36] [42][43].

TLIPSS has been observed at the moment only on metals and their direction is parallel to the electric-field vector of laser polarisation [34][35]. The period of TLIPSS is roughly equal to $\sim\lambda/2$ [34] and these periodic structures grow on the top of the surface [34][35].

Although many different theories were proposed to explain the formation of LIPSS the common opinion of the research community is that the mechanism underlying their formation was not completely uncovered.

2.2 Applications of LIPSS

An alternative for the fabrication of nanostructures is the use of femtosecond lasers as a single-step process that can lead to the formation of high quality nanostructures under an air atmosphere. The formation of laser-induced periodic surface structures has been produced for a broad range of wavelengths and pulse durations on metals [44][45][46], semiconductors [47][48][49], dielectrics [50][51] , and polymers [52] and their importance were demonstrated for various scientific, biomedical, and industrial applications. LIPSS on different materials can be a method to control and change surface characteristics in applications such as wetting control, tribology, colorizing, plasmonics, cell proliferation, adhesion and others. All the above applications are discussed in details below.

2.2.1 Wetting

Wetting control is currently one of the hottest topics in a nanotechnology field. Nature gives tips showing how to produce superhydrophobic surfaces that can be useful for many applications, such as self-cleaning surfaces, gas seal conditions, directional syringes, microprocessor cooling, high-efficiency hydropower turbines, nanoscale digital fluidics and many others. Fig. 11 shows a micro-nano structured lotus leaf. Such a microstructured surface does not permit water droplets to maintain their position, rolling on the leaf and removing dust particles on the surface. This effect is called self-cleaning surface and inspired academic curiosity

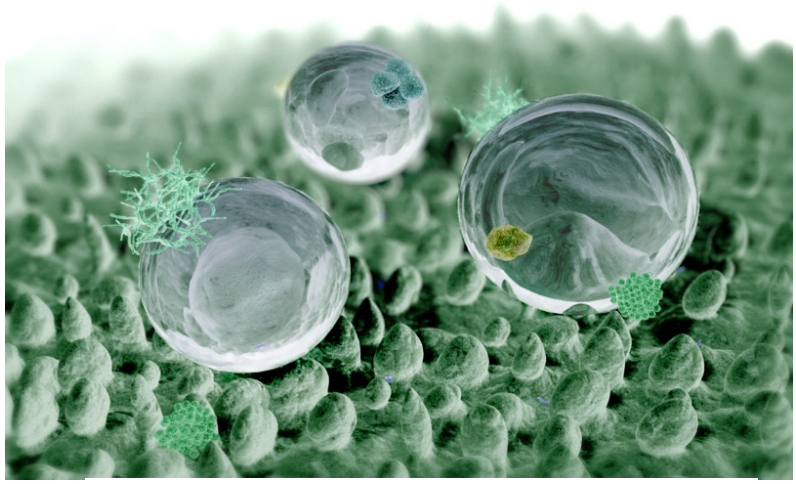

Figure 11. Computer graphic of a lotus leaf surface [51].

to generate such structures on metals in order to apply it to different fields of industry. The wettability behaviour of real surfaces is controlled both by surface chemical composition and surface morphology. Many studies present methods how to turn a metallic surface from hydrophilic to hydrophobic-superhydrophobic by changing chemical properties of surface. [53] Several approaches were attempted, namely implantation of different ions (e.g. SiF^{3+} and $MoS_2{}^{2+}$) into stainless steel; coating the surface with diamond-like carbon (DLC) via sputtering; plasma electro-chemical vapour deposition (PECVD) of DLC, DLC–Si–O coating onto the surface and treating the surface by autocatalytic Ni–P–PTFE and silica coating. In [54] and [55], the authors carried out electrolytic in-process dressing (ELID) grinding to generate a mirror-quality surface on ferritic stainless steel for surgical applications. This method is used to functionalize the surface by varying the type and quantity of abrasive materials or the operating temperature in order to induce different wettability behaviour. Some of the above methods are expensive, complicated and time consuming; others involve chemical treatments and weak coatings that are generally evanescent or fragile. The use of methods that change only the surface morphology/topography could be the safer choice if chemical stability is critical for an application and where no surface contaminations are desired. Two different recent examples can be found in [56][57] based respectively on a vibration assisted machining method and on the use of a nanosecond UV laser.

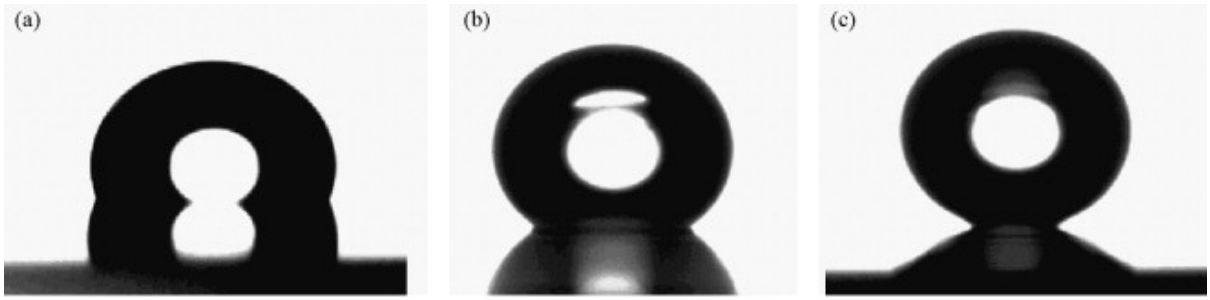

Figure 12. Photographs of water droplets on flat (a), LIPSS (b) and double-scale structure (c) AISI 316L type austenitic stainless steel-based surfaces after silanization [58].

This principle can be applied to obtain hydrophobic surfaces as investigated in [58][59], where stainless steel and titanium alloys were treated with a Ti:Sapphire femtosecond laser and eventually silanized in a low vacuum chamber (Fig. 12).

LIPSS generation turns a hydrophilic untreated metallic surface to superhydrophobic through the increasing surface roughness of the textured surface. It can be explained that liquid prohibits air from running out from nanostructures, therefore leaving air in a trap there.

Hydrophobicity changes over time, linked to the nanostructuring of the metallic surface by LIPSS [60] as follows: immediately after laser treatment and during the first day, the surface is highly hydrophilic, while after several days it becomes highly hydrophobic and this hydrophobic state remains quite stable during the experiment (Fig. 13) demonstrates that the LIPSS induced hydrophobicity is a function of time and depends on both topography and chemistry.

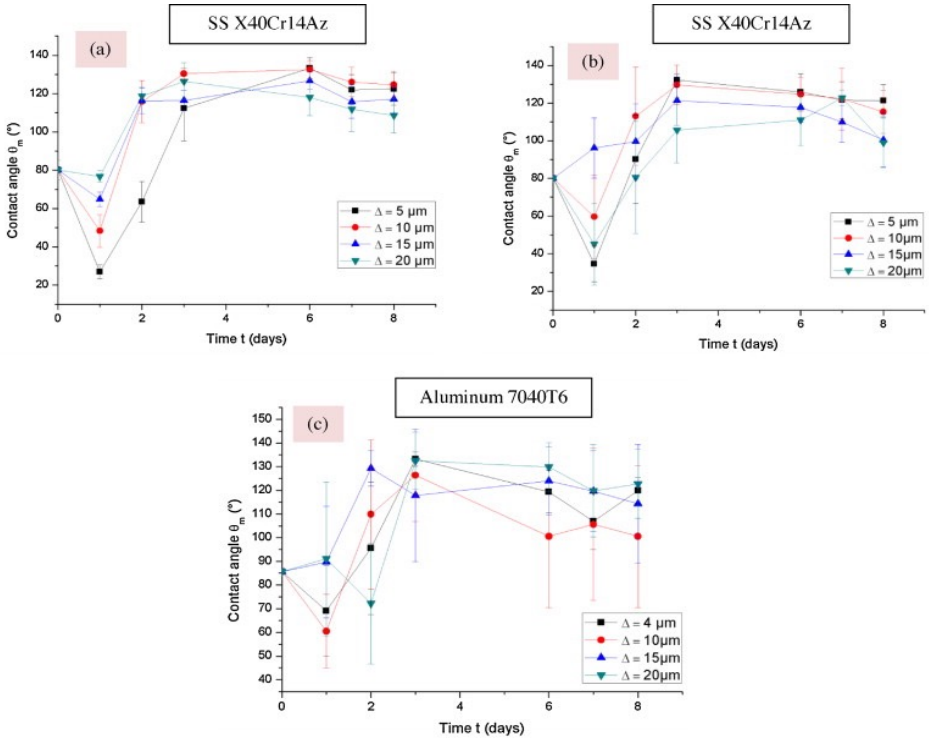

Figure 13. XPS analysis of X40Cr14Az (a) and X40Cr14Az stainless steels and commercial aluminium (7040T6) [60].

In [61] authors generated LIPSS on Ti6Al4V surface for biomedical application and evaluated the variations in the wettability depending on the direction of ripples (Fig. 14). In other words, their observed anisotropy behavior of spreading water drops on the textured surface. The droplets spread mostly in the LIPSS directions, remaining constrained in the opposite direction.

More advanced methods to obtain superhydrophobic surfaces is to generate both microstructures and LIPSS. This kind of structure is hierarchical (Fig. 15) [62][63]. The irradiation of metallic surfaces by scanning a laser beam with fluence higher than the ablation threshold lead to the formation of micro channels containing LIPSS on their surface. Such super imposed micro-and-nanostructures presents a contact angle higher than 160°. Moreover, generating

these hierarchical structures on silicon results in another unexpected effect; the surface becomes super hydrophilic and drops can even go uphill [64] while the sample is oriented vertically.

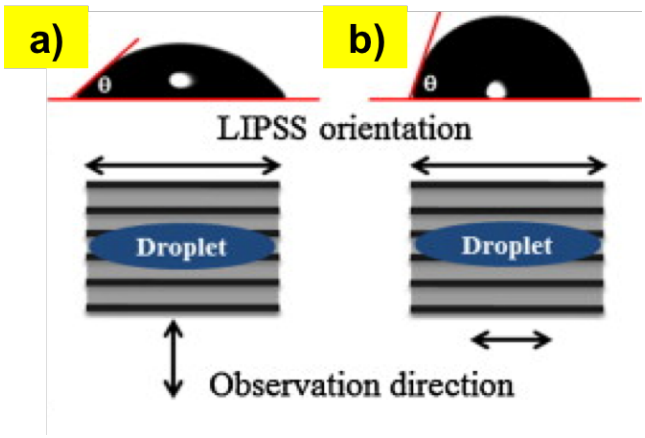

Figure 14. Contact angle values measured perpendicular and parallel to LIPSS orientation; representative droplet for both liquids when viewed perpendicular (a) and parallel (b) to LIPSS orientation [61].

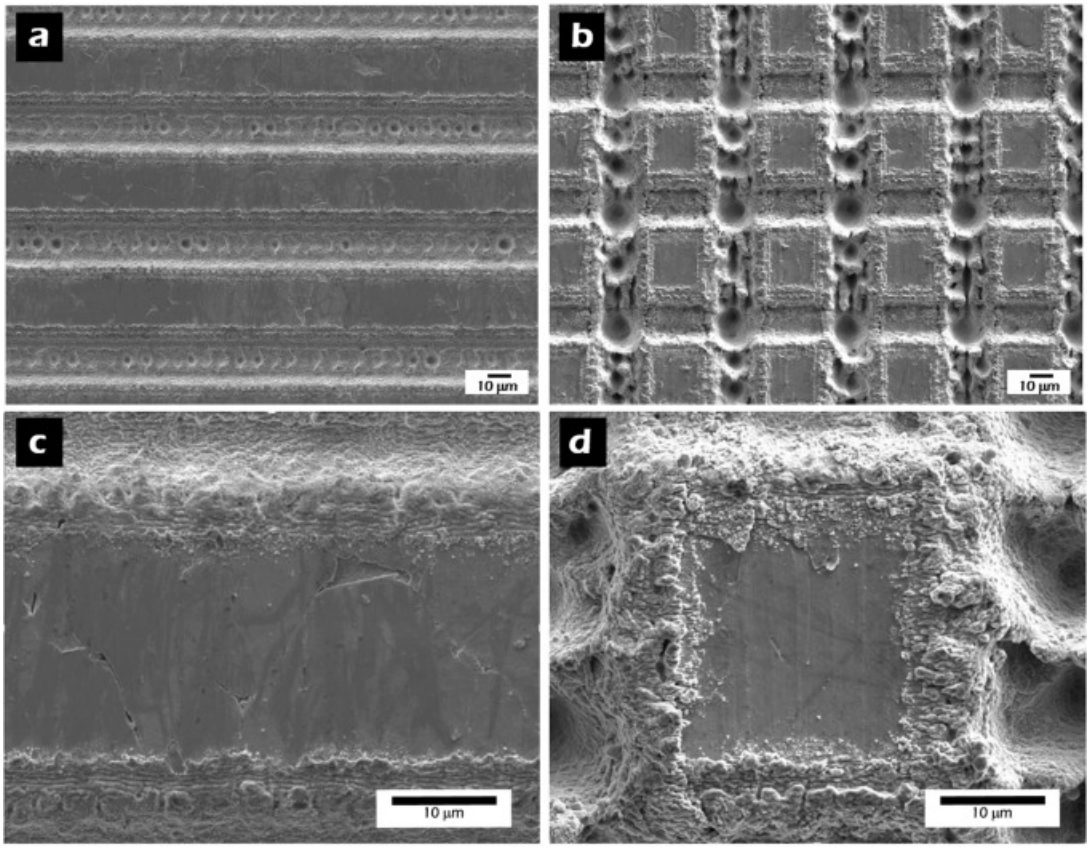

Figure 15. FE-SEM images of the fabricated micropatterned structures: (a) trench micropattern with a pitch distance of 50 µm; (b) matrix micropattern with a pitch distance of 50 µm. Detailed area scanned on: (c) trench micropattern; (d) matrix micropattern [61].

2.2.2 Tribology

The nature shows examples how periodic and self-organized surface structures decrease coefficient of friction, for example the skin of a snake, pangolin and other animals. The mutual configurations of micro-and-nanostructures show "Guiding-Effect" or "Rolling-Effect" [65] Such examples inspired surface engineering to generate surfaces with low coefficient friction. Bearing in mind the processing time requested by the different kinds of lithography, LIPSS based process can be a potentially strong candidate for improving tribological performances.

The shortcomings to apply LIPSS for tribology have been clearly recognized by Yu and Lu in 1999 [66]. They obtained microstructures by nanosecond excimer laser and demonstrated the improvement of tribological characteristics in comparison to a non-treated surface. Furthermore, Mizuno et al. [67] used femtosecond laser generated LIPSS on diamond-like carbon (DLC) and tested friction properties with atomic-force microscope. This test showed a reduction of friction on the film with LIPSS compared with the untreated ones. Yasumaru at al. [68] also tested DLC, additionally coated with thin layer of MoS_2 showing how to decrease and increase coefficient of friction (COF). Using different techniques of laser beam scanning, they generated LIPSS to reduce friction coefficient, and the net-like patterns mentioned above significantly decrease COF compared to a flat surface. The following study in [69] has observed decreasing coefficient of friction even without the lubricant in pin-on-disc tribometer on TaC coated steel surface. The first tribological tests on LIPSS-textured semiconductors was made by Eichstadt at al. [70]. Both non-lubricant conditions and lubricant ones were used to analyse COF and show increased friction coefficient.

The tribological performances were investigated on a large LIPSS-treated area of 100Cr6 stainless steel, high toughness bearing steel X30CrMoN15, pure titanium and titanium alloy (Ti6Al4V) by using a ball-on-disc tribometer under paraffin and engine oil as lubricants (Fig. 16)[71][72] .

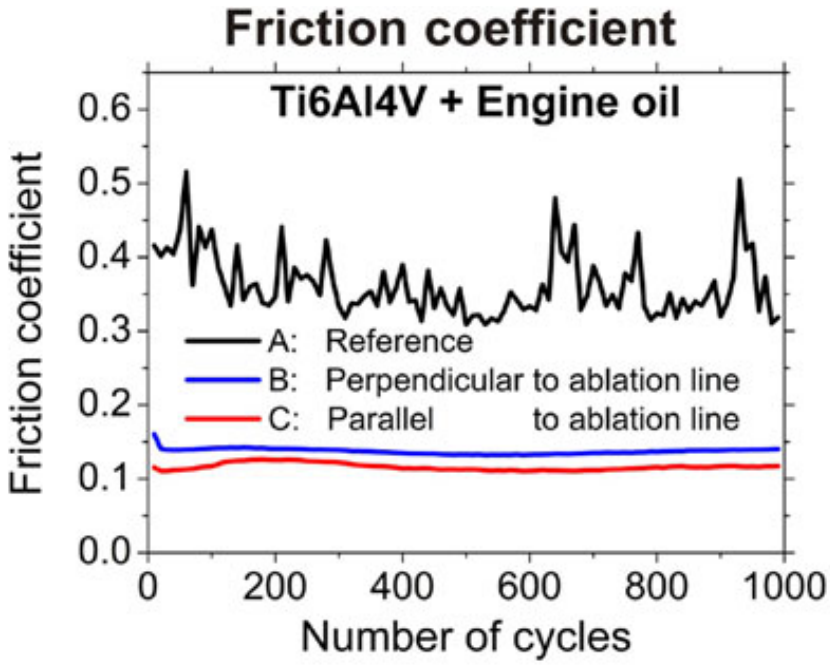

Figure 16. Friction coefficient as a function of the number of cycles as measured during reciprocal sliding (normal force 1.0 N, stroke 1 mm, frequency 1 Hz) of the fs-laser structured titanium surface against a 100Cr6 steel ball in engine oil [71].

No effect was measured on coefficient of friction for LIPSS-treated samples tested with both the mentioned dry lubricants. While a significant reduction of COF and wear for Ti and Ti6Al4V was shown with engine oil in the case of ripples that oriented perpendicularly to a sliding motion while no beneficial influence appeared with paraffin oil. It should be outlined that these were first experiments demonstrating the dependence of coefficient of friction from orientation of LIPSS and the mechanisms causing COF to decrease by nanoscale structures were not explained properly.

The first research on wear and tribological performances for HSFL was made by Bonse at al. [73]. Large titanium samples were covered by LIPSS and tested with paraffin and engine oil as lubricants. The reciprocal tribological analysis did not demonstrate the effects of HSFL on coefficient of friction. The main conclusion from those results were that the depth of LIPSS plays a crucial role in friction behaviour.

2.2.3 Cell Growth

Ultrashort pulsed lasers are increasingly utilized for the surface engineering of biocompatible materials to improve and/or enhance biological properties. They offer high flexibility and excellent accuracy and those advantages are crucial for a lot of medical applications. The surface irradiated by ultrashort pulses change the surface energy modifying both chemistry and morphology. This effect plays a fundamental role in cells adhesion and consequently influences cells differentiation and proliferation.

Recently, many works prove the ability of LIPSS to produce bioengineer multifunctional surfaces which are able to control and improve all the mentioned cell properties. The works of Matsukagi et al. [74] and Cunha et al. [75] shows that osteoblast cells align and grow along the ripples on Ti6Al4V titanium alloy (Fig. 17). Moreover, in this work [74] it was demonstrated that LIPSS enhance matrix mineralization and bone-like nodule formation as compared to the polished surface and improve osteoblastic differentiation of human mesenchymal stem cells seeded on Ti-6Al-4V alloy.

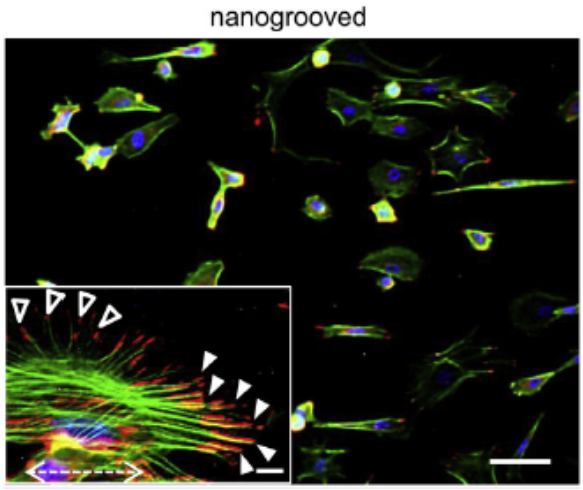

Figure 17. Immunocytochemical images of osteoblasts cultured on the nanogrooved substrate. Cell orientation against surface periodicity was quantified at 10º [74].

In work [76] titanium alloy surface covered by LIPSS essentially reduced the adhesion of *Staphylococcus aureus* and biofilm formation and it demonstrated in detail that the reduction of bacteria adhesion occurs because the size of individual features of bacteria is higher than the period of LIPSS and this prohibits the way for bacteria to penetrate the material and grow.

2.2.4 Colorizing surface

One example from nature that demonstrates cute structural coloration is the wing of the *Morpho* butterfly [77]. On the wing, the bright blue color is a consequence of solar light diffraction caused by quite complicated periodic microstructures (Fig. 18).

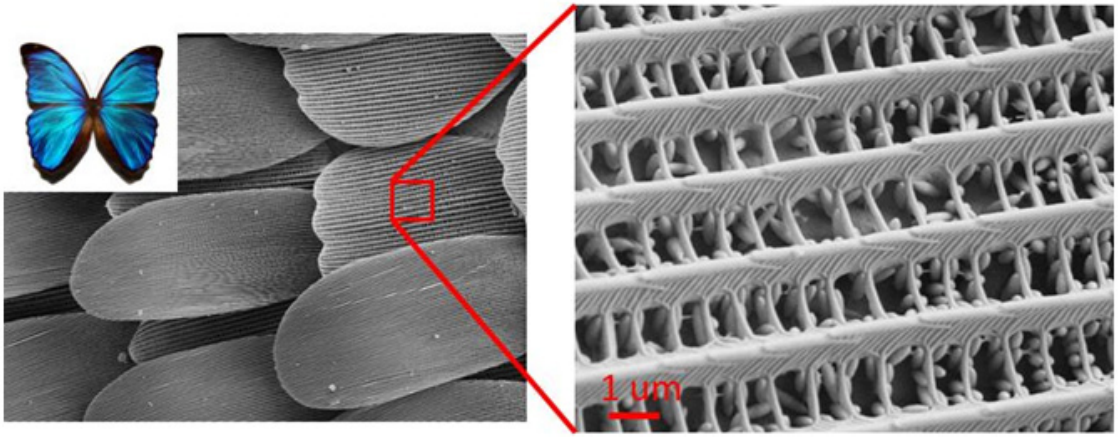

Figure 18. A blue morpho butterfly. The wings are covered by homogeneous hierarchical structures in scales containing color-producing nanostructures [77].

Here, LIPSS have some common points with surface morphology of the *blue morpho butterfly* wings: they permit to cover the surface with quite complicated hierarchical structures that simultaneously generate a structural colour due to diffract the light (Fig. 19a). Different shades of colours can be reflected, depending on the orientation of ripples, their angle and their period.

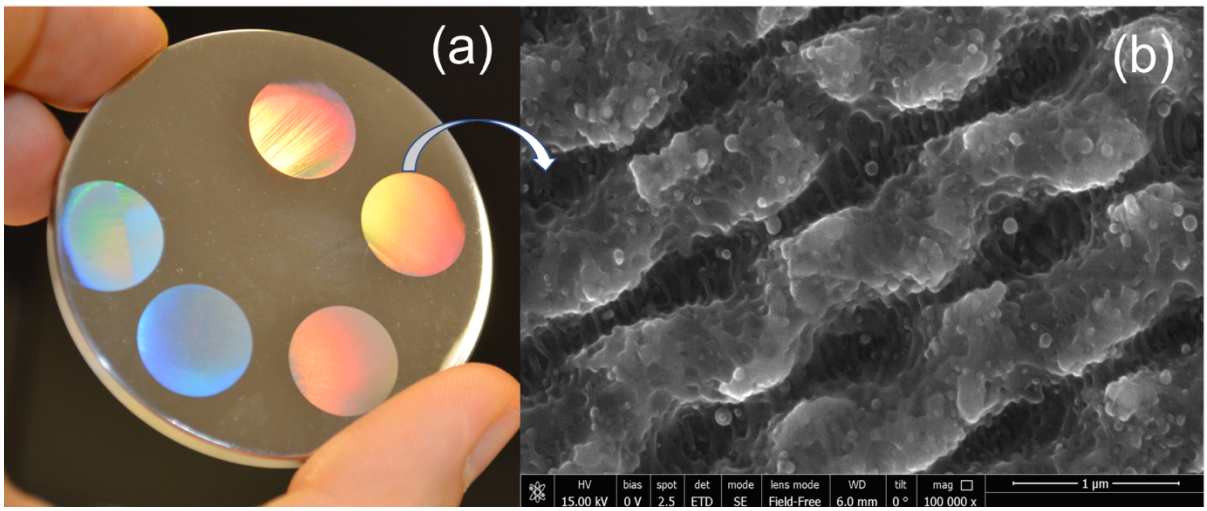

Figure 19. Example of textured by LIPSS hierarchical structure on ferritic steel: macrophoto (a) and SEM (b).

Vorobyev and Guo[62][78][79] initial works demonstrated the possibility of using LIPSS to change the colour of different metallic surfaces such as silver, aluminium, titanium and platinum. On those modified surfaces, optical properties completely change, as presented through spectral measurements of reflectance. The reflectance of the treated sample essentially decreased and their level depends by the colour, i.e. the lower reflectivity provides black colour, at this one reflectance dropped down to 10 %.

Dusser at al. [80] have demonstrated the possibility to control colours on the LIPSS covered area of stainless steel by varying laser parameters and based on that, they set a colorimetric calibration. This calibration used to draw pre-defined pictures with LIPSS. It should be noticed, that at that time (2009), what was presented was the largest area of LIPSS ever demonstrated (~ 20 x 20 mm) Yao at al. [81] also colorized steel, and show how to produce artificial surface structures on a metallic surface that can be applied as an anti-counterfeiting method. Another work presented systematic studies on how to colorize metals, like copper [82], titanium [83] and semiconductors, like silicon [83] .

Li at al. [84] investigated the effect of the laser wavelength on the colorization process for stainless steel. They used laser wavelength in the range from 400 nm to 1170 nm and showed the resulting color changes.

In summary, LIPSS based patterning permits a nanometric uniformity through a single step. This inexpensive maskless process has essential advantages, in comparison to classical marking techniques. Potentially LIPSS can be applied to numerous applications, such as optical data storage, encryption, counterfeit prevention and others.

Chapter 3 Methods for generation HR-LIPSS on metallic/semiconductor surfaces

This research was investigated together with prof. Nadezhda M. Bulgakova and Dr. Thibault Derrien, HILASE Center, Prague, Czech Republic.

In view of disadvantages inherent in the known methods of generation LIPSS with ultrashort laser pulses which are low quality structures in periodicity, presence of the bifurcation points, and low writing speed, the present approaches can ensure ultrafast laser writing of highly-regular laser-induced periodic surface structures (HR-LIPSS) on metallic and semiconductor materials. The methods of ultrafast laser writing of HR-LIPSS disclosed herein is capable to create, at a very high writing speed, bifurcation free nanostructured surface with angular dispersion that is maintained below 15º.

The method of ultrafast laser writing of HR-LIPSS on metallic and semiconductor materials is realized by irradiation these surfaces by focused laser beam in small spot at laser fluence well above the ablation threshold. Technical effect of the method is achieved by means of a telescope for expanding beam diameter, f-theta lens and galvanoscanner which enable to fulfil the requirement of high coherence of Surface Electromagnetic Waves (SEW) over the whole illuminated area. The SEWs are produced upon interaction of the electromagnetic field of the linearly polarized laser light with the metallic or semiconductor surfaces. The ultrashort laser pulses induce SEWs to propagate in the direction of polarization on the metallic or semiconductor surfaces.

To generate highly regular periodic surface structures, three conditions must be simultaneously fulfilled:

As a first condition, the size of the illuminated area must be smaller than or comparable with three characteristic lengths of the SEW decay, which is typically ≤30 μm, depending on the substrate material. In this case, the free electrons driven into motion by the SEWs oscillate coherently over the whole illuminated area, thus securing highly periodic absorption of laser energy within the illuminated area with periodicity along light polarization.

As a second condition, for efficiently drive the free electrons, the laser pulse duration must be shorter than the thermalization time that is the time requested to reach the thermodynamic equilibrium with the lattice. Typically, the laser beam pulse duration can be at sub-picosecond duration range but it may be also extended to several picoseconds.

As a third condition, the laser fluence higher than the ablation threshold applied to the small illuminated area provides large amplitude of the absorption pattern culminated by the regime of strong ablation, driven by enhanced mechanical stresses in radial direction, already at single laser pulses that allows to avoid formation of excessive volume of molten material remaining on the surface after ablation. Strong ablation followed by quick solidification of remaining shallow melt preserves the regular periodic absorption profile on the metallic surface, thus forming highly regular periodic structure. The single-pulse laser fluence has to be sufficient to melt material and induce its developed ablation and can be from fraction of J/cm 2 to several J/cm^2 (e.g., up to 20 J/cm^2) depending on the ablation threshold of particular material at particular wavelength.

Once the single illumination event results in highly regular periodic structure formation, the next laser pulse can overlap with the previous one only partially, by few structure periods, reproducing the periodic structure on the new illuminated area via inducing coherent electron oscillations which are pre-defined by overlapping with the structured area. It is preferred that the overlap is at least 30 % of the spot area, more preferably at least 50 % of the spot area. For this, the scanning speed and the repetition rate of the laser should be adjusted so that the overlap of two spots irradiated one after another is provided. High scanning speed and high repetition rate (e.g., higher than 1 kHz, preferably about 1 MHz) are particularly suitable for industrial use of the invention.

The relatively small overlapping between illuminated areas and scanlines sufficient to produce highly regular periodic structures enables high scanning speed of substrate structuring provided for example by the scanning technique which combines a high-speed scanner and translation stage. Polarization of the laser light can be at any angle relative to scanning direction. The method of ultrafast laser writing of HR-LIPSS on metallic and semiconductor mate-

rials comprises laser wavelength in a wide spectral range from UV to mid-IR. In various practices of the method, the illuminated area can be from several micrometers to dozens of micrometers with fulfilling the first condition.

Materials allowing for such possibility share specific criteria disclosed in hereby:

(I): The characteristic SEW decay length L must be of order of the laser spot size used to generate the structures. Accounting for exponential decay of SEW, the laser spot size on the material surface has not to exceed 3L. The SEW decay length is given by the expression

$$L_{SPP} = \frac{1}{2\,\mathcal{I}m\,(\beta)}, \text{ where } \beta = 2\pi(\varepsilon/(\varepsilon+1))^{0.5}/\lambda \quad (1)$$

at the air-material interface. The dielectric permittivity ε is given by experimental measurements and also available in literatures known by skilled person in the art.

(II): The dielectric permittivity ε of the material must exhibit a high damping, i.e., imaginary part of dielectric permittivity is close to or higher than the absolute value of its real part for the considered irradiation wavelength λ, as expressed by the following equation:

$$\mathcal{I}m[\varepsilon(\lambda)] \geq |\, Re[\varepsilon(\lambda)]\,| \quad (2)$$

By comparing the SEW decay length L of a material with the regularity of the obtained highly-regular periodic structures (measured by a quantity $\delta\theta$ describing the dispersion over orientation angle of the parallel structures in respect of the used laser polarization), an excellent correlation was found.

The present method provides a fast and cheap production approach for writing of the HR-LIPSS on large areas of substrate surfaces. Surface periodic structures are formed as a result of interference of incident and scattered surface electromagnetic waves (SEW) followed by self-organization effects which do not lead directly to regular periodic structures. The technical problem to be solved is to provide interference conditions to achieve highly regular periodic structures and at high writing speed. Further technical problems to be solved are minimizing of negative influence of the processes involved in the periodic structure formation (thermo-

plastic deformations, non-thermal melting) and ablation mechanisms (spallation, phase explosion, Coulomb explosion). The Method of Direct Formation of Highly-Regular Structures on Metallic Materials provides activation of Surface Electromagnetic Wave (SEW) interfering with the incident laser wave at the surface of the substrate in a manner which ensures high quality and regularity of the obtained pattern.

The optical setup used to obtain the proposed result is show in Fig. 19. The system comprises an ultrafast laser source (1) with pulse duration in the order or smaller than 1 ps and with high repetition rate. The energy per pulse is selected in order to overcome the ablation threshold of the material under treatment and the beam (2) is deflected on the surface of material by means of a galvanometric scanning head (9) connected to a f-theta lens (10).

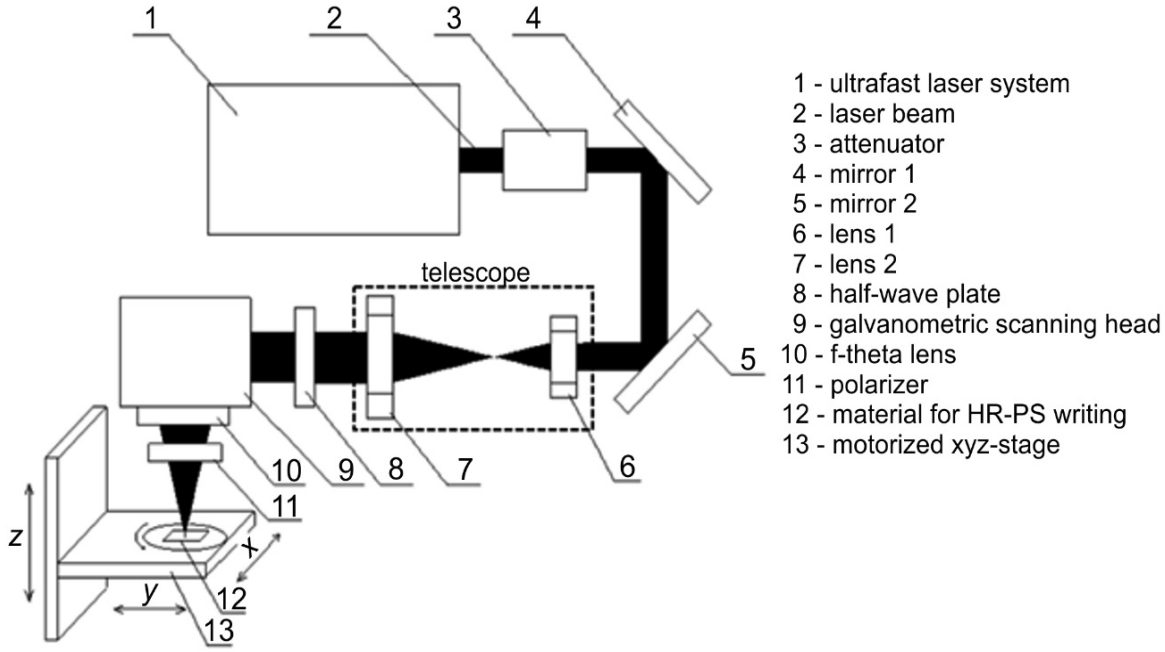

Figure 20. A laser setup for ultrafast laser writing of highly-regular periodic structures on metallic materials.

The rotation of a half-wave plate (8) is coordinated with a polarizer (11) allows to define the direction of the laser-induced structures. The laser beam (2) is focused on the different materials surface (12) and the extension of the scanned area is limited in order the angular deflection of beam (2) is negligible. Much larger areas are obtained by moving the sample with a motorized xyz-stage (13) under galvanoscanner. The proposed setup allows to obtain both regular and irregular structures with aspect ratio depending on the material but in many cases

around the unity. The use of linearly polarized light makes possible to obtain quasi-regular linear structures with periodicity below the wavelength of the laser beam.

The methods to decrease the laser spot are: increasing aperture of the beam (2) before the gavanoscanner head (9) by means of a telescope, as shown in Fig. 21, comprising two lenses (6) and (7) that expand the beam (2) coming from direction (14).

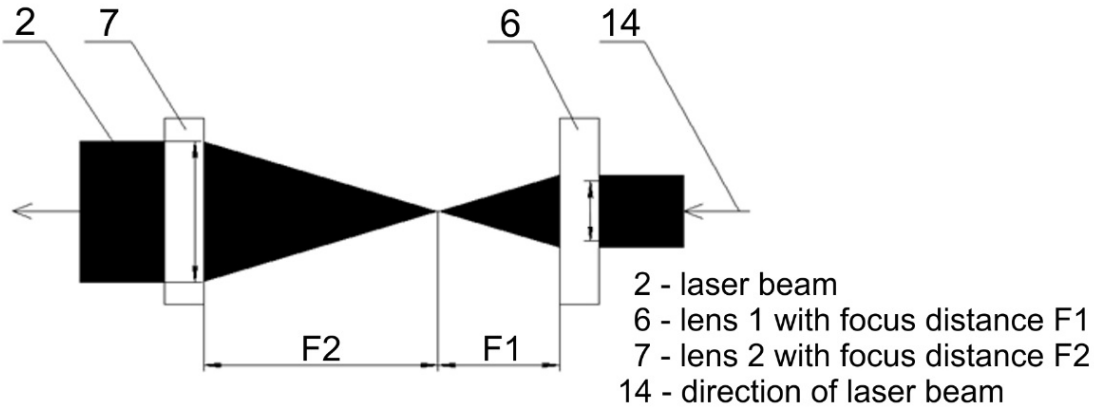

Figure 21. The scheme of laser beam expanding based on the telescope principle.

In Fig. 22, the focusing f-theta lens (10) to decrease the laser spot is presented.

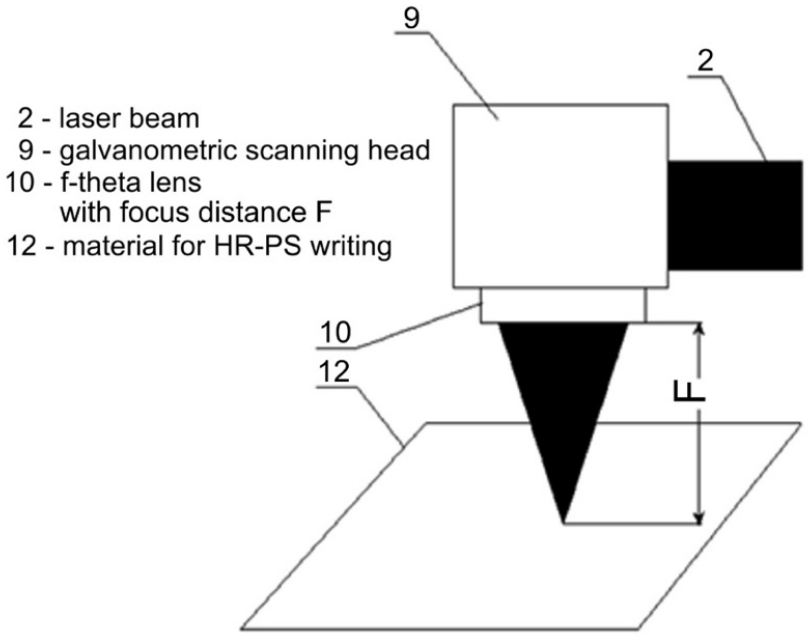

Figure 22. The scheme of laser beam focusing.

About the angle between polarization direction E and scanning direction S, polarization direction E is oriented perpendicularly to a desired direction of the structures to be obtained (Fig. 23).

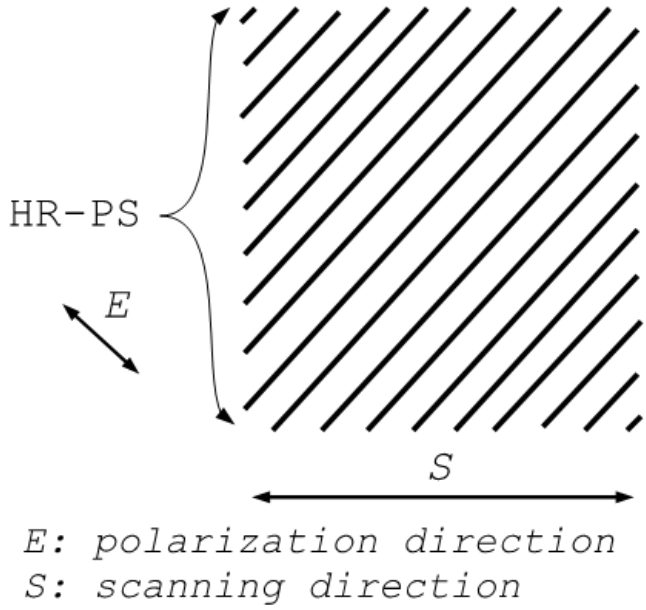

Figure 23. The angle between the polarization and the scanning directions can be arbitrary.

The optimal laser fluence is estimated depending on the material in order to obtain the material ablation and to avoid excessive volume of melt material. Small illumination spots (Fig. 24).

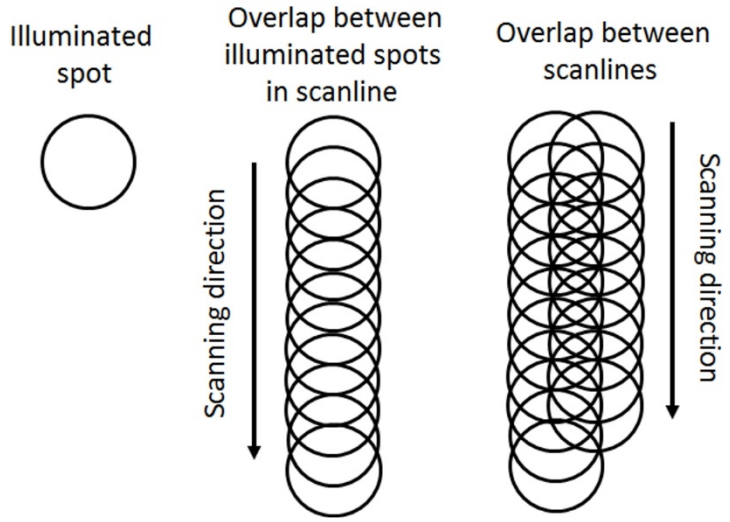

Figure 24. Overlapping of illuminated spots in a scanline and between scanlines upon scanning the material surface.

are favouring a deeper ablation of material due to higher radial stresses compared to larger spots.

Figure 25 illustrates a SEM image of HR-LIPSS produced by scanning a surface of molybdenum with the wavelength of 1030 nm, pulse duration of 213 fs, laser fluence of 33 % overlap between pulses and 50% overlap between scanlines.

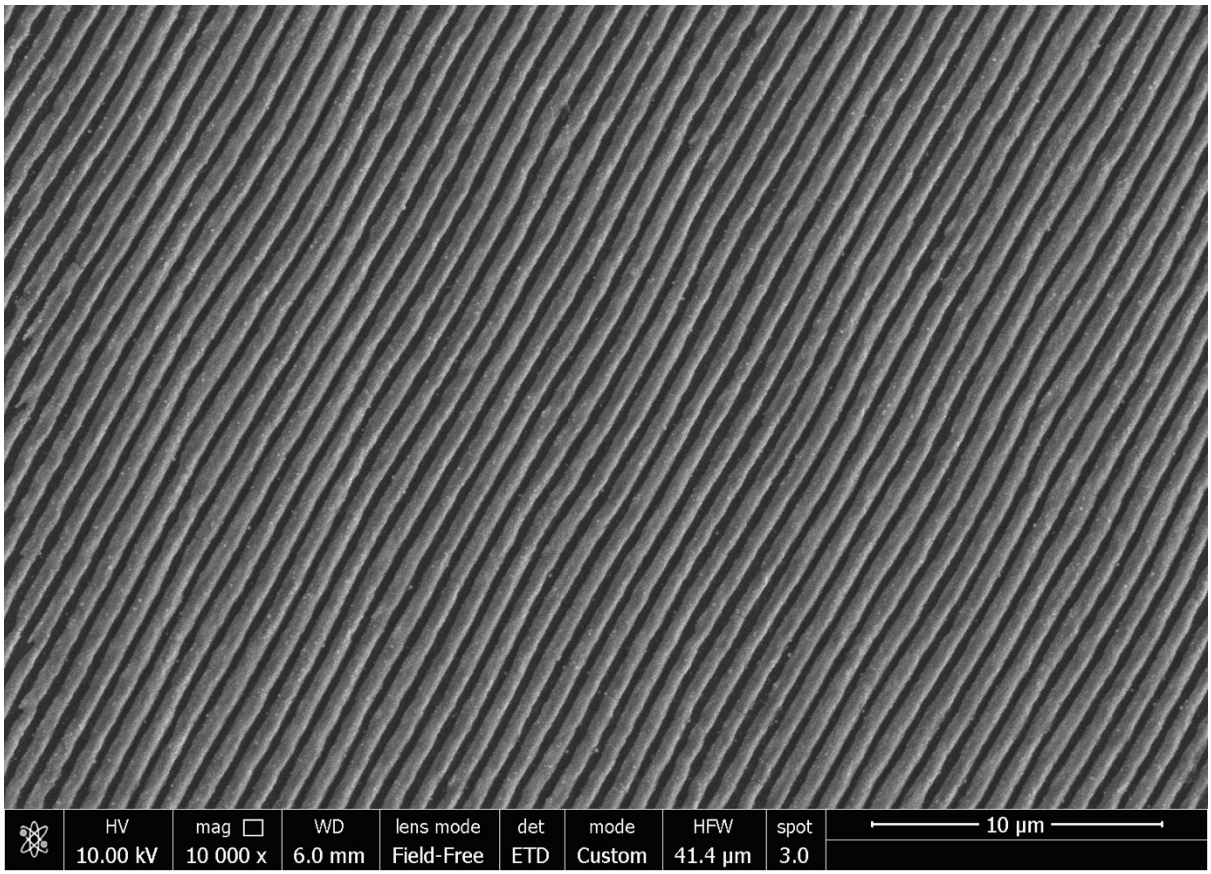

Figure 25. The typical view of highly-regular periodic structures on metallic material, molybdenum as an example.

Figure 26 illustrates the requirements for ultrafast laser writing of highly-regular periodic structures on metallic materials. Column I summarize the usual conditions for periodic structure formation on metallic surfaces. Basically, to produce such structures, multiple irradiation of the surface by polarized laser beam of ultrashort (fs/ps) duration is needed. To distribute structures on large surface area at high throughput, high repetition rate and high scanning speed of the beam are needed with enough average mean power to induce melting/ablation (Column II). According to our findings, to write HR-LIPSS, a small spot size with specific overlapping between irradiation spots in scanline and between scanlines in main requirement (Column III).

Columns I, II and III together present the way to produce HR-LIPSS on large area at high production speed, providing that material optical properties enable high regularity of the structures (see Figure 27 and description).

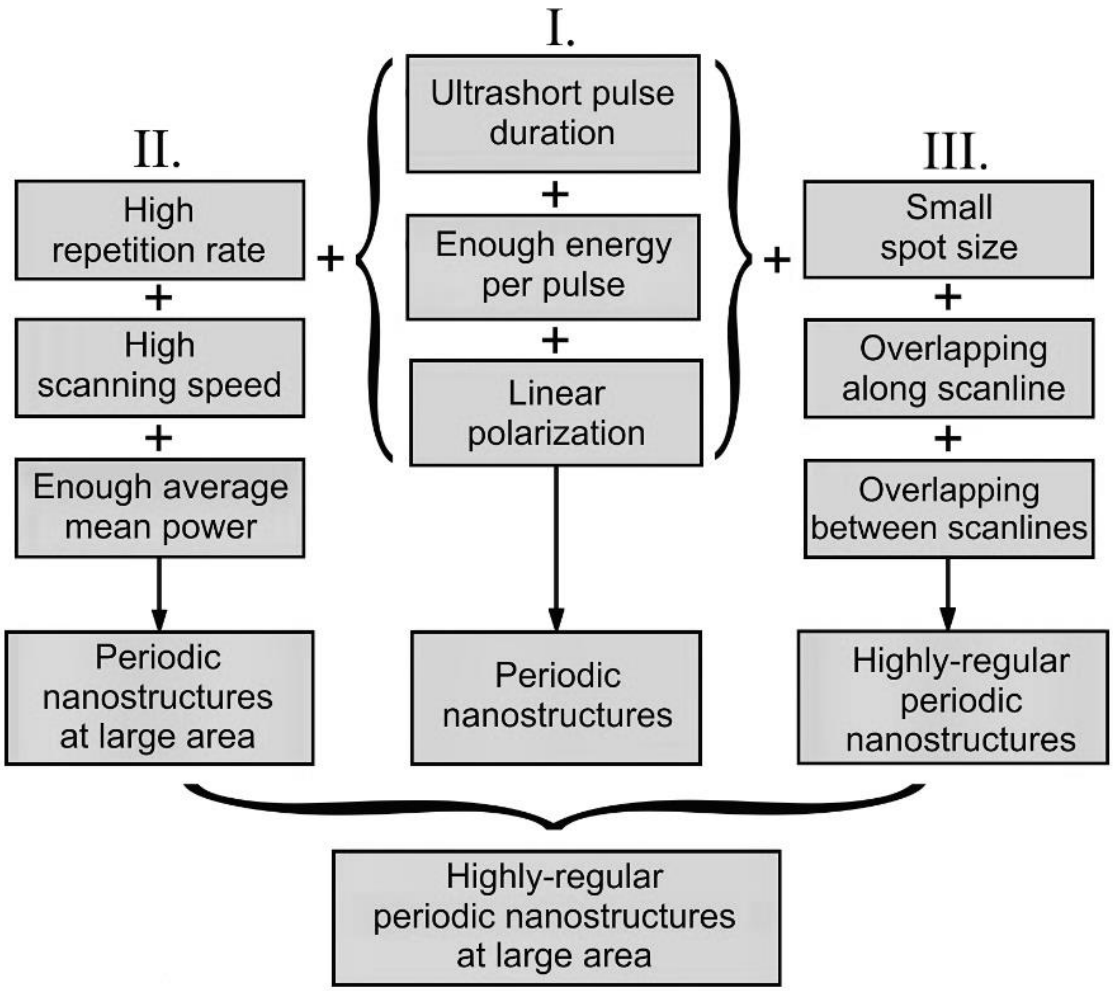

Figure 26. The scheme of algorithm of HR-LIPSS method is shown.

Figure 27 illustrates an example of selection of materials for HR-LIPSS writing at wavelength of 1030 nm based on the analysis of the mechanism of their formation (prediction of materials suitable for HR-LIPSS in details depicted in Section 4.1.6). The selected materials satisfy both Criteria (I) and (II). In the figure, the materials are presented whose SEW decay length is smaller than 10 μm (Criterion I) and which possess high optical damping (Criterion II). It is thus disclosed that the spatial coherence of the excited SEW within the laser illuminated spot is at the origin of the high regularity of the obtained periodic structures. The SEW can be initiated by any sub-wavelength scattering center. The scattering centers can be a point-like defect, a dipole-like nanotip forming the sample roughness, a bigger object like a nanoparticle

present at the surface, or even a scratch. By using a small spot size, excited SEWs interact on a small area where spatial coherence can be conserved. The distance of the excited SEW is linked with the decay length L_{SPP} of the SEWs. The usage of a small spot size allows to trigger selectively the excitation of short-range SEWs.

The Criteria I and II can be applied to any wavelengths and other materials.

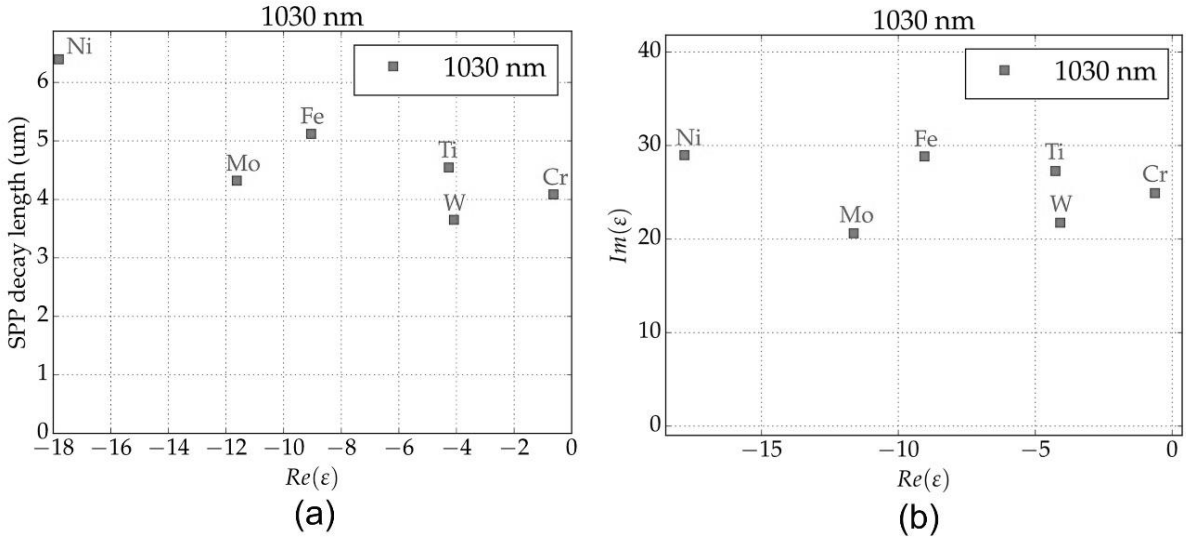

Figure 27. The requirements for selection of materials able to exhibit Highly-Regular Periodic Structures upon pulsed laser irradiation at 1030 nm wavelength. The requirements for selection of materials able to exhibit Highly-Regular LIPSS upon pulsed laser irradiation at 1030 nm wavelength: (a) shows the SEW decay length of materials; (b) presents the dielectric permittivity of materials which satisfy the selection criteria).

Chapter 4 Physical origin of LIPSS regularity on metals

4.1.1 Background

This study was implemented together with prof. Nadezhda M. Bulgakova, Dr. Thibault Derrien and Dr. Yoann Levy, HILASE Center, Prague, Czech Republic.

Ultrashort laser irradiation is proven as a robust, cheaper alternative to lithography to nano-structure surfaces of various materials via formation LIPSS [10]. Several application fields have emerged, based on this process, such as modification of surface wetting and tribology properties, surface coloration and marking [61][72][85][86]. Achieving the control over nanostructure formation in these applications remains difficult because of high sensitivity of this process to the type of material and laser irradiation parameters that hinders achieving reproducibility and uniformity of periodic patterns. Although the first observation of LIPSS revealed their good regularity [13], considerable progress in controlling precision of LIPSS fabrication was made not long ago, though limited to specific materials. More recently, the marking process was distinctly accelerated up to industrial throughputs,[47] opening the way for a faster development of nanostructure-related applications.

So far, the physical origin of the material-dependent high regularity remains unclear. Ruiz de la Cruz et al. [87] suggested an electrodynamic mechanism linked with the orientation of laser-beam scanning velocity relative to light polarization. Existing theoretical investigations of the electron dynamics at laser-irradiated materials does not yet include laser scanning [88] due to complexity of involved interrelated processes, that can be overcome in the incoming years. Large body of investigations reveal that the quality of nanostructures imprinted on surfaces of various kind depend on involved mechanisms and the processes such as surface melting [89], ablation [10], oxidation [34], or band gap modification [90] all originating from initial periodic modulation of the deposited electromagnetic energy over irradiated surface. It has been found that laser-induced oxidation [34] and partial melting [89] allows to obtain a very good regularity in the induced pattern in case of a thin-film configuration. Interestingly, adding of only 3% of second harmonic energy to that of the fundamental (800 nm) wavelength can

reduce the dispersion of the LIPSS orientation angle (DLOA), thus improving nanostructuring quality

In this chapter, present the formation of highly-regular LIPSS (HR-LIPSS) in the ablation regime on several metals processed in air and at velocities competitive with industrial standards of nanomanufacturing (1cm^2 in 10 s). A simplified methodology is proposed for explaining the regularity of periodic structures on metal/metalized surfaces, which allows to predict whether HR-LIPSS can be formed. The results reveal that only specific metals undergoing high optical losses at the processing wavelength can exhibit regular periodic structures. A list of materials, which can exhibit excellent LIPSS regularity, is provided for several wavelengths. It is predicted that reducing the laser wavelength can enable achieving HR-LIPSS on principally any metal. These results can push high-throughput laser-induced nanostructuring process to a well controllable technology.

4.1.2 Experiment

The surfaces of 6 different metals, Al, Ti, Cu, Mo, Au and steel, were processed by femtosecond laser pulses irradiation at λ = 1030 nm, through a set-up involving a galvoscanner and a translation stage. A sketch of the experimental setup is shown in Fig. 28.

Optical pulses (central wavelength 1030 nm, pulse width 213 fs (FWHM), repetition rate 600 kHz) were delivered by Yb: KGW chirped-pulse application laser system (model Pharos 20 W from Light Conversions) and were forwarded to Cambridge Technology galvanometric scanning head. Alignment of linearly polarized laser light was controlled by a half-wave plate.

The surface treatment was done in air at room temperature by scanning laser beam across sample surface. To control average power of the laser pulses at sample surface, a motorized attenuator was utilized to transmit about 2.5% of incident power of the laser system. Laser beam was forwarded to the sample surface at normal incidence. The laser beam was focused by an F-theta lens with focal length 55 mm that produced an approximate irradiation-spot diameter of 7.3 μm (1/e^2) on the sample. The peak fluence in a pulse was ~1.58 J/cm^2. The surface was scanned to nanostructure a rectangular area 10×10 mm. Much larger areas were obtained for specific experiments by additionally translating the sample with a XYZ motorized translation stage. The laser parameters are summarized in Tab. 1.

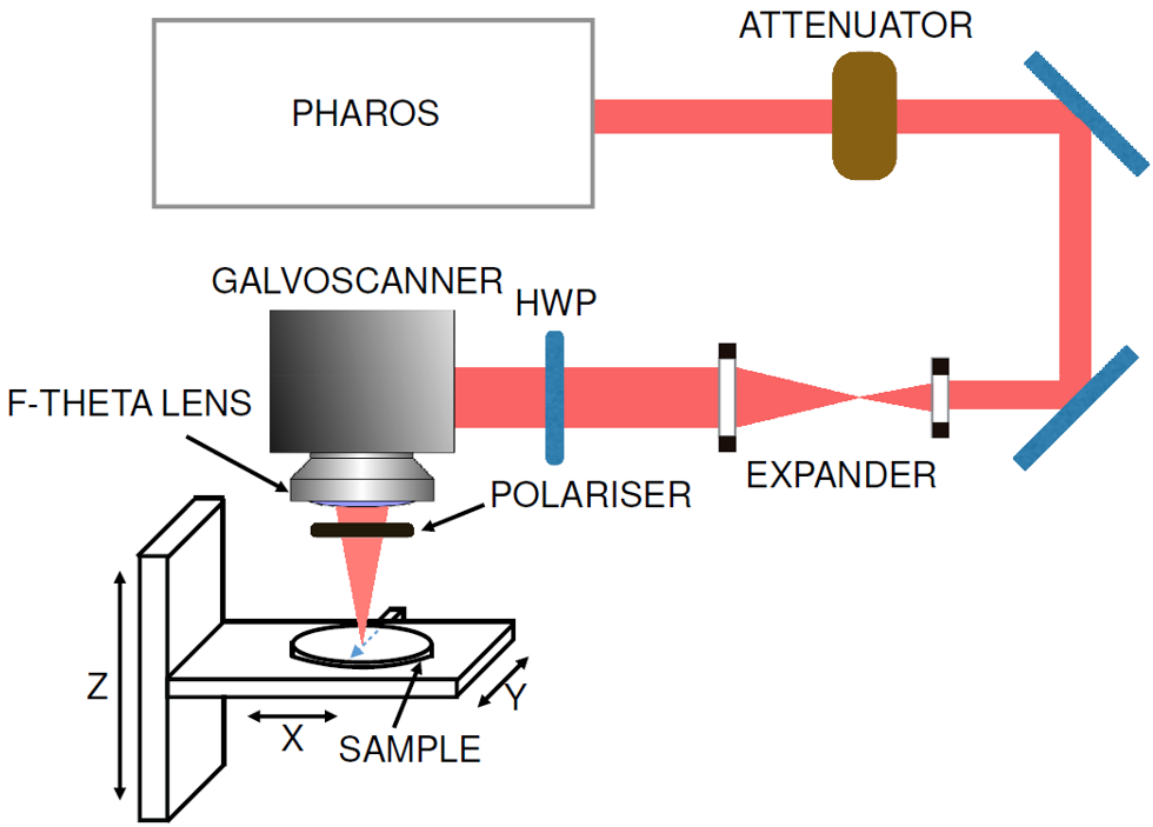

Figure 28. A setup of commercial laser "Pharos".

Materials

The samples of Ti and Mo consist of 300 nm-thick coatings deposited on glass (quartz) substrates using physical vapour deposition (PVD) by magnetron sputtering a 3-inch Mo and Ti targets (purity for both was 99.95%) in Ar atmosphere. Before deposition, the chamber was pumped to a base pressure lower than 10^{-6} Torr. During the deposition, the pressure was fixed at $5 \cdot 10^{-3}$ Torr, and the substrate was rotated to provide a uniform coating thickness. Copper (99.9% purity), aluminium (99.9% purity) and stainless steel (AISI 316L) samples with dimensions of 25x25x5 mm were mechanically polished and cleaned in ethanol before irradiation. The commercial Au alloy 18k Yellow Gold (12.5% Silver) samples were plates of 1mm thickness. Optical data for Au and Ag were taken from Ref. [91]

Table 1. Set of parameters used in the present work and in several references reporting regular LIPSS: F is the average fluence and was estimated by the expression $F = 4E/(\pi\sigma^2)$, where σ is the spot diameter at $1/e^2$ of peak intensity.

Materials	Wavelength λ (nm)	Pulse duration τ (fs)	Energy per pulse E (nJ)	Fluence F per pulse (J/cm^2)	Repetition rate f (kHz)	Scanning velocity v (mm/s)	Spot diameter σ at $1/e^2$(μm)	Effective pulse number	Overlapping (%)	Throughout (μm^2/h)	LIPSS period Λ (nm)	References
Mo	1030	213	583	0.69	600	1700	10.4	2.59	61.4	2.1×10^{10}	845± 38	This work
	800	50		0.07	1	0.04	30-40	~750	99.9	5.8×10^{6}	589± 30	[92]
Ti	800	213	500	0.59	600	3000	10.4	1.47	31.9	3.8×10^{10}	737± 26	This work
Ni	800	90		0.16	1	2	40	20	95	-	~650	[93]
	1026	232	130		1	0.5	6	120	91.7	-	760± 120	[94]
Steel	1030	213	383.3	0.45	600	3000	10.4	1.47	31.9	3.8×10^{10}	901± 38	This work
Cr	1030	500	1950	0.039	250	1500	80	13.3	92.5	9×10^{9}	913± 53	[87]
Al	1030	213	916.7	1.08	600	3000	10.4	1.47	31.9	-	842± 134	This work
Cu	1030	213	1500	1.77	600	3000	10.4	1.47	31.9	-	956± 85	This work
Au	1030	213	4080	4.82	600	3000	10.4	1.47	31.9	-	893± 160	This work

For all the irradiated materials, LIPSS with spatial periods Λ close to slightly smaller than comparable to the laser wavelength and perpendicular to the laser electric field polarization were formed. These structures are known as so-called "Low Spatial Frequency LIPSS" (LSFL) [95] Several degrees of uniformity were evidenced and, in particular, HR-LIPSS could

only be obtained on Ti, Mo and steel (see Fig. 29). The other materials (Au, Cu and Al) are given in Fig. 30.

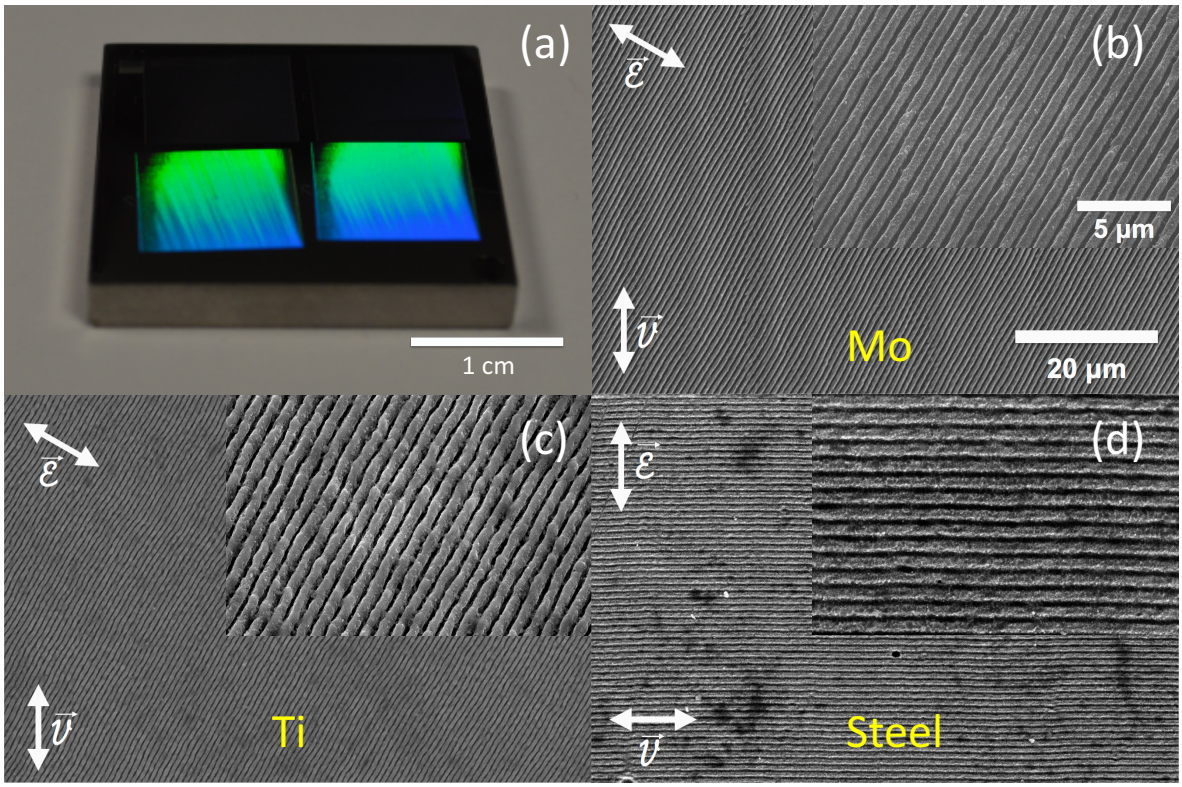

Figure 29. Femtosecond LIPSS obtained on Mo, Ti, and stainless steel. Arrows indicate directions of laser field polarization ($\vec{E}$) and of the scanning direction (v). (a) Human-scale view of a Mo sample covered with HR-LIPSS. (b) Secondary Electron Microscope (SEM) picture of the Mo sample covered with HR-LIPSS. (c) Same with Ti (d) Same for steel (Fe mixed with 16.87% Cr, 10.05% Ni). Insets in Figs (b-d) show magnification (about 2x).

Among materials studied, HR-LIPSS could only be obtained on Ti, Mo and steel (see Fig. 1). On the rest of the metals surfaces (Au, Cu and Al), we were not able to achieve a high quality of ripples (Fig. 30).

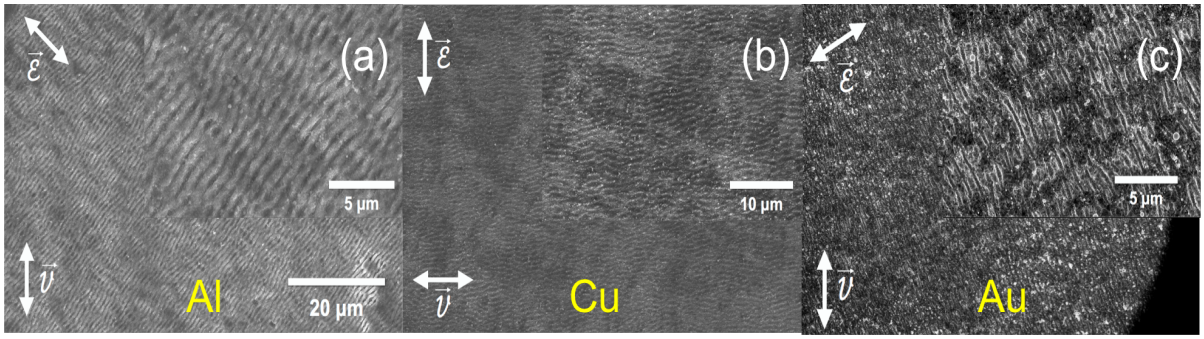

Figure 30. Set of three metals (Al, Cu and Au) exhibiting low LIPSS regularity. For each material, the laser scanning direction (v) is indicated in respect of the laser polarization ($\vec{E}$).

In particular, Figure 29 shows that, for obtaining highly regular structures in our irradiation regimes, scanning velocity has not to be obligatory perpendicular to the polarization direction but can be also up to 45◦ , in some contradiction to Ruiz de la Cruz et al. [87] To characterize the regularity in a repeatable manner, a systematic approach was used on the basis of an existing measurement procedure [95] On each SEM picture, the local orientation of the LIPSS was analyzed. From the distribution of the orientation angle, spreading of the latter was extracted which we call the dispersion in the LIPSS orientation angle (DLOA). It is comparable to the angular opening of the two-dimensional Fourier transform (2D-FT) of the original SEM image. However, the technique for determining the DLOA is more robust than an evaluation of the angular diameter which can be approximate on 2D-FT images. This procedure, using an open-source software (open software) based on structure tensor analysis of microscope images, is detailed in the next section and was systematically applied to SEM images of processed surfaces.

4.1.3 Characterization of regularity

To characterize the regularity in a repeatable manner, a systematic approach was used, on the basis of an existing measurement procedure [95]. It consists in measuring the dispersion of LIPSS orientation angles (DLOA) $\boldsymbol{\delta\theta}$ using [96] image structure tensor analysis with an open-source software. This procedure is a quite simple: from the SEM pictures, the regularity was analysed by measuring DLOA - $\delta\theta$ of the periodic pattern. A systematic and repeatable procedure was defined and applied to each sample analysis.

- We used the freely available *OrientationJ* [97] written for the ImageJ open-source software [98], based on the tensor structure analysis of the image to be processed. The specific module *Orientation Distribution* with the *Riesz Filters* structure tensor was used. No Gaussian smearing was applied. For each analysis, the angle distribution was corrected from its offset (minimum value of the spectrum) and the half width at half maximum extracted to obtain the DLOA, $\delta\theta$.
- Most important is to keep the magnification of the original SEM pictures constant between the different samples. In this study, 5.000 × magnification was employed. If a higher magnification is taken, dispersion measurements can be affected towards a seemingly lower angular dispersion, artificially reducing the DLOA.

- Orientation distribution analysis were performed over squared and large area to allow for sufficient statistics and a corresponding stabilization of the DLOA value with increasing dimension area. The Fig. 31 shows this stabilization for Al and Ti, and that, for Al, the distribution of angles globally narrows as the surface increases.
- The errors on the DLOA were estimated from the accuracy of the distribution (±1°) and from the residual fluctuations in the stabilized area.

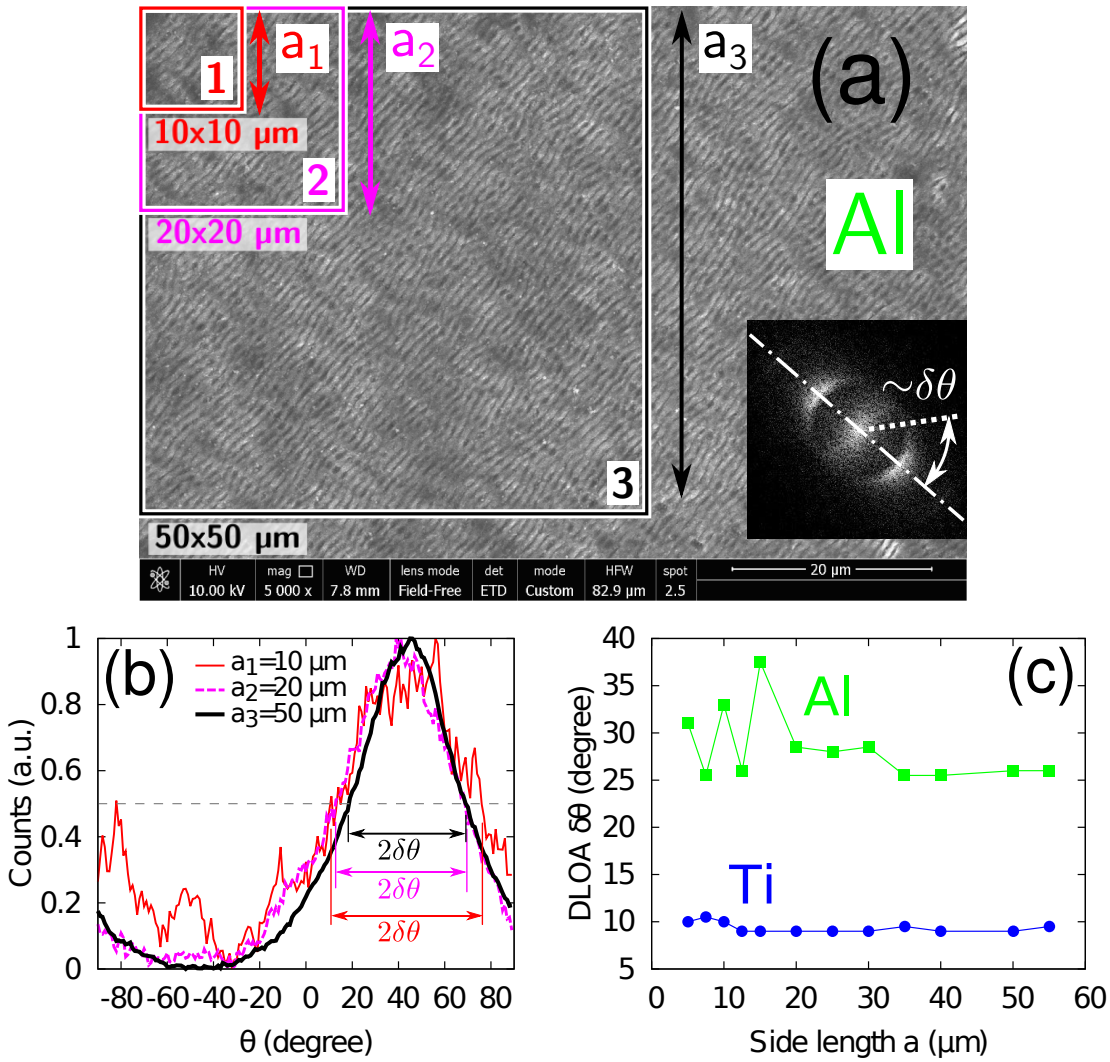

Figure 31. Effect of the measurement area on the DLOA dq. For different sizes of the LIPSS-covered area chosen for analysis (a), different spectra (b) of orientations q can be obtained with the module OrientationJ of the open software ImageJ. The normalized spectra of orientation are shown for the case of Al. The orientation axis ranges from -90◦ to +90◦ (orientation is p -periodic: the orientation angle of + 91◦ corresponds to the orientation of -89◦). Note that on (b) the distribution is centered around 45, in line with the LIPSS orientation on (a). Colors of lines in (b) correspond to areas in (a) highlighted by the same colors. (c): Good convergence of the DLOA measurements is achieved when the surface area selected for analysis is large enough. Side length a refers to the square area (of side ai, i = 1; 2; 3) in (a). The measurement performed on Ti is also reported for comparison.

The DLOA obtained for the materials are summarized in Tab. 2.

Table 2. Properties of excitable SPP at several air/metal interfaces upon λ = 1030 nm laser irradiation wavelength. DLOA $\delta\theta$ was measurement method is using two different methods, detailed in the methodology. E.M.T. stands for effective medium theory was used to calculate the dielectric permittivity of steel as function of the volume fraction of Fe, Ni and Cr contained in the sample.

Interface	Re(ε_{sample})	Im(ε_{sample})	Optical data	L_{SPP}, μm	DLOA $\delta\theta$	Exp.reference
air/Cr	-0.63	24.92	[91]	4.1±0.8	13º±0.2º	[87]
air/Mo	-11.73	20.30	[99]	4.3±0.9	5.3º±1.0º	This work
air/Ti	-4.27	27.28	[91]	4.6±0.9	9.2º±1.5º	This work
air/steel	-7.98	28.76	E.M.T.*	5.0±1.0	9.2º±0.8º	This work
air/Al	-97.59	25.27	[100]	65.0±13.4	26.7º±3.5º	This work
air/Cu	-46.60	4.72	[100]	73.8±16.6	23.8º±1.5º	This work
air/Au	-49.59	3.81	[100]	103.1±23.7	48.8º±1.0º	This work

Due to the absence of visible bifurcation point, the reported nanostructures on Mo exhibit the highest regularity available to our knowledge, in ablation regime, with a DLOA $\delta\theta$ close to 6.0º. So far, the best DLOA that we could measure from the literature (at similar wavelength, and similar throughput) was obtained by Ruiz de la Cruz et al. [87] exhibiting a DLOA $\delta\theta$ of 12.0º + 2.0º according to the measurement protocol applied for this study. It must be noted, however, that the quality of the cited picture obviously has other magnification and number of LIPSS available for measurement, which has an influence on the measurement protocol, as shown in our Methodology section.

Although showing a few bifurcation points on comparable areas, the highly regular structures generated on Ti and steel (Fig. 29 (c, d)) still exhibit DLOA below 15º. The series of experiments carried out on the different metallic sample surfaces are compared with available studies found in literature in Tab. 1. Although DLOA variations with respect to other works could be attributed to the use of a specific range of laser fluence for each material (see Tab. 1), we propose an energy-independent model to explain the periodic structure regularity as a function of the material used in the experiment, based on its" cold" optical data. In particular, within the 6 types of irradiated samples, the highest regularity was obtained on Mo using a polarization oriented by 45º in respect of the scanning velocity, i.e., the laser polarization direction was not

strictly perpendicular to the laser scanning direction, as previously supported [87]. However, similarly to [87], the poorest quality of LIPSS was obtained while the scanning $\overrightarrow{v_S}$ and polarization directions $\vec{E}$ are arbitrary aligned and address the question on the physical origin of the high regularity of the LIPSS, which are proposed below and support with a simple model matching with the observed experimental results.

4.1.4 Origin of the regularity

Although material relocation during/after the laser pulse action, and that different marking mechanisms can take part in the LIPSS formation, strong pieces of evidence indicate a common initiation by the transient excitation of Surface Electromagnetic Waves (SEW) forming a periodic pattern in the near-field distribution during the laser pulse [15][23][91][101][102], thus creating a modulated temperature distribution [103]. Assuming that LIPSS are formed via the excitation of Surface Plasmon Polaritons, [23][92] the $1/e^2$ - decay length of the SPP quasiparticle (i.e. its mean-free path) can be calculated and associated with the regularity of the obtained periodic structures for several metals. The properties of this particular type of SEW are given by their dispersion relation expressed, at an interface air/sample, via [104][105]

$$\frac{k_{air}}{\varepsilon_{air}} + \frac{k_{sample}}{\varepsilon_{sample}} = 0.$$

where ε_j is the dielectric permittivity and k_j the SPP wave vector in the medium *j*. In materials with losses (where imaginary part of the dielectric permittivity ε_{sample} is not zero), SPPs can be excited if they satisfy to the general condition expressed by [104][105].

$$\mathcal{R}e(\varepsilon_{air})\,\mathcal{R}e(\varepsilon_{sample}) + \mathcal{I}m(\varepsilon_{air})\,\mathcal{I}m(\varepsilon_{sample}) < 0 \qquad (3)$$

which reduces to $\mathcal{R}e(\varepsilon_{sample}) < 0$ at the air/material interfaces (ε_{air}=1). The SPP properties along the interface are described by the SPP wave-number β given by [104].

$$\beta = \pm\frac{w}{c}\sqrt{\frac{\varepsilon_{air}\,\varepsilon_{sample}}{\varepsilon_{air} + \varepsilon_{sample}}},$$

where ω is the laser frequency. Under the assumption that optical properties of metals do not vary much during the laser irradiation, the mean-free path of SPPs, L_{SPP}, can be calculated from the SPP wave number via the expression

$$L_{SPP} = \frac{1}{2\,\mathfrak{Im}\,(\beta)} \tag{4}$$

The spatial period of the modulated electromagnetic field Λ_{SPP} at the material interface originated from the interference of the incident laser light with the excited SPPs fields can be estimated from the real part of the SPP wave number [104][105]

$$\Lambda_{SPP} = \frac{2\pi}{Re\,(\beta)} \tag{5}$$

Assuming that this interference conditions a periodic absorption of laser energy, Λ_{SPP} represents an evaluation of the LIPSS periodicity.

This very simple model allows to perform a first comparison of the highly-regular periodic structures with the mean-free path of SPPs excited at the surface of different laser-irradiated metals. After calculating Eq. (3) and Eq. (4) at the air/sample interface for each sample of interest, the results were reported in Tab. 2 together with the orientation angle $\delta\theta$ of the formed LIPSS and plotted in Fig. 32. A strong correlation between the mean free path with the experimentally measured DLOA $\delta\theta$ is observed.

Materials which exhibited highly regular periodic structures (HR-LIPSS) have a SPP mean-free-path smaller than 15 μm, at the given irradiation wavelength. Materials with a high

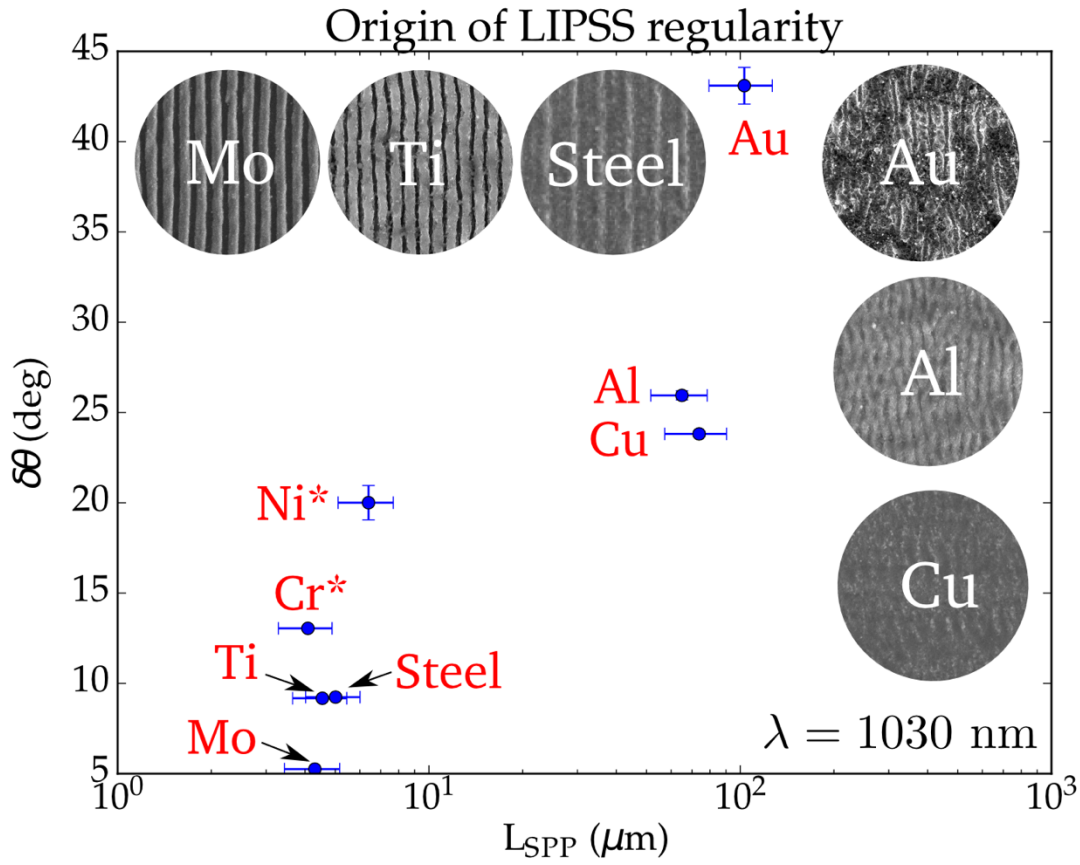

Figure 32. DLOA $\delta\theta$ as function of the calculated mean free path L_{SPP} of Surface Electromagnetic Waves. The insets contain SEM pictures made with identical magnification of each laser-irradiated material using conditions given in Tab. 2.

optical damping (with a high imaginary part compared to the real part in their dielectric permittivity) exhibited the highest regularity in the obtained LIPSS pattern. This result is supported by Fig. 33(a), displaying the values of L_{SPP}, from Eq. (4), as a function of the real and imaginary part of the metallic sample considered upon laser irradiation at $\lambda = 1030$ nm. Several metals have been placed on the figure, yielding their respective L_{SPP}, assuming no change of refractive index during the laser irradiation. Two groups of materials can be identified: (i) a group with Nb, Ni, Mo, Ti, W and Fe which present a SPP decay length of 1 to 10 µm; and (ii) a group of Al, Cu, Ag and Au exhibiting a SPP decay length of more than 60 µm. By cross-checking materials of Fig. 33(a) with Fig. 32, it is noted that for the single elements of the first group (smaller SPP decay length), the 3 experimental tests (Mo and Ti) demonstrated high regularity LIPSS formation feasible, whereas materials of the second group lead to a low regularity (Fig. 30).

4.1.5 Role of the spot size

By comparing L_{SPP} to the spot size used in this work (σ = 10 μm), we observe that materials for which $L_{SPP} \sim \sigma$ exhibit an excellent regularity (low DLOA $\delta\theta$). Materials for which $L_{SPP} >> \sigma$ exhibit a poor regularity (high DLOA $\delta\theta$). The laser spot size was recently identified as being an important parameter for reaching an excellent regularity of nanostructures formation in oxidation regime [34]. Thus, according to Ref. [34], the spatial coherence of the excited surface waves can be preserved more easily on a small irradiation area. Note that the initial observation of a coherent link between overlapping irradiation spots was proposed by Fauchet and Siegman [106].

It can thus be expected that spatial coherence of the excited SEW is at the origin of the regularity of the obtained HR-LIPSS. A SEW can be initiated by any sub-wavelength scattering center [107] [108]. A scattering center can be a point-like defect, a dipole-like nanotip forming the sample roughness, a bigger object like a nanoparticle present at the surface, or even a scratch present at the surface [109][110][111]. When propagating to a large distance and experiencing interactions with numerous scattering centers, SEWs are losing their initial coherence properties. Contrary to [34] we hypothesize that the excited SEWs remain more independent (when their mean free path is small) within the irradiation spot, thus preserving their initial coherence with incoming laser light for forming a periodic absorption pattern. This is also in line with our observations that metals with short SPP decay lengths allow for better periodicity compared to metals with long SPP decay lengths. Interaction between rapidly decaying SEWs is reduced that enables to support their coherence with the incoming light even within relatively large irradiation spots.

Further, at a given irradiation fluence needed to reach the present ablation regime, a small spot size can favour the development of deeper and cleaner single pulse craters due to higher stress confinement responsible for a better evacuation of the melt. The scattering of an overlapping spot over clean favour better development of the ripples.

The model proposed in this thesis makes possible the prediction of the SPP mean-free path for a wide range of materials and various irradiation conditions. A computation similar to that shown in Fig. 33 was performed using wavelength λ = 800 nm (see Fig. 33 (b)). Interestingly, distribution of materials exhibiting a L_{SPP} comparable to the laser spot size is very different from Fig. 33 (a) and the following predictions can be proposed: whereas (i) Mg, Au, Na,

Cu and Ag materials are predicted to exhibit low-regular LIPSS, (ii) Pt, Co, Li, Ta, Zr, Fe, Bi, Nb, Ti and Cr are expected to lead to the formation of highly regular LIPSS. Upon $\lambda = 400$ nm laser irradiation, almost all the materials reported in Fig. 33 (c) may exhibit an excellent regularity. These results also support that LIPSS obtained on Au, Al and Cu using IR wavelength showed a poor regularity (Fig. 30). With using a UV wavelength, regularity is predicted to dramatically increase for many materials. This may open extraordinary opportunities for extending our experimental results to a wide range of materials and enable the development of high-quality demanding applications (optical gratings, for example).

4.1.6 Predictions of materials suitable for Highly Regular LIPSS formation.

The simplified methodology proposed above, which is based the on L_{SPP} evaluation, to select the materials exhibiting high optical damping and hence suitable for HR-LIPSS inscription at particular irradiation conditions. The results of calculations of L_{SPP} as a function of real and imaginary parts of dielectric functions are shown in Fig. 33(a)-(c) for three laser wavelengths, $\lambda = 1030$, 800, and 400 nm. Interestingly, the number of materials with a short decay length L_{SPP}, which can enable HR-LIPSS generation, is increasing with decreasing the wavelength. At $\lambda = 1030$ nm, besides Mo, Ti, Ni, Cr, and steel, such metals as Nb, W and pure Fe are identified as candidates for HR-LIPSS formation while Ag falls to the group of low- regularity LIPSS, together with Au, Al, and Cu whose micrographs with LIPSS are shown in Fig. 33. At $\lambda = 800$ nm, the group of the HR-LIPSS metals is enriched with Pt, Co, Li, Ta, Zr, and Bi. With further decreasing laser wavelength, to $\lambda = 400$ nm, our theory predicts that the majority of analyzed metals can enable HR- LIPSS formation, including gold and copper [112] for which a high regularity of LIPSS is hardly achievable at longer wavelengths. As a whole, we predict that, using a near-UV or blue-light wavelength, regularity of the laser-induced periodic structures can be dramatically improved for many materials. This can open extraordinary opportunities for extending our experimental results to a wide range of materials and enable the development of high-quality demanding applications (optical gratings, for example).

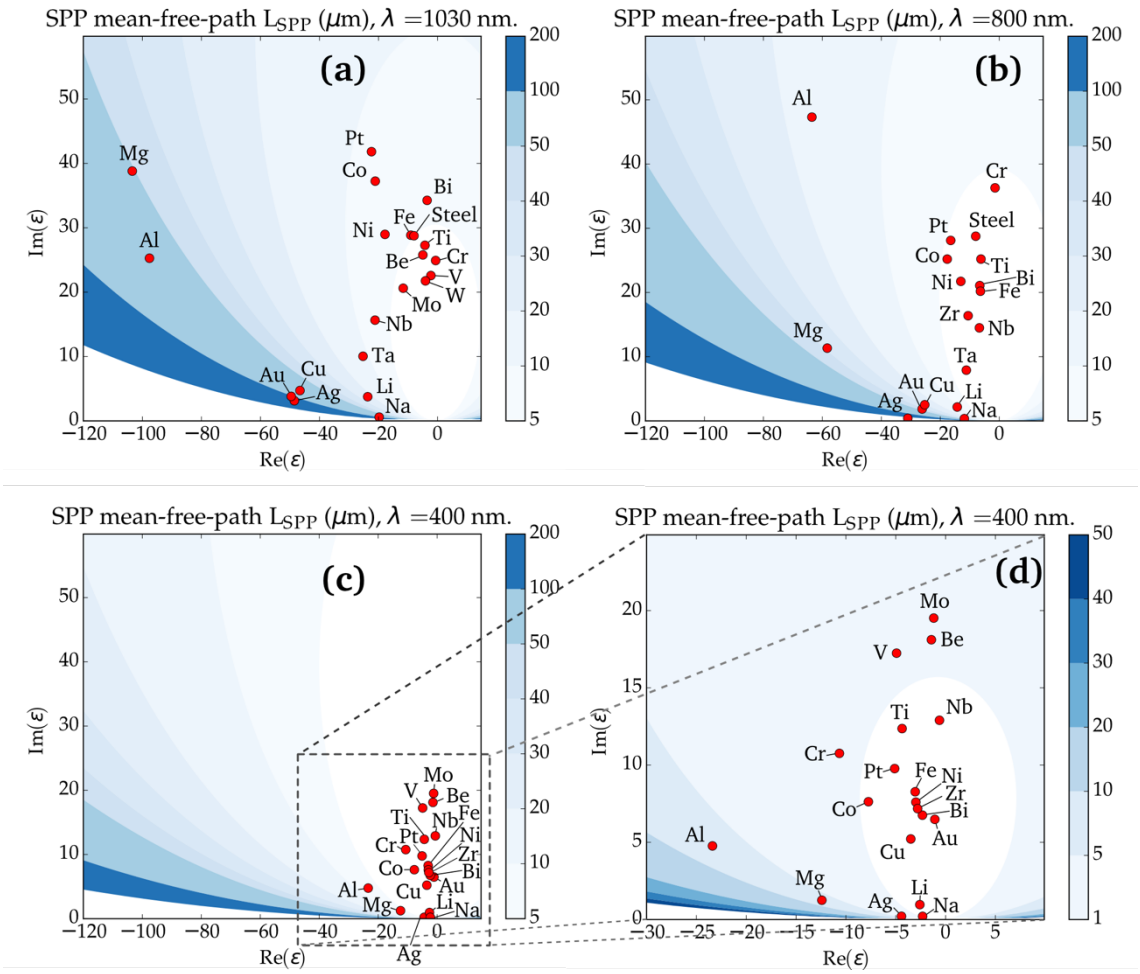

Figure 33. SPP mean free path L_{SPP} for different metals at three laser wavelengths λ = 1030 nm (a), 800 nm (b) and 400 nm (c, d). According to our prediction, metals with small L_{SPP} (located in the bright regions) are suitable for HR-LIPSS generation at the corresponding laser wavelengths.

4.1.7 Modeling of the change in the optical properties

The above predictions are based on optical properties of metals (n and k, or equivalently ε) at the room temperature under equilibrium conditions. The data on refractive indices and extinction coefficients published in different literature sources for same materials can noticeably vary. These variations can produce uncertainty in the evaluated data with consequences for the accuracy of our predictions. Calculations however show that varying the real and imaginary parts of the dielectric permittivity does not strongly affect the predicted LIPSS periodicity, L_{SPP}. The L_{SPP} and δL_{SPP} values were estimated using analytic expressions given in Section 4.1.8). One can expect a stronger effect on the SPP decay length from swift non-equilibrium

heating of the electron subsystem in metals by ultrashort laser pulses and associated dynamic change of the dielectric permittivity [113]. At relatively high laser fluences which are exploited in this work for generation of LIPSS on metal surfaces, free electrons can gain energies of several electron-Volts during the laser pulse action [113] [114]. As a consequence, their optical response can be dramatically changing, thus affecting the results of our predictions. Hence, it is vital to investigate the possible changes in the SPP mean free path during laser irradiation.

It has been shown [113] that, in the case of copper, the real and the imaginary parts of the dielectric permittivity are strongly changing functions of the electron temperature even at temperature levels well below the Fermi one. Following the approach reported in [113] the temporal variations of the dielectric permittivity were modelled numerically for titanium and molybdenum in the course of femtosecond laser irradiation. For these aims, the two temperature model (TTM) [114] was supplemented with the computation of the optical properties in the frame of the Drude model. The thermal conductivity and the heat capacity of the electron subsystem were considered as linear functions of the electron temperature [114], $k_e = k_{e;0}\, T_e/T_l$ for the thermal conductivity, $C_e = A_e T_e$ for the heat capacity, a constant coupling factor γ, and a constant heat capacity of the lattice C_l. For titanium, $A_e = 329$ *J/(m³·K²),* $k_{e;0} = 22$ W/ (m· K), $\gamma = 1.85\times10^{18}$ *W/ (m³· K)* and $C_l = 2.35\times10^{6}$ J/ (m³· K) and for molybdenum, $A_e = 350$ *J/(m³·K²),* $k_{e;0} = 135$ W/ (m· K), $\gamma = 1.3\times10^{18}$ *W/ (m³· K)* and $C_l = 2.8\times10^{6}$ J/ (m³· K).

The optical properties are determined by the dielectric permittivity expressed, for the metals considered, as

$$\varepsilon = 1 - \frac{\omega_{pe}^2}{\omega^2+\nu_{eff}^2} + i\frac{\nu_{eff}\omega_{pe}^2}{\omega(\omega^2+\nu_{eff}^2)} \tag{6}$$

ν_{eff}= min (ν_e; ν_c) is the effective collision frequency [113], ν_e is the electron collision frequency and ν_e the critical collision frequency based on the interatomic distance and the electronic velocity $v_c = (4\pi n_0 / 3)^{1/3}\sqrt{v_F^2 + k_B T_e/m_e}$ (n_0 is the atom density and v_F, the Fermi velocity). The electron collision frequency is the sum of the electron-electron and of the electron-ion collisions: $\nu_e = \nu_{ee} + \nu_{ei} = AT_e^2 + BT_l$. The expression of the first coefficient $A = \omega_{pe}\pi^2 k_B^2\sqrt{3}(\pi^2+1)/(128E_F^2(1+1/e))$ is obtained from Groeneveld et al. [115] by comparing AT_e^2 with the expression in there at E - $E_F \sim k_B Te$, with k_B the Boltzmann constant. Considering the plasma frequency in the frame of the Drude model, at room temperature ($T_e = T_l = T_0$), $\omega_{pe} = \omega\sqrt{1-\varepsilon'(T_0)+\varepsilon''^2(T_0)/(1-\varepsilon'(T_0))}$, one obtains for titanium $A = 2.2\times10^{6}$

$K^{-2}\cdot s^{-1}$. The coefficient B is deduced from this latter value and from the room temperature collision frequency, $\nu_{eff}^{opt} = \omega\varepsilon''(T_0)/(1-\varepsilon'(T_0))$, of the material based on optical properties at

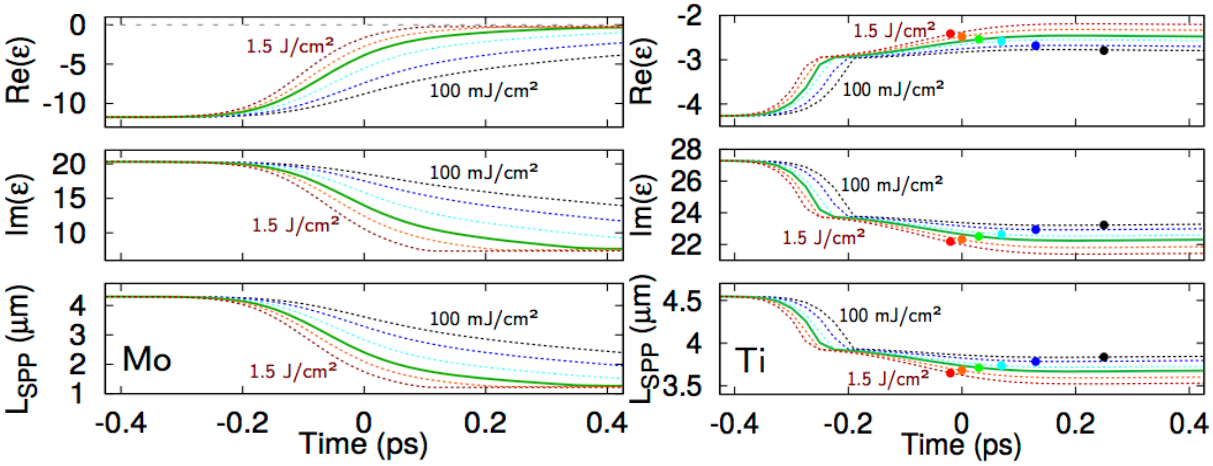

Figure 34. Estimations of dynamic changes of the optical properties upon irradiation of Ti (a) and Mo (b) by a 213 fs laser pulse at λ = 1030 nm. Variations of the real and imaginary parts of the dielectric permittivity e and the associated SPP decay length are shown at different laser fluences (colored lines with increasing fluence from right to left): 0.1, 0.2, 0.4, 0.6, 1.0 and 1.5 J/cm^2 for titanium and 0.1, 0.2, 0.4, 0.69, 1.0 and 1.5 J/cm^2 for molybdenum. In each graph, the green solid line corresponds to the experimental fluence (averaged over the irradiation spot) at which the reported LIPSS were produced.

thermodynamical equilibrium and T_0: $B = \nu_{eff}^{opt}/T_0 - AT_0$. From Johnston and Christy[91], at room temperature (see Tab. 2) we obtain, for Ti, $B = 3.2\times10^{13}K^{-1}\cdot s^{-1}$. For molybdenum, the same reasoning yields $A = 2.6\times10^{6}\ K^{-2}\cdot s^{-1}$ and $B = 9.8\times10^{12}K^{-1}\cdot s^{-1}$.

The computation of the dielectric function (3), with the associated parameters A and B, was implemented in the numerical scheme of the TTM to provides self-consistently the dielectric permittivity, from which was also derived the reflection coefficient R(t) and the absorption coefficient, $\alpha_{abc} = 4\pi Im\left(\sqrt{\varepsilon\ (z,t)}\right)/\lambda$, inverse of the optical penetration depth.

The results presented in Fig. 34 (b) and (c) also show the evolution of the dielectric permittivity on the surface of Ti and Mo and the corresponding changes in the SPP decay length, during the laser pulse irradiation and at the fluences of the reported HR-LIPSS. In the framework of the Drude model, L_{SPP} is decreasing during the irradiation and thus remains smaller than the initial modest value. No strong variations are therefore expected for these materials.

It must be precised that the validity of the presented numerical estimations holds only in the solid phase. Although it is possible to excite SPP at the interface between air and a metallic substance in the liquid phase, the variations of the optical properties in the Ti liquid phase,

driven out of equilibrium, is difficult to estimate. The development of such a non-trivial model is out of the scope of the present work. Therefore, for titanium, only the tendency can be provided since the melting, considered through latent heat of fusion, already happens during the second part of the pulse, at the fluence of interest. This again stresses the correlation between the SPP mean free path and the formation of HR-LIPSS: materials with low L_{SPP} processed with a short laser pulse exhibit the most regular structures, as indicated in Tab. 2. Therefore, keeping values of L_{SPP} low during the irradiation or limiting its variation seems to be a necessary condition to achieve high regularity patterning

4.1.8 Effect of wavelength for obtaining HR-LIPSS

As seen in Fig. 30 of the section 4.1.2, regularity of the LIPSS obtained on Au with 1030 nm wavelength was particularly poor. Using the model detailed by equations (3-4), one can calculate the SPP mean free path L_{SPP} as a function of the laser wavelength. The calculation data presented in Fig. 35b suggests that it would be possible to make highly-regular LIPSS on Au if using a laser wavelength of 400 nm (or smaller) and a spot size of several micrometers. The period of the LIPSS is linked to the used wavelength, see Fig. 35a, where the SPP period that determines the LIPSS period is given for the normal incidence of the laser beam on Au surface. As well demonstrated in previous studies, the period can be varied via increasing the angle of laser incidence [102].

Similar calculations also apply for Ti where regular structures should be obtained for a wide range of laser wavelengths (see Fig. 36). Note that changing the laser wavelength also changes the period of the structures, as shown in Fig. 36(a). This period prediction does not account for any oxide layer at the surface, which may strongly affect the obtained period [102]. The proposed predictions can be extended to a wide range of materials [105] allowing for taking control over the formation of HR-LIPSS.

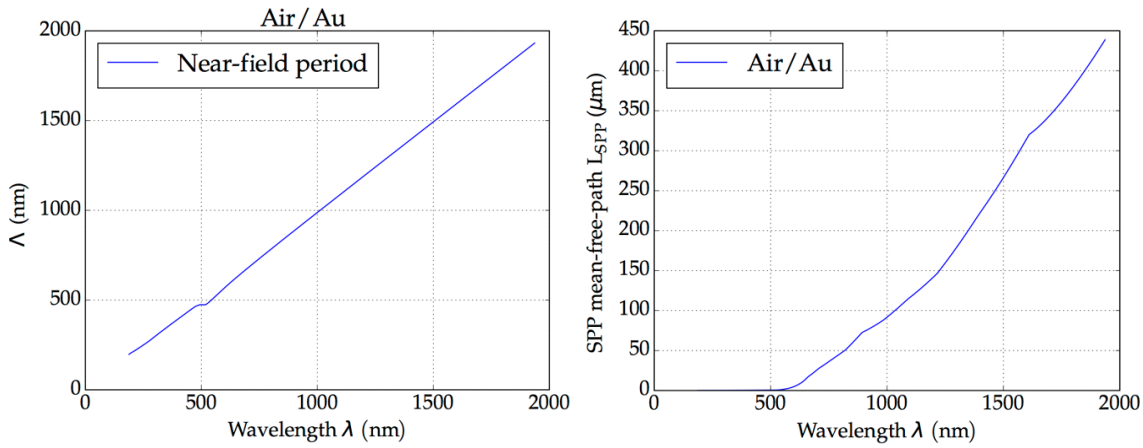

a b

Figure 35. Period (a) and mean-free-path (b) of SPPs as a function of laser wavelength for Au. HR-LIPSS may be obtained if using a wavelength smaller than 500 nm.

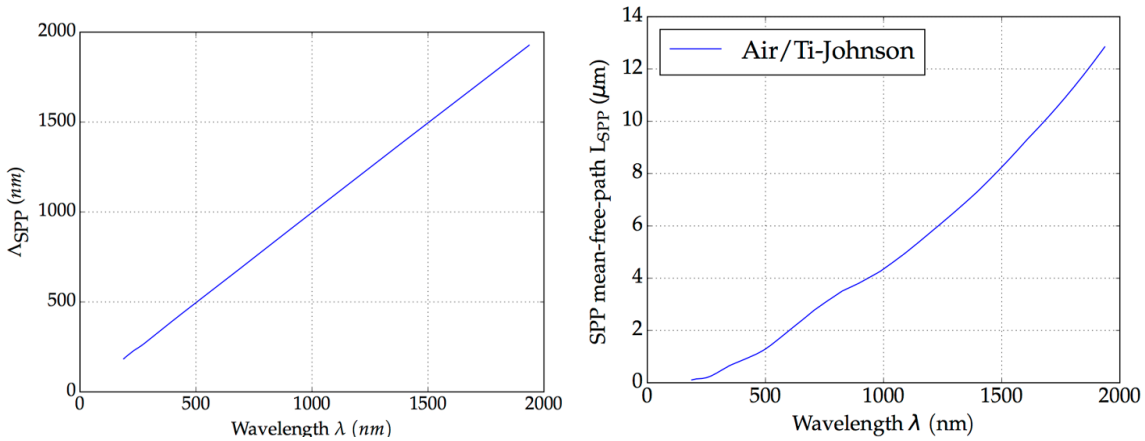

a b

Figure 36. Period (a) and mean-free-path (b) of SPPs as a function of laser wavelength for Ti.

4.1.9 Sensitivity of LIPSS period to variations of optical properties

When it is not possible to perform advanced numerical simulation of the transient refractive index of material during the irradiation, we propose in this section a small model based on the uncertainty of the dielectric permittivity e to calculate how much the SPP period can be modified during the laser pulse. As an example, for the laser wavelengths of 1030 nm and 800 nm, specific groups of metals should exhibit only small Λ_{SPP} changes of the period during the irradiation (see Figs. 37 and 38 respectively). For 800 nm wavelength, the period of SPPs excited on Na, Li, Ta, and Nb are expected to be very sensitive to the change of dielectric

permittivity. On contrary, transient variations of light absorption periods on the surfaces of Ti, Fe, Bi, Ni, Co, Pt, Cu, Ag, Au and Mg are expected to be small, within 10 nm for the case of $-5 \leq \delta\theta \leq 5$.

The spatial period Λ_{SPP} of the electromagnetic field on metallic surfaces can be calculated from the complex-valued SPP wavenumber β via[102] [104]

$$\Lambda = \frac{1}{2\,Re\,(\beta)}$$

For a general case of an interface between two media with dielectric functions ε_1 and ε_2, one can write:

$$Re(\beta) = \frac{\omega}{2c}\sqrt{2[F_1^2 + F_2^2]^{1/2} + 2F_1} \tag{7}$$

where

$$F_1 = (\varepsilon_1'\varepsilon_2' - \varepsilon_1''\varepsilon_2'')(\varepsilon_1' + \varepsilon_2')F_0 - (\varepsilon_1''\varepsilon_2' + \varepsilon_1'\varepsilon_2'')(\varepsilon_1'' + \varepsilon_2'')F_0$$

$$F_2 = (\varepsilon_1''\varepsilon_2' + \varepsilon_1'\varepsilon_2'')(\varepsilon_1' + \varepsilon_2')F_0 - (\varepsilon_1'\varepsilon_2' - \varepsilon_1''\varepsilon_2'')(\varepsilon_1'' + \varepsilon_2'')F_0,$$

and $\quad F_0 = [(\varepsilon_1' + \varepsilon_2')^2 + (\varepsilon_1'' + \varepsilon_2'')^2]^{-1}$

By assuming irradiation in air ($\varepsilon_1 = 1.0$), and assuming a monochromatic irradiation wavelength λ ($\delta\lambda/\lambda \ll 1$), the uncertainty on the SPP period Λ_{SPP} $\pm\delta\Lambda_{SPP}$ is bounded by

$$|\delta\Lambda| \leq \left|\frac{\partial[\mathcal{R}e(\beta)]}{\mathcal{R}e(\beta)^2}\right|$$

where the total differential of Eq. (7) gives the maximum error:

$$\delta[Re(\beta)] \leq \left|\frac{\partial[\mathcal{R}e(\beta)]}{\partial\varepsilon_1'}\delta\varepsilon_1'\right| + \left|\frac{\partial[\mathcal{R}e(\beta)]}{\partial\varepsilon_1''}\delta\varepsilon_1''\right| + \left|\frac{\partial[\mathcal{R}e(\beta)]}{\partial\varepsilon_2'}\delta\varepsilon_2'\right| + \left|\frac{\partial[\mathcal{R}e(\beta)]}{\partial\varepsilon_2''}\delta\varepsilon_2''\right|$$

The precision over optical constant is usually given [10] up to the 2th decimal. The real part ε'_1 and imaginary part ε''_2 may fluctuate in different directions. In addition, the dielectric permittivity may vary during the laser irradiation by a rather poorly known quantity.

Figures 37b and 38b present the calculated uncertainties δL_{SPP} for metals irradiated in air at two wavelengths, 1030 and 800 nm respectively. It is demonstrated that the "transient" LIPSS period can strongly vary for materials which exhibit a transient dielectric permittivity close to 0+0i (indicated by flower-like white region). Close to this particular point, the change

of period is dramatic and may ensure a loss of the SPP period. Out of this region, δL_{SPP} was found close to 10 nm for all metals of our study, assuming that the various factors of uncertainty on ε may be limited to $\delta\varepsilon = 5$.

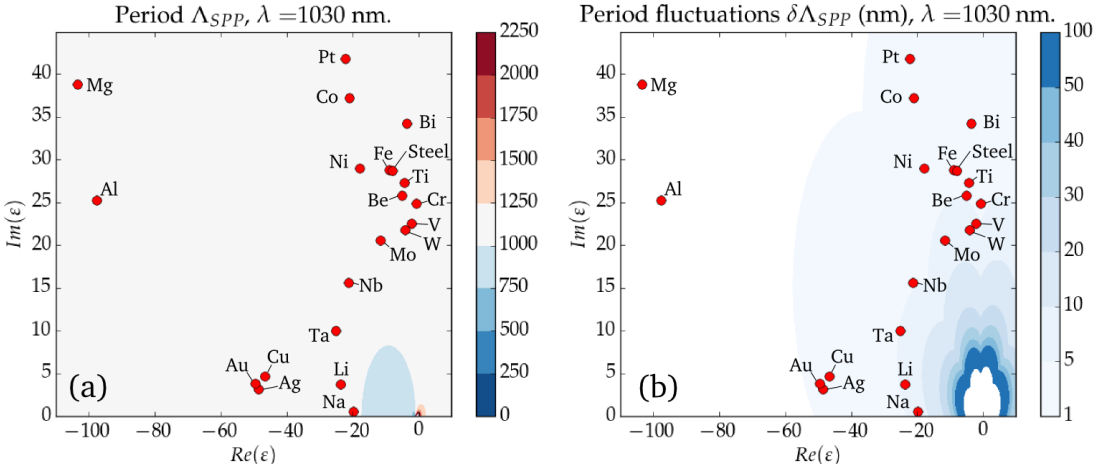

Figure 37. SPP period (a) and uncertainty over the SPP period δL_{SPP} (b) expressed in nm, as function of real and imaginary parts of the dielectric permittivity ε at the interface with air / vacuum. In these calculations, the fluctuations on the dielectric per

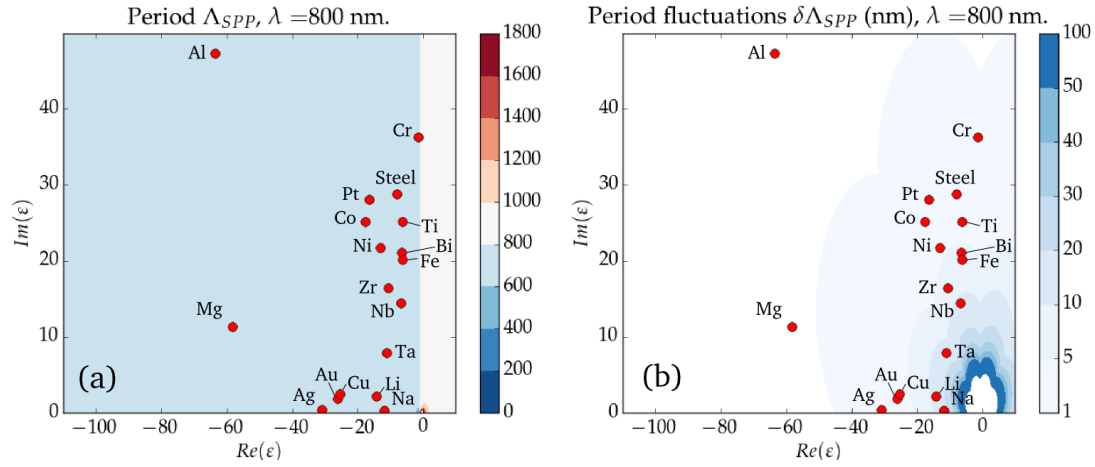

Figure 38. SPP period L_{SPP} (a) and sensitivity δL_{SPP} of the period (b) as function of real and imaginary parts of the dielectric permittivity ε at the interface with air. In this calculation, the fluctuations on the dielectric permittivity are taken equal to $\delta\varepsilon = 5$. The laser wavelength is λ = 800 nm.

For example, in the case of laser-irradiated semiconductors and dielectric materials, the transient excitation of electrons leads to a strong decrease of real part towards negative values and to an increase of the imaginary part by several units.

Note that this simplified model may overestimate the SPP period uncertainty δL_{SPP}. When using known values of dielectric permittivity (calculated using a more advanced physical

model), then e(t) is better known and leads to more precise results, as provided in the main article [102].

4.1.10 High areal-throughput nanostructuring.

Using a high repetition rate laser, large surface area A can be irradiated in a short time Δt at scanning velocities v = 1- 3 m/s, depending on the overlap between irradiation spots (see Tab. 1).

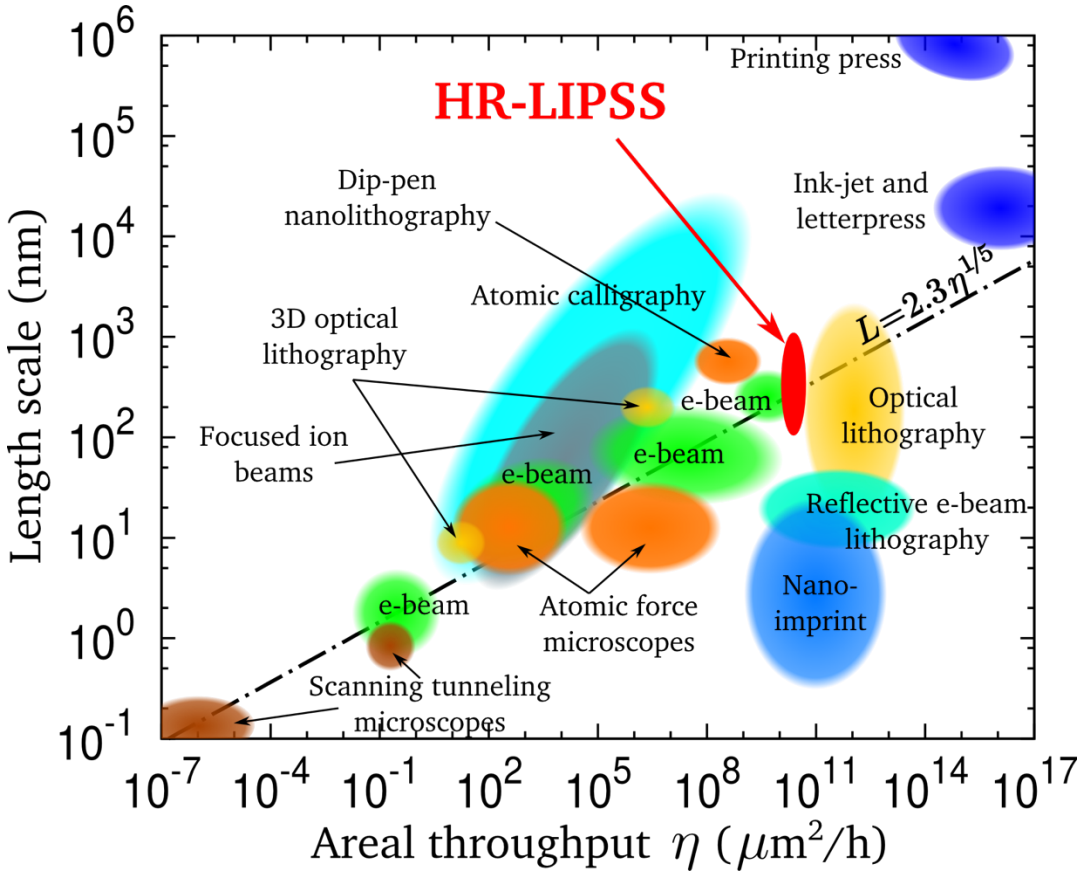

Figure 39. Summary of the nano-manufacturing techniques, adapted from [8] with some modification and addition of the data of our developed method of surface nanostructuring throughput. The black dot-dashed line stands for Tennant's law [8]. The red ellipse correponds to the process proposed in the present work. The length scale of the achievable LIPSS periods is determined by the variations of the laser angle of incidence on the surface.

This defines the areal-throughput $\eta = 3{,}6\times10^{15}A\ /\Delta t$ can be approximated by $\eta \sim 3{,}6\times10^{9}$ v$\cdot\delta\theta$, where $\delta\theta$ is a lane space. The values of 2.1×10^{10} mm^2/h for Mo and of 3.8×10^{10} mm^2/h for Ti and steel were achieved, which are only one order of magnitude below those achieved in traditional lithography techniques, while with the advantage of single step processing. This comparison is added to Fig. 39 adapted from Ref. [8] where the existing techniques of surface

nano-manufacturing and their respective areal-throughputs are summarized. Although a comparable throughput was previously reported [87], our structures exhibit higher regularity at higher throughput for several metals. In particular, the main new features introduced in our experiments are using a small laser spot size, reduced to 10.4 μm (FWHM), against 80 μm (FWHM) in Ref. [87] and considerably reduced overlapping between subsequent pulses and scanning lines as compared to other studies. It should be mentioned that further decreasing of the overlap between irradiation spots leads to a decrease of the regularity as the overlapping of the laser field with the pattern created by previous pulses replicates the latter to the new irradiated area as explained by Oktem et al [34]. Summary of the nano-manufacturing techniques, adapted from [8] with some modification and addition of the data of our developed method of surface nanostructuring throughput (Fig. 39). The black dot-dashed line stands for Tennant's law [8]. The red ellipse corresponds to the processing method developed in the present work. The length scale of the achievable LIPSS periods is determined by the variations of the laser angle of incidence on the surface.

4.1.11 Summary to the chapter

In this chapter, a very high regularity of near-wavelength periodic pattern was obtained in ablative regime on the surfaces of Mo, steel and Ti, and at a record speed of a few μm^2/h. A theoretical explanation of the regularity was proposed which supports the scaling offered by a collection of experiments performed in similar conditions for several metallic materials. The originality of this approach lies in the role of the small spot size which appears to be linked with the mean-free path of Surface Electromagnetic Waves, triggering the formation of highly regular structures which we find must be smaller or similar to the spot size and not fluctuate during the laser irradiation. Applying the proposed model allowed to explain the high LIPSS regularity on Ti, Mo steel, and the low regularity for Al, Cu and Au. Further predictions have been outlined on a wide range of materials, including semiconductors and noble metals for several laser wavelengths. It was found that using processing wavelengths close to UV should make accessible the formation of very high regularity sub-wavelength periodic structures of the surfaces of numerous materials. After carefully selecting the wavelength, the period of the structures can be modified (increased or decreased) by more than 50% via adjusting the angle of incidence and polarization, as well identified in previous studies [83][102]. The control of

laser-induced periodic structures at reduced number of pulses may now enable the new era of laser nanoprocessing on large area for the development of new applications.

Chapter 5 High-speed HR-LIPSS on metals: applications

5.1 Tribology

5.1.1 Background

This research was performed thanks to collaboration with prof. Carla Martini and Dr. Fabio Rotundo, Bologna University, Bologna, Italy.

Lubricants and coatings [116] are often used to reduce friction and wear, but lubricants have well-known drawbacks (such as their environmental impact) and coatings may significantly affect the design of the component and its final cost [117]. Among alternative surface modification technologies for the improvement of tribological behaviour, the generation of textured surfaces with laser-based technologies recently attracted a significant research interest. Surface texturing can be achieved by various techniques: in particular, the use of a laser beam deflected by a galvanometric scanner permits to generate sets of pits, grooves or ripples that are regularly or randomly distributed. As regards the application of laser texturing on steel surfaces, in [118] a UV laser was used to produce grooves with an aspect ratio of about 1, which were reported to improve wear-resistance of the material (M2 high-speed steel) and decrease the Coefficient of Friction (COF). An experimental investigation of the tribological properties of 17-4 PH stainless steel was conducted in [119] by generating dimples on the surface using a laser marking machine, where large dimples helped to reduce the COF. On the other hand, the authors pointed out an increase in the wear ratio, probably due to the reduction of the contact area. In [120], the results of unidirectional sliding tests in lubricated conditions showed that the COF decreased after surface texturing of 17-4 PH stainless steel by creating grooves with diameters between 30 to 110 μm. Generation of dimples with relatively large dimensions (15 to 800 μm) on engine parts using a nanosecond fiber laser was reported in [121]: tribological tests on carbon steel (normalized C85) and bearing steel (100Cr6), performed in conditions mimicking realistic engine working conditions, showed a COF decrease up to 80%. The use of a femtosecond laser to generate grooves 50 to 100 μm wide on the

surface of 100Cr6 steel was reported in [122], thus obtaining a reduction of COF in lubricated conditions.

In all these papers, the characteristic dimensions of the patterns on the surface are rather large. They are determined by the minimum laser spot size, always larger than the laser wavelength. However, theory suggests that the tribological properties could be further improved by decreasing the dimensions of these textures to the nanoscale, as pointed out in the recent theoretical study cited in [123].

In the present work, LIPSS with new methods of production is used to provide an effective and low-cost method for the fabrication of large-area nanotextured metal surfaces. Specifically, we report on generation of highly uniform nanostructures on AISI 316L austenitic stainless steel surface, in order to improve its tribological properties. The sliding behaviour of the induced nanostructures was assessed by dry (block-on-ring) and lubricated (ball-on-disk contact geometry) tests, using different counterbody materials. Moreover, we evaluated the effect of the orientation of nanostructures with respect to the sliding direction (parallel/perpendicular) on frictional properties.

5.1.2 Experiment

As material was used austenitic stainless steels are widely utilized in chemical, biomedical and nuclear applications. The samples were supplied as extruded bars in the as-homogenized condition followed by conventional solution treatment and presenting a hardness of 230 $HV_{0.1}$. Laser setup was a custom-built Yb-doped fiber laser system as shown in Fig. 40. The setup provides pulses of 270 fs at a central wavelength of 1037 nm with a spectral width of 15 nm (UFOLAB, Bilkent University, Ankara, Turkey). The pulse repetition rate was set to 200 kHz and at this frequency the setup has generated up to 8 μJ pulses, resulting in an average power of 1.6 W. The laser beam was then delivered to the surface thanks to a galvanometric scanner equipped with a 56 mm focal length f-theta lens. This permitted to generate a spot size measured to be around 6 μm.

Using this configuration, areas of 7 x 5 mm^2 on the material surface were treated in parallel (SS $\parallel$) and perpendicular (SS $\perp$) orientations of the ripples with respect to the scanning direction, and step between scanning lines was fixed to 3 μm. The schematics shown in Fig. 41a and 41b describe the mutual directions of the polarization plane E, the scanning direction of the beam v_S and the sliding direction v_R during tribological tests. Table 3 shows the laser parameters

used in the treatments of the samples SS || and SS ⊥, where θ_P is the angle between direction along the nanostructures and the sliding direction (v_R); E_p is the energy per pulse; τ_P is the pulse duration, f is the repetition rate; δ_S is the step; d is the spot diameter; and v_S is the scanning speed.

Table 3. The laser parameters used to generate LIPSS.

code	θ_P	E_p	τ_P	f	δ_S	d	v_S
-	$[°]$	$[nJ]$	$[fs]$	$[kHz]$	$[\mu m]$	$[\mu m]$	$[mm/s]$
SS‖	0°	200	270	200	3	6	100
SS⊥	90°	200	270	200	3	6	100

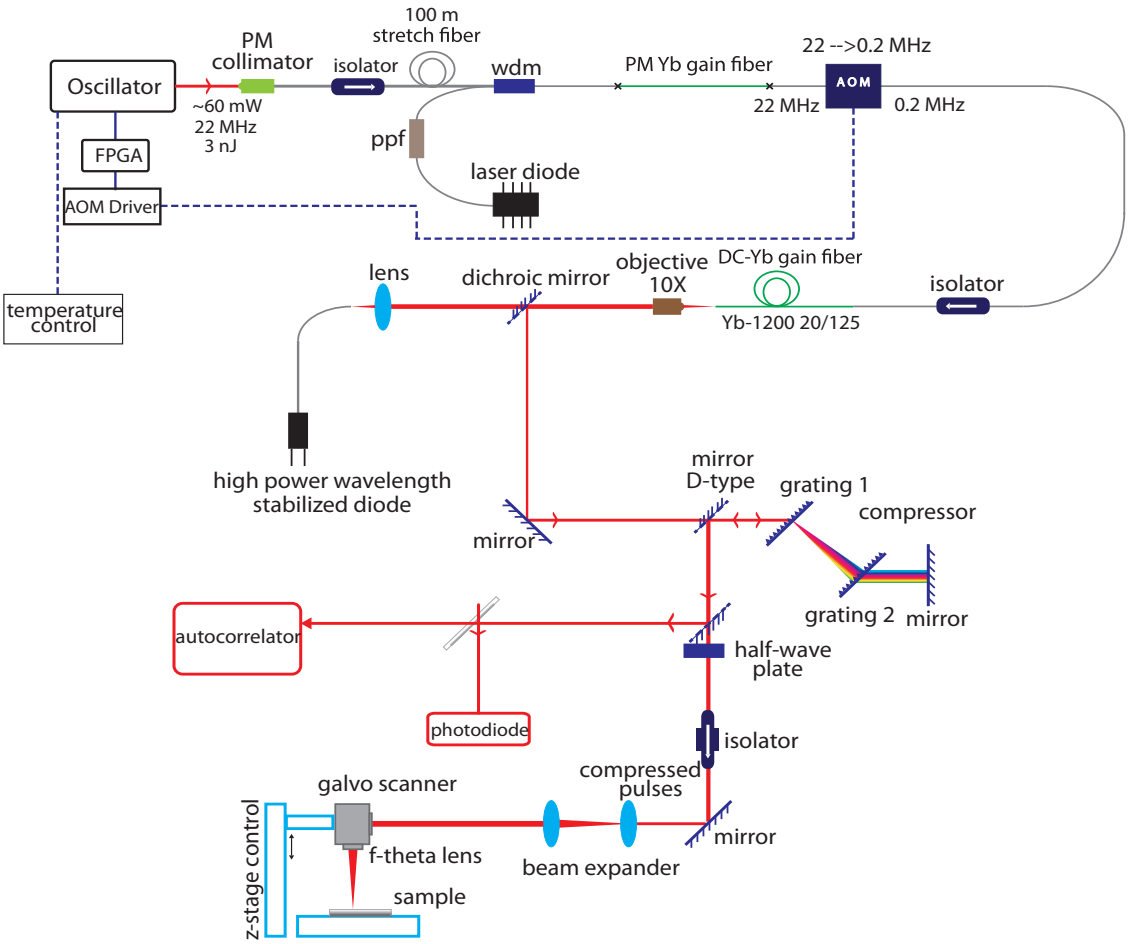

Figure 40. Schematics of treatment setup, the amplified Yb-doped fibre laser system is coupled to a computer-controlled optical galvoscanner scanner.

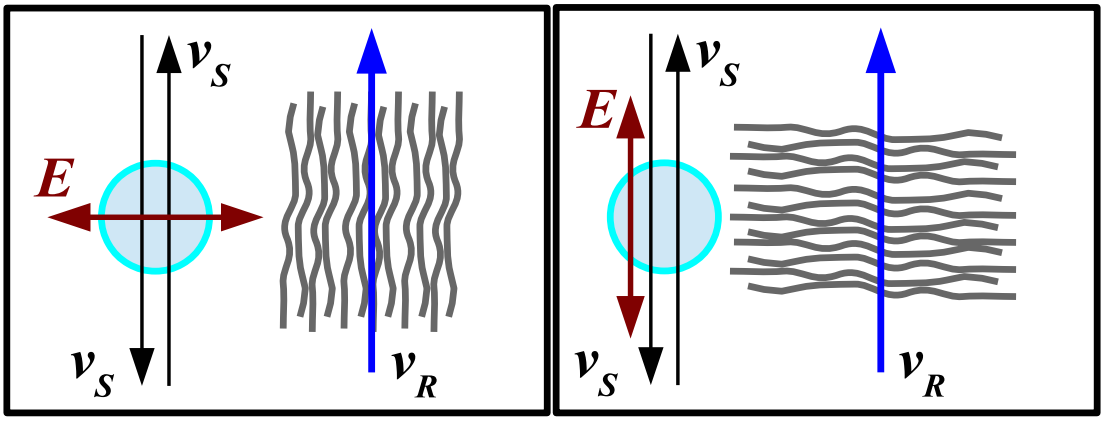

Figure 41. SS // and SS ⊥ configurations. Figures show the polarization plane E, the scanning direction of the beam vs and the sliding direction vR during the tribological test.

The tribological behaviour of the treated AISI316L surfaces was studied in sliding conditions, by means of two experimental configurations: (i) dry-sliding tests (unidirectional motion) in a block-on-ring configuration and (ii) lubricated tests (reciprocating motion) in a ball-on-disk configuration, so as to explore different contact conditions. In each configuration, two orientations of the nanopatterned surface were tested, in order to identify which one is more effective in limiting adhesion phenomena: nanostructures parallel to the sliding direction (SS //) or perpendicular to the sliding direction (SS ⊥). Dry sliding tests were carried out by a slider-on-cylinder tribometer, according to the schematic of Fig. 42a. on the sliders (prismatic blocks, 5x5x70 mm^3)

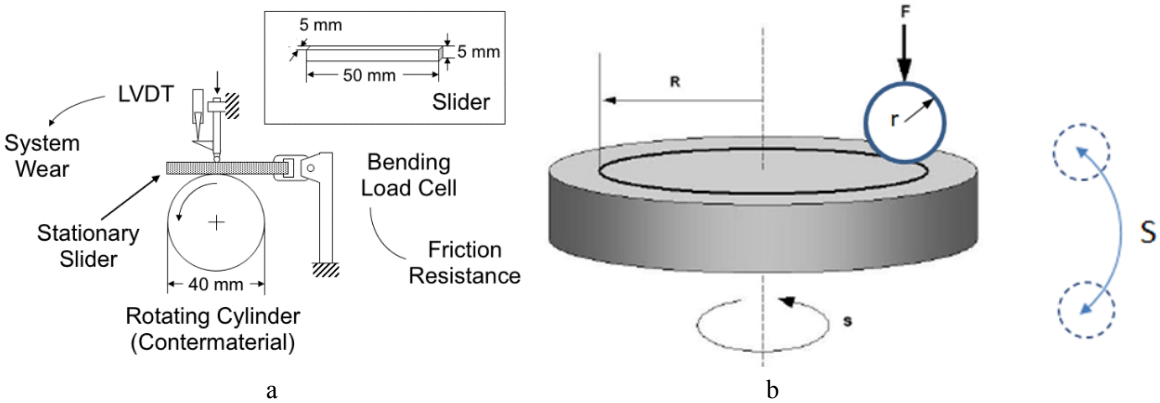

Figure 42. Schematics of the tribological testing setups used in the present work: (a) slider on cylinder (block-on-ring contact geometry) for dry sliding tests and (b) ball on disk (pin-on-disk contact geometry) in reciprocating mode, with indication of stroke l

The lubricated sliding test were performed with both disk and ball immersed in lubricating oil (Fig. 42b), under normal loads of 1 N, in reciprocating mode with a track radius (*R*) of 7.2 mm, a stroke distance (*S*) of 2 mm, a total of 1000 cycles (total sliding distance: 4000 mm), at

a frequency of 1 Hz. As in dry sliding tests, also in lubricated tests two surface configurations were tested: nanostructures parallel (SS ∥) and perpendicular to the sliding direction SS ⊥). Also, wear of counterparts was measured by profilometry.

5.1.3 Chemical and morphological analysis of results

The chemical composition of the untreated and treated stainless steel surfaces was evaluated via XPS analysis. The calculated atomic concentrations of the elements on the untreated and treated surfaces evaluated via XPS analysis are presented in Table 4.

Table 4. XPS chemical analysis (at. %) of untreated and SS ∥ -treated surfaces.

	Fe		Cr		Ni		Mo		O
Untreated	16.5		5.7		1.3		1.3		75.3
	13 Fe_2O_3	3.5 Fe^0	4.7 Cr_2O_3	1.0 Cr^0	Ni^0		0.7 MoO_3	0.6 Mo^0	
SS∥	10.0		3.1		2.0		1.6		79.3
	9.1 Fe_2O_3	0.9 Fe^0	Cr_2O_3		1.9 NiO	0.1 Ni^0	1.1 MoO_3	0.5 Mo^0	

Before the treatment, the detected metals are present on the stainless-steel surface both in their metallic and oxidized forms, except Ni which is present only in the metallic form. After the treatment, the surface was strongly oxidized: the amount of non-oxidized metals was less than 10%. Moreover, the quantitative ratios of the metals on the surface is changed after -treatment: the Fe:Cr:Ni:Mo ratios are 67:23:5:5 for un- treated and 48:34:10:8 for -treated stainless steel surfaces. After the treatment, the surface became less enriched in Fe, while other metals migrated to the surface most probably due to the oxidation process. In fact, Cr and Mo are known to increase the stability of the passive oxide film on stainless steels, while Ni is effective in promoting repassivation [124]. The analysis of O1s spectra demonstrates the increase of oxygen concentration after the -treatment, which correlates with the strong oxidation of the stainless steel surface as a consequence of the -treatment.

Figure 43 shows a representative EDX mapping image of the LIPSS-treated stainless steel surface, where the bottom part presents a zone which is not treated by the laser. As shown by the EDX map, in the untreated zone the elements are uniformly distributed, while in the -treated areas periodic Fe-/Cr-enriched stripes and O-enriched stripes are detected.

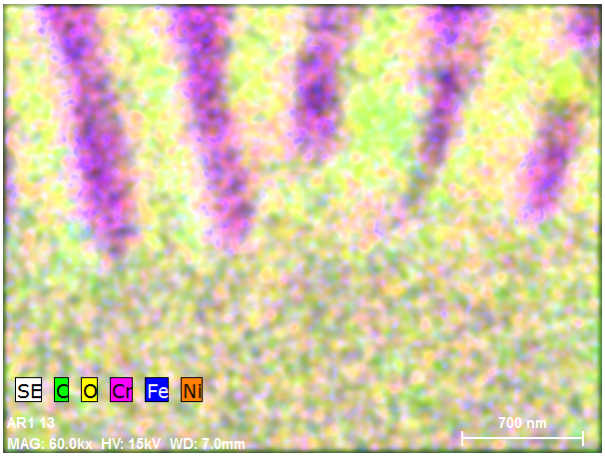

Figure 43. A representative EDS X-ray map of SS // -treated surface (stripes produced by the treatment are located in the upper half of the image, whilst the untreated steel is visible in the lower half).

The EDX map clearly shows that Fe and Cr are mostly located in the "valleys", whereas oxygen is mostly located on the “peaks” of the nanostructures. The period of the stripes is estimated to be around 500 nm.

The morphology of LIPSS-induced structures was investigated by SEM. The images in Fig. 44 reveal that periodic nanostructures were successfully obtained by irradiation with the linear-polarized femtosecond laser. Images clearly show quite uniform nanostructures that are homogeneously distributed and parallel to each other.

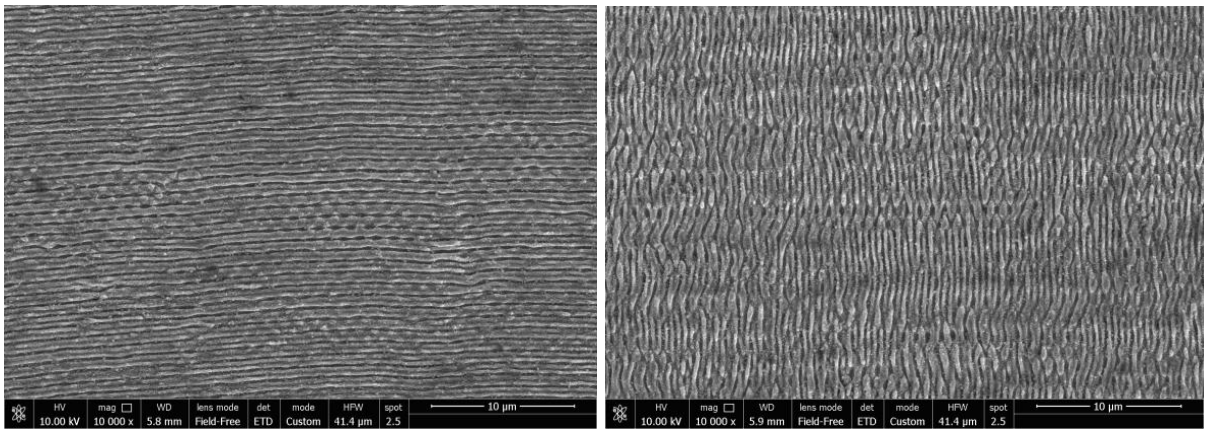

a b

Figure 44. SEM images of (a) -treated surfaces in SS⊥ conditions (perpendicular to the bar length as well as to the sliding direction) and (b) in SS // conditions (perpendicular to the bar length as well as to the sliding direction).

Fig. 44a displays nanostructures obtained in SS⊥ conditions, in which ripples orientation is perpendicular to the sliding direction. The nanostructures homogeneously cover the untreated zone with an average periodicity of 440±50 nm. SEM (Figs. 44b) shows nanostructures

obtained in SS // conditions: the nanostructures are generated parallel to the longitudinal axis of the steel bar, which corresponds to the sliding direction. The average periodicity is comparable to the one observed in SS ⊥ conditions, but also double stripes, periodically joining one another with periods of 750±40 nm, were observed.

The nanostructures analysed through SEM are not enough regular due to relatively small scanning speed. It causes that on one spot coming 10-12 pulses. Such mode leads to accumulation effect as well to distortion of regularity.

Cross-section SEM image (Fig. 45) outlines the profile of the obtained ripples. The height to width aspect ratio of the ripples is not lower than 1. This suggests that significant effects in changing wettability/tribological properties of the LIPSS-treated surface might be expected.

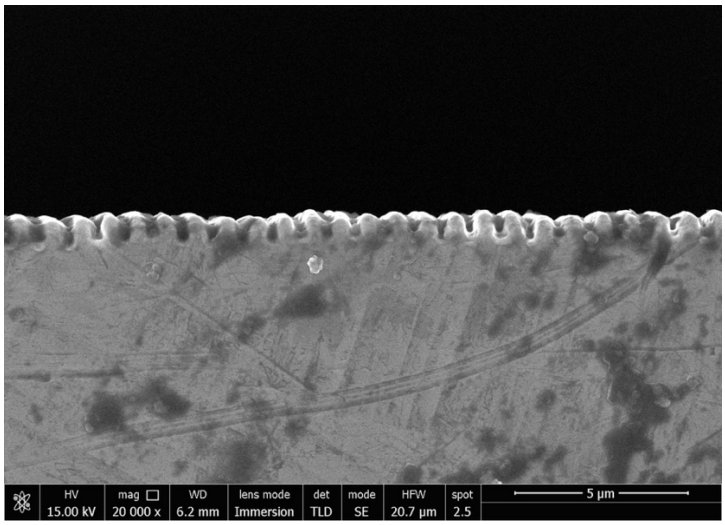

Figure 45. SEM image (cross section) of the LIPSS-treated surfaces in SS // conditions, displaying the high height/width aspect ratio of the nanostructures.

5.1.4 Analysis of dry and lubricated sliding tribological tests

Dry sliding test

The histograms in Fig. 46a show the average COF values, evaluated in the steady-state portion of the friction vs. distance plots (such as those in Fig. 46b). The results in Fig. 46a demonstrate that the average COF of LIPSS-treated surfaces is smaller than that of untreated surfaces, regardless the countermaterial.

As regards the influence of the countermaterial, in the self-mating AISI 316L vs. AISI 316L contact, the COFs are generally higher (for both untreated and LIPSS-treated steel, than

against EN100Cr6 (Fig. 46a), due to the higher adhesive contribution to friction [125]. As regards the influence of the LIPSS treatment orientation, against both countermaterials the LIPSS-treated steels with perpendicular orientation display the lowest COF values, as observed also by other authors [126]. The perpendicular alignment probably generates a lower contact area between the asperities of the mating surfaces, which in turn induces a lower adhesive component of friction. This hypothesis is also presented in [127], when discussing the influence of micro/nanogrooved surfaces on friction. A shorter stiction length contributes to decrease the friction coefficient, measured in the perpendicular orientation on samples with narrow grooves, if the ratio between the width of the grooves (b) and the radius of counterbody (R) is less than 10^{-3}, as in the case of the present work where b/R is about $2.5 \cdot 10^{-5}$.

A more detailed analysis of the evolution of friction as a function of sliding distance in the self-mating configuration (AISI 316L vs. AISI 316L) is shown in Fig. 46b. The comparison of dynamic friction curves shows that, while the untreated steel displays high COF and undergoes wide oscillations (typical of stick-slip motion in sliding systems at low speed and high adhesion [128]), the LIPSS-treated steel displays low COF, especially when the orientation of the texture is perpendicular to the sliding direction. Specifically, the perpendicular orientation generates the lowest values of dynamic friction in Fig. 46b, with negligible oscillations during sliding,

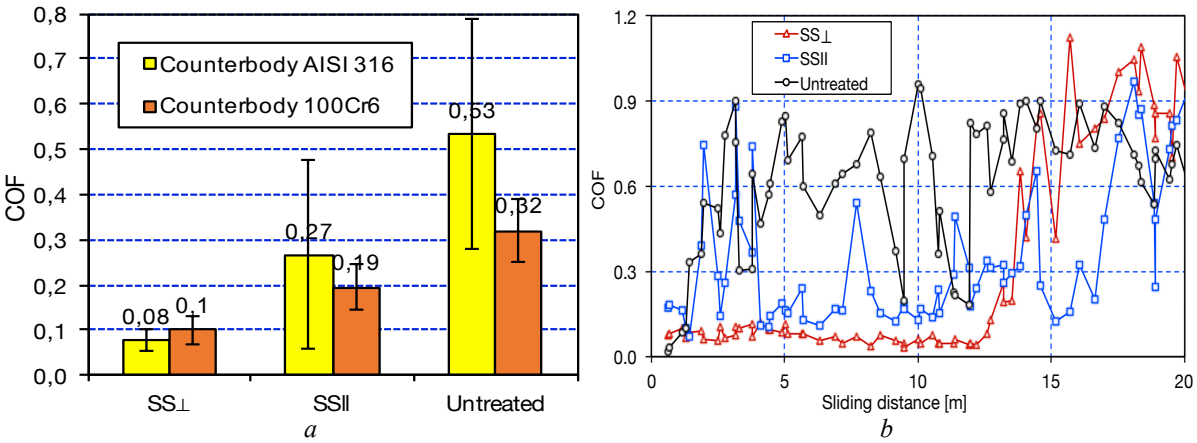

Figure 46. Dry sliding tests: (a) Coefficient of friction (COF, averaged over the first 10 m of sliding) of AISI 316L, untreated or treated with different orientations of the LIPSS-treated surfaces (SS ⊥: perpendicular; SS // : parallel) vs. different countermaterials: AISI 316L and EN 100Cr6;(b) coefficient of friction as a function of sliding distance for untreated or -textured AISI 316L steel, sliding against AISI 316L. Two different orientations of the textured surface (SS ⊥: perpendicular; SS // : parallel to the sliding direction) are compared.

up to a distance of 12 m. Then, the COF increases with increasing sliding distance and starts to display remarkable oscillations, similar to those showed by the untreated steel as well as by the

treated steel with parallel orientation (even though to a lower extent). This transition to high friction is due to the onset of wear damage of the LIPSS-treated surface, as demonstrated by morphological observation of the worn surfaces.

The morphology of wear scars, observed by SEM at the end of dry sliding tests is shown in Fig. 47. When sliding in the self-mating configuration (AISI 316L vs. AISI 316L), the untreated steel surface (Figs. 47a and d) clearly undergoes heavy plastic deformation and shows no evidence of the typical protective oxide layer, which usually forms under low loads such as 5 N, but with higher sliding distances than those used here [129]. On the contrary, the LIPSS-treated surfaces are, already after these short tests, partly covered with fine oxidized wear debris (powdery material is visible at low magnification in Fig. 47b, 47c and dark grey oxidized areas are visible in high-magnification images of Figs. 47e, 47f).

Even though the oxide debris coverage is never continuous, oxides were observed to a higher extent on the surface with perpendicular orientation (Fig. 47f), where the entrapment of debris, "wave after wave" along the sliding direction, might be favoured. With a parallel orientation, instead, oxides may be more easily removed from the bottom of the grooves aligned with the sliding direction.

When sliding against 100Cr6, the untreated steel surface (Fig. 47g and l) underwent plastic deformation, even though to a lesser extent than in the self-mating configuration. This is due to a lower incidence of adhesion phenomena (as shown by the comparison of Fig. 47a and g). Moreover, the worn surfaces are covered with a protective iron-oxide transfer layer, which was thicker and more continuous than when sliding against AISI 316L.

As already observed for the previous tribological coupling, the surface of the LIPSS-treated steel (Fig. 47m and n) is less damaged than untreated steel (Fig. 47l). The nanotextured surface with perpendicular orientation (Fig. 47i and n) seems to be able to stabilize a more continuous iron oxide layer than the parallel one (Fig. 47h and m). In general, the presence of iron oxides on the worn surface, which is typical of dry sliding contacts involving AISI 316L stainless steel under low loads and speeds [130][131][132][133][134], can play a significant role in decreasing friction.

The ability of laser-textured surfaces to trap wear debris, which is the main mechanism for the improvement of tribological behavior in dry conditions [135] may further enhance the

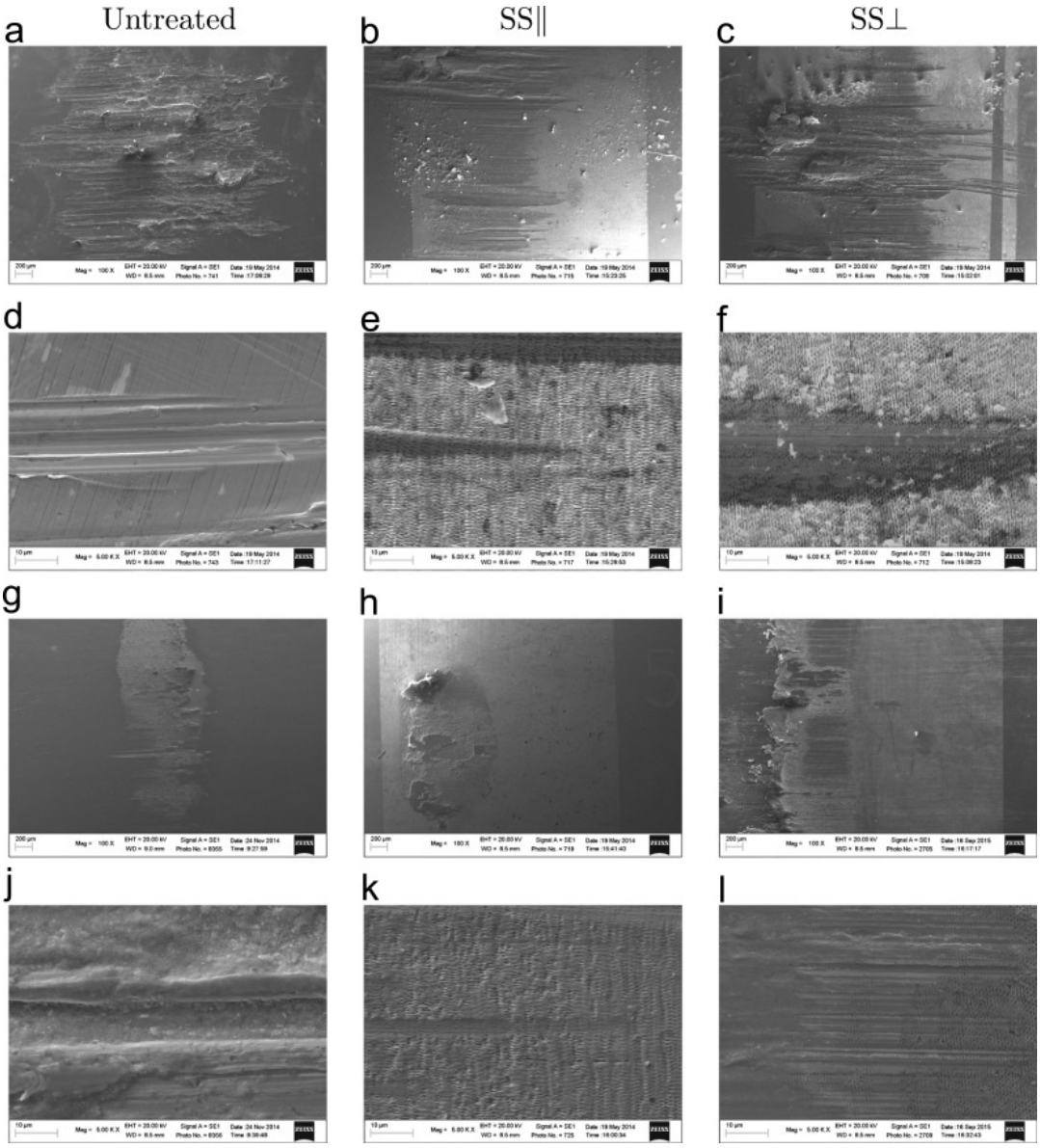

Figure 47. Dry sliding tests: morphology of worn surfaces on untreated or LIPSS-treated AISI 316L with different orientations of the textured surface (SS ⊥: perpendicular; SS // : parallel to the sliding direction) after 100 m sliding against the two countermaterials (AISI 316L (a-f), 100Cr6 (g-n). General views (a-c, g-i) and high-magnification details (d-f, l-n).

beneficial role of iron oxides in decreasing friction. The wear debris are more efficiently retained on the textured surface with perpendicular orientation due to geometrical factors, thus producing the lowest COF values when dry sliding against both countermaterials.

Lubricated sliding test

As already observed in dry sliding tests, the average COF values measured in lubricated conditions (Fig. 48a) indicate that LIPSS-treatment is able to decrease the COF of the AISI 316L austenitic stainless steel.

Fig. 48b shows an example of the dynamic evolution of COF as a function of sliding distance during lubricated sliding tests for the untreated steel and for the SS⊥ configuration. As already observed in dry sliding conditions, for the untreated steel the average values of COF are higher, the oscillations are wider and the general trend is less homogeneous than in the case of the LIPSS-treated steel.

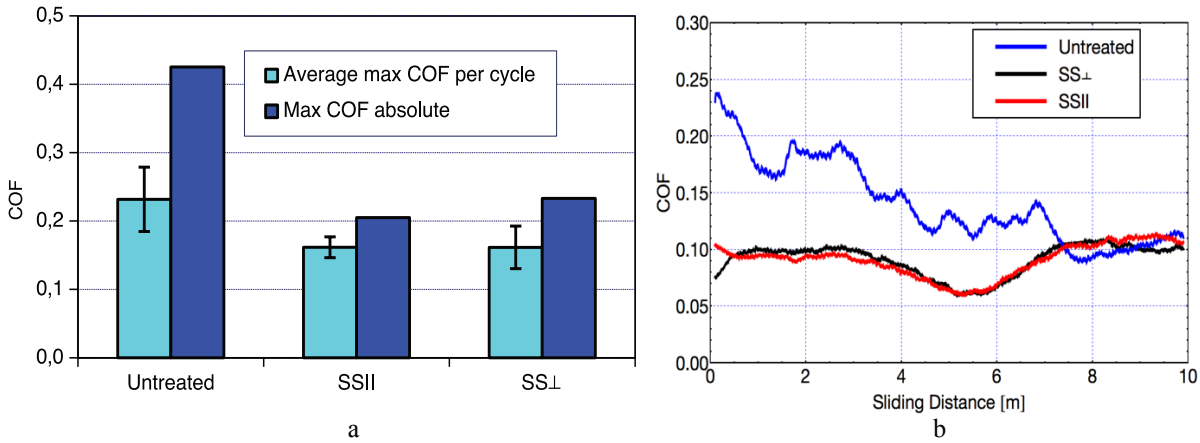

Figure 48. Lubricated sliding tests: (a) COF maximum values and average of the maximum COF for each cycle of AISI 316L, untreated or treated with different orientations (SS ⊥: perpendicular; SS ∥ : parallel); (b) dynamic COF values as a function of sliding distance

In lubricated conditions, however, the effect of the nanostructure orientation (perpendicular or parallel to the sliding direction) seems to be less prominent than in dry sliding conditions: both the parallel and the perpendicular orientation is effective in decreasing COF, with no remarkable difference between the two.

This is probably due to the ability of both the orientations to increase lubricant retention on the steel surface, thus limiting the two main components of friction: (i) adhesion due to steel-to-steel contact and (ii) abrasion of the soft AISI 316L surface by the hard 100Cr6 sphere. In addition to an increased lubricant retention effect, which is listed among the main mechanisms for the beneficial influence of laser texturing in lubricated sliding[135], also other non-directional effects might have a beneficial influence on friction. In particular, in lubricated sliding, also other authors [136] observed that the textured surfaces (regardless the shape and orientation of texture) proved to be beneficial and showed rather similar friction behaviours.

They attributed the generalized beneficial role of texture to the ability of grooves and depressions of (i) getting the interface rid of loose abrasive particles and (ii) acting as ‘‘interruptions’’ of surface deformation, thus generally limiting possibilities for local contact area growth.

In the case of lubricated reciprocating sliding, the wear scars (Fig. 49) were much more homogeneous than in the case of dry sliding (as demonstrated by the comparison between Figs. 47 and 48). Also, the iron oxide transfer layers which were discussed previously for dry sliding tests and which stabilize on the LIPSS-treated surface to an extent depending on the orientation, were not observed. In lubricated sliding, the lubricant is likely to maintain a lower contact temperature than in dry sliding, thereby limiting oxidation phenomena[137]. Due to the homogeneity of wear scars obtained in lubricated conditions, it was possible to measure representative depth profiles, as those compared in Fig. 49, which shows that detectable values of wear depth were obtained only in the case of untreated steel (depth ≈ 100 μm). The LIPSS-treated steel surfaces only show a few, shallow grooves and scratches (as shown also by the SEM images in in Fig. 49b, d).

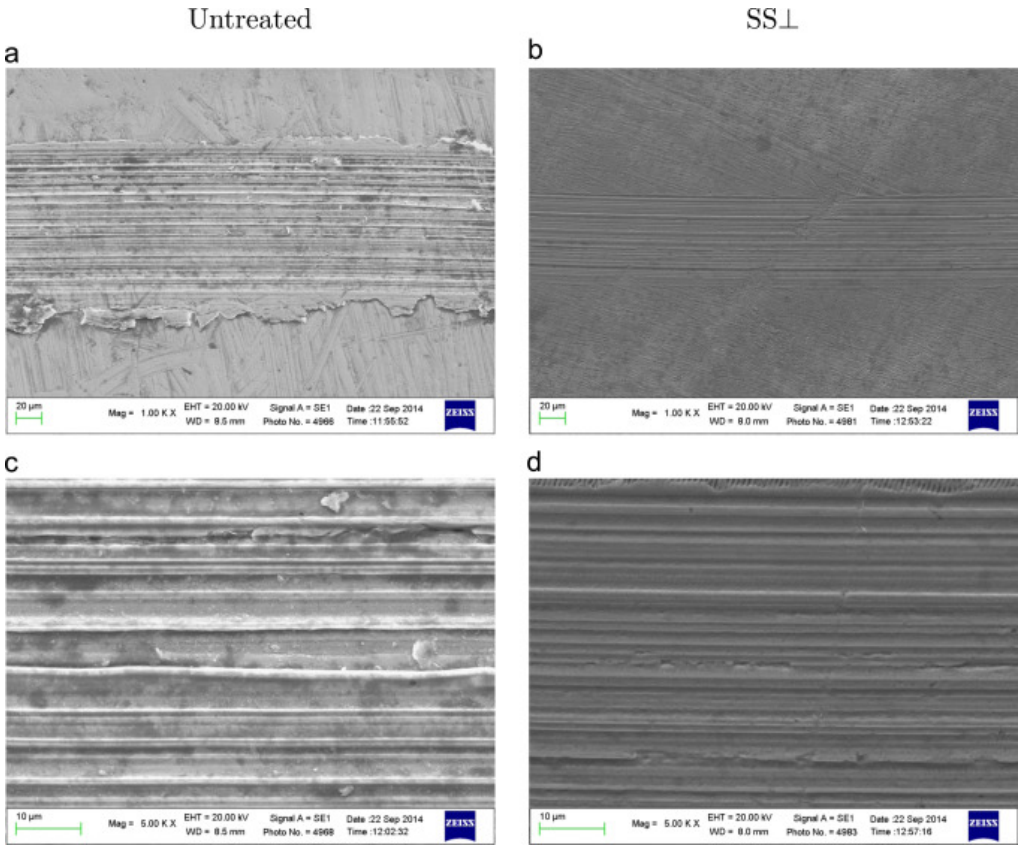

Figure 49. Lubricated sliding tests: SEM images of the worn surfaces on untreated (a and c) or LIPSS-treated AISI 316L with perpendicular orientation (SS ⊥, b and d) [131].

The untreated steel also shows the typical plastic deformation at the side of the wear scar (due to ploughing), which is absent from the LIPSS-treated surfaces. Therefore, also in this case, the improved friction and wear behaviour of LIPSS-treated surfaces might be attributed to restricted possibilities for plastic deformation and hence for local contact area growth.

5.1.5 Summary

Sub-wavelength nano-ripples with a good uniformity and on large areas were generated with different orientations to the sliding direction (perpendicular or parallel) on AISI 316L. Both dry (block-on-ring) and lubricated (ball-on-disk contact geometry) sliding tests were carried out, using different counterbody materials. The following conclusions can be drawn from this work:

- The LIPSS treatment produces a significant reduction of the coefficient of friction both in dry and lubricated conditions.
- In dry sliding conditions, the friction reduction depends on the orientation of the nanogrooves with respect to the sliding direction: the best results were obtained by the perpendicular orientation.
- In dry conditions, the beneficial influence of LIPSS on friction was attributed to the ability of the nanogrooves (i) to lower the contact area between the asperities of the mating surfaces, hence to reduce adhesion and (ii) to entrap the iron oxide wear debris. The first effect dominates in the AISI 316L-AISI 316L self-mating contact, whereas the second one is the main effect in the case of sliding against 100Cr6.
- In lubricated conditions, the decrease of friction induced by LIPSS is not significantly affected by the relative orientation between nanotextures and sliding. The beneficial influence of LIPSS on friction was attributed to the increased lubricant retention as well as to ability of the nanogrooves to limit plastic deformation and hence local contact area growth.

5.2 Dental implants

5.2.1 Background

This work was carried out with prof. Maxim Pogorelov`s medical research group, Sumy State University, Sumy, Ukraine.

Excellent mechanical properties, chemical resistance and biocompatibility allow the wide use of Ti and Zr making those metals suitable for applications in orthopedics and dental surgery. However, around 7 % of dental implants are lost during the 10 years after surgery. Implant loss may occur due to surgical trauma, infection during either the implant placement or the healing process, and instability of the implant due to premature loading [138][139]. About 50 % of implant failure are defined as late losses, which occur due to loss of bone support [140][141]. The key point of implant failure is the imbalance between implant and surrounding tissues during the osteointegration processes. Osteointegration is the direct anchorage of an implant by the formation of bony tissues around the implant without the growth of fibrous tissues at the bone/implant interface [142]. This process starts directly after implantation from blood protein and growth factors adsorption on implant surface with further cell attachment and proliferation [143]. Bone progenitor cells like mesenchymal stem cells (MSCs) and lining osteoblast produce collagen with further mineralization and bone remodeling. In this paradigm, surface topography and wettability are key parameters in determining implant/tissue interaction and osteointegration [144][145].

The implant surface should be modified to improve its biological response and to promote faster osteointegration with greater efficiency. Namely, the roughness of the implants should enhance the attachment, proliferation, and differentiation of progenitor bone cells while the implant is in contact with the surrounding tissues to accelerate bone attachment [146]. It is also important to integrate the soft tissues (mucous membrane) with the surface of the abutment.

Various treatments have been developed to modify the implants surface, include machining/micromachining, sand-blasting, acid etching, electropolishing, anodic oxidation, and plasma spraying [147][148]. But it is still not clear which is the optimal topography for a better osteointegration. It was shown that the cells need cavities or grooves on the implant surface equivalent to or larger than their own size which is of about 30 μm [149]. In the case of a Ti surface that was roughened by sand-blasting with large grit followed by acid etching shallow

spaces 20-30 μm in diameter were obtained. Cells cultured on this surface occupied preferentially those cavities. Wennerberg *et al*. [150]found on histology examination that optimal implant surface shown wavy structures with an average wavelength of 11.6 μm and with deviations in height by 1.4 μ. From rabbit intramedullary implantation studies, it was found that lamellar bone and bone remodeling are highly favored on 200 μm pores rather than on the 10–25 μm pores created by laser [151]. Hulbert *et al*. also observed a similar relation between osteons and growth on porous surface. Studies carried out on ceramic implants revealed that osteons require mini pores whose diameters range from 150 to 200 μm [152]. Also, Li *et al*. showed that bone growth on 140 μm pore size yielded the best results among all [153]. However, it was proved that scaffolds with nanoscale roughness have large surface areas to adsorb proteins, which present more binding sites to cell membrane receptors [154]. Lai *et al*. indicated that the nanostructured Ti coating enhances protein polymerization, osteoblast adhesion, or osteointegration [155][156], whereas surfaces with rough textures increase the substrate/tissue interlocking and promote osteoblast differentiation. The mechanisms of cell detection and response to the implant surface nanofeatures are still unclear. For instance, Liwen Lin proposed that proteins may "sense" the surface topography at the nanoscale; therefore, materials may be "rough or hostile" to cells with microscale surfaces but "smooth and friendly" with nanoscale surfaces [157]. Therefore, the contribution of nanostructures to osteointegration still needs further study and characterization in order to figure out the optimal method of dental and orthopedic implant surface treatment.

The objective of the research described below is to evaluate the biological response of *in_vivo* and *in_vitro* cell models attached to the surfaces of Zr and Ti alloy samples nanostructured by femtosecond laser pulses.

Materials

Commercial grade-1 of titanium alloy (Ti6Al4V) and zirconium (Zr, 99.7% purity) were purchased from Kurdumov Institute, NASU. Rods of 10 mm diameter were cut in cylindrical slabs of 2 mm thickness. Subsequently, the slab surfaces were mechanically polished, resulting in surface roughness as shown in Table 6.

Laser treatment

The HR-LIPSS were imprinted on polished Ti6Al4V and Zr samples using a commercial femtosecond laser system "Pharos", which in details depicted in Section 4.1.2. and the parameter set is presented in Table 5.

Table 5. The laser parameters

Material	Average Power	Speed	Step	Pulse duration	Repetition rate	Fluence
Ti6Al4V	400	3000	4	213	600	1.2
Zr	400	3000	4	213	600	1.1

Those laser parameters were favourable for nanostructuring an area of 0.5 cm^2, which was performed by scanning a metal surface with a linear speed of 3 m/s and equivalent production rate of about 900 mm^2/min.

Cell culturing

Samples with modified and non-modified surfaces (7 in each group) with 10 mm in diameter were sterilized in 70 % ethanol for 3 h at room temperature, washed in PBS twice and placed in 24-well plates. Dulbecco's Modified Eagle Medium (DMEM; Invitrogen, cat. no. 11960) supplemented with 10 % Fetal Bovine Serum (FBS; Invitrogen,), 2 mM L-glutamine (Invitrogen, cat. no. 25030), 0.1 mM 2-mercaptoethanol (Sigma, cat. no. M7522), 50 units/mL penicillin and 50 g/mL streptomycin (Invitrogen, cat. no. 15070) were added to each well, and incubated at 37 ºC in a humidified environment with 5 % CO_2. After 24 h, Human Dermal Fibroblasts-Adult (HDFa) were seeded at 10^4 cells per sample in 2 mL of DMEM. Samples with cells were then incubated at 370 ºC with 5 % CO_2, and media was changed every 2 days during a 10-day culture period.

Cell viability

Alamar Blue (AB) assay was used to assess cell viability on day 3, 7 and 10 after seeding. Media were removed from each well and washed with PBS. 1 mL of AB solution was added to each scaffold and incubated for 2 h. Two aliquots of 200 µL of AB solution were collected

from each scaffold and read at a wavelength of 570 nm in a colorimetric plate reader to obtain baseline values of colorimetric absorbance.

Animal model

All animal procedures approved by the Commission on Biomedical Ethics of Sumy State University (#14/06 on 14/06/2015). 30 male laboratory rats, aged 8-9 months, were involved in the experiment. Animals were housed at 22±2 ºC on a 12 h light/dark cycle and received food and water ad libitum. Keeping of the animals and experiments were carried in accordance with the Directive 2010/63/EU of the European Parliament and of the Council of 22 September 2010 on the Protection of Animals Used for Scientific Purposes.

The animals were divided into three groups according to the type of implant:

1. Group 1 (Control) –Ti alloy and Zr with smooth polished surface;
2. Group 2 – Ti alloy with modified surface;
3. Group 3 - Zr with modified surface:

The procedure of implantation included: after general anesthesia (ketamine, 10 mg per kg of animal weight) and peripheral vein catheterization, the back of animals was shaved in the interscapular region. The surgical site was treated with C-4 solution and then a longitudinal incision was made. Subcutaneous tissues were separated from the skin above the left scapula and the graft was placed under the skin 1.0 cm from the incision. Before implantation all grafts were sterilize in 70 % ethanol during 30 min. Finally, the wound was closed with simple interrupted sutures and aseptic dressing was applied.

After the operation, all the animals kept in individual boxes to prevent additional trauma of the operation site. Animals taken from experiment with an overdose of narcotic (ketamine, 70 mg per 1 kg of animal weight) in 10 days after the implantation.\

Surface characterization of samples with cells

Samples were removed with care to prevent damage of the tissues that covered implants. In the case of capsule formation (2 control samples), they were cut and implants were removed. All the samples were put in 5 % formaldehyde for 1 h, dehydrated in solutions of ethanol and dried in a vacuum set-up. To avoid surface charge accumulation in the soft tissue, surfaces all the samples were covered with a thin (30–50 nm) layer of silver in the vacuum setup VUP-5M

(SELMI). Scanning electron microscopy was performed using the electron microscope REMMA102 (SELMI).

To analyze experimental results the following aspects were taken into account:

1. The presence of cells and fibers on the surface of the sample and their distribution;
2. Cells density per 1 mm^2;
3. Fibers size.

5.2.2 Morphological and chemical analysis

The morphology of LIPSS-induced structures was investigated by SEM. The images (Fig. 50) reveal that nanostructures were successfully obtained on all the treated areas and they appear homogeneously distributed and regular. No bifurcations are present on both pure Zr and Ti alloy. The direction of the nanoripples is perpendicular to the laser polarization. The periods of nanostructures are 800 ± 50 nm for Zr and 820 ± 50 nm for Ti alloy. The roughness of the samples obtained from AFM profiles are given in Table 6.

Table 6. Roughness parameters.

Roughness parameters, µm	Polished Ti6Al4V	Polished Zr	Treated by LIPSS Ti6Al4V	Treated by LIPSS Zr
Ra	0.006	0.007	0.131	0.148
Rz	0.013	0.017	0.316	0.386

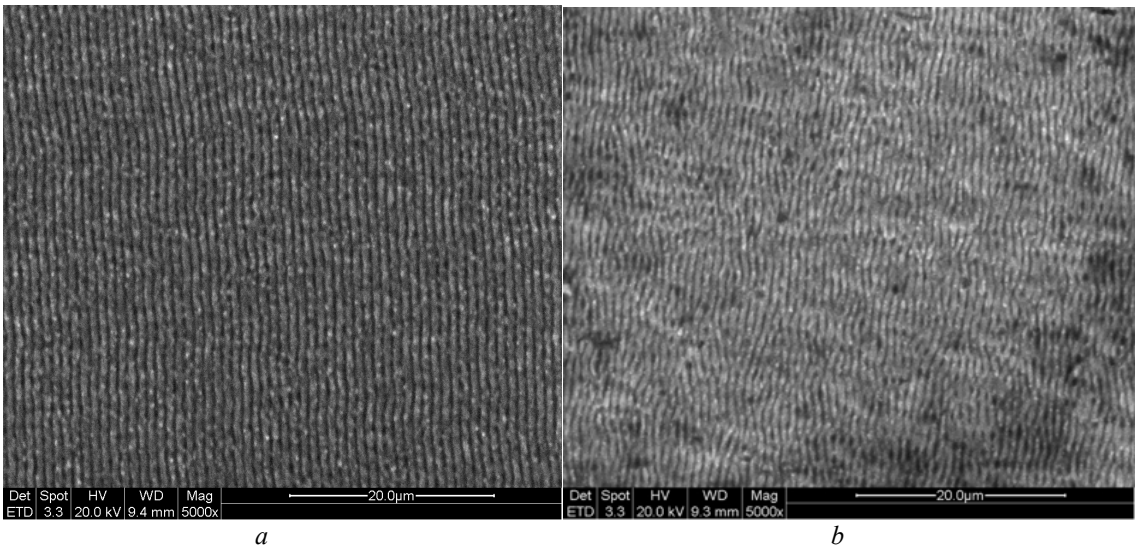

a *b*

Figure 50. Modified surfaces of Ti-6Al-4V (a) and Zr (b) by laser-induced periodic surface structures (LIPSS).

The chemical composition of the treated and untreated surfaces of both Ti alloy and pure Zr were studied by XPS. Figure 51 shows the XPS regions of interest.

The surfaces are composed mainly by metal oxides and hydroxides, in particular TiO_2 and a small amount of Al^{3+} (Al_2O_3 and $Al(OH)_3$) in the Ti alloy and ZrO_2 in the Zr sample. Vanadium is on the tail of O 1s region (Fig. 51c) and is barely detected: a not quantified peak, around ~517 eV, is assigned to V_2O_5 V $2p_{3/2}$ component. $2p_{3/2}$ peaks centred at 453.8 and 455.5 eV are assigned to Ti^0 and titanium suboxides at the interface metal/oxide, respectively; after treatment, Ti^0 is no longer detected and the relative amount of Ti suboxides decreases. Al 2p (Fig. 51b) is composed by 2 doublets, with the Al $2p_{3/2}$ peaks centred at 74.1 ± 0.2 eV and 76.2 ± 0.4 eV attributed, respectively, to Al_2O_3 and $Al(OH)_3$ or oxyhydroxides. C 1s (Fig. 51d) reveals that some carbonaceous species are also In the Ti alloy, the main doublet in Ti reveals (Fig. 51a) is assigned to TiO_2, with Ti present at the surface, in particular aliphatic carbon, carbon singly bound to oxygen and $2p_{3/2}$ centred at 458.6 ± 0.1 eV; in the untreated surface, at lower binding energies (BE), carboxylate groups, assigned to peaks in C 1s region centred at 285, 286.6 ± 0.1 and 288.8 ± 0.1 eV, respectively. In Fig. 51e, O 1s shows oxygen from metal oxides and hydroxides, centred respectively at 530.1 ± 0.1 and 531.8 ± 0.1 eV, and organic oxygen, as attested by the peak centred at 533.3 ± 0.2 eV attributed to oxygen singly bound to carbon and also by the peak assigned to the hydroxides which can also include oxygen doubly bound to carbon.

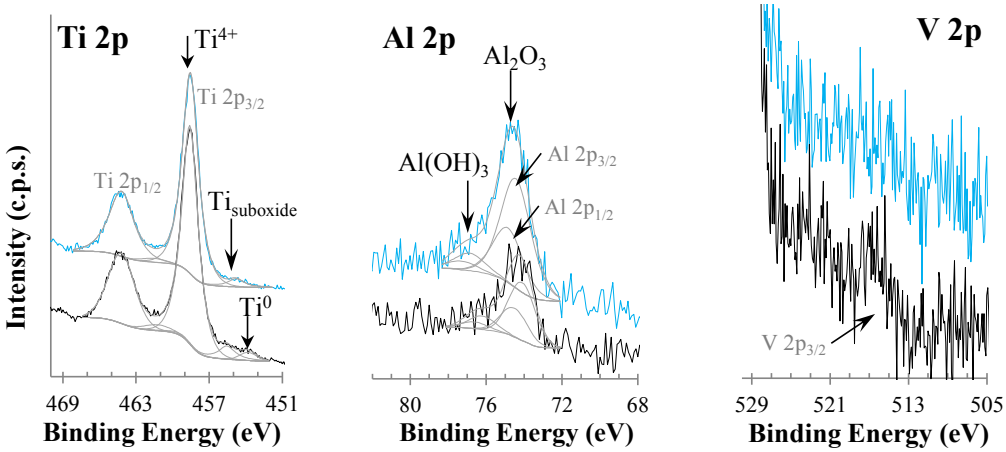

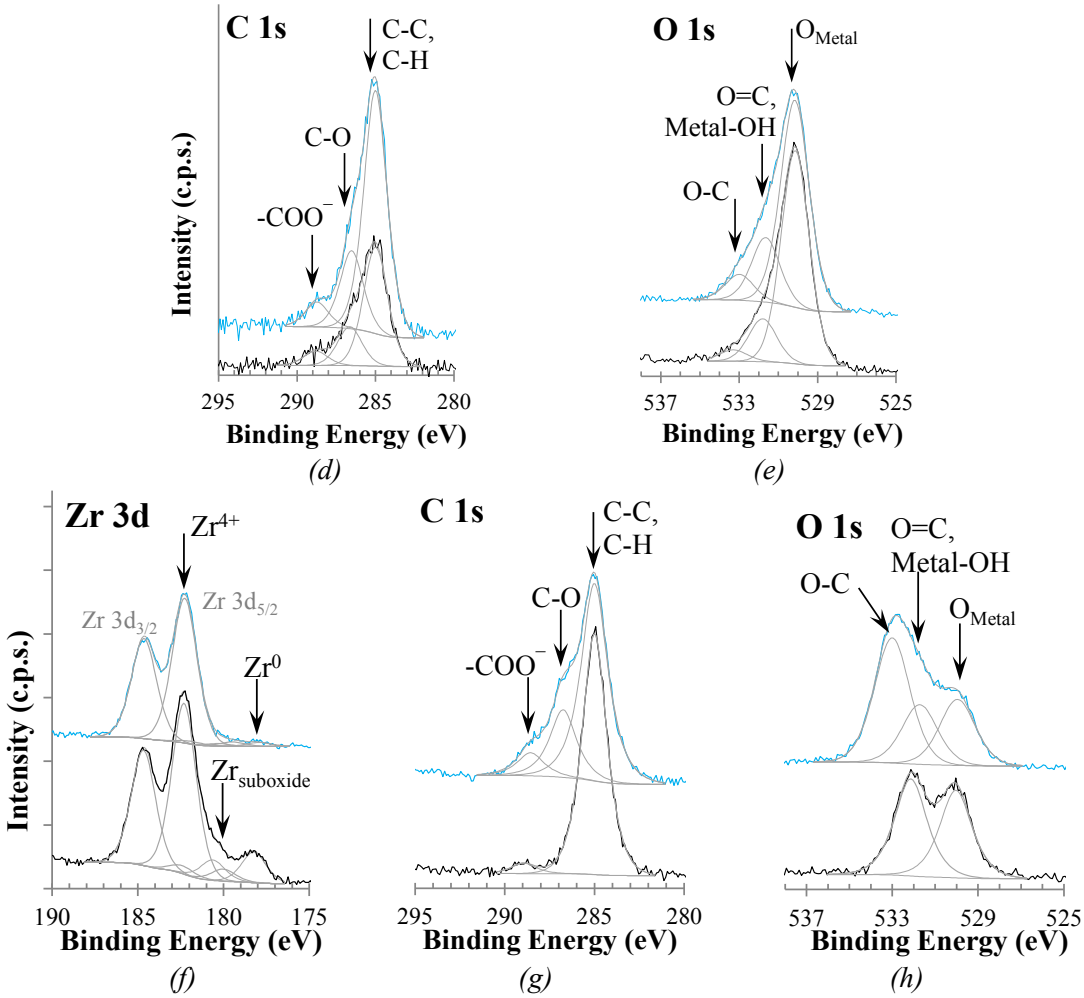

Figure 51. XPS regions of: Ti-6Al-4V (a- e); and pure Zr (f-h). Top (blue spectrum): treated surface by laser; bottom (black spectrum): untreated surface.

In pure zirconium, Zr 3d region of the untreated sample was fitted with 3 doublets (Fig. 51f, with the Zr $3d_{5/2}$ centred at 178.2 ± 0.2, 180.0 ± 0.3 and 182.3 ± 0.1 eV attributed, respectively, to Zr^0, that is hardly detected after treatment, to zirconium sub-oxides, most probably coming from the interface metal/surface oxides, which also decrease after treatment, and to ZrO_2 (the most abundant). Like in Ti-6Al-4V, the same types of carbonaceous species are species are detected at the surface of pure Zr (Fig. 51g, h).

5.2.3 Cell culture and animal model

Cell culture

There was no significant difference between cells viability on Ti alloy and Zr. HDFa proliferated on control samples and fluorescence was significantly higher on day 7 and day 10 compared to the initial time point (day 3). Day 7 was characterized by an expansive fluorescence growth on all treated samples with further significant cell proliferation on Day 10 (Fig. 52).

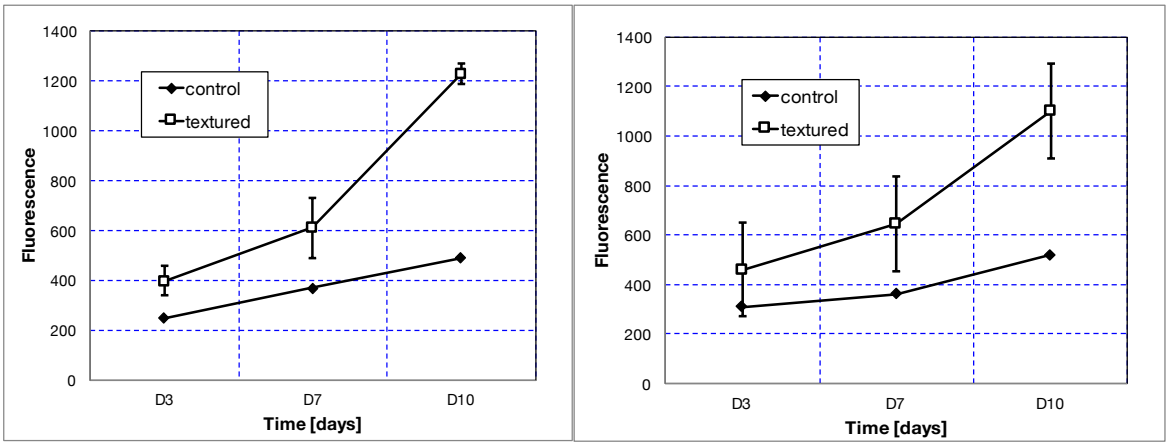

Figure 52. Cell viability of HDFa cells on Ti (a) and Zr (b) surface with different surface modification. Mean± S.D of the fluorescence of the media after the resazurin reduction assay, which is an indicator of metabolic activity. N=7.

Animal model

None of the control implants (with smooth surfaces) were covered with cells or fibers. We observed single random fibers, but probably they attached to samples during the samples removing procedure and have no bindings with the metal surface. Comparing to the control, all the modified samples were completely covered with connective fibers and cells. Three types of cells were identified in current experiments – erythrocytes, fibroblasts and leucocytes. Cells were on the fibers, that probably adsorbed to the metal surface in a first step after implantation. There is no difference in cell number and type between the Ti alloy and Zr (Fig. 53).

The number of erythrocytes and leucocytes are the same in both types of metal. The density of erythrocytes is 11.5 ± 2.9 per mm^2 and 13.3 ± 4.3 per mm^2 for the Ti alloy and for the Zr

implants, respectively; the density of leucocytes is 3.6 ± 1.2 and 2.1 ± 0.5 per mm^2 for the same set of implants. However, the density of fibroblasts ranges from 7.4 ± 0.6 per mm^2 on Ti alloy to 8.8 ± 0.4 per mm^2 on Zr samples. Fibers that cover modified metal implants are uniformly distributed on implant surface. Thin fibers with diameter less than 2 μm covered all the surface and made irregular bundles up to 20-30 μm in cross section dimension**.**

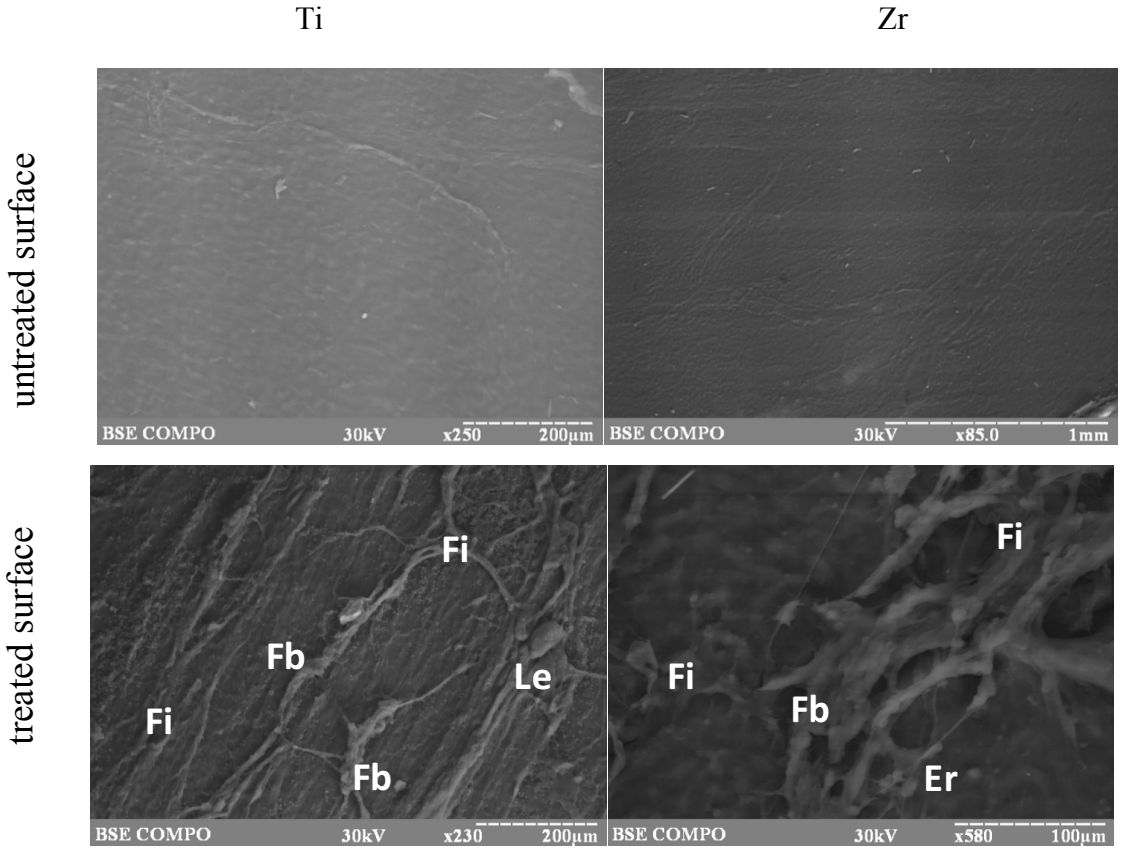

Figure 53. Surface of Ti alloy and Zr 10 days after the subcutaneous implantation. 1st row: Control samples; 2nd row: Surfaces of modified implants covered by the developed network of con-nective tissue fibres (Fi). Above the fibers we can observe erythrocytes (Er), leucocytes (Le) and fi-broblasts (Fb).

5.2.4 Analysis of results

Presented above, experimental data demonstrate pronounced improvement of biological reaction on the nano-structured implant surface when compared to polished non-structured sur-face. It is known that in a few minutes after implantation or immersion of a LIPSS-covered metal sample in the culturing media, proteins and other organics, such as ADP, ATP, serotonin,

Ca, fibrinogen, fibronectin, von Willebrand factor and growth factors get adsorbed on the implant surface [143][158]. This result (Fig. 53) signals that nanostructured surfaces have more appropriate topography for protein adhesion than the smooth one. Some of these proteins play the role of adhesives for bone and connective tissue cells that facilitate fibroblast adhesion in-vitro. Therefore, it is reasonable to expect the improvement of osteointegration of the LIPSS-covered implants with surrounding tissues. Furthermore, XPS shows that the laser treatment seems to further oxidize the surface of the metal samples, as attested by the increasing amount of TiO_2, ZrO_2 and some Al_2O_3 when compared to the non-modified surfaces (Fig. 51). These biocompatible oxides mixed with different oxidized carbonaceous species compose the outermost surface layer providing the needed adsorption sites for proteins and/or other organic molecules and enhancing, in this way, the cell adhesion and growth. HDFa proliferation on smooth surfaces is significantly lower than on the nanostructured rough materials. It is important to notice that no dependence of cell proliferation on type of metal, *i.e.* Ti alloy or Zr, was observed suggesting a predominant influence of surface topography.

In vivo experiments also showed that no cell adhesion occurred on a smooth surface contrarily to the laser-nanostructured one. *In vitro* experiments were performed in static conditions without any fluid flow, when blood flow in the rat's skin was around 2.3 mL/min/100 g [151]. These experiments confirmed that, the rough surfaces better adsorbed protein from blood plasma under the dynamic conditions, leading to further improvement of cell adhesion and proliferation.

5.2.5 Summary

Results demonstrate a higher ratio of cells growth on laser-nanostructured surfaces compared to untreated ones. The surface characterization by XPS shows that the metal surfaces are highly oxidized (metal oxides and hydroxides). The absence of dependence of cell proliferation on the type of metal (Ti alloy or Zr) and the strong dependence of cell proliferation on the topography and on the oxidation degree of the surface suggests a predominant role of the surface topography but also some influence of its composition on those biological processes. This fact opens a great prospect for the application of HR-LIPSS in the modification and improvement of the surface of dental and surgical implants.

The main scientific idea and some of our experimental results were presented at CLEO USA (San Jose, USA), held in June 2016 and World Biomaterial Congress-2016 (Montreal, Canada), held in May 2016.

5.3 Micro injection molding

5.3.1 Background

This section was performed in cooperation with prof. Giovanni Lucchetta`s group, University of Padua, Italy.

Micro injection molding (μIM) of thermoplastic polymers is widely employed for the economical mass-production of surface micro geometries, especially for optical and microfluidic applications. In these cases, the complete replication of high aspect ratio micro features, which are usually placed on a relatively thick substrate, is largely dependent on process conditions and polymer properties [159][160]. In a traditional injection molding process, under regular injection velocity and cavity geometry, the melt polymer flow is laminar with a no-slip hydrodynamic boundary condition. However, instabilities occur when geometry exhibits rapid changes, such as in the case of presence of gates or thin sections, especially if combined with high-speed injection. The so-called wall slip is a well-known phenomenon for non-Newtonian fluids which can be ascribed to a disentanglement of the bulk chains when attached to the mold walls [161][162][163] and this is more problematic in micro injection molding. Indeed, when downscaling the injection molding process, the rate between mold cavity surface and cavity volume increases, meaning that physical phenomena taking place at the polymer-mold interface increase their relevance and their influence on the whole process.

Using computer tools to simulate and optimize a process is a well-consolidated approach in traditional injection molding but when sizes are downscaled, existing numerical codes are no longer sufficient to properly simulate the flow behavior and cavity filling. Such inadequacy has to be ascribed to several limiting factors, but they all can be attributed to the fact that rheological properties of polymer used in current simulation packages are obtained from macroscopic scale measurements. Conversely, within micro scale geometries, surface tension and wall-slip conditions play a significant role, also depending on viscosity, heat transfer and temperature distribution, and topography of cavity surface [164]. More specifically, cavity surface topography, which in large scale molding is relevant only for surface finishing and appearance, can not only significantly change the cavity volume at the micro-scale but also influence the polymer flow and the heat transfer between polymer melt and mold [165].

Not only the melt flow behavior is influenced by the mold surface structure but also the molded parts wettability is heavily affected by the cavity surface topography. Wettability is a very important property of solid surfaces that is governed by both the geometrical microstructure and the chemical composition of the surface [166]. In recent years, super hydrophobicity, controllable water adhesion, anisotropic sliding and anisotropic wetting, which are four typical aspects of wettability, have attracted much interest because of their importance in fundamental research, practical applications and inspired mimetic attempts [167].

In this work, the HR-LIPSS technology was employed to generate nanostructures in the mold cavities to study its impact on the obtainable flow length during micro injection molding. A complete investigation of the surface treatment effect on the polymer flow was obtained comparing the performance of an untreated cavity surface with surfaces modified by LIPSS. The phenomenon was analysed using different channels for melt separation and taking advantage of localization of weld lines for differential characterization. To this purpose, one channel was kept untreated while the other channel was treated with LIPSS allowing a direct evaluation of the surface treatment benefits. In order to investigate a wide range of treatment solutions, several cavity inserts were developed by varying the LIPSS process parameters in order to generate surfaces with different micro-structures direction and periodicity.

5.3.2 Experiment

A commercial polystyrene was used in the experiments. The cavity design is meant to analyze the specific effect of LIPSS on wall slip and on cavity filling. The method takes advantage of a double channel with a double link configuration, as reported in Figure 54.

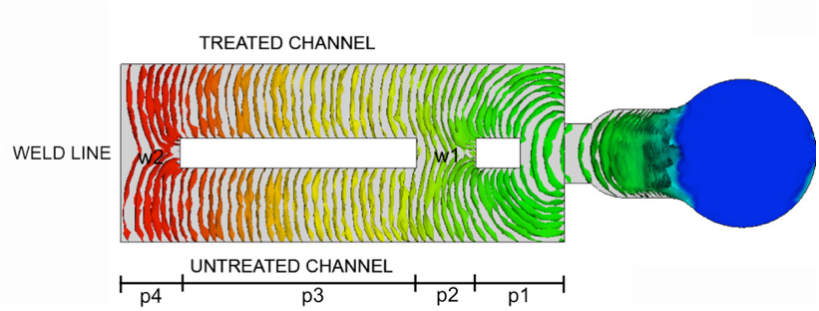

Figure 54. The cavity design filled with polymer with weld lines evidencing different wall slip behavior.

The reference cavity can be divided in 4 main sections. In the first section (p1 in Fig. 54) the channels are machined with the same width (2.5 mm), roughness and thickness (0.3 mm).

As a consequence, when the polymer melt flows meet in the second section (p2) the weld line w1 should be centered symmetrically between the two channels whenever the filling process is not influenced by any asymmetry, due for instance to a bad machining of the cavity or a different distribution of temperatures. If this is the case, the position of the weld line in the first cross-link will not be centered: the displacement can then be used to verify any presence of asymmetries within the cavity and in case to compensate it. Then w1 represent the "zero-position" for the following analysis carried out in the fourth section. The third section (p3) is machined identically to the first one except for the surface topography, which is different between the two channels. Any flow difference, to be ascribed to different wall-slip effects between the two channels, will be then quantitatively monitored in the fourth section (p4) as a relative displacement on y direction of the second weld line w2 with respect to the first one w1.

The cavity surface treatments were performed by means of a self-assembled Yb-based femtosecond laser system presented in Section 5.1.2. Two types of LIPSS have been carried out on 100Cr6 steel, one in air and the other one in argon environment characterized by the parameters of Table 7.

Table 7. Process parameters for LIPSS treatment.

Energy per pulse [nJ]	Pulse duration [fs]	Repetition Rate [MHz]	Step [µm]	Spot Diameter [µm]	Scanning Speed [mm/s]
370	120	1	4.5	9	1000

The direction of the polarization plane was set parallel to the injection flow in order to generate nanoripples perpendicularly oriented respect to the polymer flow. Figure 55 presents the morphology of the surface obtained by SEM analysis: while processing in air results in a

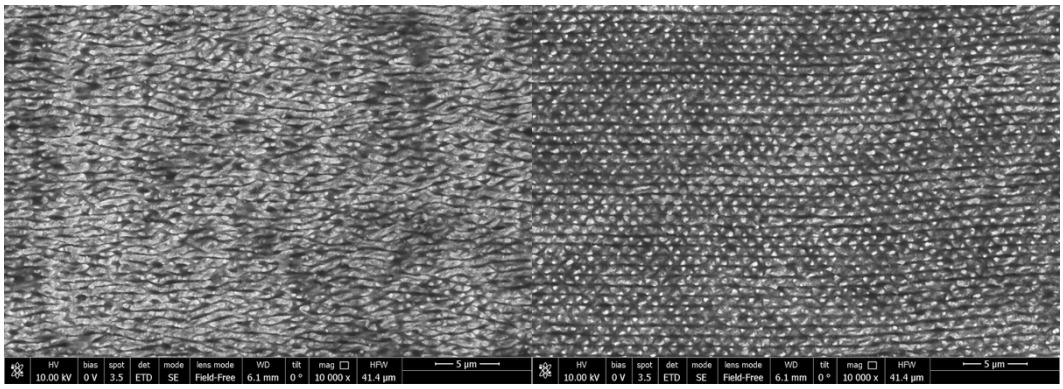

a b

Figure 55. LIPSS treated mold surfaces.

typical aligned pattern, under argon a much more regular structure with a quasi-hexagonal geometry is produced. The physical phenomena underlying these structures were not fully understood but these structures might be created as a consequence of small additional phase shift to one of the polarization components depending on the scanning speed and initial polarization.

Injection molding experiments were carried out using a micro injection molding machine [166.] In order to investigate the surface treatments influence on the flow behavior, it has been developed an experimental campaign varying the injection speed within four levels: 30, 100, 300 and 750 mm/s. The same injection molding tests were carried out also with the untreated mold insert, in order to evaluate the effect of a LIPSS surface on the filling behavior. For each combination of the processing parameters, 5 replications were performed in order to allow a statistical analysis of the results.

The weld lines locations were evaluated with a 3D optical profiler, used in confocal mode. The weld line distance from the edge "D" was measured in five different positions, as shown in Fig. 56, and the average of these measurements was calculated. All the measurements are referred to the distance between the weld line and the specimen edge from the treated side. Five replications have been measured for each combination of injection velocity and mold insert treatment.

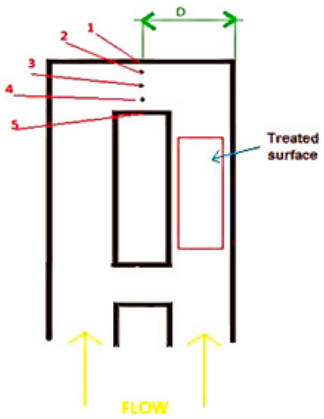

Figure 56. The measurement points and the injection flow profile

The injected parts were furthermore subjected to dynamic wettability test with *distilled-deionized* water conducted through the sessile drop method. The tests were conducted by measuring the variation of the drops contact angle with time for samples obtained by different mold and with different injection conditions.

5.3.3 Analysis of results

The results of the experimental tests are reported in Figure 57, that displays the average values of the weld line distances "D" for all the specimens molded with the investigated treatments at different injection speeds.

The results of the analysis of variance (ANOVA) show that the injection velocity significantly influences the weld line position for mold inserts treated in air. Conversely, the injection velocity is not significant for mold inserts treated in argon (p-value=0.947). In particular, for the injection speed of 30, 100 and 300 mm/s there is a significant increase of the filling length for mold inserts treated in air, compared with the untreated one. However, no variations are visible for the specimens molded at 750 mm/s. Considering the components molded with the insert treated in Argon, no evident variation in the average position of the weld line was observed.

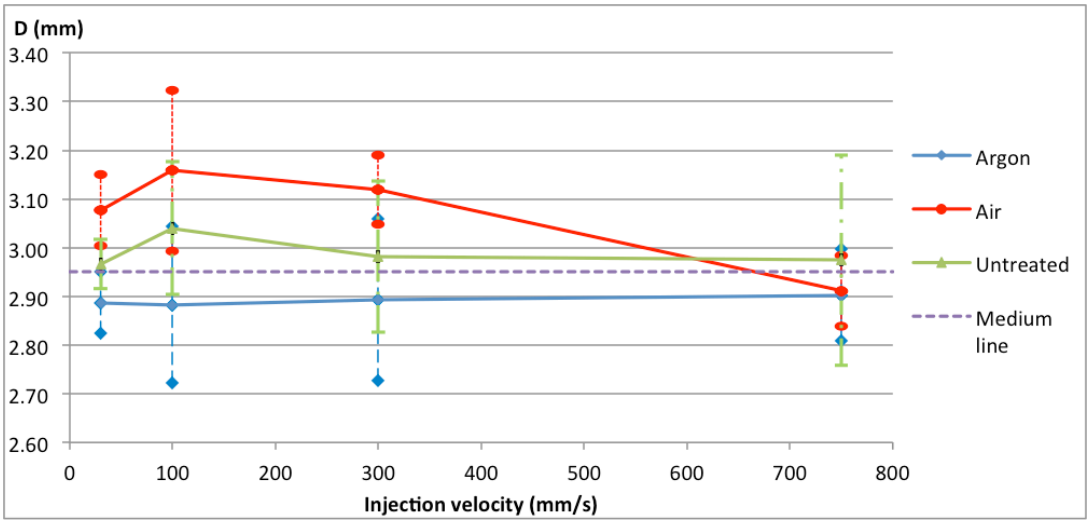

Figure 57. Weld lines distance from the specimen edges on the treated side.

The experimental results indicated that treating the mold cavity surface with LIPSS in air could improve the filling behaviour of a micro cavity, specifically when injection molding with low injection speed. The negative effect of high injection speed cannot be caused by the occurrence of the wall slip phenomenon. Indeed, its appearance is promoted by high injection speeds. In the case of LIPSS treated mold inserts, the effect of the injection speed on the flow length can be reconducted to a lower heat exchange between the melt and the modified surface that was oxidized by the treatment in air. This explanation is also in accordance with the negative influence of the injection speed on the cavity filling: the higher the injection speed, the higher

the heat flow convected into the cavity and the lower the effect of the thermal contact resistance. The analysis of variance shows that both the parameter "Treatment" and "Injection speed" are significant. Fig. 58 reports the main effects plot that indicates a decreasing of the flow length with the mold insert treated in Argon. Moreover, the flow length is maximum in correspondence of an injection speed of 100 mm/s. However, a high dispersion of experimental values was observed, in particular for the components moulded at 100 mm/s. This variability

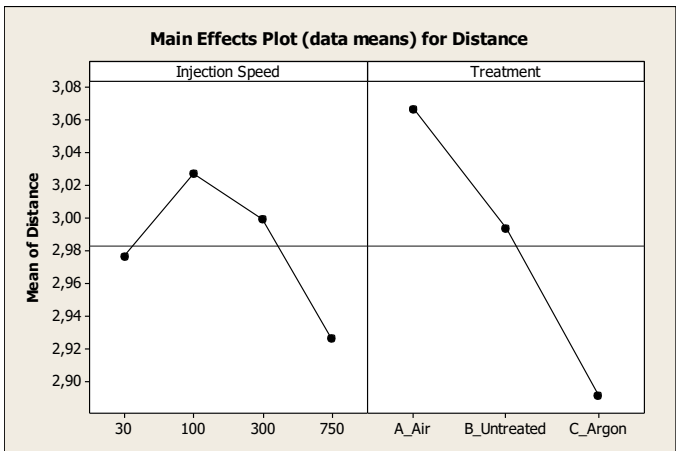

Figure 58. Main effects plots.

could be due to the local sticking of micro particles of polymer to the mold cavity during the ejection phase. These undetectable parts could easily affect the weld line position causing the high variance seen in Figure 58.

In order to understand this effect, the mold inserts were analyzed with the Scanning Electron Microscope (SEM) after the injection molding tests. The measurements were carried out in order to detect any variation of the LIPSS after the experimentations. Figure 59 shows the untreated surface cavity (left) and the in air treated surface (right). Comparing the images, it is

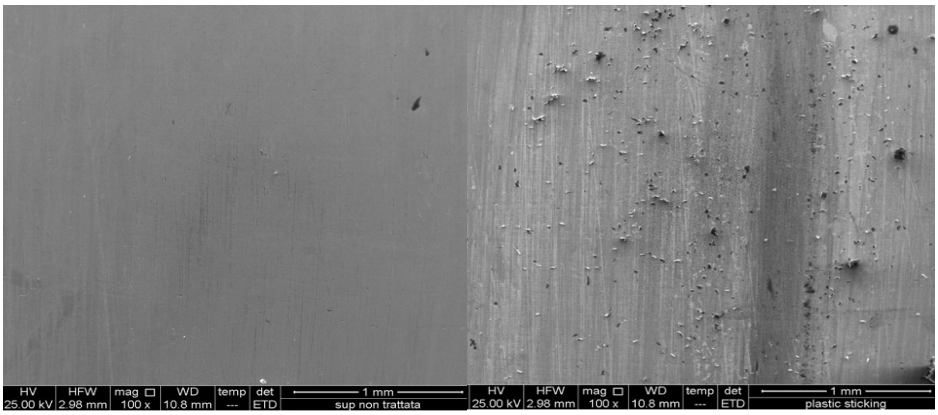

Figure 59. Sticking of polymer material on the mold insert surface treated in air on the right; untreated surface on the left (magnification: 100X).

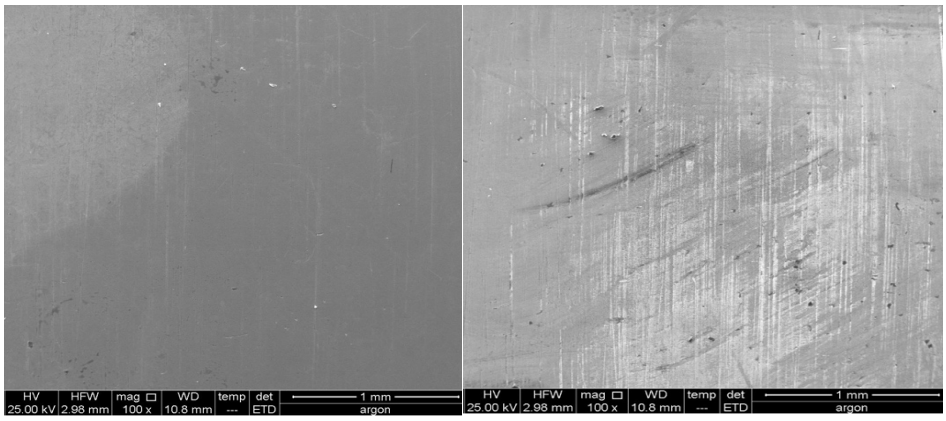

Figure 60. Mold insert surface after injection molding tests, treated in argon on the right; untreated sur-face on the left (magnification: 100X).

possible to see that a high sticking phenomenon occurred on the surfaces treated in air. This sticking phenomenon is not visible in in the analysis of the surfaces treated in argon (Fig. 60). The sticking phenomenon, observed on the cavity surface treated in air, can be explained considering the chemical adhesion between the polymer material and the oxidation layer, which develops in this process condition.

Figure 61 reports the wettability test results for specimens obtained at two different injection speeds. Each point refers to the average value of 4 different repetitions while the colored bands represent the amplitude of the standard deviation. It is evident that parts injected at low speed (30 mm/s) are influenced by the LIPSS of the molds with an average variation of the contact angle of 15 degrees between untreated and argon LIPSS treated. No appreciable effects are evidenced at high injection speed.

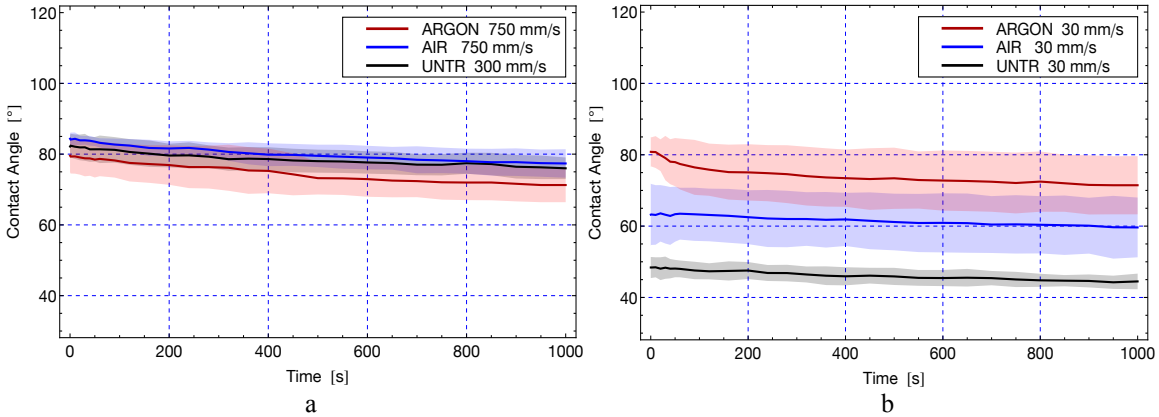

a b

Figure 61. Effects of LIPSS treatment on the dynamic wettability.

5.3.4 Summary

The influence of two different LIPSS treatment on the flow length in micro injection molding has been experimentally investigated. The effect of the injection speed was also considered. The results of the ANOVA analysis showed that the LIPSS performed in argon was no influent on the filling flow length, while the same treatment carried out in air improved the filling but only with injection speeds no higher than 300 mm/s. For higher injection speeds the surface treatment effect become negligible.

The experimental tests demonstrated that the injection speed of 100 mm/s is the optimal value to maximize the flow length. The SEM analysis of the surfaces LIPSS treated revealed a high attitude of the polymer melt to stick with the surface treated in air. On the contrary, this phenomenon was not observed with the surface treated in argon. This can be due to different factors: a direct effect of the oxide layer on the polymer flow or an indirect one caused by the higher insulation of the air treated surfaces. Also, the geometry can play an important role, the more irregular structures induced by air treatment can favourite the polymer flow.

In several studies, the induced hydrophobicity behaviour by generating LIPSS on metallic surfaces has already been investigated but the hydrophobicity achieved on polymer surfaces, replicating LIPSS has not been addressed in the scientific literature.

5.4 Wettability

5.4.1 Hydrophobicity

5.4.1.1 Background

This study was conducted together with prof. Ana Paula Serro, Superior Technical University, Lisbon, Portugal.

It is generally accepted that the surface wettability can be tuned by varying the roughness of the surface, in particular by obtaining a multimodal distribution in the periodicity and height of the surface morphology. Numerous approaches have been proposed to obtain the surface nanotexturing but many of them involve the use of vacuum chambers, creation of lithographic masks and multiple passes replication steps. The firsts direct applications of femtosecond laser to vary the wettability of material was proposed and tested on some materials, in particular in [168] femtosecond laser was used to change wettability of titanium alloy and selectively induce the carbon nanotubes growth. In [61] authors generated LIPPS on Ti6Al4V surface for biomedical application and evaluated the variations in the wettability. Superhydrophobicity behaviour on copper has been produced in [169] while an application on AISI316L stainless steel was presented in [170]. The aim of the present chapter is to evaluate the application of the new high-speed HR-LIPSS in modifying the wettability of different materials, on large areas and in the presence of surfaces mechanically polished like in the most part of industrial applications.

5.4.1.2 Experiment

Copper (99.9 % purity), Aluminium alloy and Stainless Steel AISI 316L samples with a dimension of 20x20x5 mm were mechanically polished and cleaned in ethanol before to be tested. LIPSS were performed by using a femtosecond laser system outlined in Section 4.1.2. The laser parameters set used in this work are coded in Table 8.

Table 8. Laser parameters set employed in test.

Code	Material	Angle, θ_p	Fluence, J/cm^2	Step, μm	Pulse duration, fs	RR, kHz
TAl1	Al	45	1.17	3	213	600
TAl2	Al	0	1.33	4	213	600
TAl3	Al	90	1.5	2	213	600
TCU1	Cu	90	4	3	213	600
TSS1	Stainless Steel	0	0.9	1.5	213	600
TSS2	Stainless Steel	0	0.83	1.5	213	600
TSS3	Stainless Steel	0	0.7	1.5	213	600
TSS4	Stainless Steel	90	0.9	3	213	600
TSS5	Stainless Steel	90	0.83	3	213	600
TSS6	Stainless Steel	90	0.7	3	213	600

Water contact angle measurements were carried out by using a DataPhysics OCA 20 apparatus through the sessile drop method. Static contact angle determinations were carried out on drops having a volume of 3 μl and an average value of contact angle was determined on the basis of at least five measurements.

5.4.1.3 Analysis of results

On all the materials, the laser treatment with linear polarized light resulted in the generation of nanostructures with a certain degree of regularity. The direction of LIPSS for Cu, Al and SS appears to be perpendicular to polarization of incident light.

The material properties of the nanostructures on Al, Cu and SS that are created in this process have been characterized through energy-dispersive X-ray spectroscopy (EDS). The EDS analysis in Figures 62 clearly show the presence of oxygen after the laser treatment on Al. The quantity of oxygen arises from 2.21 % on untreated surface to 14.15 % for treated ones. For Copper an increasing of oxygen part was observed from 2.79 to 5.19 %. The same behaviour appears for stainless steel, where for non- irradiated surface oxygen is absent, while for irradiated it increases up to 3.54 %.

SEM micrographs of the treated surfaces Aluminium, Copper and Stainless Steel AISI 316L are presented in Fig. 63. Scanning speed, repetition rate and pulse duration were maintained similar for all the materials. It was investigated the influence of the polarization angle θ_p that is the angle between the polarization plane and the scanning

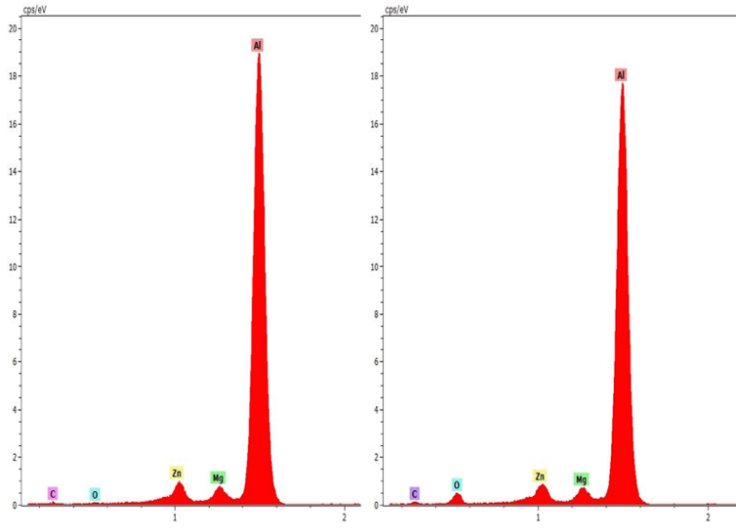

Figure 62. Energy-dispersive X-ray spectroscopy (EDS) analysis of untreated (left) and treated (right) surfaces of aluminium.

direction and the step between laser ablation lines. The surface morphology of aluminium samples was observed in depending from both laser treatment and scanning parameters. Figure 1 shows the nanostructures differently oriented respect to scanning direction. In perpendicular mode, the average period of structures is Λ = 891.3 nm that is slightly smaller than wavelength of laser beam. Image with ripples perpendicular to scanning direction θ_p = 0º shows a period equal to Λ = 866.9 nm. In angulated treatment θ_p = 45º the period of structures is Λ = 782.5 nm. Should to note that at laser fluence lower than 1.17 J/cm^2 surface nanostructures formation is not observed while at fluences between 1.33 J/cm^2 and 1.5 J/cm^2 respectively melting points are observed, this emphasizes that the morphology varies with fluence.

Treatment TCU1 was performed in perpendicular mode that is θ_p = 90º. The SEM images shows nanostructure with a period of Λ = 839.2 nm and an orientation of the structures appear to be smooth without any spikes or melting points and covered homogeneously all square 5 x 5 mm^2. It can be noted that the threshold for the creation of nanogrooves is significantly higher for Cu than for Al or Stainless Steel, 2 and 6 times respectively.

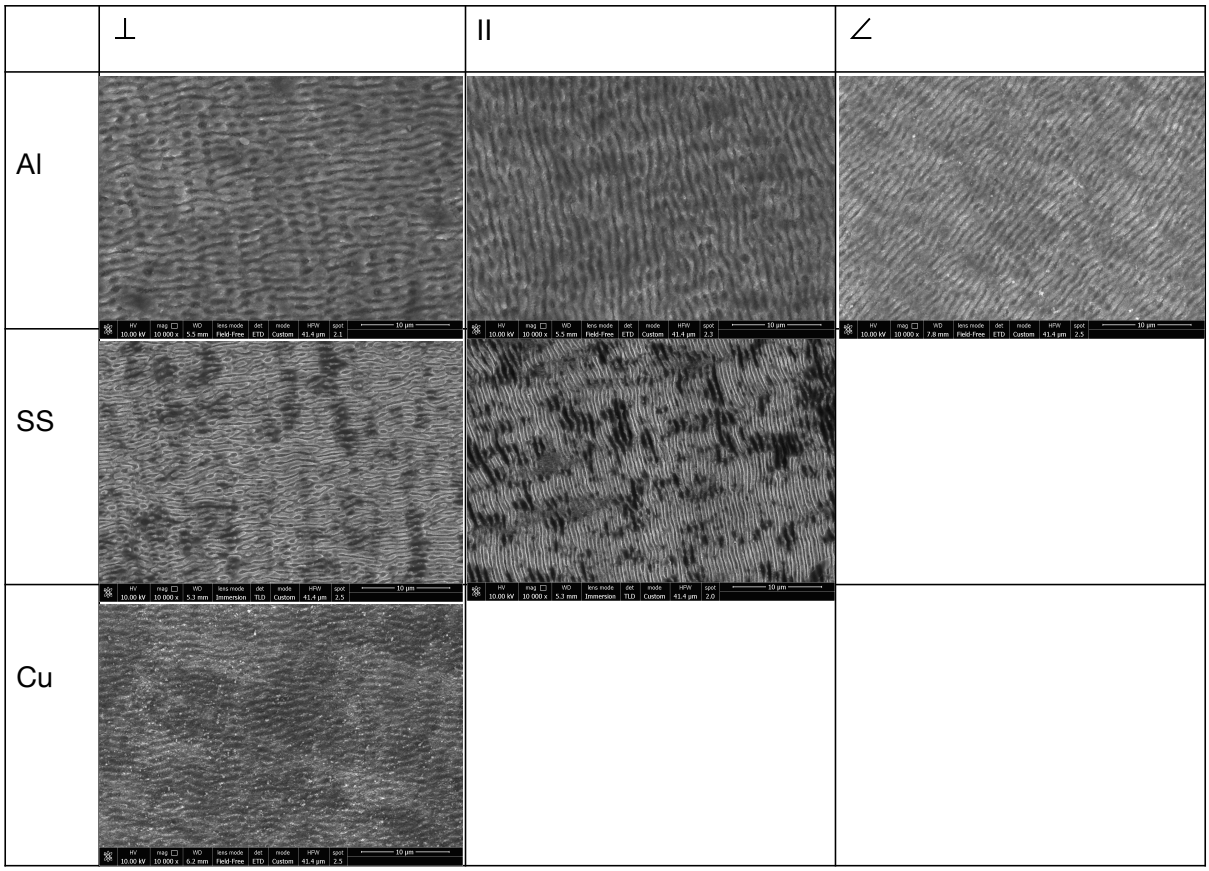

Figure 63. LIPSS on different materials obtained by changing the polarization plane angle θ_p. Scanning direction is horizontal.

Figure 63 represents the SEM images taken at on AISI 316L surface treated in TSS1 and TTS4 conditions. The nanostructures created on stainless steel are substantially different from that generated on Al or Cu. It is possible to see that in many points the oriented ripples split in two parallel ones that, after a little join together. This occurs quite periodically also if it is difficult to measure the distribution parameters. This phenomenon may occur for alloys which contains different metals, because in pure metals it is not observed, non-iron content in AISI. The observed morphology of Al, Cu and SS (Fig. 64) using AFM shows that surface is com-

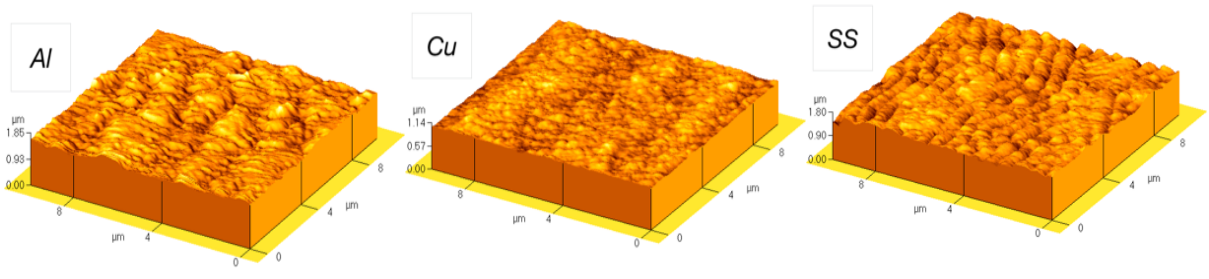

Figure 64. AFM analysis of the surfaces.

posed by parallel and periodic, homogenous nanoripples for all materials. For Al the height of profile is 270±30 nm. The average roughness is Ra = 44 nm. For SS, the height of profile is 410±20 nm and the average roughness is Ra = 50.1 nm. For Cu, the height of profile is 93±50 nm while the average roughness is Ra = 17.8 nm much lower respect the other two materials.

5.4.1.4 Wettability and analysis of main results

The wettability behaviour of materials can be controlled either by changing its surface chemistry or by modifying its surface morphology. Hydrophilicity (wetting) or hydrophobicity (non-wetting) character of a material is commonly defined by the static contact angle q between a liquid (water or oil) droplet and the material's surface. Hydrophilicity and hydrophobicity are defined by the q below and above 90º, respectively. In this study, the effect of surface chemistry and surface morphology on wettability with respect the periodicity and topology of nanoripples by changing laser polarization and fluence. Figure 65 and Table 8 summarizes the θ_p measurements performed on three aforementioned metal surfaces with slightly modified morphologies. As can be seen from the figure, all bare (untreated) metal surfaces displays hydrophilic behaviour that has changed to hydrophobic behaviour after laser treatment. This can be explained by the surface roughness that is introduced due to LIPSS formation. As Wenzel reported for the first time, the water does not wet roughened surfaces because it cannot enter inside the pores but sits on top of them, leading to a hydrophobic behaviour. However, the real-world examples also showed that if a material is initially hydrophilic, surface roughness further enhances this behaviour. This is due to the fact that Wenzel equation is only valid when the surface (roughness) is homogeneous, which is not always true for real world examples since the roughness can be nonuniform or heterogeneous or there can be chemical inhomogeneities on the surface, which again translates into heterogeneous surfaces. Wetting behaviour for such surfaces are generally explained by Cassie-Baxter model [171][172][173].

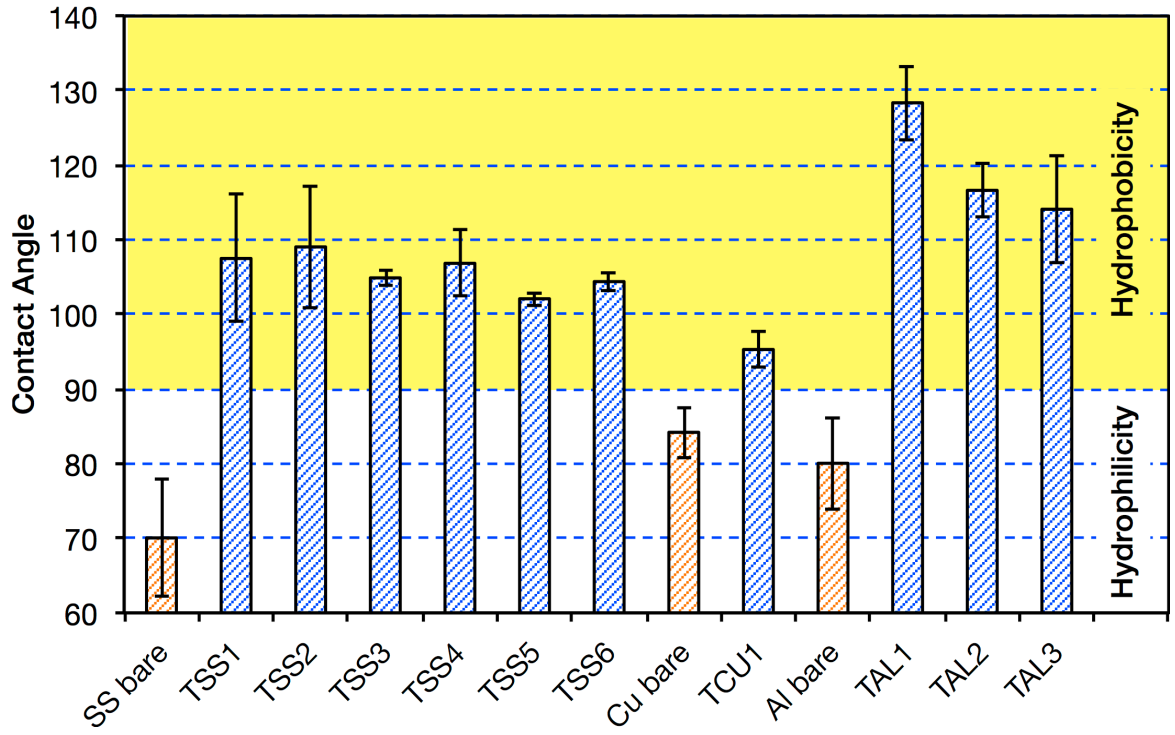

Figure 65. Comparison of wettability results on treated surface by LIPSS and untreated one on three different metals: Al, Cu and Stainless Steel.

According to this model, regardless of the initial wetting behaviour of the material, if the surface roughness allows air or gas to trap inside the cavities, air or gas also acts as a surface, where water droplet can behave as if it is on a smooth, flat surface leading to a hydrophobic behaviour. This means that the shift from hydrophilicity to hydrophobicity via induced nanoripples observed in this work should better be explained by the Cassie-Bexter model, rather than the Wenzel model. Furthermore, it is also shown that this behavioural shift is more prominent for SS and Al, where a dramatic change of θ_p from ~70º to ~110º is observed for SS and from ~80º to ~110º is observed for Al when the surface is nanopatterned with laser. This is due to the fact that the periodicity and nanoripples on these two metal surfaces are more prominent compared to that of Cu, which means the surface roughnesses of these two metals are significantly larger than that of Cu, Fig. 64. Figure 65 also shows that the polarization and laser fluence also influences the wettability behaviour, specifically for Al. It is shown that the highest q value is measured when the polarization is 45º, whereas parallel and perpendicular polarizations do not have a large effect on the hydrophobicity behaviour since the structures are isotropic on average. If the structures were anisotropic (directional) then we would have observed a significant difference in wettability measured observing in parallel and perpendicular directions. In particular, the surface wettability behaviour along the LIPSS direction appear less

hydrophobic than perpendicularly to it. This means that the wettability not only depends on the surface roughness but also dramatically influenced by its homogeneity, periodicity, uniformity, anisotropy and the length scale (dimensions of the structures and their distances to each other) of introduced roughnesses [174]. We also note that the laser fluence did not dramatically affected the overall behaviour of treated SS surface (Table 8 and Fig. 65), where the θ_p varied between ~100º and ~110º.

5.4.1.5 Summary

The obtained nanostructures are periodic and homogenous; they can be obtained for indefinitely large area and the process time appear very interesting for industrial applications. In its simple form this method does not require expensive equipment, environmental conditioning system or vacuum chamber. The process can be scaled in order to increase the productivity. This can be done by proportionally increasing the power and the scanning speed while the spot diameter cannot be increased above few microns. With a scanning speed of 1.5 m/s typical of many galvanometric systems it is possible to expect values of production rate between 450 and 1200 mm^2 /min. Results on surface wettability appear very interesting, LIPSS treatments permit to change the surface behaviour from hydrophilic to hydrophobic behaviour, in particular on Aluminium the surface morphology results in very high contact angles.

5.4.2 Anisotropic and isotropic properties of nanostructured surfaces

5.4.2.1 Experiment

The material under study is a common AISI 316 subjected to a process of Low Temperature Carburizing (LTC) (Fig. 66). The surface of the material was polished and lapped with diamond paste and squares 10x10 mm were generated on it.

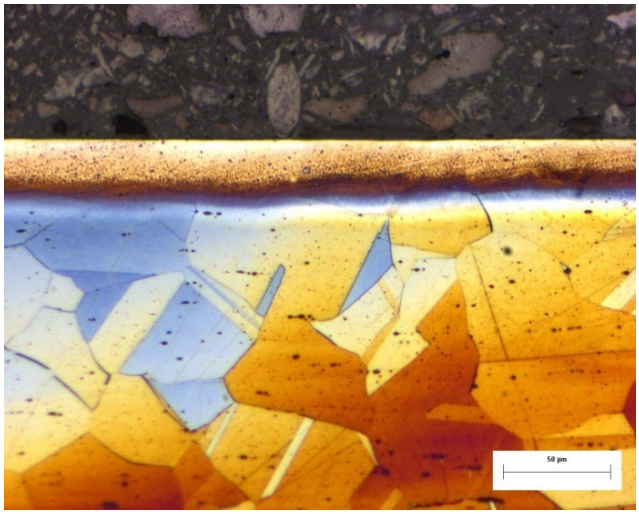

Figure 66. A metallographic section of the AISI LTC under study. The treated zone is clearly visible.

The LIPSS treatments were conducted by using Yb-doped fiber laser system (Section 5.1.2). Table 9 shows the coding of the experimental tests; two parameters were varied: the angle θ_p between the polarization plane and the scanning direction and the energy per pulse.

Table 9. Coded process parameters in the experimental campaign.

Code	Polarization angle θ_p [°]	Energy per pulse [nJ]
PPA	0	160
PPB	0	170
PPC	0	180
PTA	90	160
PTB	90	170
PTC	90	180

The wettability of the surfaces was determined through the measurement of distilled and deionized (DD) water contact angles by the sessile drop method. Drops of ≈ 2-4 μL were generated with a micrometric syringe and deposited on the substrates surface, inside a chamber previously saturated with water. Drop images were acquired at pre-defined intervals during 2000 s, with a video camera.

5.4.2.2 Analysis of results

Fig. 67 shows SEM image of a PP-coded specimen where the polarization plane is parallel to the scanning direction. As can be seen from the figure, formation of a quasi-regular linear pattern is evident with all the basic aspects of HR-LIPSS present: the coherent propagation of structures along the surface that are obtained by scanning the laser beam with a small diameter. The obtained nanostructures are not enough regular via reason described in Section 5.1.3.

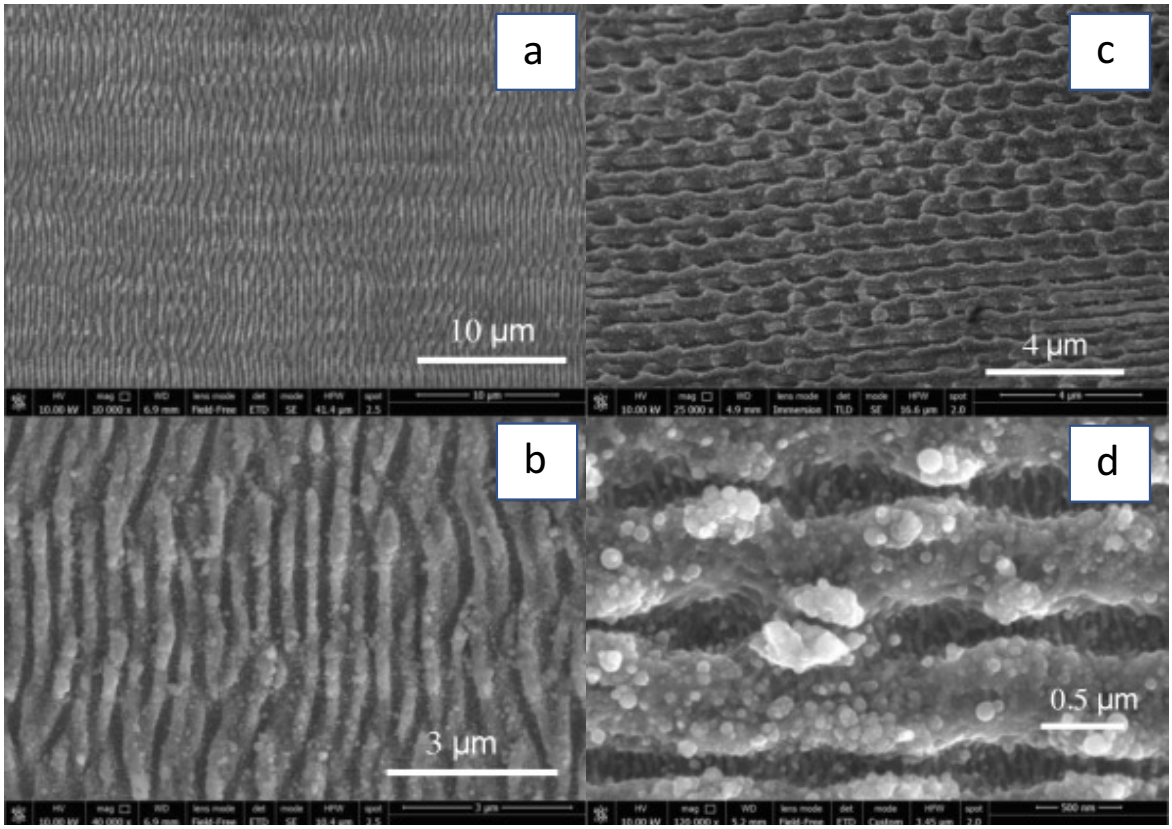

Figure 67. SEM images of the specimen coded as PPC, where the scanning direction and the polarization plane are parallel to each other: (a) a large area image, and (b) the focused image taken in higher magnification. SEM images of the specimen coded as PTB, where the scanning direction and the polarization plane are perpendicular to each other: (c) a large area image, and (d) the focused image taken at a higher magnification.

The periodicity of LSFL was measured as 380±50 nm. AFM analyses indicated that the width and the height of the ripples are 320±40 nm and 420±30 nm, respectively. Fig. 67d shows the presence of high spatial frequency LIPSS (HSFL) inside the valleys between periodic structures. A nanostructure parallel to the polarization direction is evident with a period significantly smaller than the laser wavelength and in the order of 77±20 nm.

Fig. 68 shows the AFM mapping of the specimen coded as PTB, where the scanning direction and the polarization plane are perpendicular to each other. The nanostructures are clearly different with respect to the specimen coded as PPC, with quasi-hexagonal structures in three principal directions that are mutually oriented at 60° to one another. It seems like two small ripples are periodically joined in a bigger ripple. The period between these double ripples was measured as 790±30 nm, while the period between the smaller ripples was measured as 350±50 nm, almost half of the period of double ripples.

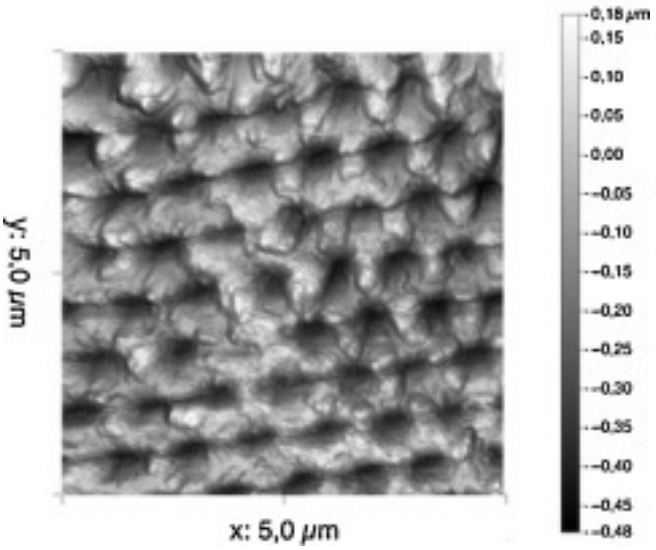

Figure 68. AFM maps of PTB treatment with a quasi-hexagonal structure, clearly visible.

The quasi-hexagonal structures were already obtained and observed in previous studies, where the structures were produced by scanning the surface with a circularly polarized laser beam or by using double scans with two orthogonal polarizations [175]. In our case, it is possible that the galvoscanner perturbs the polarization state to elliptical depending on the scanning speed and initial polarization. The structures are clearly evident in SEM images shown in Fig. 65a, where they are taken from a 45° tilted specimen. Fig. 65b depicts the high-resolution image showing the joint of two ripples. Chemical compositions of the untreated specimen and LIPSS-treated specimen coded as PTB were analysed through an EDS probe. The values obtained for the untreated specimen are in a good agreement with the nominal chemical composition of an AISI 316L that is subjected to a low temperature carburizing treatment. On the other hand, similar to the last research of EDS on treated surface, it is possibly oxidized as a result of laser-material interaction in the atmospheric conditions.

Wettability tests with DD water were conducted through the sessile drop method on both types of surfaces.

Measurements were performed in two directions: parallel and perpendicular to LIPPS (Fig. 69), to evaluate the effect of the LIPSS treatments on anisotropic wettability measured as the difference between the contacts angles observed in those directions.

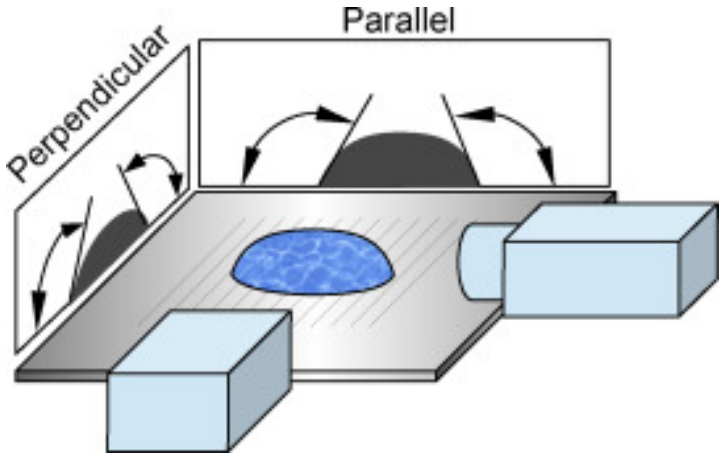

Figure 69. Schematic representation of the contact angle measurements in parallel and perpendicular directions.

The results are presented in Fig. 70a and Fig. 70b for the specimens coded as PPC and PTB, respectively. Data obtained for the untreated specimen are included for the purpose of comparison. Results scattering is shown as light-coloured bands.

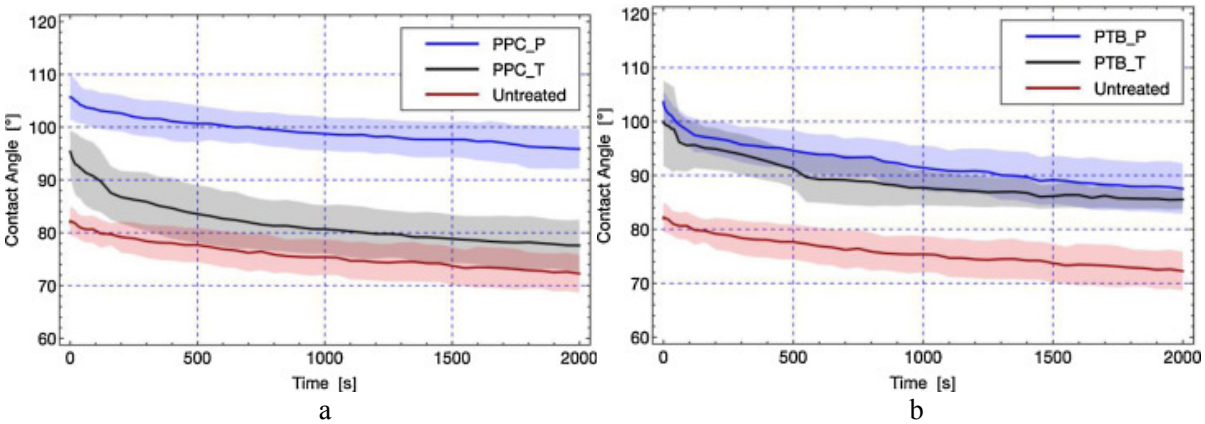

a b

Figure 70. Evolution of the water contact angles with time for the specimen coded as PPC (a) and PTB (b) PPC_P represents the measurements performed when the contact angle is in a plane perpendicular to the LIPPS direction, while PPC_T represents the measurement performed when the contact angle is in a plane parallel to the LIPPS direction as indicated in Fig. 67. PTB_P represents the measurements performed when the contact angle is in a plane perpendicular to the LIPPS direction, while PTB_T represents the measurements performed when the contact angle is in a plane parallel to the LIPPS direction as indicated in Fig. 67

Both LIPSS treated surfaces present an appreciable hydrophobicity. This is coherent with earlier studies, where femtosecond laser irradiation is used to treat stainless steel surfaces

[170] [176] and [177]. Depending on the experimental conditions, some of them have managed to achieve super-hydrophobic surfaces. Obviously, the increase in hydrophobicity may be attributed not only to changes in roughness and topography as predicted by the Wenzel model [171] but also due to the oxidation induced by the laser treatment as evidenced by data from EDS analysis.

The main difference in the wettability behaviour of the two surfaces is related with the degree of anisotropy. As expected, contact angles observed perpendicularly to the LIPPS direction are smaller than those observed in the parallel direction because grooves drive water by capillary force. The difference between the contact angles in the two directions, however, is more pronounced in PPC surfaces (Fig. 68). From the morphological analysis carried out above, it was concluded that LIPSS treatments led to a strong linearly structured texture on PP surfaces and a more isotropic (quasi-hexagonal) structure on PT surfaces. This is reflected by the wettability results. Moreover, as observed by other researchers [178], the contact angle anisotropy is strongly correlated to the surface arithmetic mean roughness (Sa); rougher samples (as is the case of PP, see Table 10) show larger wetting anisotropy than the smoother ones. The average increase in contact angle measured on the entire set of wettability tests performed is 15.8° while the average anisotropy calculated as the difference between the contact angle in the two directions appears to be 8.4° for PP test conditions and 5.8° for PT ones, respectively.

5.4.2.3 Summary

The LIPSS as a technique to modify surface appears to be a very promising method for the control of the wettability properties of stainless steel. The presented setup permitted an increase in hydrophobicity by using a low power and not particularly expensive femtosecond laser. The process seems to be quite robust and repeatable also if conducted in open air, while it can be easily scaled to mass production by increasing power and scanning speed.

All the results confirm it is possible to increase the surface hydrophobicity with the possibility to tune, in a single pass treatment, the degree of anisotropy by varying the experimental conditions.

5.5 Adhesion properties

5.5.1 Background

This investigation was performed with research group of prof. Giovanna Rotella, University of Calabria, Italy.

Adhesive bonding is currently a very wide spread joining technique in aircraft and automotive industries due to many advantages provided over conventional methods, such as mechanical fastening and welding, which include reduced corrosion and stress concentration as well as cost effectiveness [179][180]. However, the main challenge limiting a widespread use of adhesive bonding for primary structural applications is to find an effective, simple, economic and ecological method for surface preparation prior to bonding able to provide good bond strength and toughness as well as long term durability. In fact, titanium alloys are very sensitive to surface oxidation which affects the strength and long-term durability of the joint [181].

Among the various surface preparation strategies, laser irradiation has been proven to be very effective on a wide variety of materials, including metals, polymers and composites [182][183][184][185]. Lasers provide the ability to accurately deliver large amounts of energy into small regions of a material so that to achieve a desired response. This energy is absorbed into the near surface region without altering the bulk properties of the target. The size of the heat affected zone, as well as surface features, strongly depend on the laser-material interaction time, namely pulse duration, scanning speed and on the achievable spot diameter. The last parameter is constrained by the diffraction limit and it is normally difficult to obtain features with size less than 10 μm. Femtosecond laser generates energy pulse in the so-called ultrafast regime with a negligible dispersion of energy due to the bulk conduction. As a result, thermal effects are strongly reduced. Femtosecond laser irradiation has been successfully employed in surface modification, drilling, and cutting because of the minimal heat affected zone [186][187].

In the present chapter, a novel method to generate a quasiuniform distribution of LIPSS on a metallic surface has been deployed on Ti6Al4V titanium alloy substrates for adhesive bonding. The main objective is to enhance the mechanical performance of Ti6Al4V/epoxy joints. For comparison, similar adhesive joints were prepared using standard degreasing and a

chemical treatment as surface preparation strategies prior to bonding. Moreover, surface wettability was probed using the sessile drop technique. Finally, mechanical tests were carried out under peel loading to probe the joint strength. In order to analyse the aging effect on the joint response, a selected set of sample was subjected to a boiling water treatment [186] prior to mechanical tests.

5.5.2 Experiment

The material employed for sample fabrication is a 1 mm thick 1000Å~1000 mm^2 metal sheet made up of commercial grade 5 titanium alloy (Ti6Al4V) obtained by rolling process.

In the present work three different surface preparation strategies were compared in order to fabricate Ti6Al4V/epoxy joints. Namely, three sets of samples were bonded using the following surface preparation techniques: (a) simple degreasing; (b) chemical treatment, (c) femtosecond laser irradiation or LIPSS. Simple degreasing has been carried out in an ultrasound bath of ethanol for 10 minutes followed by air drying. The chemical treatment was carried out as follows. At first a simple degreasing step, as already described above, was carried out. Afterward, the samples were subjected to an acid–base process [190] because, as reported in previous related works [188], acid treatments are appropriate to achieve suitable titanium surfaces for adhesive bonding in dry conditions. The laser treatment (LT) or LIPSS has been conducted in two different configurations depending on the direction of the polarization in order to obtain submicron sized surface ripples parallel (LT//) and perpendicular (LT$\perp$) in the longitudinal direction of the titanium substrates. As laser source, we used commercial femtosecond laser system "Pharos", which in details presented in Section 4.1.2. The remaining processing parameters were set as follows: pulse duration, τ =213 fs, repetition rate, f=600 kHz and pulse energy, Ep=0.58 nJ; the laser spot diameter at the focal plane was d=6 μm while the scanning speed was v=3 m/s and the spacing between each laser scan was set equal to d=3 μm. Surface irradiation of the samples (40 substrates) required about 3 hours, thereby resulting in an overall production rate of about 250 mm^2/min.

Bonding procedure provides after surface preparation; the samples have been bonded using a bi-component toughened epoxy adhesive. Distinct sets of ten adhesive joints were fabricated for the various surface preparation strategy, which provided a total of 40 samples. Within each set, five samples have been subjected to accelerated aging prior to mechanical testing as described in the next section. Accelerated joint aging in hot water ensured by selected

adhesive joints were subjected to an accelerated aging procedure in order to analyze the evolution of joint strength after exposure to aggressive environmental conditions. After adhesive curing, the samples were placed in a water bath at 100°C for 72 h (i.e. boiling water test) as recommended by [186].

5.5.3 Analysis of results

The surface topography of the as received (AR), LT and CT (chemical treated) samples has been probed by atomic force microscopy (AFM). The periodicity of LSFL was measured as 380 ± 50 nm. AFM analyses indicated that the period and the height of the ripples are 810 ± 50 nm and 380 ± 20 nm, respectively. Table 10 reports the principles topography features measured through AFM. The trend displayed by surface roughness indicates the effectiveness of the laser treatment to modify substrates topography through the generation of surface features, which increased surface roughness, and, as a result, the area available for bonding. On the other hand, the chemical treatment had the opposite effect, i.e. it led to a decrease of the mean surface roughness. It is therefore expected that the chemical treatment will not enhance mechanical interlocking. Therefore, any improvement in bond strength will be associated to an improved chemical interaction at the adhesive/substrate interface.

Table 10. Surface morphology analysis obtained through AFM measurements

Samples	Sa [nm]	Sq [nm]	Skew [-]	Kurtosis [-]	Relative Area [-]
AR	107	136	-0.25	0.40	1.11
CT	63	83	-1.14	1.34	1.03
LT	294	346	-0.44	-0.75	1.29

.

The contact angle (CA) was determined by means of the sessile drop technique Drops of ultrapure water (V=3 μl) were gently placed on the probed surfaces to test the corresponding wettability. Typical results are reported in Figure 71. In order track the evolution of wettability, measurements were carried over an interval lasting 300 s so that to spread capillarity effect and measure the equilibrium contact angle. Figure 71 displays the configurations assumed by the liquid drops on the probed surfaces at two elected time instants. The results testify that AR samples have reasonable wettability and a stable contact angle (i.e. no significant variations with time). The CT surfaces exhibited a hydrophilic behavior displaying an average contact

angle of approximately 18°. This result is also due to the γ-APS primer was applied to the treated surfaces, just after the formation of the fresh oxide layer [189].

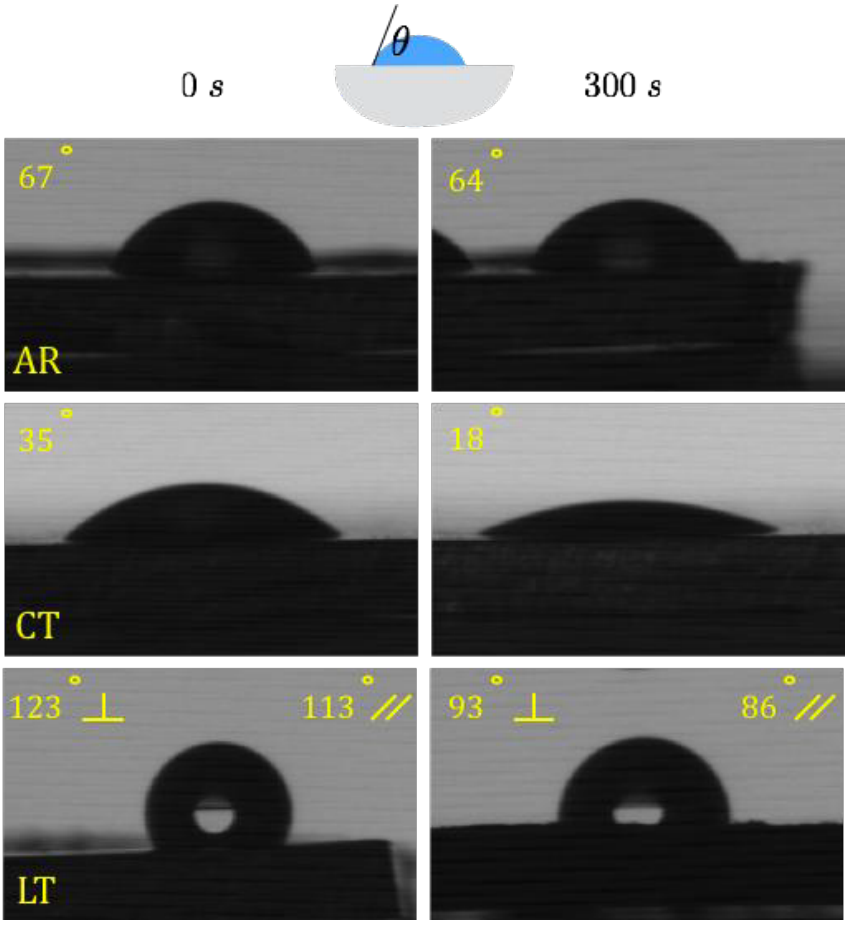

Figure 71. Contact angle of the AR, CT and LT samples.

Notice that a hydrophilic surface has good capability to be wet by the adhesive leading to improved joint strength. On the other hand, the LT samples displayed a hydrophobic behavior. However, this result does not necessarily imply a weak bond with the adhesive. For such patterned surfaces, it has been demonstrated that the Cassie- Baxter model is more adequate to describe the wettability regime. In particular, it assumes that the contact of the droplet with the probed surface is affected by the air trapped within surface asperities [190]. Therefore, the increase in contact angle does not necessarily lead to poor wetting of the treated surface by the adhesive. This point will be also assessed afterward through the analysis of the fracture surfaces.

Energy-dispersive X-ray spectroscopy (EDS) analysis

The chemical composition of the untreated and processed surfaces has also been probed through the EDS analysis. Figure 72 reports some of the chemical elements detected during the analysis on LT and CT coupons. The LT cross section highlights a set of elements in agreement with the nominal chemical composition of the bulk material. The analysis on the top surface did not reveal the presence of oxygen confirming that the small amount of heat involved during the process did not lead to a substantial formation of any oxide layer. In contrast, the presence of Si and O detected on the CT surface was in agreement with the performed chemical procedure aiming to generate chemical bonds between the adherend and the adhesive.

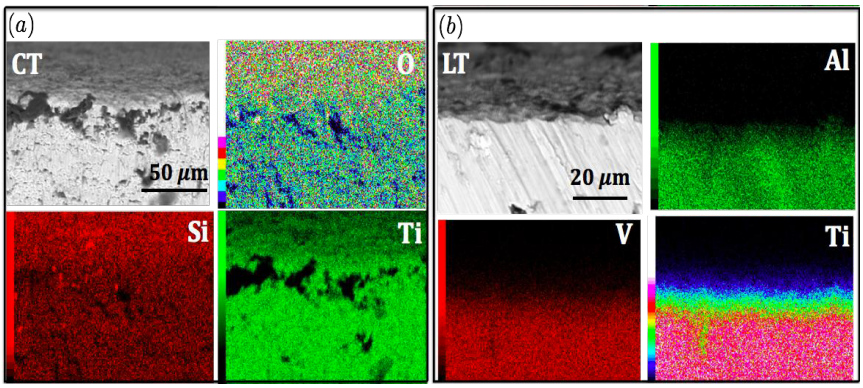

Figure 72. EDS elements mapping on LT and CT cross sections prior to bonding.

Static tests on bonded and aged joints

Figure 73 shows the results obtained in peel tests. The results obtained on aged samples suggest that the failure mode does not change for any of the probed surface treatments. However, while it was reasonable to expect a deterioration of the mechanical response, for almost all the cases the aging conditions did not lead to significant variations of joints' strength. The reason can be attributed to the ability of the treated surfaces to withstand the effect of water. In particular, the eventual oxide layer on the titanium surface is more stable than that generated in other materials such as aluminum slowing down the effect of aging on the joint.

Figure 74 reports the SEM images of the fractured surfaces after the mechanical tests. The scope of this analysis was to highlight the differences in the failure mode of the laser and chemically treated samples that led to a different average load during the static tests. Both CT and LT samples displayed a cohesive failure even though the chemical treated samples showed, in some area (micron sized), a full detachment of the adhesive from the surface. This is probably

due to the high sensitivity of the chemically treated surface to be easily contaminated after the process, leading to a more difficult bonding procedure. However, the chemical treatment was able to provide almost the same level of joint strength due to the strong chemical bond created between the treated surface and the epoxy resin [189].

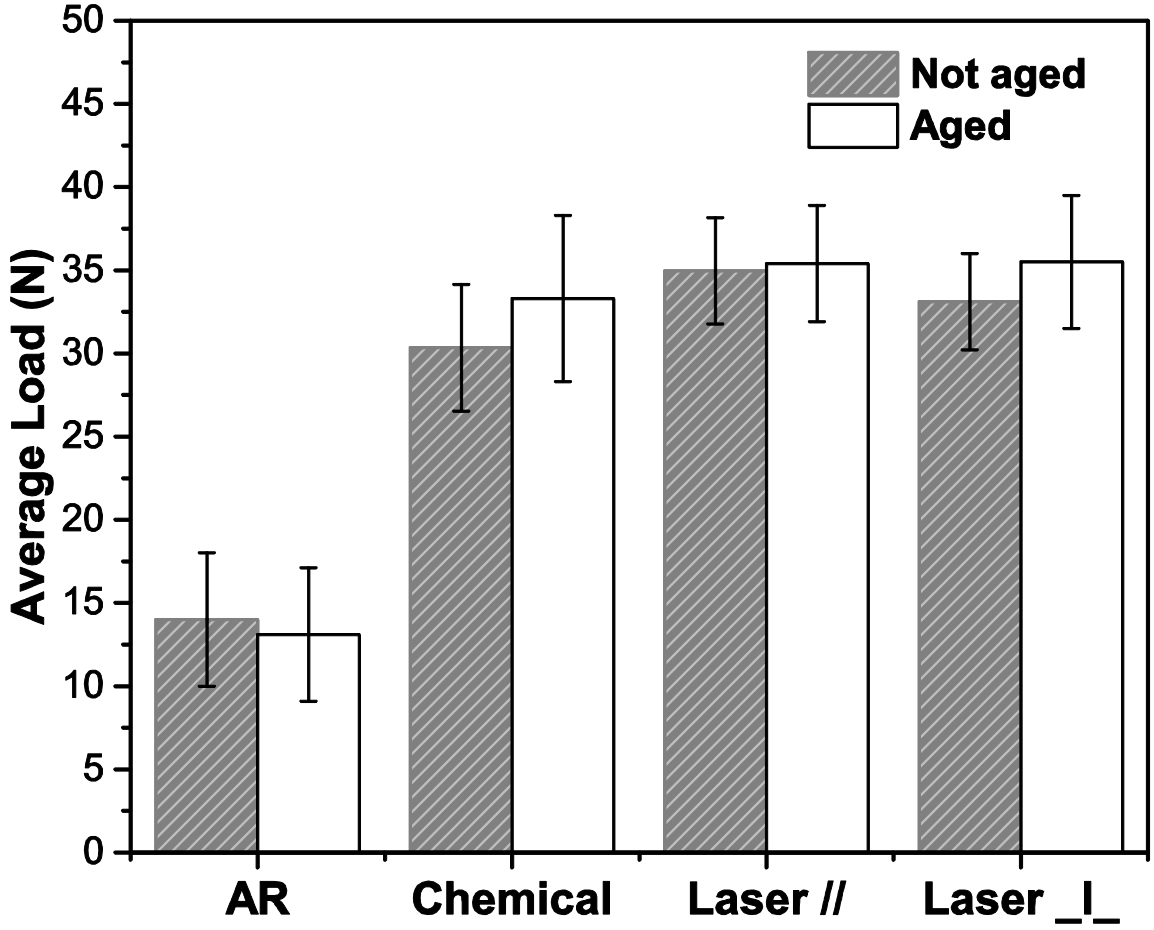

Figure 73. Average load recorded on Ti6Al4V/epoxy joints before and after aging.

From the other hand, the cohesive failure during the debonding of the LT surfaces was revealed more uniform under the SEM. It is clear how the adhesive was able to penetrate into the periodic structures generated by laser process improving the joint strength (see Fig. 74c). Thus, while for LT samples the effect is mainly addressed to the enhanced mechanical inter-locking of the adhesive in surface asperities, in the case of chemical treatment it is associated to an improved chemical interaction at the adhesive substrate interface.

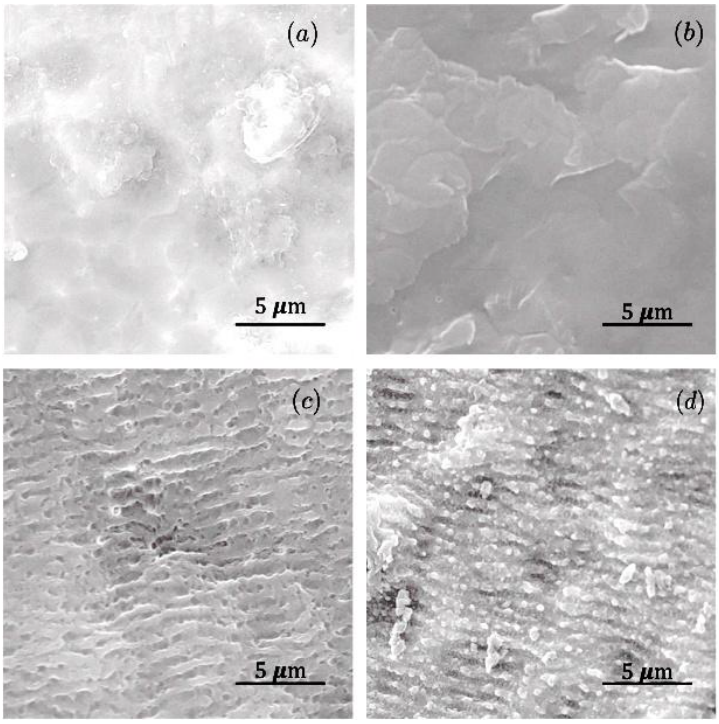

Figure 74. SEM images of the mating fracture surfaces for CT (a, b) and LT (c, d) bonded joints.

5.5.4 Summary

In this chapter, the effect of femtosecond laser and chemical treatments on Ti6Al4V surfaces for enhanced adhesive bonding is addressed. Laser irradiation was performed by scanning the laser beam over the sample with high precision and, through the control of laser polarization, it was possible to generate in a single-step complex surface pattern. Furthermore, the creation of such precise structures does not involve the need of surface preparation before treatment and it demonstrate the capability of the method to be easily customable. From the other side, the chemical treatment was also effective in generating a good surface preparation prone to create covalent bonds with the adhesive. The presented results show that both laser treatments increased surface roughness and, in turn, the area available for bonding thereby leading to improved joint strength before and after aging. Finally, it is worth noting that the laser treatment presented herein is provided with an extremely high production rate that can be tailored to different materials and is amenable to mass production.

5.6 Counterfeit prevention with surface-colorizing via HR-LIPSS

A unique technique called highly-regular laser-induced periodic structures for laser nanostructuring (HR-LIPSS) of metal and non-metal surfaces has a great potential to thwart counterfeit distribution of these materials. HR-LIPSS can be used to induce surface colour on the material, reducing the possibility for fraudulent substitutes. This technology has record-high speed and productivity, desirable for industrial applications.

5.6.1 Experiment

The samples from stainless steel AISI 316L were utilized in experiment. The set of laser parameters used in present work are reported in Table 11. HR-LIPSS on stainless steel were formed using a commercial Yb-doped solid-state laser system "Pharos", which in details described in Section 4.1.2.

Table 11. Set of laser parameters

Material	Average Power	Speed	Step	Pulse duration	Repetition rate	Fluence
AISI 316L	150	3000	4	213	600	0.7

The surface morphology of the patterned samples was investigated by scanning electron microscopy (SEM), imagine with secondary electrons and custom modes using a FEI Nova NanoSEM 450 with X-EDS Bruker QUANTAX-200 X-EDS.

5.6.2 Analysis of results

Fig. 75a present rainbow picture due to diffraction of light. If nanostructures cover area uniformly than colour shining looks brighter. Colours depend from direction of ripples and angle of incident light. Fig. 75b reveal SEM of HR-LIPSS on stainless steel. The spatial period Λ estimated to be 800±50 nm, that is slightly smaller than the laser wavelength λ. The ripples oriented perpendicularly to the laser polarization. Interestingly, the modified surface is free from bifurcation points and double ripples. Such surface with dimensions 10 x 10 mm was treated less than a 10 s. Such speed is unprecedentedly high for LIPSS generation and push this

technique to industrial applications. Such speed is unprecedentedly high for LIPSS generation and push this technique to industrial applications.

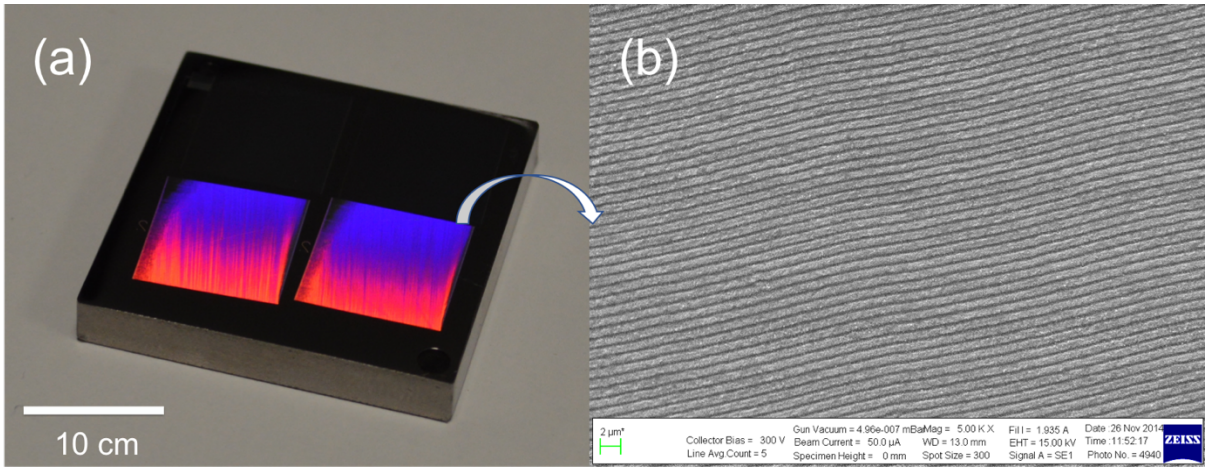

a b

Figure 75. HR-LIPSS generated on Stainless Steel: (a) macroimage reflect rainbow colour via diffraction from a room light.

The SEM images reveal that period of structures are around 800 nm, that is 80 % from laser wavelength. All expected areas are uniformly covered by HR-LIPSS.

This technology can be used in counterfeit prevention by uniquely marking a product. The Figure 76 is an artistic rendition of how this process can be used to mark an iPhone with HR-LIPSS.

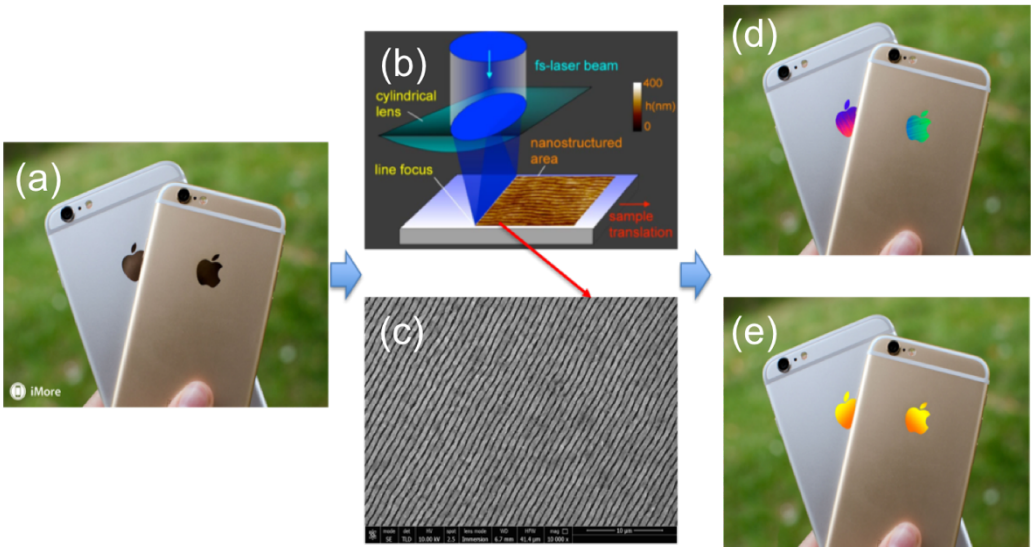

Figure 76. Artistic rendition of laser nanostructuring on iPhone 6s.

An unmodified iPhone 6s is shown in Fig. 76a. After treatment with femtosecond laser pulses (76b), HR-LIPSS are generated (Figs. 76c). Finally, the Apple logo has an eye-catching appearance that can additionally serve as a decoration (Figs. 76d, e).

Nanostructured surface produces specific pattern of reflected light (Fig. 77c), but untreated surface reflects single spot of light (Fig. 77b). Nanostructured surface can be identified by reflection pattern using a cheap and simple source of light, for example laser pointer (Fig. 77a). Different products can be marked with different nanostructures for fast identification.

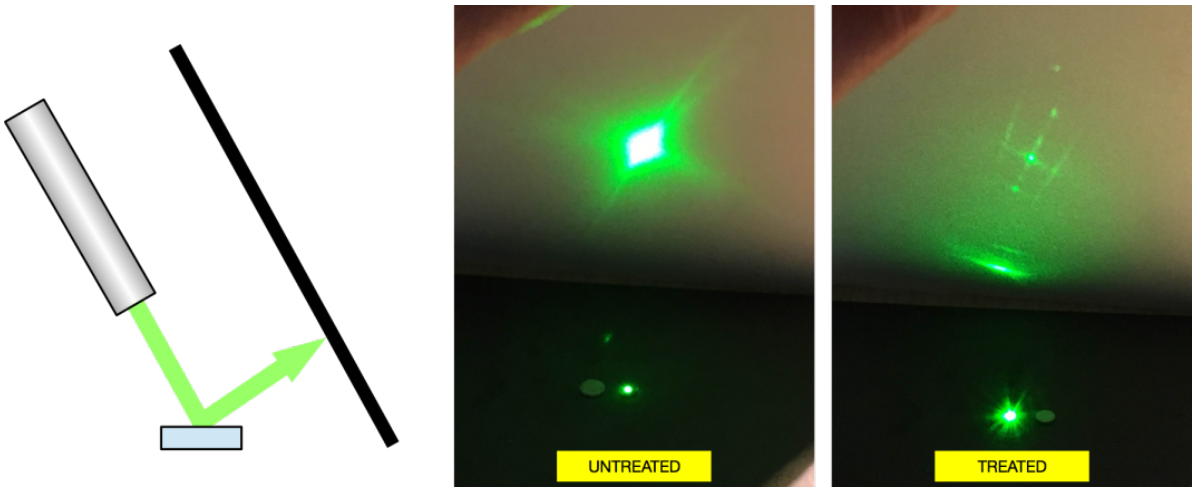

a *b* *c*

Figure 77. Identification of nanostructured surface by reflected light. (a) carton of scheme to check the counterfeit products; (b) demonstration on the clean surface reflection of laser pointer's light from unstructured surface; (c) demonstration on the clean surface reflection laser pointer's light from nanostructured surface (light transforms in peaks of frequencies according to fast Fourier transformation (FFT)).

5.6.3 Summary

This chapter has demonstrated the application of HR-LIPSS to prevent counterfeit devices, materials and use of HR-LIPPS to provide identification of company products. Results so far have been very encouraging and show that HR-LIPSS marking has eye-catching appearance and can also serve as a decoration, with customizable colors. Moreover, real products can be under protection, as nanostructured surface can be identified via a distinct reflection pattern using a cheap and simple source of light, for example laser pointer. HR-LIPPS provide a "finger-print" which is unique to the product, and counterfeit patterns will be challenging to replicate especially with such periodicity.

Chapter 6 HR-LIPSS formation mechanisms on semiconductors

6.1 Background

This research was provided together with prof. Nadezhda Bulgakova, HILASE, Prague, Czech Republic and prof. Vitaly Gruzdev, University of Missouri, USA.

Silicon is one of the most abundant materials which is used in many areas of modern research and technology. A variety of those applications require surface nanopatterning with minimum structure defects. However, the high-quality nanostructuring of large areas of silicon surface at industrially acceptable speed is still a challenge.

One of the frequently cited mechanisms of LIPSS formation is attributed to mild ablation that produces ripples by etching an unperturbed surface at laser fluence very close to ablation threshold [28][44][45][191][37]. Majority of previous publications report the mild-ablation LIPSS on metals, semiconductors, dielectrics, and polymers, but their periodic ripples suffer from irregularity due to multiple branching points where several ripples merge together. Those bifurcations of the LIPSS are characteristic of that approach because the process of ripple formation is distorted by localized perturbations of either laser fluence around the ablation threshold (e.g., due to scattering at surface roughness) or material response. Also, attempts to cover large areas with LIPSS by scanning techniques have faced the fundamental challenge of low speed of surface processing by the ablation at fluence about ablation threshold.

Although the use of femtosecond lasers has brought the possibility to produce finer structures by high spatial frequency LIPSS (or HSFL), [10][45][47] nanostructuring large areas with a high-quality bifurcation-free LIPSS remains a challenge due to a highly-reduced throughput. A relatively low speed of the ablation-LIPSS generation (estimated as ~30 mm^2/min for the irradiation conditions of Ref. [71]) strongly limits the transfer of LIPSS direct-writing methods from laboratories to industry. Recently, a thermochemical mechanism of LIPSS formation was proposed [34] that delivers more regular ripple structure over large areas [34][35][192] by forming oxide layers on the top of original surface [34][192]. De la Cruz *et al*. [87] have

demonstrated an optimized LIPSS generation by utilizing a galvanometric scanner to cover 9-cm^2 area of chromium surface with regular LIPSS in less than 6 minutes. Although a record-high speed of the surface nanostructuring has been reported for the thermochemically produced LIPSS (1.0-1.5 m/s, Ref. [192]), the limited speed of the oxidation processes involved in that method puts several fundamental limitations on the range of applications of this approach. In particular, it is advantageous for metal surfaces while nanostructuring of non-metal materials with the thermochemical LIPSS is not feasible at a high speed.

Here we report production of highly regular LIPSS at laser fluence significantly above the ablation threshold to nanostructure large areas of non-metal surfaces, e.g., silicon (Figure 78) at a rate that significantly exceeds the speed of the thermochemical nanostructuring. The ablation ripples show bifurcation-free structure on large areas of the surface evenly treated at the rate acceptable for industrial use. The specific regime of the LIPSS formation by fast scanning of Si surface with high-power (well above the ablation threshold) laser pulses at a repetition rate of the order of 10^2 kHz calls for a substantial revision of existing concepts of LIPSS formation. For such regime of strong ablation, evolution of a laser-excited surface toward im-

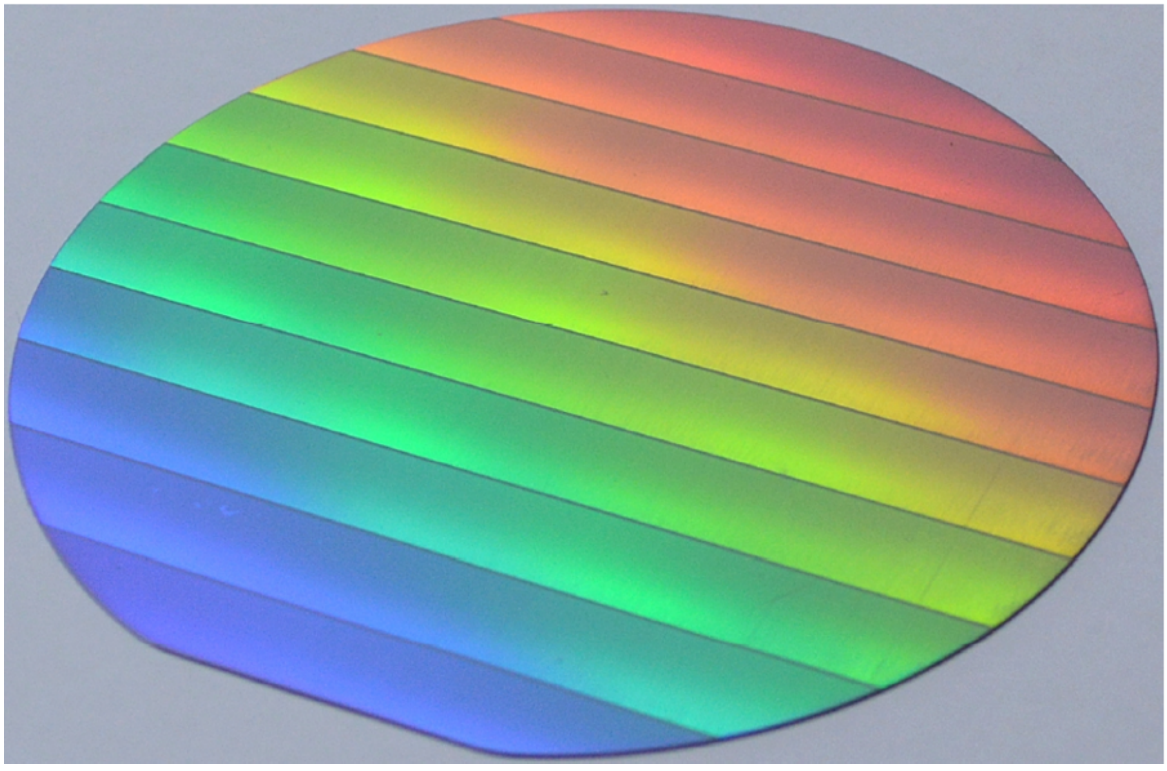

Figure 78. 4-inch diameter Si wafer (the total nanostructured area is 78 cm^2) covered by highly regular LIPSS within 12 minutes. The perfect rainbow colour of the wafer indicates the highly regular structure of the LIPSS.

printing of highly-reproducible ripple structures by single or very few overlapping pulses should involve several competing and complementary processes. Below we analyse conditions of the LIPSS formation at high speed of scanning and propose a plausible scenario of the physical processes responsible for the rapid LIPSS formation.

6.2 Experiment

To generate periodic nanostructures on silicon as a laser source we used commercial femtosecond laser system "Pharos", which in details described in Section 4.1.2. For the scanning approach, 10-mm long lines were formed in Y-direction by moving the laser spot with the galvanoscanner while switching from line to line was done in X-direction by moving the sample with a motorized stage so as to provide approximately 4-μm interline spacing.

For this work, the sample was a single crystalline undoped Si <111> wafer, of 4 Ohm·cm resistivity and thickness of 300 μm. The treated-surface morphology was characterized with both secondary electron microscopy (SEM) imaging and custom modes using a FEI Nova NanoSEM 450 equipped with X-EDS, model Bruker QUANTAX-200. The cross sections of the laser-treated samples and the corresponding images were obtained by means of a FEI Strata 235 M dual beam system. The system combines a Focused Ion Beam (FIB) equipped with a Ga Liquid Metal Ion Source (LMIS) and a SEM column equipped with a Schottky field-emission gun in a single apparatus. A cross section of silicon surfaces were obtained using FIB (E-beam = 30 keV) for milling, setting 1 nA as the ion beam current for milling and 300 pA for the final polishing. The typical speed of linear scanning of the laser spot along the sample surface was about 10^2 cm/s.

6.3 Analysis of results

The SEM images (Figures 79(a) and 79(b)) uncover highly regular and homogeneous linear ripples with no bifurcations over entire treated surface except small areas (~10 μm wide) next to the edges of the treated surface. Nanoparticles observed on the ripples indicate possible back-deposition of the ablation products on the LIPSS. The EDX map clearly shows almost pure silicon in the "valleys", whereas “peaks” of the nanostructures have slightly increased

(approximately by 2%) content of oxygen, while carbon can be attributed to polishing-induced contamination (Figure 79(d)).

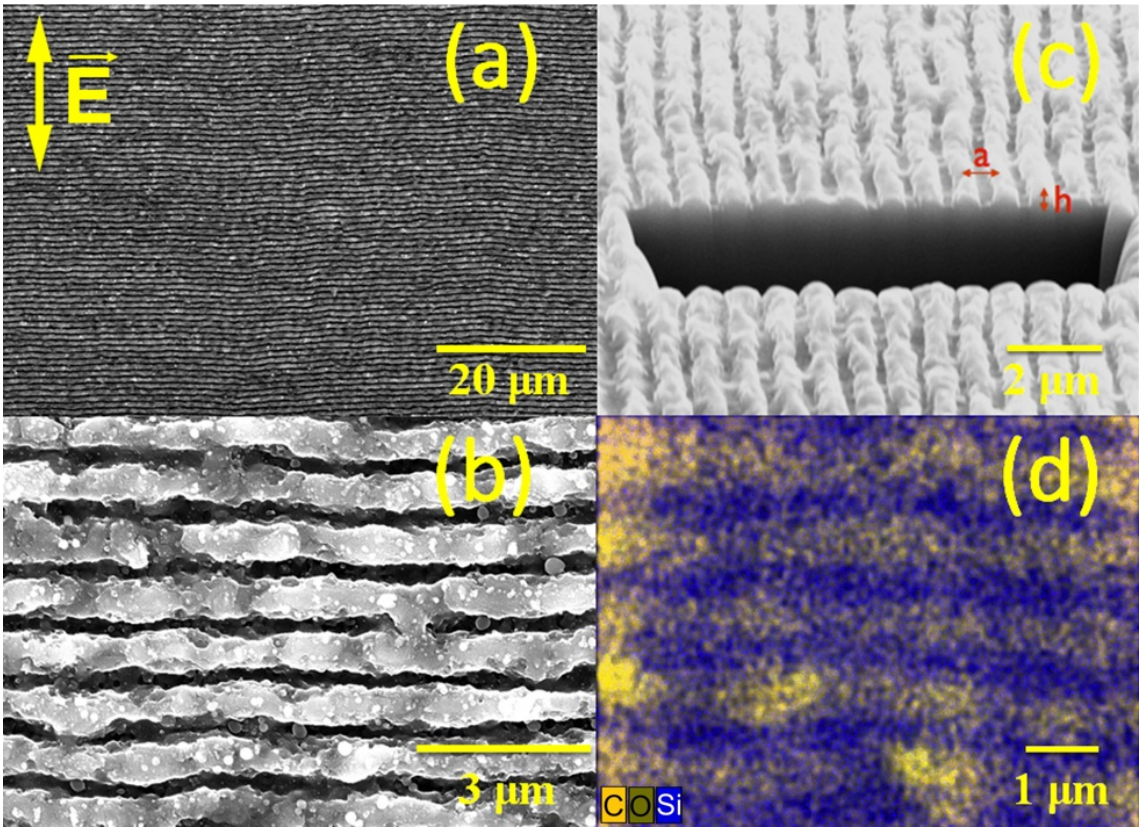

Figure 79. HR-LIPSS produced on Si wafer by scanning laser spot at the velocity of 300 cm/s with average overlapping of two consequent pulses by area of about 50%. (a) SEM image and (b) its magnification; (c) FIB image showing LIPSS cross section view; (d) EDX image confirms presence of oxygen (olive), silicon (blue), and carbon (yellow).

Contrary to the thermochemical LIPSS, [34][71][192] the ablation LIPSS do not show a remarkable increase of oxygen. The FIB images (Figure 79 (c)) reveal highly regular structure of LIPSS cross-section with the depth of the ripples (h) of ~340 nm (from top to bottom) and the period (a) of ~900 nm. Due to the ablation mechanism of the nanostructuring, peaks of the ripples are below the initial surface.

Exceptional reproducibility of LIPSS over large area implies that the LIPSS formation is mainly driven by highly deterministic microscopic processes that are totally controlled by laser parameters rather than by stochastic processes in the laser-excited material. Majority of the reported methods of the LIPSS formation utilize overlapping of many pulses at either sub-ablation-threshold[8] or slightly above the ablation-threshold fluence that result in accumulation of the action of many pulses. Those conditions are favourable for the thermochemical mechanisms of LIPSS formation [34][71][192] or mild-ablation LIPSS. [28][44][45][191][37]. By

contrast, the high-speed nanostructuring reported here considers no more than 3-4 partially overlapping pulses at high fluence that implies a strong ablation regime. Based on the presented experimental data, we propose the following scenario of the high-speed HR-LIPSS formation on silicon.

Interference of incident laser beam with a scattered surface wave (Figures 80a, i) leads to a periodic distribution of absorbed energy of light across a laser spot on the surface in accord with the Sipe-Drude mechanism [15][28][193]. One of dominating contributions to the absorption is provided by electron excitation from valence to conduction band (Figure 80b) paralleled with heating of conduction electrons [193]. Energy of a single laser photon (about 1.2 eV) supports several channels of the inter-band electron transitions: direct three-photon, indirect one-photon, and indirect two-photon (Figure 80b). The indirect processes involve electron-phonon collisions with characteristic frequency about 10^{12} - 10^{13} 1/s [194]. Therefore, rates of those processes make a negligible contribution to the total process of electron excitation within a single laser pulse at the specific fluence. The direct inter-band three-photon transitions involve the states near the Γ-point of the Brillouin zone (Figure 80b): (band gap E_0'=3.28 – 3.5 eV); $\Gamma_8^+ \rightarrow \Gamma_8^-$ (band gap $E_0'+\Delta_0'$=3.29 – 3.57 eV); and $\Gamma_7^+ \rightarrow \Gamma_8^-$ (band gap $E_0'+\Delta_0'+\Delta_0$=3.36 eV). Since the Keldysh adiabatic parameter [195] is about 0.9 for the direct transitions in silicon, the rates of these transitions are evaluated from the Keldysh formula [195] with proper values of direct energy gaps and effective masses [194]. The total rate of the three-photon transitions is in the range of 10^{18} - 10^{19} fs^{-1} cm^{-3} at intensity 3.5 TW/cm^2 utilized in the experiments.

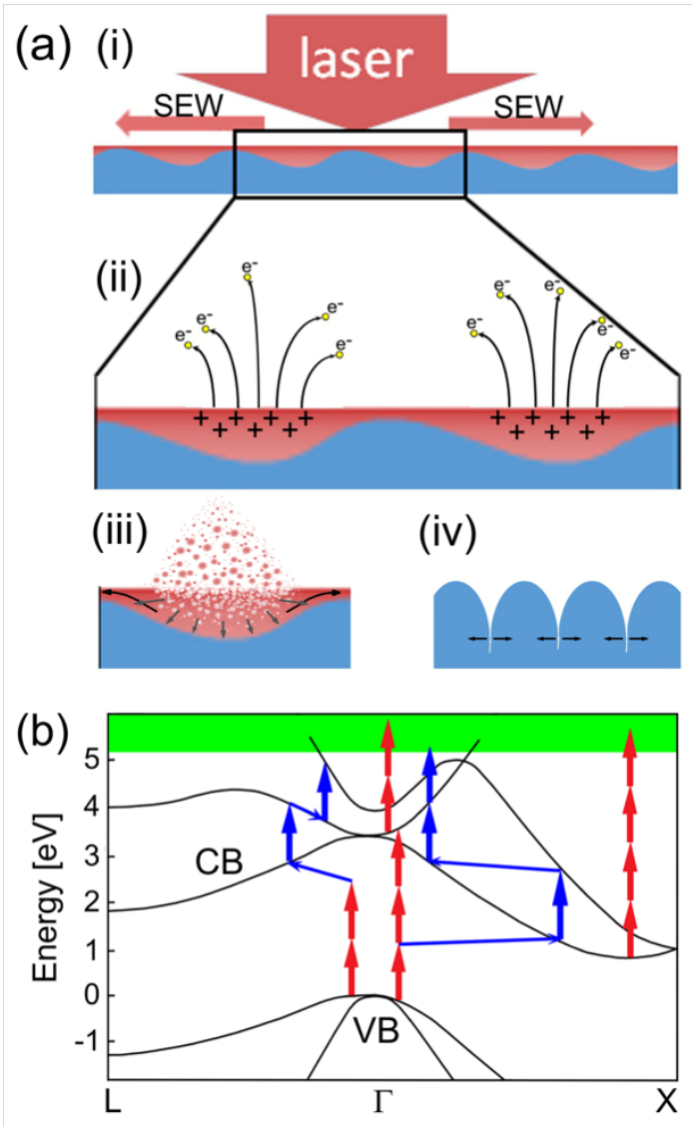

Figure 80. (a) Schematics of stages of LIPSS formation on silicon surface in the developed ablation regime. (i) Laser pulse coupling with a surface with a certain roughness experiences scattering. The scattered electromagnetic wave (SEW) interferes with the incident laser wave, thus resulting in periodic absorption of laser energy. (ii) In the regions of enhanced absorption, silicon bonds are softened due to both photoionization and electron photoemission. This can yield in some non-thermal ablation already from solid phase. (iii) Main ablation occurs after electron-lattice thermalization via the phase explosion mechanism. Preferable ablation from hotter periodic regions leads to displacement of melt toward the colder sites, thus promoting formation of periodic surface relief. (iv) After solidification of non-ablated melt remains, cooling of the solid phase can result in formation of cracks along the LIPSS tranches, thus deepening the periodic structure relief deepening the periodic structure relief. (b) A sketch of laser-induced electron excitation. Red arrows show multiphoton excitation and photoemission. Blue arrows correspond to thermal excitation pathways and thermionic emission. The vacuum states of photo-emitted electrons are shown by green area. Involved symmetry points and energy bands (CB for conduction band; VB for valence bands, and VS for vacuum states) are marked correspondingly.

Therefore, the three-photon transitions make a dominating contribution to the nonlinear energy absorption in silicon energy gaps and effective masses [194]. The total rate of the three-photon transitions is in the range of 10^{18} - 10^{19} fs^{-1} cm^{-3} at intensity 3.5 TW/cm^2 utilized in the experiments. Therefore, the three-photon transitions make a dominating contribution to the nonlinear energy absorption in silicon and increase of conduction-electron density at the beginning stage. Due to strong nonlinear dependence on laser intensity, the three-photon absorption is more favourable for stronger confinement and localization of energy deposition from each individual laser pulse and makes the process of electron-hole plasma formation substantially deterministic and efficient at the local sites of the enhanced absorption as shown in Figure 80a, (ii).

Increase of conduction-electron density due to the nonlinear absorption and parallel heating of the electron-hole plasma stimulates photoemission (J_{MP}) and thermionic emission (J_{TH}) of electrons (tunnelling mechanism is banned by the parallel alignment of the electric field and the surface). [201] Their rates are given by the following equations: [196]

$$J_{MP} = \sigma_N I^N; \quad N = \left\langle \frac{W}{\hbar\omega} + 1 \right\rangle, \quad \text{and} \quad J_{TH} = \frac{4\pi m k^2 e}{h^3} T^2 \exp\left[-W/kT\right]$$

where σ_N – the coefficient of multiphoton photoemission evaluated from the Keldysh formula [196] for interband transition between two parabolic bands; N is the minimum number of laser photons required to bridge the electron affinity W; ω is the laser frequency; h and $\hbar$ are the Plank and Dirac constants; k is the Boltzmann constant; T and m are the electron temperature and mass respectively. The parametric dependence of the emission rates suggests that the photoemission dominates at the early stage of the laser-surface interaction. It involves the conduction electrons of the X-valley (the corresponding electron affinity is 4.05 eV) [194] and the non-equilibrium electrons appearing around the Γ-point of the conduction band due to the direct interband excitation (the corresponding energy gap W is about 1.89 eV). Electron transport from the Γ-point states to the X-valley states requires significant variations of electron momentum that can be provided only by inter-valley phonons (both optical and acoustic).[26] Low electron-phonon collision rate (10^{11} – 10^{12} 1/s) [194] suggests that the inter-valley electron transport can be neglected compared to significantly faster processes of the nonlinear absorption and electron emission. Therefore, the contributions to photoemission are independently made by 4-photon and 2-photon excitations of the two groups of conduction electrons. The thermionic emission is delayed and dominates at the tail part of laser pulse

because it requires heating of the conduction electrons by 2-4 eV via electron-photon-phonon collisions. For the given laser parameters, the total emission yield from the two mechanisms is about 10^{19} 1/cm^3 per pulse that supports formation of sub-micrometer domains of silicon surface with a reduced electron density and a transient localized positive charge [193] An interference-induced modulation of the electromagnetic field intensity within the laser spot [103] should inevitably lead to a modulation of the positive-charge density across the surface. The partial positive charge may not be high enough to eject ions, [193] but being combined with the high rate of the interband electron excitation, it can support a periodically-modulated bond softening that facilitates ablation from an electrostatically unstable surface sites. [197] Followed by non-thermal ablation from solid phase, [198] the electrostatic instability of the silicon surface can be the main mechanism of LIPSS formation at laser fluence close to the ablation threshold. [199] Note that thermionic emission does not require direct action of electric field and can continue contributing after the laser-pulse termination, [193] further facilitating surface instability.

For the specified above irradiation regimes, massive ablation should occur at picosecond timescale after electron-lattice thermalization and melting of a surface layer. As shown in Ref. [103], a periodic temperature modulation on molten silicon surface, if generated, can preserve for as long time as ~100 ps. At ultrashort laser pulses, ablation of molten phase occurs mainly through the phase explosion mechanism [58] with creation of periodic surface relief (Figure 80a, (iii)). Note that, in silicon whose melting proceeds with material compaction by ~9%, mechanical expulsion of melt due to lateral stress generation [200] cannot noticeably contribute to ablation because the relatively low expansion coefficients of solid and liquid silicon do not sufficiently counterbalance compaction upon melting. However, a recoil pressure of the ablation plume can push remaining melt to the colder (lower absorption) sites as shown schematically by arrows in Figure 80a, (iii), thus helping to form a more pronounced periodic relief.

It has been proven that crack formation is one of fundamental constituents of laser-induced nanograting formation inside fused silica and a number of other transparent crystals and glasses [201]. Similarly, cracking can play an important role in deepening of the LIPSS and making them more pronounced after the strong ablation phase. Upon solidification and further cooling, formation of cracks can be expected along the formed tranches due to tensile stress applied to "weak", laser-scribes sites (Figure 80a, (iv)). The process of crack formation can be facilitated

by rapid solidification of melt remains which occurs far from thermodynamic equilibrium [202][203] For the most of materials which experience compaction upon solidification, the rapid solidification can lead to the formation of cavitation voids and bubbles in the LIPSS valleys due to rapid drop in pressure. For silicon whose behaviour upon solidification is opposite, the pressure in the LIPSS valleys can swiftly increase, thus leading to dislocations which in their turn will facilitate crack formation. Subsequent laser pulses are better absorbed in the LIPSS valleys, thus exacerbating the process of crack-assisted LIPSS trenches' deepening. However, non-equilibrium thermodynamics aspects of LIPSS formation call for further studies.

The incident laser fluence is, at the first glance, incompartible with LIPSS formation. However, LIPSS formation is driven by *effective absorbed fluence* that is significantly affected by increase of silicon reflectivity produced by electron-hole plasma density generated during the laser pulse action. For femtosecond IR laser pulses, the reflection coefficient of silicon can increase up to 70-80% at laser fluences four times above the melting threshold. [204] Hence, the effective absorbed fluence can be as low as ~0.5 J/cm^2 in the irradiation spot center that is comparable to that of single IR laser pulses creating ripples on steel [205] whose reflectivity is ~60-65% at wavelengths ~1 μm. However, according to simulations which are under progress, such level of absorbed fluence brings the external layer of material to a supercritical fluid state[39] that culminates in strong ablation of several dozens of nanometers. Also note that, according to the heat flow estimations for the repetition rate exploited in this work, heat accumulation has no pronounced effect. Those effects can become important for silicon at repetition rates of several MHz and higher and/or at reduced scanning rate favorable for increase of the number of laser pulses coupling to the same irradiation spot.

6.4 Summary

In summary, the exceptionally regular LIPSS have been produced on large area of silicon surface by infrared femtosecond laser pulses with sub-MHz repetition rate at extremely high processing speed. Covering 1 cm^2 by HR-LIPSS requires less than a minute that makes this technique appropriate for industrial applications. Theoretical analysis of the physical processes involved into formation of the HR-LIPSS suggests that the electrostatically-assisted bond softening may noticeably contribute to initializing the ablation process.

Chapter 7 High-speed HR-LIPSS on semiconductors: applications

7.1 Self-assembling of gold nanoparticles on HR-LIPSS for sensors and biosensors

7.1.1 Background

The research was carried out with prof. M. Dusheyko (Kyiv Polytechnic Institute), prof. S. Mamykin (NASU) and prof. T. Borodinova (NASU). All universities are from Ukraine.

Nanoscale metal structures (e.g., dots and nanowires) assembled into one-dimensional (1D) or two-dimensional (2D) periodic arrangements similar to diffraction gratings exhibit anomalous optical extinction for visible light. This property is associated with the unique ability of regular periodic configurations to support specific surface waves [206][207]. Excitation of surface plasmon polaritons (SPP) can be achieved in continuous metal films as well as in closely packed metal nanoparticles deposited on the diffraction grating while excitation of surface plasmon (SP) can be seen in individual metal nanoparticles [206][207]. Sensors based on SP and SPP are widely used to detect small changes in refractive indices of the environment induced by reactions in bio- and chemical sensor systems [208]. For some geometry, simultaneous excitation of SP and SPP can enhance each other thus improving the resulting sensitivity [209]. Fabrication of diffraction gratings is usually a quite complicated and time-consuming step which includes lithography and increases the final cost of sensors. To improve manufacturing technology different methods can be used, for example, microcontact printing or selective etching of semiconductor substrate illuminated by a pattern created by interfering laser beams.

We propose to use highly-regular laser-induced periodic surface structures (HR-LIPSS) produced by direct ablation of semiconductor substrate by femtosecond laser. HR-LIPSS result from local superheating followed by ablation and provide low-cost single-step

technique which allows to cover a large area surface of virtually any material by highly periodic nanostructures.

7.1.2 Experiment

Here we report the creation of the photonic structure on Si substrates by HR-LIPSS. The structures presented below (Fig. 81) were manufactured in 3 steps and combined a p-n junction, HR-LIPSS, and gold nanoparticles deposited on peaks of LIPSS. First, a shallow p-n junction was formed in a p-type Si (111) wafer by diffusion of phosphorus followed by removal of oxide layer from the polished side of the wafer (Fig. 81a). The depth of p-n junction was about 100 nm and sheet resistivity was 90 Ω /sq.

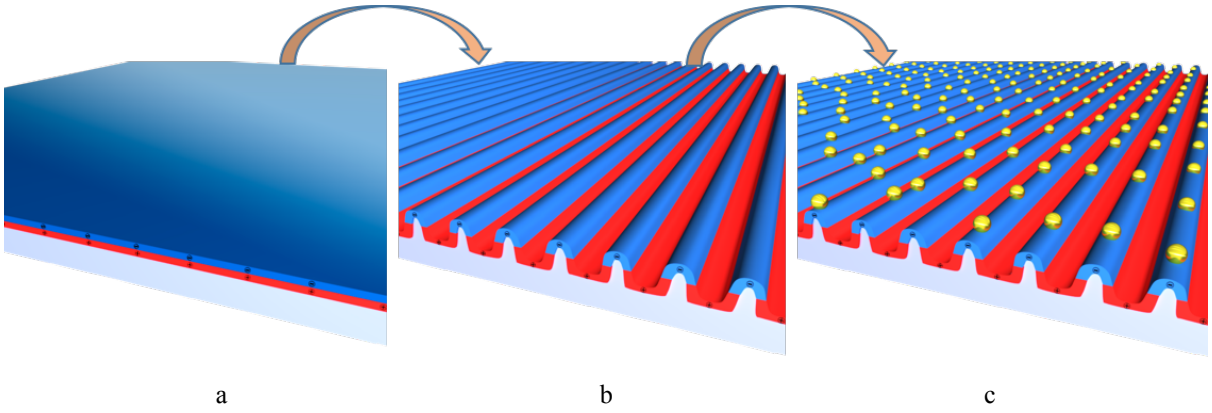

Figure 81. Three steps for fabrications of photonic platform: (a) formation of p-n junction, (b) generation HR-LIPSS on formed p-n junction and (c) deposition of gold nanoparticles on the periodic structures.

Second, HR-LIPSS were etched by femtosecond pulses on the silicon substrate (Fig. 81b) to the depth small enough to avoid destruction of the p-n junction. To form periodic nanostructures as a laser source we used commercial femtosecond laser system "Pharos", which in details described in Section 4.1.2. The laser beam was focused on Si surface and scanned with galvo-scanner to obtain 1 cm^2 area. In order to obtain larger areas motorized translation stage was moved under galvo-scanner. In our work, the structured area was up to 4 inches. The macroscopic image of structured by HR-LIPSS surface is presented in Fig. 82. Third, gold nanoparticles (NP) on surface of Si treated by HR-LIPSS preformed (Fig. 81c) has been realized by 3 methods. According to a *method I* formation of NP Au occurs at room temperature in the water medium where a reducer of ions $AuCl^{4-}$ is $NaBH_4$, and the stabilizer of gold NP is trisodium citrate. The *method II* allows to receive triangular and hexagonal nanoprisms of gold in water

solution $HAuCl_4$ and polysaccharides of microalgae *Chlorella vulgaris* $LARG^{-3}$ at temperature 40 ºC and illumination 1000 lux. In this process polysaccharides are used as a reducing agent

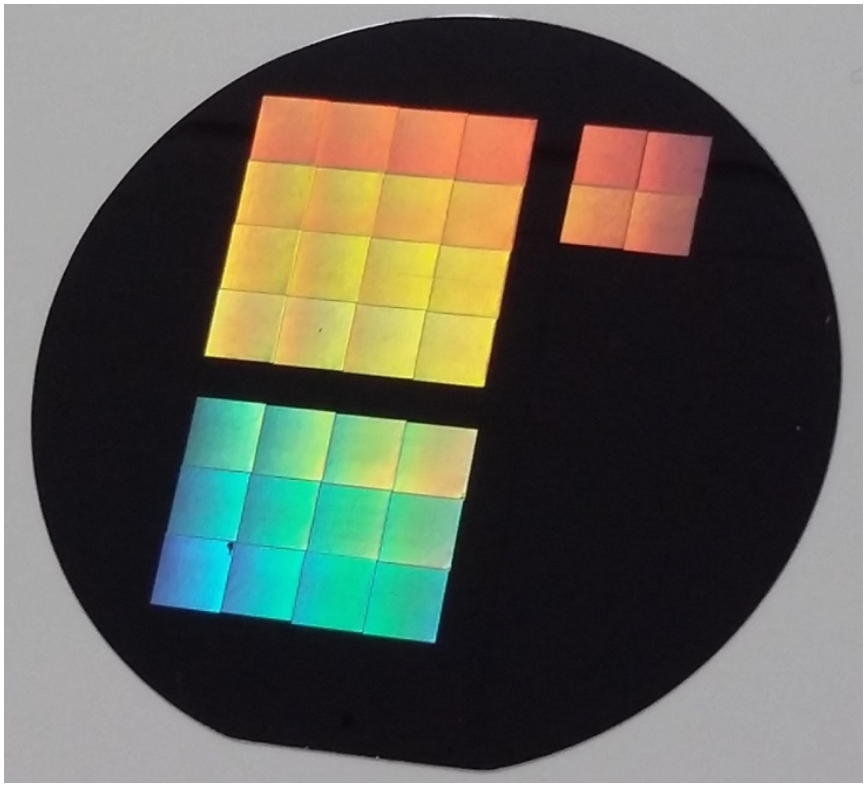

Figure 82. Macrophoto of laser-induced periodic surface structures (LIPSS) of Silicon.

and the stabilizer. The *method III* assumes formation anisotropic nanoparticles of gold in a mixture of alcohols (ethanol, ethylene glycol, glycerine), containing $HAuCl_4$ and the surfactant polyvinylpyrrolidone, at temperature 80 ºC.

7.1.3 Analysis of results

The Fig. 83a displays SEM images of HR-LIPSS. The period of the structures is found to be around 800 nm. Figures 83b-f reveal three different types of self-assembled gold nanoparticles on LIPSS nanotextured Si surface. As present on fig. 83, a size and a shape of nanoparticles depends from precursor, reducer and stabilizer. In the first method, as precursor was $AuCl_4$, reducer of ions $AuCl_4$ - $NaBH_4$, while stabilizer of gold NP - trisodium citrate. As a consequence, gold NP become granular-like with the size of NP equal to ~1 μm (Fig. 83c). In case, when precursor was $HAuCl_4$, but stabilizer and reducer were polysaccharides of microalgae *Chlorella vulgaris* LARG-3, shapes of nanoparticles tunes from quasitriangular to hexagonal with size up to 4 μm (Figs. 83d, e). Finally, in the third method, as precursor served

$HAuCl_4$, while stabilize was polyvinylpyrrolidone. In the results, the shapes of the NP were spherical and size up to 1 μm (Fig. 83f).

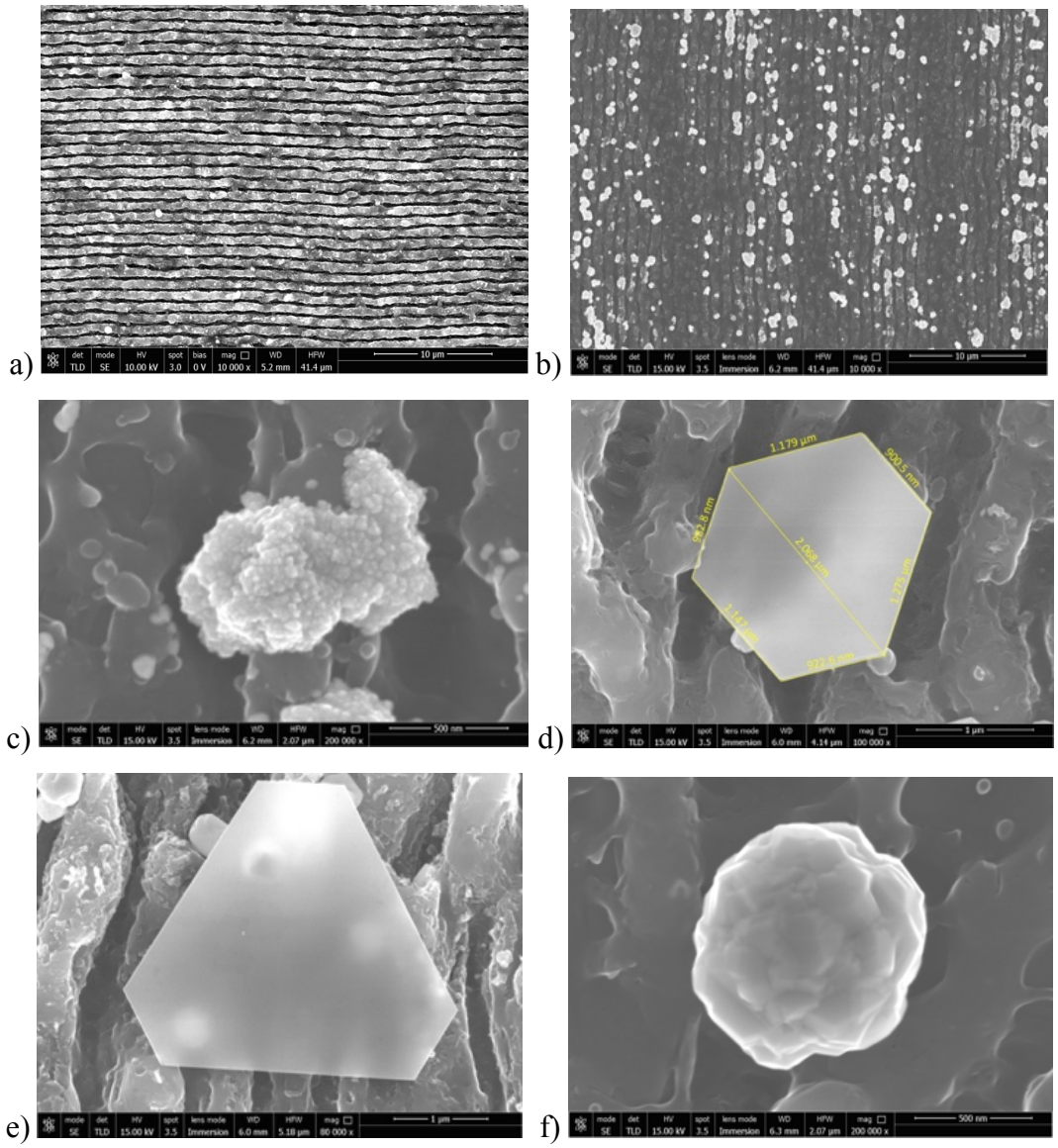

Figure 83. Highly-regular laser-induced periodic surface structures on Si: pure nanostructures (a) and covered by gold nanoparticles: b, c - method I, d, e - method II, f - method III.

In Tab. 12 presents calculated statistical parameters for the obtaining samples - effective thickness of Au, most probable size of spherical Au particles, average size of spherical particles.

Table 12. Au nanoparticles size distribution and nanoparticles density (per μm^2).

Sample	Effective thickness of Au, nm	Most probable size of spherical Au particles, nm	Average size of spherical particles, nm	Number of particles per μm^2
I	128	404	418	10.5
II	2.47	340	352	0.079
III	4.03	72	90	5.5

On Fig. 84 outlines results of depending size of nanoparticles from their numbers per μm^2

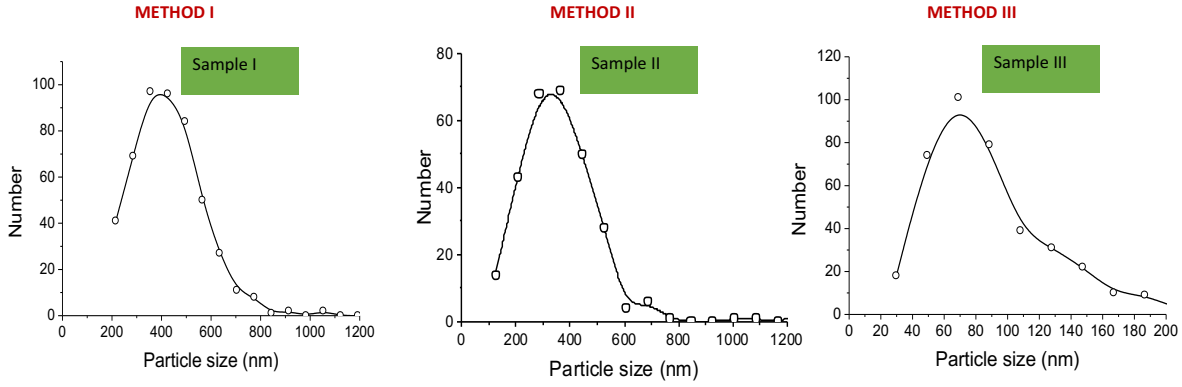

a b c

Figure 84. Depends of size from density of nanoparticles of Au (per μm^2).

In order to determine the period and the depth of nano-gratings the light diffraction was measured in p-polarization from sample, placed at 45° incident angle (Fig. 85).

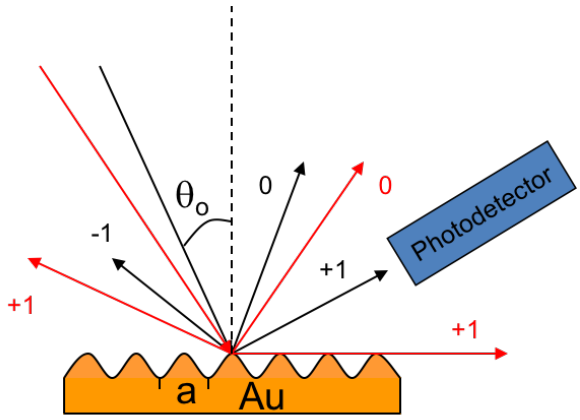

Figure 85. Scheme of reflectivity measurements for mirror and diffracted beams. The red beams show the case when surface plasmon resonance occur, while the black ones display usual diffraction of light. In the first case, one from diffracted beams (+1) slides on the surface and exciting SPPR.

The wavelength of incident light was 0.6328 µm. The angular distance between the mirror and "-1" order determines period of the ratio of intensities – the deep, in assuming of sinusoidal lattice. That, that it takes no absolute values, but related – allow in some extent compensate for the fact that the lattice not purely silicic but with the inclusion of gold. As the model was considered the structure of Au/Si with homogeneous layer 20 nm. If the real average thickness is lower, hence the deep will be lower. The calculation was carried out according with [210], the solution of Maxwell equations in curvilinear coordinates. The example of measurements of diffraction present in Fig. 86. Results reveal in Table 13.

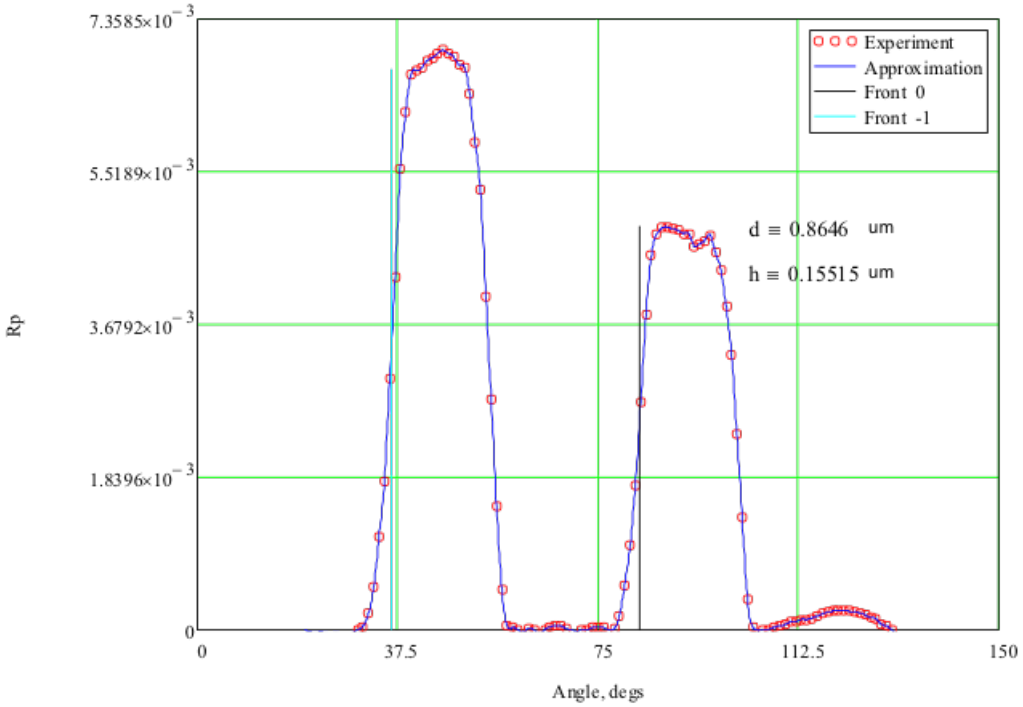

Figure 86. Measurements of the intensity both diffracted ("-1" order peak near 37.5°) and mirror-reflected (peak 77°) light from the sample 1Tl, located at 45°, the wavelength of the incident light 0.6328 µm. Rp - reflectivity of p-polarized light. Retrieved period - 0,865 mm, depth - 0.155 µm.

Table 13. Parameters of diffracted gratings on samples.

Name of sample	Periods, µm	Depth, µm
I	0.865	0.155
II	0.898	0.157
III	0.873	0.224

The excitation of SPP results in decreasing of P-polarized light reflectance and looks as a minimum in corresponding spectral or angular dependencies and was observed on all samples

(Figures 87-89). Spectral and angular position of the SPP excitation is obtained by equating the components of SPP wave vector and the component of wave vector of the incident radiation that is parallel to the metal/non-metal interface [211]:

$$k\, n\, sin\theta + mG = k_{pp} \tag{8}$$

where k = 2π/(λ/n) - wave vector of the incident radiation with a wavelength λ in a vacuum; θ - angle of incidence; m - an integer (m ≠ 0) and denotes the diffraction order; G = 2π/a - reciprocal vector of LIPSS grating with period a, ε = n^2 - permittivity and refractive index of non-metal environment; and k_{pp} - wave vector of SPP. To estimate approximately the magnitude of SPP wave vector the expression obtained for a flat interface of two semi-infinite media can be applied:

$$k_{pp} = \pm (2\pi/(\lambda/n))\, [\varepsilon_{Me}\varepsilon/(\varepsilon_{Me}+\varepsilon)]^{1/2} \tag{9}$$

where k_{PP} has "+" sign at $m > 0$ and "–" at $m < 0$. Here, $\varepsilon_{Me} = \varepsilon'_{Me} + i\varepsilon''_{Me} = (n + ik)^2$ - complex permittivity of the given metal at the laser wavelength.

The light reflectance spectra are shown on Fig. 87 for P- and S- polarized light.

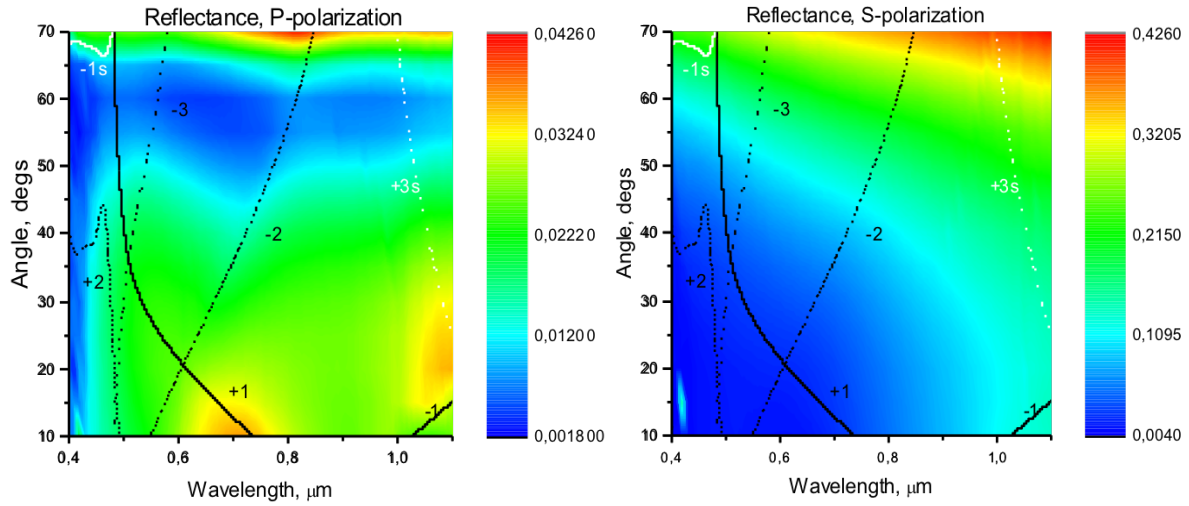

Figure 87. Spectral-angular dependence of the reflectance of light in the p- (v) and s- (b) polarization of the sample 2 with a period of 867 nm, which imposed plasmon dispersion relations of sur-face-polariton modes on the interface of the air/gold (1, 2, 3, 1 ', 2', 3 '), gold/substrate (1s, 1s', 2s, 2s', 3s, 3s') for m = + 1 (1, 1s), m = + 2 (2, 2s), m = + 3 (3, 3s), m = -1 (1 ', 1s'), m = -2 (2 ', 2s') and m = -3 (3 ', 3s') order diffraction light.

The light reflectance spectra are shown on Figures 87, 88, 89 for P- and S- polarized light. The most intensively excitation of SPP waves was observed for m= ±1 (+1, -1 ') at the gold/air interface because efficiency of their excitation is the highest for angles of incidence close to

normal at wavelengths varying from 0.8 to 1 μm, where the ratio of real to imaginary part reaches a maximum for gold.

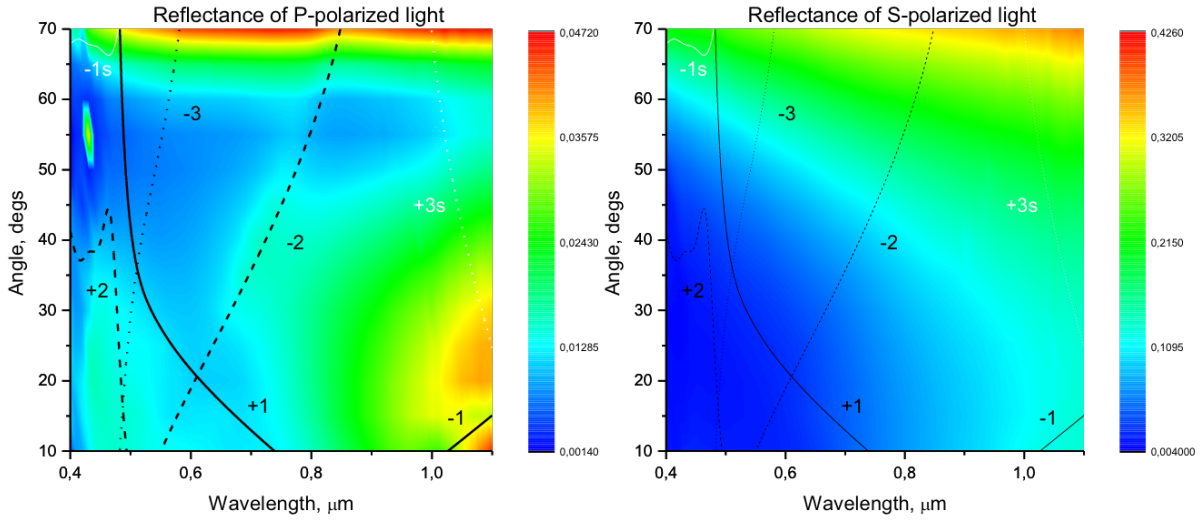

a b

Figure 88. Spectral-angular dependence of the reflectance of light in the p- (a) and b- (b) the polarization pattern of 3 wxith period of 898 nm, which imposed plasmon dispersion relations of sur-face-polariton modes on the interface of the air / gold (1, 2, 3, 1', 2', 3 '), gold / substrate (1s, 1s', 2s, 2s ', 3s, 3s') for m = + 1 (1, 1s), m = + 2 (2, 2s), m = + 3 (3, 3s), m = -1 (1 ', 1s'), m = -2 (2 ', 2s') and m = -3 (3 ', 3s') order diffraction light.

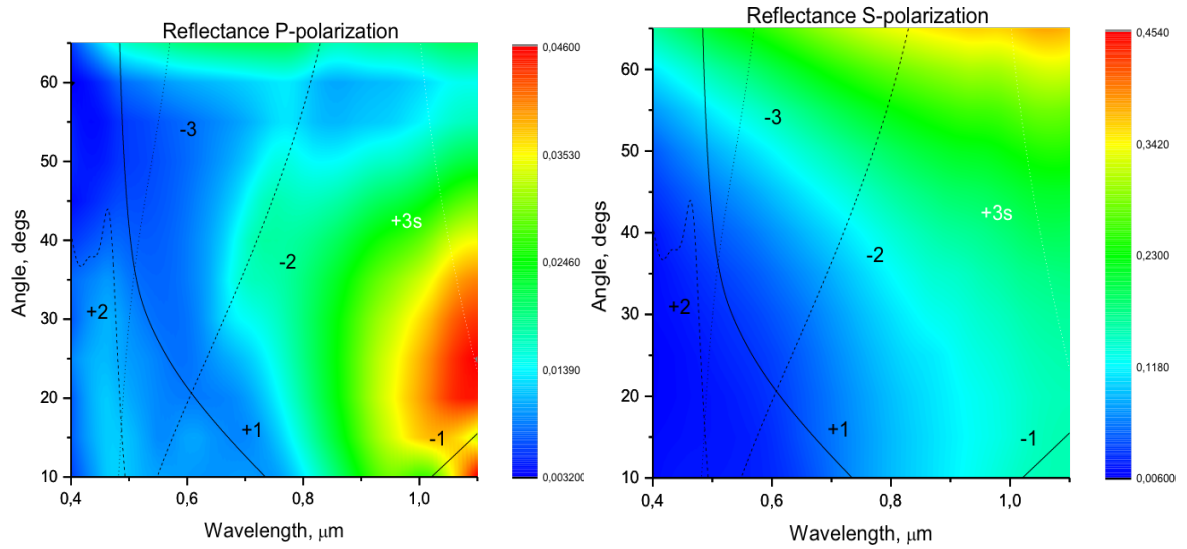

a b

Figure 89. Spectral-angular dependence of the reflectance of light in the p- (a) and b- (b) polarization of the sample 3 with a period of 873 nm, which imposed plasmon dispersion relations of sur-face-polariton modes on the interface of the air / gold (1, 2, 3, 11 ', 2', 3 '), gold / substrate (1s, 1s', 2s, 2s ', 3s, 3s') for m = + 1 (1, 1s), m = + 2 (2, 2s), m = + 3 (3, 3s), m = -1 (1 ', 1s'), m = -2 (2 ', 2s') and m = -3 (3 ', 3s') order diffraction light.

A proof of SPP excitation is given by absence of polarized light reflectance minimum for S-polarized light (Fig.87b) at those wavelengths and angles of incidence where it is observed for P-polarized light (Fig.87a). SPP dispersion curves are next to the valleys on the map of reflectance (Fig. 87a), and this fact is also considered as a proof of the SPP excitation for these samples.

The excitation of SPP on sample I (Fig. 87) is most evident in comparison to samples II and III. This is well correlated with number of NP per μm^2 (Table 12), as the number of NP for sample 1 is much higher with respect to samples II and III.

The main feature of the excitation of local surface plasmons (LSP) in periodic array of Au nanoparticles, placed on the peaks of diffraction grating is weak dependence of the spectral position from the angle of the incident light [212]. This is due to the angle dependence from the width of the projection of nanowire in a plane of wave vector of light k_x. In order to estimate the upper boundary of the high-frequency spectral position of LSP, it's possible to use the formula for the polarization spherical nanoparticles in dielectric environment [206]:

$$\alpha = (\varepsilon \text{ Me}/ \varepsilon -1)/(\varepsilon \text{ Me}/ \varepsilon +2),$$

which for the case of the nanoparticle of gold in vacuum reaches maximum around $\lambda \approx 0.5$ μm. With increasing of nanoparticles size (with of nan-wires), the dielectric constant environment resonant wavelength can significantly increase [211] and reach of the infrared region of spectrum. It could increase if in around present metallic nanoparticles due to the interaction between them. For these samples, such stripes (wide minimum) is in reflection around 0.5-0.8 μm in P-polarized light ($\vec{E}$ of light directed perpendicularly to the nanowires, because the width of cross-section is the smallest one), especially for samples 2 (Fig. 88a), 3 (Fig. 89a). In S-polarization, where $\vec{E}$ directed along the nanoripples and their width of the cross-section in this direction is maximum, LSP being observed in the infrared spectrum.

7.1.4 Summary

In the examined samples the excitation of SPPW and LSP resulting in a significant decrease in light reflection, depending on the angle of incidence and wavelength of light and consistent to dispersion related between SPPW and LSP. The geometrical parameters of nanostructures are still not optimal and there are a lot of opportunities to improve them; hence this luck may further reduce reflectivity of light. The highest intensity of plasmon-polariton resonance was obtained for the structures with the highest density of Au particles: 10,5 per μm^2 (method 1). HR-LIPSS technology is low cost and highly-productive for fabrication of high-quality periodic structures on Si substrate, and with following Au nanoparticles self-assembling on the top of grating grooves support excitation of the surface plasmon resonance. Combination of two types of surface excitations – plasmon resonances of individual gold nanoparticles and surface plasmon-polariton waves of overall periodic structure – opens a perspective for fabrication of unique and cheap plasmonic sensors.

7.2 HR-LIPSS for photovoltaics

7.2.1 Background

This work was performed thanks to collaboration with research group of prof. Omer Ilday (Bilkent University, Turkey).

Nowadays Si-based solar cell (SC) remains the most diffused photovoltaic device in the world due to the low cost of material, relatively simple and industrially acceptable technology. In spite of significant progress on increasing efficiency of these devices (the best laboratory samples demonstrated efficiency as much as 43.5%), for most industrially manufactured SC`s, the efficiency remains in the range of 10-18% [213]. One of the promising ways to minimize thermodynamic losses for high efficiency Si-based photovoltaic device is the photonic optimization of the device surfaces to trapping light into the device, due to light interaction with micro- nano-structures on the surface, thus increasing the density of photon interacting with active material. However, the most part of proposed methods for Si surface modification do not match industrial production requirements, such as fast manufacturing, environmental issues, and low cost per watt for final devices.

HR-LIPSS, which is a low cost, maskless and single step technique, allows a large area surface of many materials to be covered by a highly periodic structure. In this section, we report the creation of the photonic structure on Si-based SC by using HR-LIPSS.

7.2.2 Experiment

As a laser source, we used a home-made 1 MHz femtosecond laser system (Section 5.1.2), which can generate up to 1 μJ of pulse energy with ~120 fs of pulse duration. The laser beam was focused on Si surface and raster scanned with galvoscanner to obtain an area of 0.5x0.5 cm^2. In order to set how laser parameters effect regularity of HR-LIPSS, both the step between the scanning lines d and scanning velocity v_s were tuned. So, d was changed from 3 μm to 4.5 μm while v_s from 1500 to 2300 mm/s. After setting the optimal laser parameters, much larger areas were obtained by translating the sample with the translation stage under galvo-scanner. In our work, the structured area was 4x4 cm^2. The macroscopic image of structured surface is presented in Fig. 78.

The sample was a single crystalline p-doped Si wafer, with 4 Ω·cm resistivity and thickness equal to 300 µm. Both untreated and LIPSS treated SC`s were produced on the same Si wafer under the same production conditions. The p-n junction was formed by phosphorous diffusion in the doping furnace. The final step was back and front surface metallization in order to form electrical contacts. The SC`s were produced on the same Si wafer for both structured and unstructured areas under the same production conditions.

7.2.3 Analysis of results

Analysis of LIPSS morphology through the SEM show the effect of scanning parameters on their regularity. As shown in Table 11, with a speed of 1500 mm/s, the number of laser impulses on one spot are around 15 that create an accumulation effect with the presence of bifurcations points within the melting process. On the other hand, if the scanning velocity is 2100 mm/s and higher, no LIPSS are observed on the surface. So, the optimal scanning velocity for generation LIPSS is from 1700 to 1900 mm/s. The step between the scanning lines also critically influence the generation of LIPSS. When overlapping equals 50 % (scanning step 3 µm), HR-LIPSS can be produced. At the scanning steps, 3.5 and 4 µm some hierarchical structures are formed (mix of nano- and micro- structures. Scanning parameters are displayed in Tab. 14.

Table 14. Optimal scanning parameters for generation HR-LIPSS.

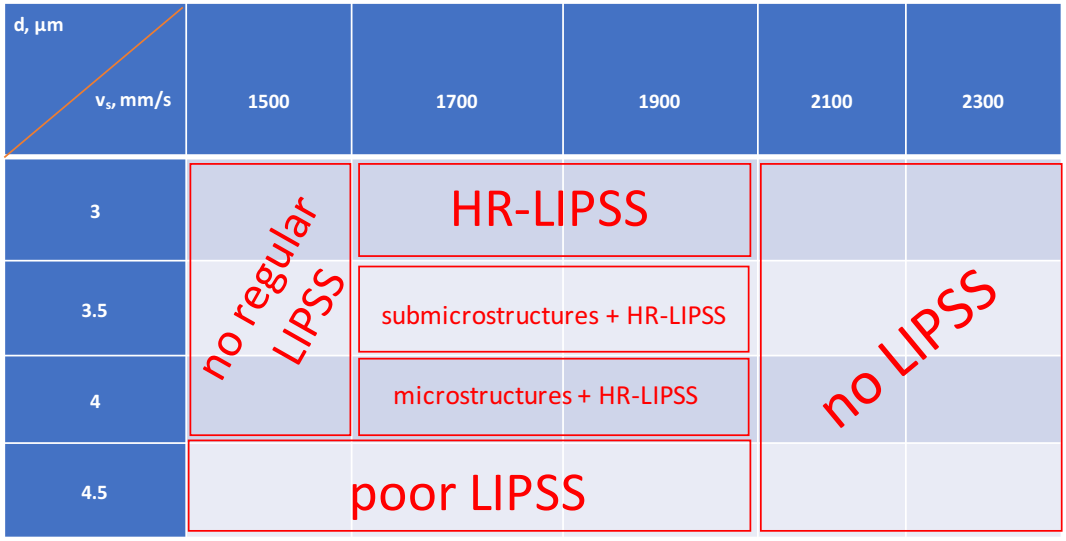

Table 15 shows two columns: HR-LIPSS and HR-LIPSS after oxidation etching at the best scanning parameters. From SEM analysis, the period of the nanostructures is found to be around 800 nm.

Table 15. SEM of HR-LIPSS and HR-LIPSS after chemical etching with the best optimal scanning parameters.

	HR-LIPSS	HR-LIPSS after chemical etching
h=3 μm, v_s=1,7 m/s,	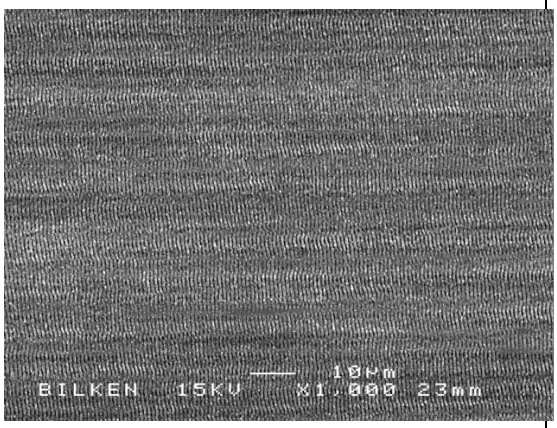	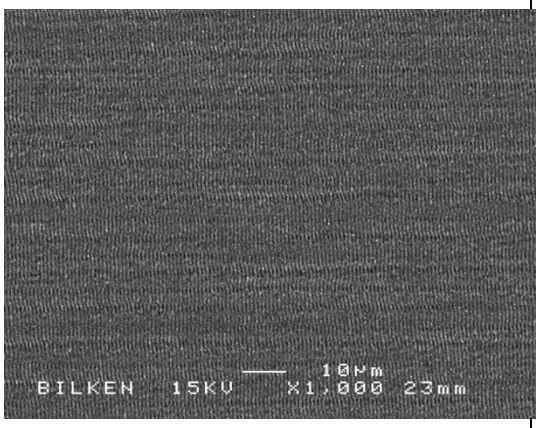
h=3,5 μm, v_s=1,7 m/s,	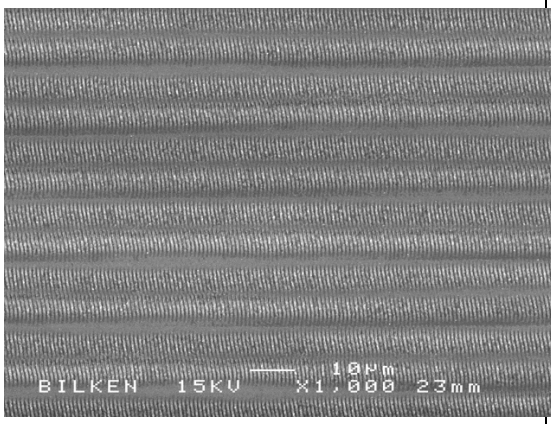	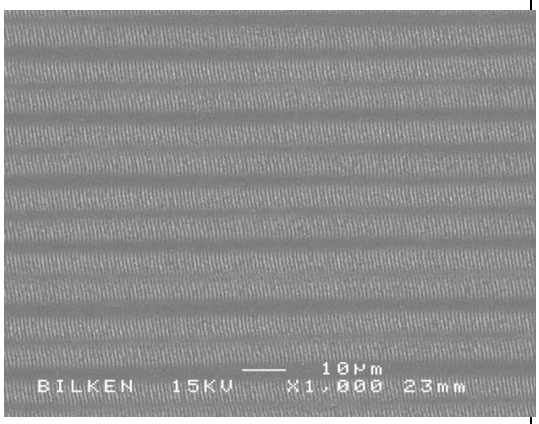
h=4 μm, v_s=1,9 m/s,	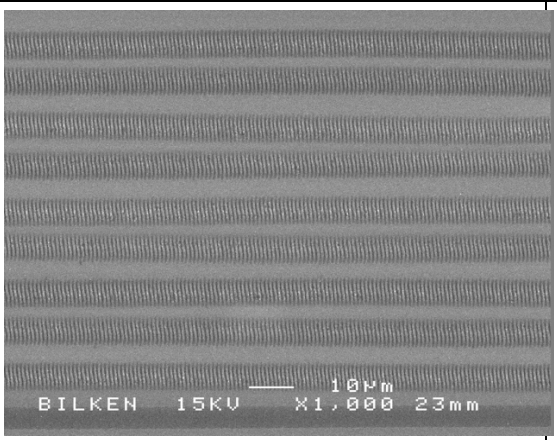	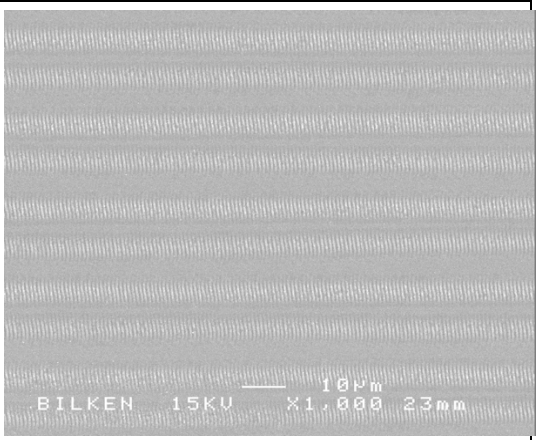

The photovoltaic parameters were examined on HR-LIPSS after phosphorous diffusion in the doping furnace. The front surface metallization formed in order to create electrical contacts.

Transmission and reflection graphs for treated and untreated areas are presented in Fig. 90a. The reflection graphs show decreasing reflectivity of treated area, especially in the region of 800 nm and longer, which clearly demonstrates photonic effects on the surface, where the period of the structure become comparable with the wavelength of the light. As a result, the External Quantum Efficiency (EQE) of processed area is higher (Fig. 90b).

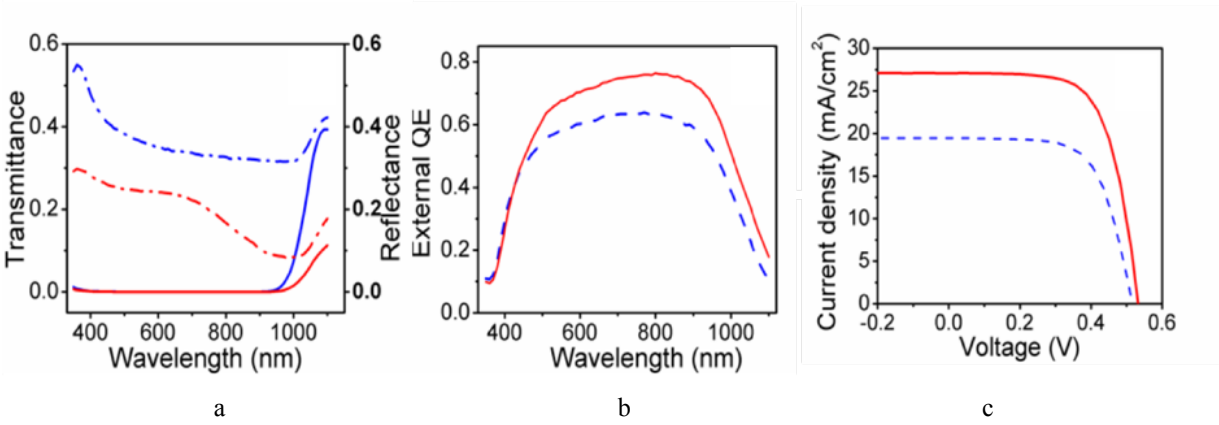

Figure 90. (a) – transmittance (solid) and reflectance (dashed) curves for unstructured (red), and structured (blue) areas. (b) – EQE graphs for unstructured (red) and structured (blue) solar cell. (c) – I-V graph for unstructured (blue) and structured (red) solar cell.

In the range between 400 nm to 800 nm the relative increase in EQE is ~20%, while in the range 800 nm and longer it is more than 30%. From the current-voltage curve (fig. 90c), the open circuit voltage (V_{OC}) and short circuit current (J_{SC}) density for untreated SC is 0.516 V and 19.44 mA/cm^2, respectively. For the treated one V_{OC} and J_{SC} are 0.532 V and 27.09 mA/cm^2. Conversion efficiency and fill factor for unstructured SC 6.6% and 65.7% respectively. For structured SC efficiency increases to 9.6% with fill factor value of 66.5%.

7.2.4 Summary

As a conclusion, it was demonstrated the applications of HR-LIPSS as a low cost single step technique for the photonic design of Si-based solar cells. For high resistive single crystalline Si wafer, the relative increase of conversion efficiency is found to be 45%. We expect this technique to be successfully applicable for industrial production of the solar cell, as well as for other photovoltaic and sensing devices.

Chapter 8 Summary and Recommendations

8.1 Summary

The main aim of this thesis was to investigate the main challenges of LIPSS and then overcome them, in order to apply this technique for industrial applications. It was estimated that LIPSS suffer either from irregularity due to multiple branching points where several ripples merge together or due to the low speed for covering a large area. These limits strongly restrict the transfer of the LIPSS-direct writing methods from laboratories to industry.

Here, the methods how to circumvent all challenges to produce LIPSS on metallic or non-metallic surfaces are presented. For the first time, highly-regular LIPSS with an unprecedented processing speed on a cm-sized area was demonstrated. The experiment is supported by the theoretical explanation of highly-regular LIPSS on metals and semiconductors.

The HR-LIPSS were experimentally obtained by using a home-made fiber Yb-femtosecond laser and then replicated on a commercially available femtosecond laser system "Pharos". Experiments demonstrate unprecedented control and record regularity at velocities competitive with current industry standards, which were achieved for a set of 3 metals.

As the main difficulty of the physics of laser-induced nanostructuring lies in the specific response of each material, it has developed a material-dependent model compatible with currently available theories on laser-induced periodic surface structure (LIPSS) formation. Using this model, it succeeded in the explanation and description of all experimental results that were obtained and, in addition, results from several studies taken from literature. The fundamental novelty of the theory lies in the demonstration that the mean-free path of Surface Plasmon Polaritons, excited by the laser at the surface of the metal, is directly linked with the regularity of the LIPSS. Within a multi-material analysis, the validity of such criterion was demonstrated for 6 different metals. On this basis, further theoretical predictions on nanostructure periodicities and regularities have been made for a set of ~20 materials irradiated by several laser processing wavelengths. It is also predicted that decreasing of the laser wavelength can lead to achieving high-regularity of the laser-induced nanostructures on principally any metal. Numerical modeling based on the TTM supplemented by the Drude model with electron-temperature-

dependent electron collision frequency has demonstrated that, at ultrafast laser heating, L_{SPP} of metals is decreasing that can result in a higher regularity of periodic surface structures.

The experimental results on Si surface represent the largest area covered by HR-LIPSS (78 cm^2) in less than 12 minutes. Therefore, during the investigations of mechanisms for production HR-LIPSS on Si surface, it has been noted that novel physical effects are involved. By theoretical estimations, we arrive at the conclusion that the mechanisms include ultrafast laser-induced electron emission followed by delayed and highly localized periodical modulation of electrical neutrality of the silicon surface.

Further, HR-LIPSS on metals and semiconductors were systematically investigated in various fields including mechanics, medicines, optoelectronics, photovoltaics, plasmonics, nano-and-microfluidics, wettability and others. In fact, tribological applications showed that LIPSS treatment effects the coefficient of friction (COF) both in dry and lubricated conditions and lead to an essential decreasing of COF in 3-4 and 2 times respectively. Results demonstrate a higher ratio of cell growth, differentiation and proliferation on laser-nanostructured surfaces compared to untreated ones for both in-vitro and in-vivo experiments for numerous types of medical implants. It outlines the preliminary results of LIPSS treatment on surfaces of molds for micro injection molding to improve filling. Results on surface wettability demonstrate that HR-LIPSS treatment permits the surface behaviour to change from hydrophilic to hydrophobic on aluminium, copper and stainless steel surfaces. The presented results on the test of adhesive properties of nanotextures Ti6Al4V show significantly enhanced adhesive properties of LIPSS treated surface in comparison with chemical treatment and untreated surfaces. This technology also showed eye-catching appearance and can serve as a decoration for counterfeit prevention and identification marking of any company products.

A few applications for HR-LIPSS on semiconductors (Si) were investigated. Highly uniform laser-induced 1D periodic surface structures on Si substrate with Au nanoparticles self-assembling on the top of grating grooves support excitation of the surface plasmon resonance that opens a perspective for the fabrication of unique and cheap plasmonic sensors. Furthermore, HR-LIPSS were imprinted for producing Si-based solar cells. For high resistive single crystalline Si wafer, the relative increase of conversion efficiency is found to be 45%. We expect this technique to be successfully applicable for industrial production of solar cells.

To sum up, the discovery of high quality and uniform sub-microstructures (nanostructures) has been presented for the first time since 1965. Accomplished with the high speed of HR-LIPSS generation, it can take one of the first places in the nanomanufacturing techniques.

8.2 Recommendations

In this thesis, the new approaches and methods to obtain high quality LIPSS were used. Mainly, all experiments, where we have demonstrated HR-LIPSS were carried out on the laser wavelength 1030 nm. For future work, we are going to obtain HR-LIPSS at different laser wavelengths from UV to thulium 2 μm wavelength.

It should be noted that the phenomenological model presented in the thesis serves mainly to propose a qualitative explanation of the mechanisms of HR-LIPSS formation under the novel regime. The report of a full-size simulation of the HR-LIPSS formation on metallic and non-metallic surfaces for direct comparison with experiments is under development.

In addition, melting and redistribution of the molten material may also be involved in the formation of HR-LIPSS. To investigate this deeply we are going to perform large-scale atomistic simulation. The insights into the mechanisms of the HR-LIPSS formation may help in designing approaches aimed at increasing the processing speed and improving the quality of HR-LIPSS.

Respectively on applications of HR-LIPSS, a significant step was presented to move the technology to the real industry. The essential approach to give a platform to throughput is to use galvo-scanner and motorized XYZ-stage simultaneously, therefore we used it only on the flat surface. The following progress will be to obtain highly uniform LIPSS on free form surfaces. Such a hint will allow to treat mechanical parts and test it in real machines.

Bearing in mind all superior features of the HR-LIPSS, with the potential impact in tribology, wettability, medical implants, enhanced adhesion, solar cells, counterfeit prevention, surface colorizing, plasmon resonance, sensors and biosensors. However, the technique is new and its potential for these applications needs to be evaluated systematically.

Bibliography

[1] "Nanotechnology," *Wikipedia*. 09-Mar-2017.

[2] W.-S. Liao, S. Cheunkar, H. H. Cao, H. R. Bednar, P. S. Weiss, and A. M. Andrews, "Subtractive Patterning via Chemical Lift-Off Lithography," *Science*, vol. 337, no. 6101, pp. 1517–1521, Sep. 2012.

[3] B. D. Gates, Q. Xu, M. Stewart, D. Ryan, C. G. Willson, and G. M. Whitesides, "New Approaches to Nanofabrication: Molding, Printing, and Other Techniques," *Chem. Rev.*, vol. 105, no. 4, pp. 1171–1196, Apr. 2005.

[4] M. Gecevičius, M. Beresna, and P. G. Kazansky, "Polarization sensitive camera by femtosecond laser nanostructuring," *Opt. Lett.*, vol. 38, no. 20, pp. 4096–4099, Oct. 2013.

[5] R. F. Pease and S. Y. Chou, "Lithography and Other Patterning Techniques for Future Electronics," *Proc. IEEE*, vol. 96, no. 2, pp. 248–270, Feb. 2008.

[6] A. Pimpin and W. Srituravanich, "Review on Micro- and Nanolithography Techniques and their Applications," *Eng. J.*, vol. 16, no. 1, pp. 37–56, Jan. 2012.

[7] R. P. Seisyan, "Nanolithography in microelectronics: A review," *Tech. Phys.*, vol. 56, no. 8, p. 1061, Aug. 2011.

[8] M. Imboden and D. Bishop, "Top-down nanomanufacturing," *Phys. Today*, Nov. 2014.

[9] T. Fujii, T. Asahata, and T. Kaito, "Focused ion beam systems as a multifunctional tool for nanotechnology," in *Focused Ion Beam Systems*, N. Yao, Ed. Cambridge: Cambridge University Press, 2007, pp. 355–390.

[10] J. Bonse, J. Krüger, S. Hohm, and A. Rosenfeld, "Femtosecond laser-induced periodic surface structures," *J. Laser Appl.*, vol. 24, no. 4, p. 042006, Jul. 2012.

[11] A. Y. Vorobyev and Chunlei Guo, "Femtosecond laser-induced periodic surface structure formation on tungsten," *J. Appl. Phys.*, vol. 104, no. 6, p. 063523, Sep. 2008.

[12] B. Tan and K. Venkatakrishnan, "A femtosecond laser-induced periodical surface structure on crystalline silicon," *J. Micromechanics Microengineering*, vol. 16, no. 5, p. 1080, 2006.

[13] M. Birnbaum, "Semiconductor Surface Damage Produced by Ruby Lasers," *J. Appl. Phys.*, vol. 36, pp. 3688–3689, Nov. 1965.

[14] D. C. Emmony, R. P. Howson, and L. J. Willis, "Laser mirror damage in germanium at 10.6 μm," *Appl. Phys. Lett.*, vol. 23, no. 11, pp. 598–600, Dec. 1973.

[15] J. E. Sipe, Jeff F. Young, J. S. Preston, and H. M. van Driel, "Laser-induced periodic surface structure. I. Theory," *Phys. Rev. B*, vol. 27, no. 2, pp. 1141–1154, Jan. 1983.

[16] H. M. van Driel, J. E. Sipe, and Jeff F. Young, "Laser-Induced Periodic Surface Structure on Solids: A Universal Phenomenon," *Phys. Rev. Lett.*, vol. 49, no. 26, pp. 1955–1958, Dec. 1982.

[17] Jeff F. Young, J. S. Preston, H. M. van Driel, and J. E. Sipe, "Laser-induced periodic surface structure. II. Experiments on Ge, Si, Al, and brass," *Phys. Rev. B*, vol. 27, no. 2, pp. 1155–1172, Jan. 1983.

[18] J. Bonse, H. Sturm, D. Schmidt, and W. Kautek, "Chemical, morphological and accumulation phenomena in ultrashort-pulse laser ablation of TiN in air," *Appl. Phys. A*, vol. 71, no. 6, pp. 657–665, Dec. 2000.

[19] J. Reif, F. Costache, M. Henyk, and S. V. Pandelov, "Ripples revisited: non-classical morphology at the bottom of femtosecond laser ablation craters in transparent dielectrics," *Appl. Surf. Sci.*, vol. 197, pp. 891–895, 2002.
[20] A. Borovicc and H. K. Haugen, "Subwavelength ripple formation on the surfaces of compound semiconductors irradiated with femtosecond laser pulses," *Appl. Phys. Lett.*, vol. 82, no. 25, pp. 4462–4464, Jun. 2003.
[21] X.-F. Li, C.-Y. Zhang, H. Li, Q.-F. Dai, S. Lan, and S.-L. Tie, "Formation of 100-nm periodic structures on a titanium surface by exploiting the oxidation and third harmonic generation induced by femtosecond laser pulses," *Opt. Express*, vol. 22, no. 23, pp. 28086–28099, Nov. 2014.
[22] F. Liang, R. Vallée, and S. L. Chin, "Mechanism of nanograting formation on the surface of fused silica," *Opt. Express*, vol. 20, no. 4, pp. 4389–4396, Feb. 2012.
[23] D. Dufft, A. Rosenfeld, S. K. Das, R. Grunwald, and J. Bonse, "Femtosecond laser-induced periodic surface structures revisited: A comparative study on ZnO," *J. Appl. Phys.*, vol. 105, no. 3, p. 034908, Feb. 2009.
[24] J. Z. P. Skolski, G. R. B. E. Römer, J. V. Obona, V. Ocelik, A. J. Huis in 't Veld, and J. T. M. De Hosson, "Laser-induced periodic surface structures: Fingerprints of light localization," *Phys. Rev. B*, vol. 85, no. 7, p. 075320, Feb. 2012.
[25] J. Z. P. Skolski, G. R. B. E. Romer, J. Vincenc Obona, and A. J. Huis in 't Veld, "Modeling laser-induced periodic surface structures: Finite-difference time-domain feedback simulations," *J. Appl. Phys.*, vol. 115, no. 10, p. 103102, Mar. 2014.
[26] E. L. Gurevich, "Mechanisms of femtosecond LIPSS formation induced by periodic surface temperature modulation," *Appl. Surf. Sci.*, vol. 374, pp. 56–60, Jun. 2016.
[27] E. L. Gurevich, "Self-organized nanopatterns in thin layers of superheated liquid metals," *Phys. Rev. E*, vol. 83, no. 3, p. 031604, Mar. 2011.
[28] J. Bonse, A. Rosenfeld, and J. Kruger, "On the role of surface plasmon polaritons in the formation of laser-induced periodic surface structures upon irradiation of silicon by femtosecond-laser pulses," *J. Appl. Phys.*, vol. 106, no. 10, p. 104910, Nov. 2009.
[29] K. Sokolovski-Tinten *et al.*, "Short-pulse Laser Induced Transient Structure Formation and Ablation Studied with Time-resolved Coherent XUV-scattering," *AIP Conf. Proc.*, vol. 1278, no. 1, pp. 373–379, Oct. 2010.
[30] M. Huang, F. Zhao, Y. Cheng, N. Xu, and Z. Xu, "Origin of Laser-Induced Near-Subwavelength Ripples: Interference between Surface Plasmons and Incident Laser," *ACS Nano*, vol. 3, no. 12, pp. 4062–4070, Dec. 2009.
[31] G. Miyaji and K. Miyazaki, "Origin of periodicity in nanostructuring on thin film surfaces ablated with femtosecond laser pulses," *Opt. Express*, vol. 16, no. 20, pp. 16265–16271, Sep. 2008.
[32] A. V. Zayats, I. I. Smolyaninov, and A. A. Maradudin, "Nano-optics of surface plasmon polaritons," *Phys. Rep.*, vol. 408, no. 3–4, pp. 131–314, Mar. 2005.
[33] V. S. Makin, R. S. Makin, A. Y. Vorobyev, and C. Guo, "Dissipative nanostructures and Feigenbaum's universality in the 'Metal-high-power ultrashort-pulsed polarized radiation' nonequilibrium nonlinear dynamical system," *Tech. Phys. Lett.*, vol. 34, no. 5, pp. 387–390, May 2008.
[34] B. Oktem *et al.*, "Nonlinear laser lithography for indefinitely large-area nanostructuring with femtosecond pulses," *Nat. Photonics*, vol. 7, no. 11, pp. 897–901, Nov. 2013.
[35] A. V. Dostovalov, V. P. Korolkov, and S. A. Babin, "Simultaneous formation of ablative and thermochemical laser-induced periodic surface structures on Ti film at femtosecond irradiation," *Laser Phys. Lett.*, vol. 12, no. 3, p. 036101, 2015.

[36] J. Bonse, S. Höhm, S. Kirner, A. Rosenfeld, and J. Krüger, "Laser-induced Periodic Surface Structures (LIPSS) - A Scientific Evergreen," in *Conference on Lasers and Electro-Optics (2016), paper STh1Q.3*, 2016, p. STh1Q.3.
[37] F. Garrelie *et al.*, "Evidence of surface plasmon resonance in ultrafast laser-induced ripples," *Opt. Express*, vol. 19, no. 10, pp. 9035–9043, May 2011.
[38] J. E. Sipe, H. M. van Driel, and J. F. Young, "Surface electrodynamics: radiation fields, surface polaritons, and radiation remnants," *Can. J. Phys.*, vol. 63, no. 1, pp. 104–113, Jan. 1985.
[39] T. Tomita, R. Kumai, S. Matsuo, S. Hashimoto, and M. Yamaguchi, "Cross-sectional morphological profiles of ripples on Si, SiC, and HOPG," *Appl. Phys. A*, vol. 97, no. 2, pp. 271–276, Nov. 2009.
[40] Q. Wu, Y. Ma, R. Fang, Y. Liao, Q. Y. Chen, and K. Wang, "Femtosecond laser-induced periodic surface structure on diamond film," *Appl. Phys. Lett.*, vol. 82, no. 11, pp. 1703–1705, Mar. 2003.
[41] A. M. Ozkan, A. P. Malshe, T. A. Railkar, W. D. Brown, M. D. Shirk, and P. A. Molian, "Femtosecond laser-induced periodic structure writing on diamond crystals and microclusters," *Appl. Phys. Lett.*, vol. 75, no. 23, pp. 3716–3718, Nov. 1999.
[42] J. Bonse, S. Höhm, A. Rosenfeld, and J. Krüger, "Sub-100-nm laser-induced periodic surface structures upon irradiation of titanium by Ti:sapphire femtosecond laser pulses in air," *Appl. Phys. A*, vol. 110, no. 3, pp. 547–551, Mar. 2013.
[43] X. Sedao *et al.*, "Growth Twinning and Generation of High-Frequency Surface Nanostructures in Ultrafast Laser-Induced Transient Melting and Resolidification," *ACS Nano*, vol. 10, no. 7, pp. 6995–7007, Jul. 2016.
[44] A. Y. Vorobyev, S. Makin, and C. Guo, "Periodic ordering of random surface nanostructures induced by femtosecond laser pulses on metals," *J. Appl. Phys.*, vol. 101, no. 3, p. 034903, Feb. 2007.
[45] A. A. Ionin *et al.*, "Nonlinear evolution of aluminum surface relief under multiple femtosecond laser irradiation," *JETP Lett.*, vol. 101, no. 5, pp. 350–357, Mar. 2015.
[46] J. Wang and C. Guo, "Ultrafast dynamics of femtosecond laser-induced periodic surface pattern formation on metals," *Appl. Phys. Lett.*, vol. 87, no. 25, p. 251914, Dec. 2005.
[47] R. L. Harzic *et al.*, "Large-area, uniform, high-spatial-frequency ripples generated on silicon using a nanojoule-femtosecond laser at high repetition rate," *Opt. Lett.*, vol. 36, no. 2, pp. 229–231, Jan. 2011.
[48] O. Varlamova, M. Bounhalli, and J. Reif, "Influence of irradiation dose on laser-induced surface nanostructures on silicon," *Appl. Surf. Sci.*, vol. 278, pp. 62–66, Aug. 2013.
[49] S. He, J. J. Nivas, A. Vecchione, M. Hu, and S. Amoruso, "On the generation of grooves on crystalline silicon irradiated by femtosecond laser pulses," *Opt. Express*, vol. 24, no. 4, pp. 3238–3247, Feb. 2016.
[50] I. Ursu *et al.*, "Periodic structures on the surface of fused silica under multipulse 10.6-μm laser irradiation," *Appl. Opt.*, vol. 24, no. 22, pp. 3736–3739, Nov. 1985.
[51] S. Höhm, M. Rohloff, J. Krüger, J. Bonse, and A. Rosenfeld, "Formation of Laser-Induced Periodic Surface Structures (LIPSS) on Dielectrics and Semiconductors upon Double-Femtosecond Laser Pulse Irradiation Sequences," in *Progress in Nonlinear Nano-Optics*, S. Sakabe, C. Lienau, and R. Grunwald, Eds. Springer International Publishing, 2015, pp. 85–99.
[52] E. Rebollar, M. Castillejo, and T. A. Ezquerra, "Laser induced periodic surface structures on polymer films: From fundamentals to applications," *Eur. Polym. J.*, vol. 73, pp. 162–174, Dec. 2015.

[53] O. Santos *et al.*, "Modified stainless steel surfaces targeted to reduce fouling—surface characterization," *J. Food Eng.*, vol. 64, no. 1, pp. 63–79, Sep. 2004.
[54] H. Ohmori, K. Katahira, J. Komotori, and M. Mizutani, "Functionalization of stainless steel surface through mirror-quality finish grinding," *CIRP Ann. - Manuf. Technol.*, vol. 57, no. 1, pp. 545–549, 2008.
[55] H. Ohmori, K. Katahira, J. Komotori, Y. Akahane, M. Mizutani, and T. Naruse, "Surface generation of superior hydrophilicity for surgical steels by specific grinding parameters," *CIRP Ann. - Manuf. Technol.*, vol. 58, no. 1, pp. 503–506, 2009.
[56] P. Guo, Y. Lu, K. F. Ehmann, and J. Cao, "Generation of hierarchical micro-structures for anisotropic wetting by elliptical vibration cutting," *CIRP Ann. - Manuf. Technol.*, vol. 63, no. 1, pp. 553–556, 2014.
[57] D.-M. Chun, G. Davaasuren, C.-V. Ngo, C.-S. Kim, G.-Y. Lee, and S.-H. Ahn, "Fabrication of transparent superhydrophobic surface on thermoplastic polymer using laser beam machining and compression molding for mass production," *CIRP Ann. - Manuf. Technol.*, vol. 63, no. 1, pp. 525–528, 2014.
[58] B. Wu, M. Zhou, J. Li, X. Ye, G. Li, and L. Cai, "Superhydrophobic surfaces fabricated by microstructuring of stainless steel using a femtosecond laser," *Appl. Surf. Sci.*, vol. 256, no. 1, pp. 61–66, Oct. 2009.
[59] P. Bizi-Bandoki, S. Benayoun, S. Valette, B. Beaugiraud, and E. Audouard, "Modifications of roughness and wettability properties of metals induced by femtosecond laser treatment," *Appl. Surf. Sci.*, vol. 257, no. 12, pp. 5213–5218, Apr. 2011.
[60] P. Bizi-bandoki, S. Valette, E. Audouard, and S. Benayoun, "Time dependency of the hydrophilicity and hydrophobicity of metallic alloys subjected to femtosecond laser irradiations," *Appl. Surf. Sci.*, vol. 273, pp. 399–407, May 2013.
[61] A. Cunha, A. P. Serro, V. Oliveira, A. Almeida, R. Vilar, and M.-C. Durrieu, "Wetting behaviour of femtosecond laser textured Ti–6Al–4V surfaces," *Appl. Surf. Sci.*, vol. 265, pp. 688–696, Jan. 2013.
[62] A. Y. Vorobyev and C. Guo, "Multifunctional surfaces produced by femtosecond laser pulses," *J. Appl. Phys.*, vol. 117, no. 3, p. 033103, Jan. 2015.
[63] M. Martínez-Calderon, A. Rodríguez, A. Dias-Ponte, M. C. Morant-Miñana, M. Gómez-Aranzadi, and S. M. Olaizola, "Femtosecond laser fabrication of highly hydrophobic stainless steel surface with hierarchical structures fabricated by combining ordered microstructures and LIPSS," *Appl. Surf. Sci.*, vol. 374, pp. 81–89, Jun. 2016.
[64] A. Y. Vorobyev and C. Guo, "Metal pumps liquid uphill," *Appl. Phys. Lett.*, vol. 94, no. 22, p. 224102, Jun. 2009.
[65] F. A. Müller, C. Kunz, and S. Gräf, "Bio-Inspired Functional Surfaces Based on Laser-Induced Periodic Surface Structures," *Materials*, vol. 9, no. 6, p. 476, Jun. 2016.
[66] J. J. Yu and Y. F. Lu, "Laser-induced ripple structures on Ni–P substrates," *Appl. Surf. Sci.*, vol. 148, no. 3–4, pp. 248–252, Jul. 1999.
[67] T. Honda and K. Miyazaki, "Friction Properties of the DLC Film with Periodic Structures in Nano-scale (PDF Download Available)," *ResearchGate*. [Online]. Available: https://www.researchgate.net/publication/245552377_Friction_Properties_of_the_DLC_Film_with_Periodic_Structures_in_Nano-scale. [Accessed: 08-Mar-2017].
[68] N. Yasumaru, K. Miyazaki, and J. Kiuchi, "Control of tribological properties of diamond-like carbon films with femtosecond-laser-induced nanostructuring," *Appl. Surf. Sci.*, vol. 254, no. 8, pp. 2364–2368, Feb. 2008.

[69] M. Pfeiffer *et al.*, "Ripple formation in various metals and super-hard tetrahedral amorphous carbon films in consequence of femtosecond laser irradiation," *Appl. Phys. A*, vol. 110, no. 3, pp. 655–659, Mar. 2013.
[70] J. Eichstädt, G. R. B. E. Römer, and A. J. Huis in 't Veld, "Towards Friction Control using laser-induced periodic Surface Structures," *Phys. Procedia*, vol. 12, no. Part B, pp. 7–15, 2011.
[71] J. Bonse *et al.*, "Femtosecond laser-induced periodic surface structures on steel and titanium alloy for tribological applications," *Appl. Phys. A*, vol. 117, no. 1, pp. 103–110, Oct. 2014.
[72] J. Bonse *et al.*, "Tribological performance of femtosecond laser-induced periodic surface structures on titanium and a high toughness bearing steel," *Appl. Surf. Sci.*, vol. 336, pp. 21–27, May 2015.
[73] J. Bonse *et al.*, "Tribological performance of sub-100-nm femtosecond laser-induced periodic surface structures on titanium," *Appl. Surf. Sci.*, vol. 374, pp. 190–196, Jun. 2016.
[74] A. Matsugaki, G. Aramoto, T. Ninomiya, H. Sawada, S. Hata, and T. Nakano, "Abnormal arrangement of a collagen/apatite extracellular matrix orthogonal to osteoblast alignment is constructed by a nanoscale periodic surface structure," *Biomaterials*, vol. 37, pp. 134–143, Jan. 2015.
[75] A. Cunha *et al.*, "Human mesenchymal stem cell behavior on femtosecond laser-textured Ti-6Al-4V surfaces," *Nanomed.*, vol. 10, no. 5, pp. 725–739, 2015.
[76] A. Cunha *et al.*, "Femtosecond laser surface texturing of titanium as a method to reduce the adhesion of Staphylococcus aureus and biofilm formation," *Appl. Surf. Sci.*, vol. 360, Part B, pp. 485–493, Jan. 2016.
[77] J. Rothchild, "Masters of Light: The Science Behind Nature's Brightest Colors," *Yale Scientific Magazine*, 30-Dec-2014. .
[78] A. Y. Vorobyev and C. Guo, "Colorizing metals with femtosecond laser pulses," *Appl. Phys. Lett.*, vol. 92, no. 4, p. 041914, Jan. 2008.
[79] A. Y. Vorobyev and C. Guo, "Spectral and polarization responses of femtosecond laser-induced periodic surface structures on metals," *J. Appl. Phys.*, vol. 103, no. 4, p. 043513, Feb. 2008.
[80] B. Dusser *et al.*, "Controlled nanostructrures formation by ultra fast laser pulses for color marking," *Opt. Express*, vol. 18, no. 3, pp. 2913–2924, Feb. 2010.
[81] J. Yao *et al.*, "Selective appearance of several laser-induced periodic surface structure patterns on a metal surface using structural colors produced by femtosecond laser pulses," *Appl. Surf. Sci.*, vol. 258, no. 19, pp. 7625–7632, Jul. 2012.
[82] Z. Ou, M. Huang, and F. Zhao, "Colorizing pure copper surface by ultrafast laser-induced near-subwavelength ripples," *Opt. Express*, vol. 22, no. 14, pp. 17254–17265, Jul. 2014.
[83] A. A. Ionin *et al.*, "Femtosecond laser color marking of metal and semiconductor surfaces," *Appl. Phys. A*, vol. 107, no. 2, pp. 301–305, May 2012.
[84] G. Li *et al.*, "Femtosecond laser color marking stainless steel surface with different wavelengths," *Appl. Phys. A*, vol. 118, no. 4, pp. 1189–1196, Mar. 2015.
[85] A. Y. Vorobyev and C. Guo, "Direct femtosecond laser surface nano/microstructuring and its applications," *Laser Photonics Rev.*, vol. 7, no. 3, pp. 385–407, May 2013.
[86] A.-M. Kietzig, S. G. Hatzikiriakos, and P. Englezos, "Patterned Superhydrophobic Metallic Surfaces," *Langmuir*, vol. 25, no. 8, pp. 4821–4827, Apr. 2009.

[87] A. R. de la Cruz, R. Lahoz, J. Siegel, G. F. de la Fuente, and J. Solis, "High speed inscription of uniform, large-area laser-induced periodic surface structures in Cr films using a high repetition rate fs laser," *Opt. Lett.*, vol. 39, no. 8, pp. 2491–2494, Apr. 2014.
[88] N. M. Bulgakova, V. P. Zhukov, and Y. P. Meshcheryakov, "Theoretical treatments of ultrashort pulse laser processing of transparent materials: toward understanding the volume nanograting formation and 'quill' writing effect," *Appl. Phys. B*, vol. 113, no. 3, pp. 437–449, Dec. 2013.
[89] A. G. Kovačević *et al.*, "Surface nanopatterning of Al/Ti multilayer thin films and Al single layer by a low-fluence UV femtosecond laser beam," *Appl. Surf. Sci.*, vol. 326, pp. 91–98, Jan. 2015.
[90] T. Q. Jia *et al.*, "Formation of nanogratings on the surface of a ZnSe crystal irradiated by femtosecond laser pulses," *Phys. Rev. B*, vol. 72, no. 12, p. 125429, Sep. 2005.
[91] P. B. Johnson and R. W. Christy, "Optical Constants of the Noble Metals," *Phys. Rev. B*, vol. 6, no. 12, pp. 4370–4379, Dec. 1972.
[92] J. Cong, J. Yang, B. Zhao, and X. Xu, "Fabricating subwavelength dot-matrix surface structures of Molybdenum by transient correlated actions of two-color femtosecond laser beams," *Opt. Express*, vol. 23, no. 4, pp. 5357–5367, Feb. 2015.
[93] C. S. R. Nathala *et al.*, "Experimental study of fs-laser induced sub-100-nm periodic surface structures on titanium," *Opt. Express*, vol. 23, no. 5, pp. 5915–5929, Mar. 2015.
[94] J.-W. Yao *et al.*, "High spatial frequency periodic structures induced on metal surface by femtosecond laser pulses," *Opt. Express*, vol. 20, no. 2, pp. 905–911, Jan. 2012.
[95] J. Bonse, M. Munz, and H. Sturm, "Structure formation on the surface of indium phosphide irradiated by femtosecond laser pulses," *J. Appl. Phys.*, vol. 97, no. 1, p. 013538, Dec. 2004.
[96] "https://bitbucket.org/tjyderrien/spp-extended-theory/wiki/Home."
[97] Z. Püspöki, M. Storath, D. Sage, and M. Unser, "Transforms and Operators for Directional Bioimage Analysis: A Survey," *Adv. Anat. Embryol. Cell Biol.*, vol. 219, pp. 69–93, 2016.
[98] J. Schindelin, C. T. Rueden, M. C. Hiner, and K. W. Eliceiri, "The ImageJ ecosystem: An open platform for biomedical image analysis," *Mol. Reprod. Dev.*, vol. 82, no. 7–8, pp. 518–529, Jul. 2015.
[99] M. A. Ordal, R. J. Bell, R. W. Alexander, L. A. Newquist, and M. R. Querry, "Optical properties of Al, Fe, Ti, Ta, W, and Mo at submillimeter wavelengths," *Appl. Opt.*, vol. 27, no. 6, pp. 1203–1209, Mar. 1988.
[100] "Handbook of Optical Constants of Solids - ScienceDirect." [Online]. Available: http://www.sciencedirect.com/science/book/9780080547213. [Accessed: 05-May-2017].
[101] T. J.-Y. Derrien, J. Krüger, T. E. Itina, S. Höhm, A. Rosenfeld, and J. Bonse, "Rippled area formed by surface plasmon polaritons upon femtosecond laser double-pulse irradiation of silicon: the role of carrier generation and relaxation processes," *Appl. Phys. A*, vol. 117, no. 1, pp. 77–81, Oct. 2014.
[102] T. J. Y. Derrien, T. E. Itina, R. Torres, T. Sarnet, and M. Sentis, "Possible surface plasmon polariton excitation under femtosecond laser irradiation of silicon," *J. Appl. Phys.*, vol. 114, no. 8, p. 083104, Aug. 2013.
[103] Y. Levy, T. J.-Y. Derrien, N. M. Bulgakova, E. L. Gurevich, and T. Mocek, "Relaxation dynamics of femtosecond-laser-induced temperature modulation on the surfaces of metals and semiconductors," *Appl. Surf. Sci.*, vol. 374, pp. 157–164, Jun. 2016.
[104] *Plasmonics: Fundamentals and Applications | Stefan Alexander Maier | Springer*. .

[105] T. J.-Y. Derrien, J. Krüger, and J. Bonse, "Properties of surface plasmon polaritons on lossy materials: lifetimes, periods and excitation conditions," *J. Opt.*, vol. 18, no. 11, p. 115007, 2016.
[106] P. M. Fauchet and A. E. Siegman, "Surface ripples on silicon and gallium arsenide under picosecond laser illumination," *Appl. Phys. Lett.*, vol. 40, no. 9, pp. 824–826, May 1982.
[107] H. Shimizu, S. Yada, G. Obara, and M. Terakawa, "Contribution of defect on early stage of LIPSS formation," *Opt. Express*, vol. 22, no. 15, pp. 17990–17998, Jul. 2014.
[108] W. L. Barnes, A. Dereux, and T. W. Ebbesen, "Surface plasmon subwavelength optics," *Nature*, vol. 424, no. 6950, pp. 824–830, Aug. 2003.
[109] G. Gay *et al.*, "The response of nanostructured surfaces in the near field," *Nat. Phys.*, vol. 2, no. 12, pp. 792–792, Dec. 2006.
[110] G. Gay, O. Alloschery, B. Viaris de Lesegno, C. O'Dwyer, J. Weiner, and H. J. Lezec, "The optical response of nanostructured surfaces and the composite diffracted evanescent wave model," *Nat. Phys.*, vol. 2, no. 4, pp. 262–267, Apr. 2006.
[111] M. Ardron, N. Weston, and D. Hand, "A practical technique for the generation of highly uniform LIPSS," *Appl. Surf. Sci.*, vol. 313, pp. 123–131, Sep. 2014.
[112] T. T. D. Huynh, A. Petit, and N. Semmar, "Picosecond laser induced periodic surface structure on copper thin films," *Appl. Surf. Sci.*, vol. 302, pp. 109–113, May 2014.
[113] S. E. Kirkwood, Y. Y. Tsui, R. Fedosejevs, A. V. Brantov, and V. Y. Bychenkov, "Experimental and theoretical study of absorption of femtosecond laser pulses in interaction with solid copper targets," *Phys. Rev. B*, vol. 79, no. 14, p. 144120, Apr. 2009.
[114] S.-S. Wellershoff, J. Hohlfeld, J. Güdde, and E. Matthias, "The role of electron–phonon coupling in femtosecond laser damage of metals," *Appl. Phys. A*, vol. 69, no. 1, pp. S99–S107, Dec. 1999.
[115] R. H. M. Groeneveld, R. Sprik, and A. Lagendijk, "Femtosecond spectroscopy of electron-electron and electron-phonon energy relaxation in Ag and Au," *Phys. Rev. B*, vol. 51, no. 17, pp. 11433–11445, May 1995.
[116] *Handbook of Stainless Steels*. McGraw-Hill, 1977.
[117] "ASM Handbook Volume 18: Friction, Lubrication, and Wear Technology - ASM International." [Online]. Available: http://www.asminternational.org/materials-resources/results/-/journal_content/56/10192/06185G/PUBLICATION. [Accessed: 10-Mar-2017].
[118] P. Andersson *et al.*, "Microlubrication effect by laser-textured steel surfaces," *Wear*, vol. 262, no. 3–4, pp. 369–379, Feb. 2007.
[119] Y. Qiu and M. M. Khonsari, "Experimental investigation of tribological performance of laser textured stainless steel rings," *Tribol. Int.*, vol. 44, no. 5, pp. 635–644, May 2011.
[120] A. Ramesh, W. Akram, S. P. Mishra, A. H. Cannon, A. A. Polycarpou, and W. P. King, "Friction characteristics of microtextured surfaces under mixed and hydrodynamic lubrication," *Tribol. Int.*, vol. 57, pp. 170–176, Jan. 2013.
[121] D. Braun, C. Greiner, J. Schneider, and P. Gumbsch, "Efficiency of laser surface texturing in the reduction of friction under mixed lubrication," *Tribol. Int.*, vol. 77, pp. 142–147, Sep. 2014.
[122] M. Scaraggi, F. P. Mezzapesa, G. Carbone, A. Ancona, D. Sorgente, and P. M. Lugarà, "Minimize friction of lubricated laser-microtextured-surfaces by tuning microholes depth," *Tribol. Int.*, vol. 75, pp. 123–127, Jul. 2014.
[123] G. Daschiel, M. Perić, J. Jovanović, and A. Delgado, "The holy grail of microfluidics: sub-laminar drag by layout of periodically embedded microgrooves," *Microfluid. Nanofluidics*, vol. 15, no. 5, pp. 675–687, Nov. 2013.

[124] "ASM Handbook, Volume 1: Properties and Selection: Irons, Steels, and High-Performance Alloys - ASM International." [Online]. Available: http://www.asminternational.org/home/-/journal_content/56/10192/06181G/PUBLICATION/. [Accessed: 11-Mar-2017].
[125] I. M. Hutchings, *Tribology: Friction and Wear of Engineering Materials*. Edward Arnold, 1992.
[126] A. Rosenkranz, L. Reinert, C. Gachot, and F. Mücklich, "Alignment and wear debris effects between laser-patterned steel surfaces under dry sliding conditions," *Wear*, vol. 318, no. 1–2, pp. 49–61, Oct. 2014.
[127] C. Yu, H. Yu, G. Liu, W. Chen, B. He, and Q. J. Wang, "Understanding Topographic Dependence of Friction with Micro- and Nano-Grooved Surfaces," *Tribol. Lett.*, vol. 53, no. 1, pp. 145–156, Jan. 2014.
[128] "Engineering Tribology - 3rd Edition." [Online]. Available: https://www.elsevier.com/books/engineering-tribology/stachowiak/978-0-7506-7836-0. [Accessed: 11-Mar-2017].
[129] L. Ceschini, C. Chiavari, A. Marconi, and C. Martini, "Influence of the countermaterial on the dry sliding friction and wear behaviour of low temperature carburized AISI316L steel," *Tribol. Int.*, vol. 67, pp. 36–43, Nov. 2013.
[130] A. F. Smith, "The friction and sliding wear of unlubricated 316 stainless steel in air at room temperature in the load range 0.5–90 N," *Wear*, vol. 110, no. 2, pp. 151–168, Jul. 1986.
[131] A. F. Smith, "The influence of surface oxidation and sliding speed on the unlubricated wear of 316 stainless steel at low load," *Wear*, vol. 105, no. 2, pp. 91–107, Sep. 1985.
[132] A. F. Smith, "The friction and sliding wear of unlubricated 316 stainless steel in air at room temperature in the load range 0.5–90 N," *Wear*, vol. 110, no. 2, pp. 151–168, Jul. 1986.
[133] L. J. O'Donnell, G. M. Michal, F. Ernst, H. Kahn, and A. H. Heuer, "Wear maps for low temperature carburised 316L austenitic stainless steel sliding against alumina," *Surf. Eng.*, vol. 26, no. 4, pp. 284–292, May 2010.
[134] F. Rotundo, L. Ceschini, C. Martini, R. Montanari, and A. Varone, "High temperature tribological behavior and microstructural modifications of the low-temperature carburized AISI 316L austenitic stainless steel," *Surf. Coat. Technol.*, vol. 258, pp. 772–781, Nov. 2014.
[135] I. Etsion, "State of the Art in Laser Surface Texturing," in *Advanced Tribology*, Springer, Berlin, Heidelberg, 2009, pp. 761–762.
[136] U. Pettersson and S. Jacobson, "Textured surfaces for improved lubrication at high pressure and low sliding speed of roller/piston in hydraulic motors," *Tribol. Int.*, vol. 40, no. 2, pp. 355–359, Feb. 2007.
[137] H.-S. Hong, "The role of atmospheres and lubricants in the oxidational wear of metals," *Tribol. Int.*, vol. 35, no. 11, pp. 725–729, Nov. 2002.
[138] B. E. Pjetursson, K. Tan, N. P. Lang, U. Brägger, M. Egger, and M. Zwahlen, "A systematic review of the survival and complication rates of fixed partial dentures (FPDs) after an observation period of at least 5 years," *Clin. Oral Implants Res.*, vol. 15, no. 6, pp. 625–642, Dec. 2004.
[139] C. J. Goodacre, G. Bernal, K. Rungcharassaeng, and J. Y. K. Kan, "Clinical complications with implants and implant prostheses," *J. Prosthet. Dent.*, vol. 90, no. 2, pp. 121–132, Aug. 2003.

[140] Y. Manor, S. Oubaid, O. Mardinger, G. Chaushu, and J. Nissan, "Characteristics of early versus late implant failure: a retrospective study," *J. Oral Maxillofac. Surg. Off. J. Am. Assoc. Oral Maxillofac. Surg.*, vol. 67, no. 12, pp. 2649–2652, Dec. 2009.
[141] T. Berglundh, L. Persson, and B. Klinge, "A systematic review of the incidence of biological and technical complications in implant dentistry reported in prospective longitudinal studies of at least 5 years," *J. Clin. Periodontol.*, vol. 29 Suppl 3, pp. 197-212; discussion 232-233, 2002.
[142] G. Cordioli, Z. Majzoub, A. Piattelli, and A. Scarano, "Removal torque and histomorphometric investigation of 4 different titanium surfaces: an experimental study in the rabbit tibia," *Int. J. Oral Maxillofac. Implants*, vol. 15, no. 5, pp. 668–674, Oct. 2000.
[143] Y. Wu, J. P. Zitelli, K. S. TenHuisen, X. Yu, and M. R. Libera, "Differential response of Staphylococci and osteoblasts to varying titanium surface roughness," *Biomaterials*, vol. 32, no. 4, pp. 951–960, Feb. 2011.
[144] A. Bagno and C. Di Bello, "Surface treatments and roughness properties of Ti-based biomaterials," *J. Mater. Sci. Mater. Med.*, vol. 15, no. 9, pp. 935–949, Sep. 2004.
[145] J. Xiao *et al.*, "The effect of hierarchical micro/nanosurface titanium implant on osseointegration in ovariectomized sheep," *Osteoporos. Int.*, vol. 22, no. 6, pp. 1907–1913, Jun. 2011.
[146] W.-C. Chen, Y.-S. Chen, C.-L. Ko, Y. Lin, T.-H. Kuo, and H.-N. Kuo, "Interaction of progenitor bone cells with different surface modifications of titanium implant," *Mater. Sci. Eng. C*, vol. 37, pp. 305–313, Apr. 2014.
[147] D. Li *et al.*, "Biomechanical comparison of the sandblasted and acid-etched and the machined and acid-etched titanium surface for dental implants," *J. Biomed. Mater. Res.*, vol. 60, no. 2, pp. 325–332, May 2002.
[148] O. Cissé, O. Savadogo, M. Wu, and L. Yahia, "Effect of surface treatment of NiTi alloy on its corrosion behavior in Hanks' solution," *J. Biomed. Mater. Res.*, vol. 61, no. 3, pp. 339–345, Sep. 2002.
[149] D. J. Hornbach, P. S. Prevey, and E. F. Loftus, "Application of Low Plasticity Burnishing (LPB) to Improve the Fatigue Performance of Ti-6Al-4V Femoral Hip Stems," *J. ASTM Int.*, vol. 3, no. 5, pp. 1–10, Apr. 2006.
[150] A. Wennerberg, C. Hallgren, C. Johansson, and S. Danelli, "A histomorphometric evaluation of screw-shaped implants each prepared with two surface roughnesses," *Clin. Oral Implants Res.*, vol. 9, no. 1, pp. 11–19, Feb. 1998.
[151] R. Stangl, A. Pries, B. Loos, M. Müller, and R. G. Erben, "Influence of pores created by laser superfinishing on osseointegration of titanium alloy implants," *J. Biomed. Mater. Res. A*, vol. 69, no. 3, pp. 444–453, Jun. 2004.
[152] S. F. Hulbert, F. A. Young, R. S. Mathews, J. J. Klawitter, C. D. Talbert, and F. H. Stelling, "Potential of ceramic materials as permanently implantable skeletal prostheses," *J. Biomed. Mater. Res.*, vol. 4, no. 3, pp. 433–456, Sep. 1970.
[153] J. Li, H. Liao, B. Fartash, L. Hermansson, and T. Johnsson, "Surface-dimpled commercially pure titanium implant and bone ingrowth," *Biomaterials*, vol. 18, no. 9, pp. 691–696, May 1997.
[154] H. Yun, C. Lin, J. Li, J. Wang, and H. Chen, "Low-temperature hydrothermal formation of a net-like structured TiO2 film and its performance of photogenerated cathode protection," *Appl. Surf. Sci.*, vol. 255, no. 5, Part 1, pp. 2113–2117, Dec. 2008.
[155] Y. Lai, C. Lin, H. Wang, J. Huang, H. Zhuang, and L. Sun, "Superhydrophilic-superhydrophobic micropattern on TiO2 nanotube films by photocatalytic lithography," *Electrochem. Commun.*, vol. 10, no. 3, pp. 387–391, 2008.

[156] H. Wang, C. Lin, and R. Hu, "Effects of structure and composition of the CaP composite coatings on apatite formation and bioactivity in simulated body fluid," *Appl. Surf. Sci.*, vol. 255, no. 7, pp. 4074–4081, Jan. 2009.
[157] L. Lin *et al.*, "Enhanced osteointegration of medical titanium implant with surface modifications in micro/nanoscale structures," *J. Orthop. Transl.*, vol. 2, no. 1, pp. 35–42, Jan. 2014.
[158] J. Y. Park, C. H. Gemmell, and J. E. Davies, "Platelet interactions with titanium: modulation of platelet activity by surface topography," *Biomaterials*, vol. 22, no. 19, pp. 2671–2682, Oct. 2001.
[159] G. Tosello, A. Gava, H. N. Hansen, G. Lucchetta, and F. Marinello, "Characterization and analysis of weld lines on micro-injection moulded parts using atomic force microscopy (AFM)," *Wear*, vol. 266, no. 5–6, pp. 534–538, Mar. 2009.
[160] J. Zhao, X. Lu, M. Lin, G. Chen, S. Liu, and M. S. Yong, "Effects of rheological properties of polymer blends on micro mold filling behavior," *Mater. Res. Innov.*, vol. 10, no. 4, pp. 111–112, 2006.
[161] B. Sha, S. Dimov, C. Griffiths, and M. S. Packianather, "Micro-injection moulding: Factors affecting the achievable aspect ratios," *Int. J. Adv. Manuf. Technol.*, vol. 33, no. 1–2, pp. 147–156, May 2007.
[162] K. M. Awati, Y. Park, E. Weisser, and M. E. Mackay, "Wall slip and shear stresses of polymer melts at high shear rates without pressure and viscous heating effects," *J. Non-Newton. Fluid Mech.*, vol. 89, no. 1–2, pp. 117–131, Feb. 2000.
[163] R. Komuro, K. Kobayashi, T. Taniguchi, M. Sugimoto, and K. Koyama, "Wall slip and melt-fracture of polystyrene melts in capillary flow," *Polymer*, vol. 51, no. 10, pp. 2221–2228, May 2010.
[164] M. Otsuka, A. Oyabe, and H. Ito, "Effects of mold surface conditions on flow length in injection molding process," *Polym. Eng. Sci.*, vol. 51, no. 7, pp. 1383–1388, Jul. 2011.
[165] M. Burgsteiner *et al.*, "Investigation of the Influence of Different Coatings on the Filling Behavior and Replication Quality of Microstructures in Injection Molding," 2014.
[166] J. Yong *et al.*, "A simple way to achieve superhydrophobicity, controllable water adhesion, anisotropic sliding, and anisotropic wetting based on femtosecond-laser-induced line-patterned surfaces," *J. Mater. Chem. A*, vol. 2, no. 15, pp. 5499–5507, Mar. 2014.
[167] G. Lucchetta, F. Marinello, G. Tristo, M. Balcon, and M. Berton, "Effects of the cavity surface finishing on the polymer filling flow in micro injection moulding," *J. Phys. Conf. Ser.*, vol. 311.
[168] M. Tang, M. H. Hong, Y. S. Choo, Z. Tang, and D. H. C. Chua, "Super-hydrophobic transparent surface by femtosecond laser micro-patterned catalyst thin film for carbon nanotube cluster growth," *Appl. Phys. A*, vol. 101, no. 3, pp. 503–508, Nov. 2010.
[169] J. Long, P. Fan, M. Zhong, H. Zhang, Y. Xie, and C. Lin, "Superhydrophobic and colorful copper surfaces fabricated by picosecond laser induced periodic nanostructures," *Appl. Surf. Sci.*, vol. 311, pp. 461–467, Aug. 2014.
[170] D. H. Kam, S. Bhattacharya, and J. Mazumder, "Control of the wetting properties of an AISI 316L stainless steel surface by femtosecond laser-induced surface modification," *J. Micromechanics Microengineering*, vol. 22, no. 10, p. 105019, 2012.
[171] R. N. Wenzel, "RESISTANCE OF SOLID SURFACES TO WETTING BY WATER," *Ind. Eng. Chem.*, vol. 28, no. 8, pp. 988–994, Aug. 1936.
[172] R. N. Wenzel, "Surface Roughness and Contact Angle.," *J. Phys. Colloid Chem.*, vol. 53, no. 9, pp. 1466–1467, Sep. 1949.

[173] A. B. D. Cassie and S. Baxter, “Wettability of porous surfaces,” *Trans. Faraday Soc.*, vol. 40, no. 0, pp. 546–551, Jan. 1944.
[174] M. Nosonovsky and B. Bhushan, “Roughness-induced superhydrophobicity: a way to design non-adhesive surfaces,” *J. Phys. Condens. Matter*, vol. 20, no. 22, p. 225009, 2008.
[175] G. Anzolin, A. Gardelein, M. Jofre, G. Molina-Terriza, and M. W. Mitchell, “Polarization change induced by a galvanometric optical scanner,” *JOSA A*, vol. 27, no. 9, pp. 1946–1952, Sep. 2010.
[176] C. Liang *et al.*, “Preparation of Hydrophobic and Oleophilic Surface of 316 L Stainless Steel by Femtosecond Laser Irradiation in Water,” *J. Dispers. Sci. Technol.*, vol. 35, no. 9, pp. 1345–1350, Sep. 2014.
[177] M. Oberringer *et al.*, “Reduced myofibroblast differentiation on femtosecond laser treated 316LS stainless steel,” *Mater. Sci. Eng. C Mater. Biol. Appl.*, vol. 33, no. 2, pp. 901–908, Mar. 2013.
[178] A. Calvimontes, M. Mauermann, and C. Bellmann, “Topographical Anisotropy and Wetting of Ground Stainless Steel Surfaces,” *Materials*, vol. 5, no. 12, pp. 2773–2787, Dec. 2012.
[179] *Structural Adhesive Joints in Engineering | Robert Adams | Springer*. .
[180] *Adhesion and Adhesives - Science and Technology | Anthony Kinloch | Springer*. .
[181] T. Mertens and H. Kollek, “On the stability and composition of oxide layers on pre-treated titanium,” *Int. J. Adhes. Adhes.*, vol. 30, no. 6, pp. 466–477, Sep. 2010.
[182] G. Rotella, M. Alfano, and S. Candamano, “Surface modification of Ti6Al4V alloy by pulsed Yb-laser irradiation for enhanced adhesive bonding,” *CIRP Ann. - Manuf. Technol.*, vol. 64, no. 1, pp. 527–530, 2015.
[183] G. Rotella, M. Alfano, T. Schiefer, and I. Jansen, “Evaluation of mechanical and laser surface pre-treatments on the strength of adhesive bonded steel joints for the automotive industry,” *J. Adhes. Sci. Technol.*, vol. 30, no. 7, pp. 747–758, Apr. 2016.
[184] G. Rotella, M. Alfano, T. Schiefer, and I. Jansen, “Enhancement of static strength and long term durability of steel/epoxy joints through a fiber laser surface pre-treatment,” *Int. J. Adhes. Adhes.*, vol. 63, pp. 87–95, Dec. 2015.
[185] P. Molitor and T. Young, “Investigations into the use of excimer laser irradiation as a titanium alloy surface treatment in a metal to composite adhesive bond,” *Int. J. Adhes. Adhes.*, vol. 24, no. 2, pp. 127–134, Apr. 2004.
[186] R. Malhotra, I. Saxena, K. Ehmann, and J. Cao, “Laser-induced plasma micro-machining (LIPMM) for enhanced productivity and flexibility in laser-based micro-machining processes,” *CIRP Ann. - Manuf. Technol.*, vol. 62, no. 1, pp. 211–214, 2013.
[187] L. Romoli *et al.*, “Ultrashort pulsed laser drilling and surface structuring of microholes in stainless steels,” *CIRP Ann. - Manuf. Technol.*, vol. 63, no. 1, pp. 229–232, 2014.
[188] I. G. Zewi, F. Flashner, H. Dodiuk, and L. Drori, “Durability of structural adhesive joints,” *Int. J. Adhes. Adhes.*, vol. 4, no. 3, pp. 137–139, Jul. 1984.
[189] P. Molitor, V. Barron, and T. Young, “Surface treatment of titanium for adhesive bonding to polymer composites: a review,” *Int. J. Adhes. Adhes.*, vol. 21, no. 2, pp. 129–136, 2001.
[190] K. Liu, X. Yao, and L. Jiang, “Recent developments in bio-inspired special wettability,” *Chem. Soc. Rev.*, vol. 39, no. 8, pp. 3240–3255, Jul. 2010.
[191] M. Huang, F. Zhao, Y. Cheng, N. Xu, and Z. Xu, “Large area uniform nanostructures fabricated by direct femtosecond laser ablation,” *Opt. Express*, vol. 16, no. 23, pp. 19354–19365, Nov. 2008.

[192] D. Puerto *et al.*, "Femtosecond laser-controlled self-assembly of amorphous-crystalline nanogratings in silicon," *Nanotechnology*, vol. 27, no. 26, p. 265602, 2016.
[193] N. M. Bulgakova, R. Stoian, A. Rosenfeld, I. V. Hertel, W. Marine, and E. E. B. Campbell, "A general continuum approach to describe fast electronic transport in pulsed laser irradiated materials: The problem of Coulomb explosion," *Appl. Phys. A*, vol. 81, no. 2, pp. 345–356, Jul. 2005.
[194] S. Adachi, "Front Matter," in *Properties of Group-IV, III-V and II-VI Semiconductors*, John Wiley & Sons, Ltd, 2005, pp. i–xvii.
[195] L. V. Keldysh, "Ionization in the Field of a Strong Electromagnetic Wave," *Zh Eksperim Teor Fiz*, vol. Vol: 47, Nov. 1964.
[196] S. Anisimov, V. Benderskii, and D. Farkas, "Nonlinear photoelectric effect in laser-bombarded metals," *Sov Phys*, vol. 122, no. 6, pp. 185–222, Jun. 1977.
[197] M. Henyk, D. Wolfframm, and J. Reif, "Ultra short laser pulse induced charged particle emission from wide bandgap crystals," *Appl. Surf. Sci.*, vol. 168, no. 1–4, pp. 263–266, Dec. 2000.
[198] A. V. Bulgakov, I. Ozerov, and W. Marine, "Silicon clusters produced by femtosecond laser ablation: non-thermal emission and gas-phase condensation," *Appl. Phys. A*, vol. 79, no. 4–6, pp. 1591–1594, Sep. 2004.
[199] F. Costache, S. Kouteva-Arguirova, and J. Reif, "Sub–damage–threshold femtosecond laser ablation from crystalline Si: surface nanostructures and phase transformation," *Appl. Phys. A*, vol. 79, no. 4–6, pp. 1429–1432, Sep. 2004.
[200] Y. Zhang, B. Lauer, B. Neuenschwander, and V. Romano, "Numerical study of the influence of picosecond laser spot size on ablated depth and threshold fluence of metal," 2016, vol. 9735, p. 97350M–97350M–11.
[201] F. Zimmermann, A. Plech, S. Richter, S. Döring, A. Tünnermann, and S. Nolte, "Structural evolution of nanopores and cracks as fundamental constituents of ultrashort pulse-induced nanogratings," *Appl. Phys. A*, vol. 114, no. 1, pp. 75–79, Jan. 2014.
[202] P. Glansdorff and I. Prigogine, *Thermodynamic Theory of Structure, Stability and Fluctuations*. Wiley, 1971.
[203] P. Galenko, "Extended thermodynamical analysis of a motion of the solid-liquid interface in a rapidly solidifying alloy," *Phys. Rev. B*, vol. 65, no. 14, p. 144103, Mar. 2002.
[204] C. V. Shank, R. Yen, and C. Hirlimann, "Time-Resolved Reflectivity Measurements of Femtosecond-Optical-Pulse-Induced Phase Transitions in Silicon," *Phys. Rev. Lett.*, vol. 50, no. 6, pp. 454–457, Feb. 1983.
[205] D. Perez and L. J. Lewis, "Molecular-dynamics study of ablation of solids under femtosecond laser pulses," *Phys. Rev. B*, vol. 67, no. 18, p. 184102, May 2003.
[206] M. V. Sosnova, N. L. Dmitruk, A. V. Korovin, S. V. Mamykin, V. I. Mynko, and O. S. Lytvyn, "Local plasmon excitations in one-dimensional array of metal nanowires for sensor applications," *Appl. Phys. B*, vol. 99, no. 3, pp. 493–497, May 2010.
[207] Y. Du, L. Shi, M. Hong, H. Li, D. Li, and M. Liu, "A surface plasmon resonance biosensor based on gold nanoparticle array," *Opt. Commun.*, vol. 298–299, pp. 232–236, Jul. 2013.
[208] "Encyclopedia of Sensors, 10-Volume Set." [Online]. Available: http://www.aspbs.com/eos.html. [Accessed: 11-Mar-2017].
[209] L. Fedorenko, S. Mamykin, O. Lytvyn, Y. Burlachenko, and B. Snopok, "Nanostructuring of Continuous Gold Film by Laser Radiation Under Surface Plasmon Polariton Resonance Conditions," *Plasmonics*, vol. 6, no. 2, pp. 363–371, Jun. 2011.

[210] J. Chandezon, M. T. Dupuis, G. Cornet, and D. Maystre, “Multicoated gratings: a differential formalism applicable in the entire optical region,” *JOSA*, vol. 72, no. 7, pp. 839–846, Jul. 1982.
[211] S. Malynych, “SURFACE PLASMON RESONANCES AND THEIR MANIFESTATION IN THE OPTICAL PROPERTIES OF NANOSTRUCTURES OF NOBLE METALS,” *Ukr. J. Phys.*
[212] C. F. Bohren and D. R. Huffman, “Frontmatter,” in *Absorption and Scattering of Light by Small Particles*, Wiley-VCH Verlag GmbH, 1998, pp. i–xiv.
[213] A. Polman and H. A. Atwater, “Photonic design principles for ultrahigh-efficiency photovoltaics,” *Nat. Mater.*, vol. 11, no. 3, pp. 174–177, Mar. 2012.